

**Development of a novel method and apparatus for analysis of
die dynamics of an isothermal thermoset pultrusion process**

Entwicklung einer neuen Methode und Apparatur zur
Untersuchung der Werkzeugdynamik
beim isothermischen Duroplast-Pultrusionsverfahren

Von der Fakultät für Energie-, Verfahrens- und Biotechnik
der Universität Stuttgart
zur Erlangung der Würde eines
Doktor-Ingenieurs (Dr.-Ing.) genehmigte Abhandlung

vorgelegt von
Sathis Kumar Selvarayan
aus Poomandampalayam, Indien

Hauptberichter: Prof. Dr.-Ing. Götz T. Gresser
Mitberichter: Prof. Dr.-Ing. Christian Bonten

Tag der mündlichen Prüfung: 02.06.2021

Deutsche Institute für Textil- und Faserforschung Denkendorf in Zusammenarbeit mit
dem Institut für Textil- und Fasertechnologien der Universität Stuttgart

2021

...what learnt is mere handful and what yet to learn amounts the world...

-Avvaiyaar, poetess 3rd century BCE

To my beloved Parents and Wife, respected Teachers and the Almighty

Acknowledgements

This dissertation is a part of my work as a DAAD-PhD scholar and as a research associate at the German Institutes of Textile and Fibre Research (DITF) in Denkendorf.

First and foremost, I would like to express my deepest appreciation to my main supervisor Prof. Dr. Götz T. Gresser for his continuous support and guidance during my work. His encouragement throughout the work was the key to conduct rewarding and memorable research. I appreciate all his contributions of time, ideas, and funding to make my experience productive and stimulating. My sincere thanks and deep gratitude to my co-supervisor Prof. Dr. Markus Milwich, for his constant motivation and untiring help during my work. He was always willing to give his best suggestions and out of the box ideas. I also sincerely thank my external co-supervisor Prof. Dr. Christian Bonten for his support and help during this work.

I express my sincere thanks and gratitude to DAAD for providing me with the funding at the beginning of this work.

I thank my colleagues Martin Uwe-Witt, Patrick Kaiser and my ex-colleagues Dr. Simon Küppers, Dr. Ravand Gohmeshi and Dagmar Ewert for the fruitful discussions and suggestions on the pultrusion process. I would like to extend my thanks to my colleagues Larissa Born and Lena Müller and my ex-colleagues Benjamin Lehman and Hans Christof for their support in the laboratory and organisation of materials. I also thank my colleagues of the mechanical and electrical workshops without whose help realisation of the Die Dynamic Simulator wouldn't have been possible.

The names of the students who extended their help and assistance in the form of HiWi are not cited in this work. Therefore, I explicitly thank Tessa Rudolf, Christine Kettenbach, Bianca Schwabe, Ashok Rajpurohit, Thomas Kaiser and Alexander Kapp here for their assistance.

Finally, and most importantly, I thank my wife Kavitha for her endless support, love and patience and my daughter Mullai for rejuvenating my mind from work and pointing out the truly important things in life.

Denkendorf, 09 September 2020

Sathis Kumar Selvarayan

Contents

List of figures.....	VII
List of tables.....	XIII
List of symbols.....	XV
List of abbreviations.....	XIX
Terms and definitions.....	XXI
Abstract.....	XXIII
Kurzfassung.....	XXV
1 Introduction.....	1
1.1 Background.....	1
1.2 Motivation.....	2
2 Pultrusion – State-of-the-art.....	5
2.1 Pultrusion process.....	5
2.2 Reinforcements and matrices for pultrusion.....	7
2.2.1 Fibre reinforcements.....	8
2.2.2 Matrices.....	8
2.2.3 Mould release agents.....	9
2.3 Resistive forces during pultrusion.....	10
2.4 Material behaviour and characterisation.....	14
2.4.1 Reinforcement behaviour.....	14
2.4.2 Characteristic analysis of resin formulation.....	18
2.5 Conclusion of the state-of-the-art.....	24
3 Objectives and approach.....	27
3.1 Research hypothesis.....	27
3.2 Objective and scope of the thesis.....	27
3.3 Thesis methodology.....	28
4 Development of rotating core method.....	31
4.1 Rotating core method.....	31
4.1.1 Representation of pultrusion in linear cartesian coordinates.....	32
4.1.2 Transformation from the linear system to a rotational system.....	33
4.2 Development of an apparatus to quantify die dynamics.....	36
4.2.1 Design strategy.....	37

4.2.2	Hardware setup.....	41
4.2.3	System control and data acquisition setup.....	43
4.2.4	Software interface	44
4.2.5	Calibration of DDS	45
4.3	Conclusion of the development of the rotating core method.....	48
5	Measurement process development for DDS	49
5.1	Materials used	49
5.2	Development of measurement process for DDS	50
5.2.1	Fibre volume fraction determination	51
5.2.2	Preparation of the core with impregnated fibres	51
5.2.3	Torque measurement on DDS.....	58
5.2.4	Temperature measurement in winding layers	60
5.3	Influence of preparatory process variables on torque measurements.....	63
5.4	Optical evaluations	66
5.4.1	Influence of winding tension	66
5.4.2	Through-thickness resin flow	67
5.4.3	Fibre distribution	69
5.4.4	Resin layer thickness	70
5.5	Conclusion of measurement process development	71
6	Characterisation of properties of resin formulation	73
6.1	Resin formulations.....	73
6.2	Curing kinetics determination using DSC	73
6.3	Rheological behaviour analysis using rheometer.....	76
6.4	Surface energy analysis.....	79
6.5	Conclusion of resin formulation characterisation.....	81
7	Experimental investigation on torque evolution	83
7.1	Experimental design.....	83
7.2	Parametric study on DDS.....	84
7.2.1	Process parameters.....	85
7.2.2	Geometrical parameters	87
7.2.3	Effect of fibre volume fraction	90
7.2.4	Effect of internal mould release	91
7.3	Viscous and frictional components estimation	94
7.4	Die dynamics model.....	95

7.5	Statistical analysis on process parameter interactions	98
7.6	Conclusion of torque evolution behaviour investigation	101
8	Validation of rotating core method using pultrusion.....	103
8.1	Bench-scale pultrusion	103
8.1.1	Fibre volume fraction	104
8.1.2	Temperature profile measurement	105
8.1.3	Pulling force measurement	106
8.2	Comparison and validation of the pulling force models.....	108
8.3	Conclusion of rotating core method validation	111
9	Summary and future scope.....	113
9.1	Summary	113
9.2	Future scope	115
Bibliography		XXVII
Appendix		XXXVIII

List of figures

Figure 1.1:	Typical cross-sections of pultruded profiles.	1
Figure 1.2:	Examples of application of pultruded profiles: (a) train luggage rack and (b) spar caps in a windmill blade.	2
Figure 1.3:	Example of a tensile failure of the profile caused by mould sticking.	3
Figure 2.1:	Schematic representation of a typical thermoset pultrusion line.	5
Figure 2.2:	Schematic of impregnation chambers: (a) variants of open bath impregnation, (b) variants of closed injection pultrusion.	6
Figure 2.3:	Cross-section of a typical linear pultrusion die.	7
Figure 2.4:	Schematic of typical reinforcement structures of a pultrusion profile.	8
Figure 2.5:	Pultrusion die dynamics (resin phases and force components).	11
Figure 2.6:	Schematic illustration of the compaction zone of a typical pultrusion die with – (a) tapered, (b) parabolic, and (c) rounded entrance geometry.	16
Figure 2.7:	Resin flow mechanisms during composite processing.	17
Figure 2.8:	Schematic of typical DSC curves showing the area under the exothermic peaks H_{tot} and H_t up to time t : (a) dynamic temperature scan, (b) isothermal scan.	19
Figure 2.9:	Schematic representation of cross-linking phenomena during the curing of thermosets: (a) monomer stage, (b) linear growth and branching (c) gelling incomplete cross-linked network, (d) fully cured thermoset.	21
Figure 2.10:	Schematic illustration of – (a) contact angle formed by sessile liquid droplet with a solid surface and (b) liquid lamella on the Wilhelmy plate.	23
Figure 3.1:	Transformation from linear motion to rotational motion.	29
Figure 3.2:	Flow diagram representing the approach of the thesis.	29
Figure 4.1:	Schematic of the cylindrical die and core setup in the rotating core method.	31
Figure 4.2:	Generic representation of a simple rectangular profile in an Eulerian and a Lagrangian frame of reference in the cartesian coordinates.	32
Figure 4.3:	Schematic representation of transformation of the infinitesimal width of fibre-matrix from the linear cartesian to rotational cylindrical coordinates.	33
Figure 4.4:	Illustration of torque exerted by the rotating fibre-matrix on the die wall and planar Couette flow as well as the resin velocity profile in the thin fibreless resin layer between moving fibre-matrix and the stationary die wall in the die-core setup.	34
Figure 4.5:	Schematic of the cross-sections of the die-core assembly with different radii and annular thicknesses utilised in this work.	38
Figure 4.6:	Cross-section of the die-core assembly showing rounded entry edge and the cavity for a thermocouple.	39
Figure 4.7:	Cross-section of – (a) the die-core arrangement with sealing rings and (b) isometric view of the sealing ring.	39
Figure 4.8:	The dies and cores utilised in this work: (a) dies with inner radius 11 mm and 5.5 mm (left to right); (b) cores with radius 10 mm, 9 mm, 4.5 mm and 3.5 mm with respective sealing rings (left to right).	40

Figure 4.9: Concept of the DDS for quantifying the die dynamics of an isothermal thermoset pultrusion process – (a) front view with the lowered lifting table and (b) side view with the raised lifting table.....	41
Figure 4.10: Heating module assembly offset-section showing the die and core arrangement within the heating module and magnification showing fibre-matrix between the die and core.....	42
Figure 4.11: Schematic setup of data acquisition, processing and visualisation systems as well as control systems in DDS.	43
Figure 4.12: The user interface of the DDS and its modules.	44
Figure 4.13: The DDS apparatus and its components.	45
Figure 4.14: The temperature difference between the set temperature and the heating module and die temperatures.	46
Figure 4.15: Linear relationship between the control voltage and the angular velocity of the core on DDS.....	47
Figure 4.16: Torque measured at various temperatures and angular speeds with the 10 mm radius core and sealing rings on the DDS.....	47
Figure 5.1: Experimental steps involved in quantifying die dynamics using the rotating core method.	50
Figure 5.2: Preparation of pre-impregnated fibre wound core using a 4-axis filament winding machine: (a) schematic representation of the fibre path from the spool to the core; (b) filament winding machine and its components.	52
Figure 5.3: The delivery head and a 10 mm radius DDS core being wound with impregnated roving.	53
Figure 5.4: Selected winding parameters: (a) the traverse speeds of winding unit for various initial core radii at fibre volume fractions $\varphi_{fa} = 0.61$ and $\varphi_{fa} = 0.56$; (b) the decreasing winding speed with increasing winding thickness.....	55
Figure 5.5: Effect of increasing brake pressure on (a) the mean winding tension, and (b) the calculated total compaction pressure on the core.	56
Figure 5.6: Final diameter of the cores wound for $\varphi_{fa} = 0.61$ with increasing applied brake pressure: (a) 20 mm and 18 mm cores; (b) 9 mm and 7 mm cores.	57
Figure 5.7: Final diameter of the cores wound for $\varphi_{fa} = 0.56$ with increasing applied brake pressure: (a) 20 mm and 18 mm cores; (b) 9 mm and 7 mm cores.	57
Figure 5.8: DDS at (a) the core mounting position with lowered lifting table and (b) the measuring position with raised lifting table.	59
Figure 5.9: Characteristic torque and temperature data measured on the DDS.....	60
Figure 5.10: Thermocouples integrated during filament winding in between the layers of the windings, the die and the core – (a) Photograph of the core with thermocouples and (b) schematic illustration of the position of the thermocouples in the winding cross-section.....	61
Figure 5.11: Temperature profiles measured with integrated thermocouples at set die temperature of 120 °C: measurements with die having 11 mm inner radius and (a) annular gap of 1 mm, and (b) annular gap of 2 mm.	61
Figure 5.12: Predicted temperature profiles of the in-between layers for the windings in an: (a) annular gap of 1 mm, and (b) annular gap of 2 mm.	62
Figure 5.13: Relative change in the cross-sectional area of the core (ΔA_{Co}) with respect to the cross-sectional area of the fibre-matrix (A_w) with increasing temperature for different core radius (r_{Co}) and annular gaps (h_a).	63

Figure 5.14: Torque measured with varying core rotational velocity and fibre volume fractions in the 11 mm radius die with dry fibres wound at 0.3 MPa applied brake pressure on 10 mm radius core.....	64
Figure 5.15: Torque measured with impregnated fibre windings: change in the initial torque with (a) varying applied brake pressure during filament winding for $\varphi_{fa} = 0.61$; and (b) varying fibre volume fraction with 0.3 MPa applied brake pressure during filament winding.....	65
Figure 5.16: Schematic illustration of fibre compaction and excess resin squeeze out at the rounded entry edge of the die during the core insertion phase.	65
Figure 5.17: Scanning electron micrographs of the surface of composite samples from DDS wound with varying winding tensions: micrographs of samples wound with (a1) 0.1 MPa, (b1) 0.2 MPa and (c1) 0.3 MPa applied brake pressure; (a2), (b2) and (c2) respective micrographs analysed for the fibre orientation showing colour-coded orientations (cyan = 0° , blue = $+\theta$ and green = $-\theta$) and; (a3), (b3) and (c3) respective distribution of fibre orientation.	67
Figure 5.18: Micrographs of the coloured samples: (a1) as wound-cured, (b1) cured in the die with stationary core, and (c1) cured in the die with rotating core; (a2 - c2) respective colour filtered images.	68
Figure 5.19: Images of the sample cured on a stationary core showing colour gradience from bottom to top of the sample – (a) photograph and (b) colour filtered photograph.	68
Figure 5.20: Scanning electron micrographs of longitudinal cross-section of the samples: (a) with $\varphi_{fa} = 0.61$ and $h_a = 1$ mm, (b) with $\varphi_{fa} = 0.61$ and $h_a = 2$ mm, and (c) with $\varphi_{fa} = 0.56$ and $h_a = 1$ mm.....	69
Figure 5.21: (a) Scanning electron micrograph showing resin layer thickness between the die wall and the outer edge of the sample at $\varphi_{fa} = 0.61$ and (b) the gaussian distribution of resin layer thickness.	70
Figure 6.1: Specific heat flow measured in the DSC experiments for various resin formulations – (a) Isothermal runs at different temperatures, and (b) dynamic scans of samples using various heating rates.....	74
Figure 6.2: Calculated curing behaviour of the resin formulations – (a) degree of cure and (b) rate of curing.....	75
Figure 6.3: Curve fitting of KS model to the experimental DSC data – (a) isothermal runs data and (b) dynamic scan data.	76
Figure 6.4: Viscosity development of the resin formulations measured at various temperatures	77
Figure 6.5: (a) Gelation time estimated from the cross-over point of the storage and loss modulus data and (b) degree of conversion estimated from the curing kinetics for the respective gelation time.....	78
Figure 6.6: Surface tension of the resin formulations and their components measured using the Wilhelmy plate method.....	79
Figure 6.7: (a) Contact angles of the resin formulation droplets with the steel die surface at different temperatures measured using contact angle goniometer and (b) work of adhesion calculated from the contact angle and surface tension measurements.....	80
Figure 7.1: Characteristic torque-time curves measured at $T_{die} = 120$ °C and 140 °C. 85	

Figure 7.2:	Characteristic torque-time curves measured at surface velocities $v_s = 100 \text{ mm min}^{-1}$, 200 mm min^{-1} , and 300 mm min^{-1}	86
Figure 7.3:	Typical torque-time curves for varying die-core geometry.....	88
Figure 7.4:	Typical torque-time curves for varying winding thickness.....	89
Figure 7.5:	(a) Torque-time curve for varying fibre volume fraction and (b) photographs of the cured samples from respective DDS measurements.....	90
Figure 7.6:	(a) Measured torque-time curves of the samples with varying IMR concentration in the resin formulation and (b) photographs of the cured samples with respective IMR concentrations.	92
Figure 7.7:	Schematic illustration of phenomenon taking place during polymerisation at the die wall-resin film interface in the DDS: (a) as introduced fibre-matrix; (b) formation of IMR interphase in the fibreless resin-film; (c) scenario of cohesive fracture within cured matrix; and (d) scenario of cohesive fracture in IMR interphase.	93
Figure 7.8:	Gelation point determination for DDS measurements from the degree of conversion determined at the gel point on the rheometer (measurement temperature $140 \text{ }^\circ\text{C}$).	94
Figure 7.9:	Typical viscous and frictional zones in the torque-time curve separated by the gelation line.....	95
Figure 7.10:	Torque-time relationship model for the tested fibre-matrix system.....	96
Figure 7.11:	Sum of the shear stress calculated from the measured torque for a measurement period of 800 s.	98
Figure 7.12:	Pareto plot of the standardised effects of the parameters on the calculated shear stress.....	99
Figure 7.13:	Contour plots of the shear stresses ($\tau_{r\theta,800s}$) at various parameter combinations. (<i>Axis to be read as: ordinate*abscissa. e.g. V*T in graph title denotes velocity in ordinate and temperature in abscissa</i>).	100
Figure 8.1:	Core components of the bench-scale pultrusion line – (a) side view and (b) front view.....	103
Figure 8.2:	Schematic of the cross-section and the dimensions of the pultrusion die used for the pultrusion experiments.	104
Figure 8.3:	Temperature profile measured in-line during the pultrusion experiments at $120 \text{ }^\circ\text{C}$ and $140 \text{ }^\circ\text{C}$ at the pulling velocities 100 mm min^{-1} and 300 mm min^{-1} respectively.	105
Figure 8.4:	Characteristic pulling force measured in-line during the pultrusion with the varying process and material parameters	107
Figure 8.5:	Average pulling force measured during the pultrusion experiments with the varying process and material parameters.	107
Figure 8.6:	Calculated degrees of conversion for a residence time of 210 s in the pultrusion die and the respective time required for the equivalent degree of conversion on DDS at die temperatures of – (a) $140 \text{ }^\circ\text{C}$ and (b) $120 \text{ }^\circ\text{C}$...	108
Figure 8.7:	Typical lower and upper limits of the torque-time curve considered for the calculation of the force equivalence between DDS and pultrusion.....	109
Figure 8.8:	Scanning electron micrographs of the cross-section of the pultruded profiles with fibre volume fraction (a) $\varphi_f = 0.61$ and (b) $\varphi_f = 0.56$	110

Figure A 1: T120-V100-R5.5-H1-FV0.61-IMR3.0.....	XXXVIII
Figure A 2: T140-V100-R5.5-H2-FV0.61-IMR3.0.....	XXXVIII
Figure A 3: T120-V300-R5.5-H2-FV0.61-IMR3.0.....	XXXIX
Figure A 4: T140-V300-R5.5-H1-FV0.61-IMR3.0.....	XXXIX
Figure A 5: T120-V300-R11-H1-FV0.56-IMR0.5.....	XXXIX
Figure A 6: T140-V300-R11-H1-FV0.61-IMR0.5.....	XL
Figure A 7: T120-V300-R11-H1-FV0.61-IMR0.5.....	XL
Figure A 8: T120-V100-R11-H2-FV0.61-IMR3.0.....	XL
Figure A 9: T140-V100-R11-H1-FV0.61-IMR3.0.....	XLI
Figure A 10: T120-V300-R11-H1-FV0.61-IMR3.0.....	XLI
Figure A 11: T140-V300-R11-H1-FV0.61-IMR3.0.....	XLI
Figure A 12: T140-V200-R11-H1-FV0.61-IMR3.0.....	XLII
Figure A 13: T120-V300-R11-H2-FV0.61-IMR3.0.....	XLII
Figure A 14: T120-V300-R11-H1-FV0.56-IMR3.0.....	XLII
Figure A 15: T140-V300-R11-H1-FV0.61-IMR1.5.....	XLIII
Figure A 16: T140-V100-R11-H1-FV0.61-IMR0.5.....	XLIII
Figure B 1: Gelation point determination for DDS measurements from the degree of conversion determined at the gel point on the rheometer (measurement temperature 120 °C).	XLIV
Figure C 1: Characteristic pulling force measured in-line during the pultrusion with the varying process and material parameters.	XLIV

List of tables

Table 2.1:	State-of-the-art inline pulling force measurement methods.	13
Table 2.2:	List of kinetic models for predicting the degree of cure in epoxy pultrusion.	20
Table 5.1:	Properties of the resin and the curing agent employed in this work.	49
Table 5.2:	Properties of the glass rovings used.	50
Table 5.3:	Properties of the release agents used	50
Table 5.4:	The possible winding angles for the annular length of 100 mm in combination with listed parameters.	54
Table 6.1:	Resin formulations and their nomenclature.....	73
Table 6.2:	Kinetic parameters determined from curve fitting DSC experimental data using KS model.	76
Table 7.1:	List of parameters studied and the selected trial space.	83
Table 7.2:	List of test set generated using DOE.....	84
Table 8.1:	Comparison of measured forces from pultrusion and DDS measurements.	109

List of symbols

Symbol	Unit	Description
A_{die}	mm ²	Cross-sectional area of the pultrusion die
A_i	min ⁻¹	Arrhenius constant
A_{roving}	mm ²	Cross-sectional area of the roving
A_{sc}	mm ²	Inner surface area of the cylindrical die in the annular region
A_{sr}	mm ²	Surface area of the pultrusion die cavity
c	-	Dimensionless shape factor
C_1	-	Gebart's model constant
$dx, d\theta$	mm	Infinitesimal length of the fibre-matrix
E	N m ⁻¹	Fibre bending stiffness
E_i	J mol ⁻¹	Activation energy
E_η	J mol ⁻¹	Viscous activation energy
F_{die}	N	Sum of forces that arise inside the straight segment of the pultrusion die
F_{cdie}	N	Force acting on the cylindrical die in DDS
F_{coll}	N	Collimation force
F_{comp}	N	Compaction force
F_{fric}	N	Frictional force
F_{pull}	N	Total pulling force
F_{roving}	N	Winding tension of the roving
F_{vis}	N	Viscous force
G	MPa	Shear modulus
H	W g ⁻¹	Specific rate of heat transfer
h	mm	Thickness of the pultrusion die cavity
h_a	mm	Thickness of the annular gap
h_{roving}	mm	Thickness of the roving
K	m ²	Permeability of the reinforcements
k, m, n	-	Reaction rate constants
K_η	-	Empirical constant in rheological model
L	mm	Length of the straight segment of the pultrusion die cavity
L_a	mm	Length of the annulus
L_{roving}	mm	Length of roving wound on the core for DDS measurements
L_{WP}	m	Contact surface length of Wilhelmy plate
M	N m	Torque
M_{cdie}	N m	Torque experienced by the cylindrical die in DDS
m_{roving}	g	Mass of the roving

List of symbols

n	-	Number of winding layers
n_r	-	Number of rovings utilised for pultrusion experiments
p	MPa	Fibre network compaction pressure
p_n	MPa	Normal pressure exerted by the composite on the die wall
p_r	MPa	Resin pressure
r	mm	Radius
r_{Co}	mm	Radius of the core
r_{Di}	mm	Inner radius of the cylindrical die
r_{rf}	mm	Wound radius of the fibre-matrix
r_f	mm	Radius of the fibre
R	J mol ⁻¹ K ⁻¹	Universal gas constant
R_a	µm	Roughness parameter
t	s	Time
t_0	s	Time at which the moving fibre-matrix enters the straight segment of the pultrusion die cavity
t_{gel}	s	Time at which the resin formulation undergoes gelation
t_L	s	Time at which the fibre-matrix exits the die cavity
T_i	°C	Temperature of the i^{th} layer of the winding in DDS
T_{cure}	°C	Curing temperature
T_g	°C	Glass transition temperature
T_{cdie}	°C	Temperature measured in the cylindrical die in DDS
$T_{cdie\ wall}$	°C	Temperature measured on the cylindrical die wall in DDS
$T_{(n-1)^{th}\ layer}$	°C	Temperature measured between n^{th} and $(n-1)^{\text{th}}$ layer of the windings in DDS
$T_{core\ surface}$	°C	Temperature measured on the core surface in DDS
T_{tex}	g km ⁻¹	Linear density of the roving
U_w	rpm	Rotational speed of the winding core
$V_{annulus}$	mm ³	Volume of the annulus
V_{resin}	mm ³	Volume of the matrix
V_{roving}	mm ³	Volume of fibre present in annular volume
w	mm	Width of the pultrusion die cavity
W_A	mJ m ⁻²	Work of adhesion
W_{roving}	mm	Spread width of the roving
x_0	-	Beginning position of the straight segment of the pultrusion die cavity
x_{gel}	-	Position in the die cavity at which the resin formulation gels
x_L	-	End position of the die cavity

α	-	Degree of cure
α_T	$\text{m m}^{-1} \text{K}^{-1}$	Thermal expansion coefficient
β	-	Fibre span length to span height constant
δ	$^\circ$	Phase angle
Δt	s	Residence time of the fibre-matrix inside the die cavity
η	Pa s	Viscosity of the resin formulation
η_∞	Pa s	Empirical constant in rheological model
μ_k	-	Kinetic friction coefficient
θ	$^\circ$	Taper angle of the die entry
θ_c	$^\circ$	Young's contact angle
θ_w	$^\circ$	Winding angle
λ	μm	Thickness of the fibreless resin film
ρ_f	g mm^{-3}	Density of the fibres
ρ_{resin}	g mm^{-3}	Density of the resin formulation
σ	MPa	Stresses experienced by the fibre network
σ_{adh}	MPa	Adhesive strength of resin to die wall
φ_f	-	Fibre volume fraction
φ_{fa}	-	Fibre volume fraction in annular volume
ω	rad s^{-1}	Angular velocity
γ	-	Shear strain
$\dot{\gamma}$	s^{-1}	Shear rate
γ_{lv}	mN m^{-1}	Interfacial tension between liquid and vapour
γ_{sv}	mN m^{-1}	Interfacial tension between solid and vapour
γ_{sl}	mN m^{-1}	Interfacial tension between solid and liquid
v_{fluid}	m s^{-1}	Fluid flow velocity
v_{pull}	mm min^{-1}	Pulling speed in pultrusion process
v_s	mm min^{-1}	Outer surface velocity of the fibre-matrix in DDS
v_w	mm s^{-1}	Traverse speed of winding head
τ	MPa	Shear stress or stress tensor
τ_{ij}	MPa	Directional stress components

List of abbreviations

BPA	Bisphenol-A
BADGE	Bisphenol-A-di-glycidyl ether
CAGR	Compounded annual growth rate
CFM	Cut fibre mat
DDS	Die Dynamics Simulator
DITF	Deutsche Institute für Textil- und Faserforschung
DSC	Dynamic Scanning Calorimetry
DOE	Design of experiments
FRP	Fibre reinforced plastic
FSR	Force sensing resistors
FTIR	Fourier transform infrared spectroscopy
IMR	Internal Mould Release
ISO	International Organisation for Standardisation
KS	Kamal-Sourour
phr	Parts per hundred parts of the resin
PID	Proportional-Integral-Derivative
POM	Polyoxymethylene
PTFE	Polytetrafluoroethylene
rpm	Revolution per minute
UD	Unidirectional
UP	Unsaturated Polyester
VE	Vinyl ester

Terms and definitions

The following glossary of terms eases the understanding of the terms used in this dissertation.

Die: The term die means a solid body that gives shape to the fibre reinforced plastics or composites being consolidated. Literature uses the terms **form, tool, mould** and **die** to define such solid bodies.

Fibre: The term fibre means the continuous fibres or filaments unless otherwise explicitly stated as short fibre.

Roving: The term roving means a collection of continuous fibres or filaments.

Resin formulation: The term resin formulation means a mixture of resin or pre-polymer, curing agent and additives which on polymerised or cured state binds the fibres together. Literature uses the term **matrix** to define the cured resin system.

Fibre-matrix: The term fibre-matrix means a formulation containing a resin system and fibres. Literature uses the term **pre-impregnated fibres or pre-impregnated rovings** to define such formulations.

Abstract

Pultrusion is a continuous process to manufacture constant cross-sectional fibre reinforced composite profiles. The profiles take their shape as the continuously moving fibre-matrix combination consolidates inside the cavity of a pultrusion die. The temperature-induced viscosity and volumetric changes of the fibre-matrix during the consolidation as well as the friction between the die wall and the moving fibre-matrix generates shear and normal forces that act on the die wall – phenomena known as “die dynamics”. Quantification and analysis of the die dynamics are crucial to understand and control the pultrusion process. However, state-of-the-art methods available to characterise the pultrusion process have limited capability to record the forces that act on the die wall at each position along the length of the pultrusion die. Further, the on-line measurement techniques demand full-scale pultrusion line which, in general, are resource intensive. In addition, the available methodologies have not considered the impact of process additives on the die dynamics.

This research work, therefore, focuses on developing a resource-efficient offline testing method to characterise the die dynamics of a thermoset pultrusion process and to pre-determine the required process parameters for a given fibre-matrix combination. In the newly developed approach, called rotating core method, pre-impregnated rovings wound on a solid core with defined fibre volume fraction rotates about the axis of the core inside a hollow cylindrical heated die. The rotational velocity of the rotating core is set to be identical to the line speed of the pultrusion process. The rotating fibre-matrix undergo temperature-induced polymerisation leading to the transformation of the fibre-matrix into a solid composite within the cylindrical die. This mimics the dominant phenomena that occur inside a pultrusion die in the pultrusion process.

An apparatus developed within the scope of this work, the Die Dynamics Simulator (DDS), for the first time allows to continuously measure the torque exerted by the rotating fibre-matrix on the DDS die during the polymerisation process. The measured torque represents the resistive forces that arise within the die during the consolidation of the fibre-matrix combination. Evaluation of the curing kinetics and rheology of the resin formulations facilitates the characterisation of their polymerisation behaviour enabling identification of the components of the resistive forces. Further, this work investigates the influence of the following parameters on die dynamics using the developed apparatus: (1) die temperature, (2) velocity of the fibre-matrix, (3) contact area of the die and the fibre-matrix, (4) part thickness, (5) fibre volume fraction, and (6) process additive – internal mould release (IMR). Subsequently, the developed methodology is validated against the pultrusion process using a lab-scale pultrusion line.

The results show the dependency of the resistive forces on the individual and the interactions between multiple parameters. More importantly, the experiments conducted with varying concentrations of IMR permitted to evaluate the implication of the mould release on the evolving resistive forces within the die. The results further provide insight at which phase of the polymerising matrix is the IMR most effective. Comparison of the measured forces on the DDS and from that measured on the pultrusion line show good fit for higher fibre volume fractions of the consolidated composite.

Kurzfassung

Die Pultrusion ist ein kontinuierlicher Prozess zur Herstellung von faserverstärkten Verbundwerkstoffprofilen mit konstantem Querschnitt. Die Profile nehmen ihre Form an, während dem die sich kontinuierlich bewegende Faser-Matrix-Mischung in der Kavität eines Pultrusionswerkzeugs aushärtet. Die durch die Temperatur induzierte Änderung der Viskosität und des Volumens der Faser-Matrix-Mischung während der Matrix-Polymerisation sowie die Reibung zwischen der Werkzeugwand und der sich bewegenden Faser-Matrix-Mischung führen zur Entwicklung von Widerständen an der Werkzeugoberfläche – Phänomene, die als "Werkzeugdynamik" bezeichnet werden. Die Quantifizierung und Analyse der Werkzeugdynamik ist für das Verständnis und die Steuerung des Pultrusionsprozesses entscheidend. Die verfügbaren Methoden nach dem Stand der Technik zur Charakterisierung des Pultrusionsprozesses sind jedoch in der Lage, die auftretende Widerstandskräfte entlang der Oberfläche einer Pultrusionswerkzeuge, nur begrenzt zu erfassen. Darüber hinaus erfordern die Inline-Messtechniken eine Serien-Pultrusionslinie, was im Allgemeinen ressourcenintensiv ist. Außerdem berücksichtigen die verfügbaren Methoden nicht den Einfluss von Prozessadditiven auf die Werkzeugdynamik.

In dieser Arbeit wird daher eine ressourceneffiziente Offline-Prüfmethode zur Untersuchung der Werkzeugdynamik eines Duroplast-Pultrusionsprozesses entwickelt. Darüber hinaus ermöglicht die Methode die Vorbestimmung der erforderlichen Prozessparameter für eine gegebene Faser-Matrix-Kombination. Bei dem neu entwickelten Ansatz, die „Rotating core method“, rotieren vorimprägnierte Rovings, die auf einem festen Dorn mit definiertem Faservolumengehalt gewickelt sind, innerhalb eines zylindrischen beheizten Werkzeuges. Entsprechend der Liniengeschwindigkeit eines Pultrusionsverfahrens wird die Rotationsgeschwindigkeit des rotierenden Kerns identisch eingestellt. Die rotierende Faser-Matrix-Mischung durchläuft eine temperaturinduzierte Aushärtung, die zur Umwandlung der Faser-Matrix-Mischung in einen festen Verbundwerkstoff innerhalb des zylindrischen Werkzeuges führt. Dies ahmt die Phänomene nach, die während des Pultrusionsprozesses in einem Pultrusionswerkzeug auftreten.

Eine im Rahmen dieser Arbeit entwickelte Apparatur, der Die Dynamics Simulator (DDS), ermöglicht es erstmals, das von der rotierenden Faser-Matrix auf die DDS-Werkzeuge während des Polymerisationsprozesses ausgeübte Drehmoment kontinuierlich zu messen. Das gemessene Drehmoment stellt die Widerstandskräfte, die während der Polymerisation der Faser-Matrix im Werkzeug entstehen, dar. Die Untersuchung der Aushärtungskinetik und Rheologie der Harzformulierungen ermöglicht die Charakterisierung des Polymerisationsverhaltens und damit die Identifizierung der verschiedenen Komponenten der Widerstandskräfte. Darüber hinaus wird im Rahmen dieser Arbeit der Einfluss der folgenden Parameter auf die Werkzeugdynamik mit der entwickelten Apparatur untersucht: (1) Werkzeugtemperatur, (2) Geschwindigkeit der Faser-Matrix-Mischung, (3) Kontaktfläche des Werkzeugs und der Faser-Matrix-Mischung, (4) Bauteildicke, (5) Faservolumenanteil und (6) Prozessadditiv – internes Trennmittel (IMR). Anschließend wurden Pultrusionsversuche durchgeführt, um die entwickelte Methodik zu validieren.

Die Ergebnisse beweisen die Abhängigkeit der Widerstandskräfte von den einzelnen untersuchten Parametern und die Wechselwirkungen zwischen mehreren Parametern. Die mit unterschiedlichen Konzentrationen von IMR durchgeführten Experimente erlauben es, die Wirkungsweise der IMR auf die sich entwickelnden Widerstandskräfte zu beurteilen. Die Ergebnisse zeigen zudem, in welcher Phase der polymerisierenden Matrix die IMR am wirksamsten sind. Im Vergleich zeigen die gemessenen Kräfte am DDS und an der Pultrusionlinie eine gute Übereinstimmung für höhere Faservolumenanteile.

1 Introduction

1.1 Background

Fibre reinforced plastics (FRPs), commonly known as composites, are increasingly being used in diverse applications since the beginning of their industrial-scale production in the 1940s. High specific stiffness and strength together with the properties such as low coefficient of thermal expansion, corrosion resistance, better thermal, electrical insulation as well as damping behaviour compared to metals make them attractive for high-performance lightweight applications. Further, FRPs allow the engineers and designers to tailor their properties according to the end application. The anisotropic nature of FRPs allows the design of load-path oriented lightweight components, opening many possibilities to extend their usage. Although in the beginning primarily aircraft and aerospace industries used FRPs, industries including automobile, construction, and sports are quick adaptors of the composite materials since the recent decades [1].

Albeit their excellent properties, continuous fibre reinforced composites are still not cost-effective compared to traditional materials like metals in many applications. The main reasons being high material costs, for example, carbon fibres (approx. 18 €/kg and above), as well as the maturity and limited availability of low-cost processing technologies. Industries are continually looking for most efficient and automated processes to manufacture FRPs that enable to minimise the costs and increase productivity. Compression moulding, resin transfer moulding, filament winding, and pultrusion are the high productive composite manufacturing techniques. Compared to the open-mould composite forming technologies, for example, vacuum-assisted resin infusion, the high-production technologies mentioned above involve relatively high capital investment [2].

Among all the others, pultrusion is the only manufacturing technology that produces FRP profiles of constant cross-sections continuously. Figure 1.1 shows the typical cross-sections of pultruded profiles. Pultrusion allows producing profiles with high fibre volume fraction at an economic scale.

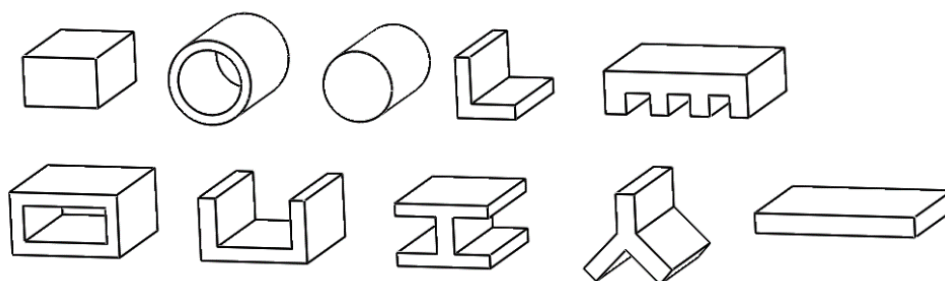


Figure 1.1: Typical cross-sections of pultruded profiles.

Since the last few years, the pultrusion market is experiencing significant growth, primarily driven by demand in the transportation, wind energy and construction industries. Figure 1.2 shows examples of the application of typical pultruded profiles in transportation and wind energy industries. According to a recent market report [3], the global pultrusion market grows at a Compound Annual Growth Rate (CAGR) of 4.0 % from 2019 to 2024.

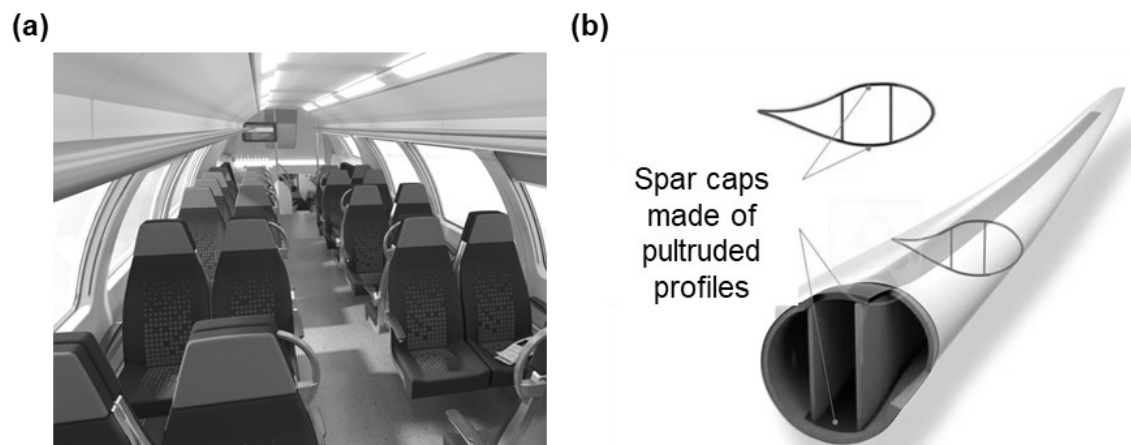


Figure 1.2: Examples of application of pultruded profiles: (a) train luggage rack [4] and (b) spar caps in a windmill blade [5].

From the beginning of its industrial adoption in the 1950s, pultrusion in principle remains as a simple process to produce continuous length high-quality composite profiles. However, manufacturing of first quality engineering composite profiles using pultrusion requires significant know-how of the process. The variables like fibre type, fibre volume fraction, resin formulation (matrix), additives, temperature profile of the die, line speed, and profile geometry substantially influence the process dynamics and composite quality. It is therefore of immense interest for the industry and academia to advance the technology to meet the ever-changing requirements and challenges faced by the pultrusion industry.

1.2 Motivation

Pultrusion is a continuous composite manufacturing process (described in detail in Section 2.1) in which a pulling device pulls the impregnated reinforcements through a heated die. The profiles get their shape as the resin formulation polymerises within the die. Hence, the pultrusion die (also referred as tool or mould in literature) is termed the “heart of the pultrusion” process [6]. The primary parameters die temperature profile, pulling speed, fibre volume fraction for a given profile geometry play a vital role in the process dynamics and profile quality. Likewise, the “pulling force” is a quantifiable feedback which can be used to gain insight into the progress of the polymerisation within the die and the overall stability of the process. The pulling force is, therefore, referred to as the “pulse of the pultrusion” [7].

Pulling force is the sum of resistive forces that arise from fibre creel to the exit point of the pultrusion die. Before the reinforcements enter the die, the holding tension as well as the friction between guiding elements and the fibres cause the resistive forces. Within the pultrusion die, the friction between fibre and the die wall, the temperature-induced viscosity and the volumetric changes (thermal expansion) of the curing matrix as well as the friction between formed composite and the die wall are the sources of the resistive forces. The pulling device must overcome these resistive forces to keep the process stable. However, because of “mould sticking” or “pilling” (described in Chapter 2) the resistive forces could increase beyond the tensile strength of the composite profile being pultruded. In such case, the process terminates due to tensile failure of the profile (Figure 1.3). Restarting the pultrusion after process failure involve enormous efforts. The efforts include cooling down

the die, cleaning and repeating the preparatory procedure (i.e. redrawing the reinforcements into the die cavity and die reheating). This significantly affects the process economics and reduces the efficiency of the process. Therefore, measurement and analysis of the pulling force are vital to understand and control the pultrusion.

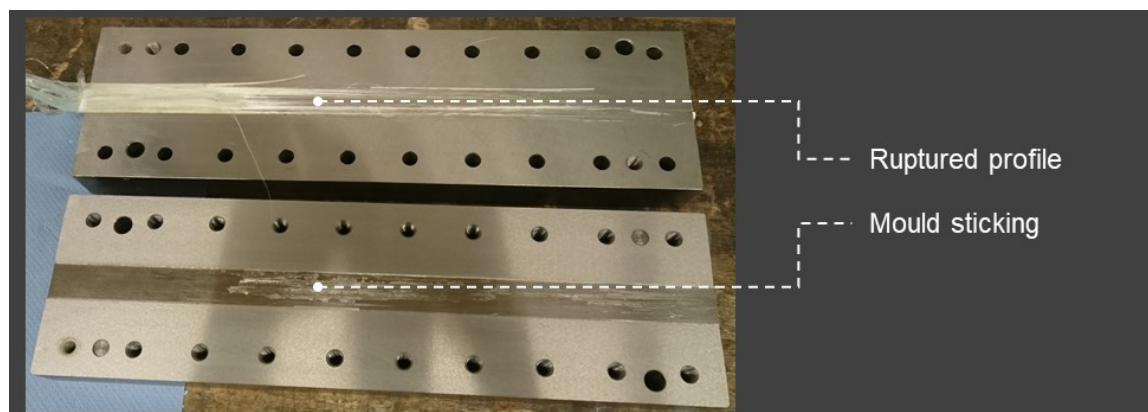


Figure 1.3: Example of a tensile failure of the profile caused by mould sticking.

Many investigations attempted to identify and study the sources of the resistive forces inside the pultrusion die, its effects on product quality and proposed analytical and numerical models for the pultrusion process. Nevertheless, monitoring the changes in the physical states of the polymerising resin formulation and hence arising resistive forces, or in other words “die dynamics”, along the entire length of the pultrusion die remains tedious. Chapter 2 presents a detailed review of the research published on this subject.

2 Pultrusion – State-of-the-art

The following sections review the state-of-the-art techniques in practice and the literature on methods and theories relevant to the research approach of this thesis. The review encompasses an overview of the pultrusion process, fibres and matrices generally used in pultrusion and their characterisation techniques. Further, the sections systematically review the published research reports on resistive forces in pultrusion and their measurement techniques.

2.1 Pultrusion process

Etymologically the term *pultrusion* originates from the words *pull* and *extrusion*. As opposed to the extrusion process, in which an extruder pushes the material into a die, in pultrusion a puller pulls the material through a die. Pultrusion is one of the highly automated continuous composite manufacturing processes that produce constant cross-sectional composite profiles [8]. Generally, the technique allows processing both thermosets and thermoplastics. However, the base materials used in thermosetting pultrusion and the thermoplastic pultrusion are different. Prepolymers or monomers are the base material for thermosetting and in-situ thermoplastics pultrusion. Whereas for thermoplastic pultrusion, amorphous or semi-crystalline polymers in the form of fibres, foils or pellets serve as input matrix materials. Therefore, the above processes are different from each other. In the case of thermoset or in-situ thermoplastic pultrusion, the prepolymers or monomers polymerise inside the die to form a cross-linked solid material. In contrast, in thermoplastic pultrusion, the amorphous or semi-crystalline polymer melts inside a heated die and subsequently solidify or recrystallise in a cooling die to transform into a solid profile. A considerable amount of literature reports the in-situ thermoplastic [9–14] and thermoplastic [15–23] pultrusion process and its modelling approaches. Since the research within the scope of this thesis focuses on the study of phenomena occurring in a thermoset pultrusion process, the further literature review will consider only the relevant studies on thermoset processing.

Typically, a thermoset pultrusion line (Figure 2.1) consists of a rack/creel to hold fibrous reinforcements (in the form of rovings, fabrics or continuous filament mats), guiding roller assemblies, a resin bath, perforated guiding plates to guide the reinforcements, a heated die, a pulling device, and a cut-off saw that cuts the formed profiles to the desired length.

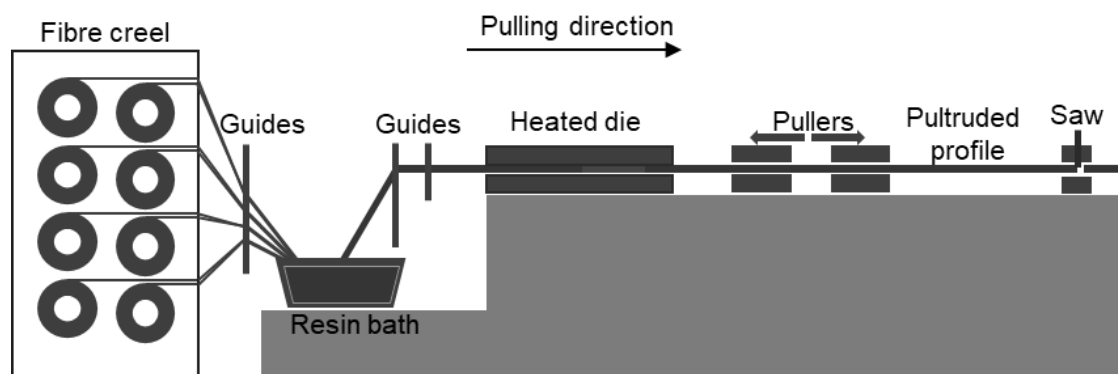


Figure 2.1: Schematic representation of a typical thermoset pultrusion line.

Depending on the composite profile geometry and the fibre volume fraction, the process involves unwinding and pulling multiple fabrics or mats together with a large number of rovings out from the creel. Guiding rollers and plates control the path of the reinforcements preventing intertwining and allow better collimation before the reinforcements enter the die. In the process, the guiding system should not damage or exert resistance to the movement of the reinforcements. Avoiding rough surfaces, sharp edges or protrusions on the guiding elements minimises the fibre damage and the pulling resistance. Therefore, polished metals, ceramic eyelets or PTFE (Polytetrafluoroethylene) are the materials of choice for making the guiding elements.

Mostly, pultrusion process employs two different techniques for impregnating the reinforcements, namely open bath impregnation and closed injection methods. In case of open bath impregnation, the reinforcements pass through an open tank filled with the resin formulation. The guiding rollers split and spread the reinforcements to favour complete fibre wetting. Two variants of open bath impregnation shown in Figure 2.2 (a) are common in the industry. An enclosed resin impregnation system recently developed by *Irfan et al.* [24] allows spreading of the fibres before the wetting and injects resin providing more through-thickness permeability for quick and better wetting. Open impregnation technique is the most used technique and favoured by its simplicity and cost-efficiency. However, the open bath possesses environmental issues since the volatile solvents can easily escape from the resin bath.

On the other hand, closed injection pultrusion utilises a resin injection unit that directly injects the resin formulation into the die cavity (Figure 2.2 (b)). A specially designed pultrusion die permits the injection of the resin directly into the cavity. The die consists of an injection (impregnation) chamber at the reinforcement entry side appended to a straight curing segment.

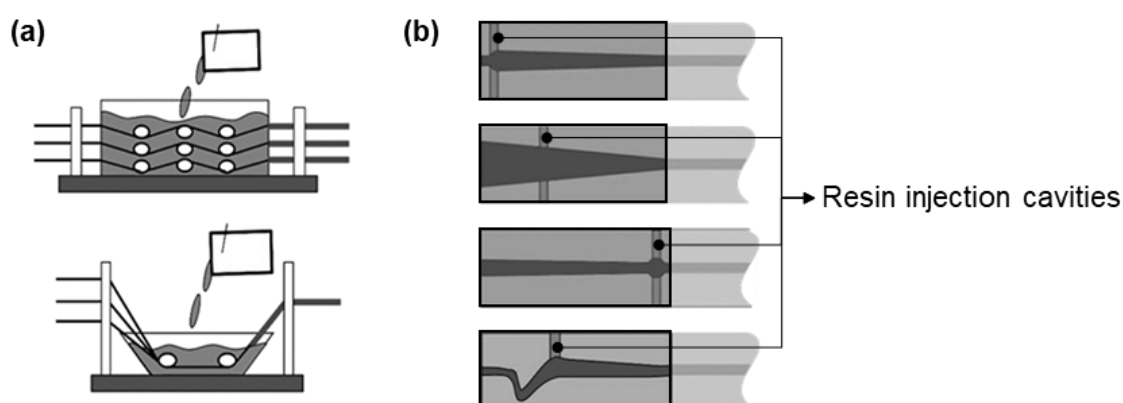


Figure 2.2: Schematic of impregnation chambers: (a) variants of open bath impregnation, (b) variants of closed injection pultrusion (redrawn from [25]).

The type of reinforcement, the geometry of the profile, chemo-rheological properties of the resin formulation and the fibre volume fraction are the parameters that decide the configuration of the impregnation chamber. Therefore, various strategies are practised in designing the impregnation chamber for the closed injection pultrusion [26–28]. Further, the temperature of the injection chamber needs critical control to prevent pre-curing of the

resin formulation within the impregnation chamber. These factors make the closed injection pultrusion complex compared to the open bath impregnation.

The reinforcements, impregnated with resin formulation, enter the die where the heat or other forms of electromagnetic radiation (e.g. Ultra-Violet, Microwave or Electron beam) triggers the polymerisation. A typical pultrusion die, as shown in Figure 2.3, has a tapered entry geometry to favour smooth entry of reinforcements as well as to collimate and compact the reinforcements to remove excess resin. The compaction also favours good fibre wetting. Successive to the tapered entry segment, the curing or consolidation segment of the die has the cross-section of the composite profile. This segment can be either straight (more common for linear pultrusion) or curved (for radial pultrusion [29]) along the length depending on the type of pultruded profile.

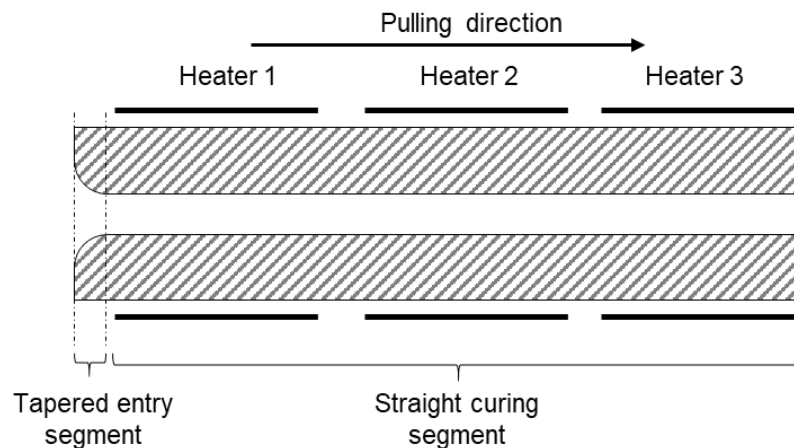


Figure 2.3: Cross-section of a typical linear pultrusion die.

Usually, in a pultrusion process in which heat energy triggers the polymerisation, heating platens with different temperature settings clamp the die in its position during pultrusion and supply the necessary heat energy to the die. Proportional-Integral-Derivative (PID) controllers are generally employed to regulate the temperature of the platens and in turn, the temperature of the die. As the polymerisation progress, the resin transforms from viscous liquid to viscoelastic solid inside the die. In a successful pultrusion process, the composite profile exits die in a solid-state. Section 2.4 presents a more detailed review of the polymerisation process and the phenomenological changes that occur during the curing of the resin formulation from liquid to solid within the pultrusion die.

As the reinforcements pass through the guiding elements, the resin bath and the die, each contact point exerts resistive forces on the fibre-matrix. Section 2.3 reviews in detail the resistive forces that arise during a pultrusion process. The pulling device must overcome these forces to pull the cured composite profile continuously out of the die. Reciprocating gripper pullers and continuous tractor pullers are the commonly used pulling devices in the pultrusion industry. *Starr* [2] reports detailed mechanisms and descriptions of the pulling devices.

2.2 Reinforcements and matrices for pultrusion

Pultrusion can process almost any kind of fibre-matrix combination depending on the end-use applications and the profile geometry. This section reviews the commonly used fibres,

matrix materials and the process additives (e.g. mould release additives) in the pultrusion industry.

2.2.1 Fibre reinforcements

Pultruded profiles contain the reinforcements mostly in the longitudinal direction. Figure 2.4 shows schematic of typical reinforcement structures of a pultrusion profile. Glass fibres in the form of unidirectional (UD) continuous rovings, chopped strand mats (veils) and fabrics take the highest share as reinforcing material in the pultruded products [30]. Particularly, E-glass fibres, due to their price-performance ratio and their insulation properties favour them to be the material of choice for the pultruders. On the other hand, carbon fibres find its use in the applications that demand high mechanical properties, low thermal expansion coefficient and lightweight. For example, wind energy industry is utilising pultruded carbon fibre reinforced profiles for the spar caps (Figure 1.2 (b)) of the larger windmill blades. Other fibres such as aramid, ultra-high molecular weight polyethylene and polypropylene find their usage in niche applications. In the recent days, due to their environmental advantages, natural fibres like flax, hemp and other cellulosic fibres are regaining their usage as reinforcements in combination with bio-based thermosets in pultruded products [31,32].

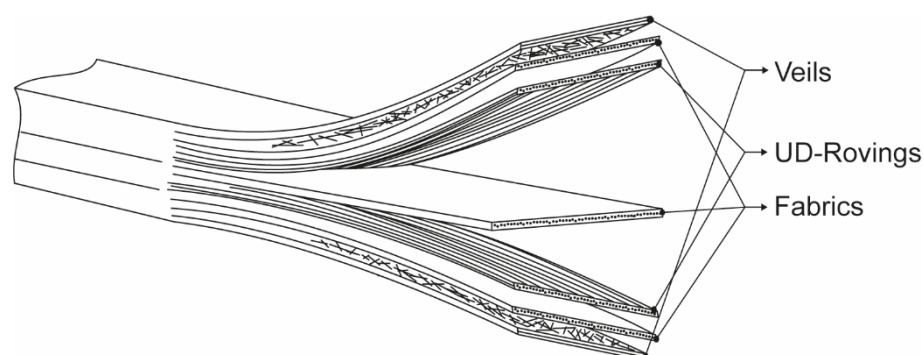


Figure 2.4: Schematic of typical reinforcement structures of a pultrusion profile.

One of the essential aspects that determine the mechanical properties of the composite materials is the bonding between the fibre and the matrix [33,34]. The sizing present on the surface of the fibre enhance the bonding. Although the sizing formulation remains proprietary of the fibre manufacturers, the commercial fibres are mostly compatible with the resin formulations for the pultrusion process.

2.2.2 Matrices

Among thermoplastics and thermosets, thermosets dominate the market share in composite applications. Many types of thermosets are currently available explicitly formulated to meet the product performance and the fabrication technology requirements (e.g. accelerated cross-linking and increased production speed). Pultrusion process typically employs unsaturated polyester (UP), vinyl ester (VE), phenolic, and epoxide resins.

Owing to their low viscosity, favouring quick wettability and high reactivity with controllable cure UP resins are the most widely used thermosets in the pultrusion process. The VE resins that are similar in characteristics to UP resins possess additional functionalities like

better corrosion resistance to caustic and chemical environments as well as improved toughness [35].

Phenolic resins, one of the oldest synthetic resin systems, find their use in the applications that demand high-temperature stability and excellent fire-smoke-toxicity properties, e.g. in aircrafts. The polymerisation of phenol, urea, resorcinol, or melamine with formaldehyde catalysed by an acid or base, results in high molecular weight phenolic resins [36].

Epoxy resins typically contain two or more epoxide groups (oxirane rings) within their molecular structure. Modifying the number or position of epoxide groups present in a molecular structure allows tailoring the physical characteristics and the reactivity of the epoxy resin [37,38]. The interest in the epoxy resins originates because of their tailorability in combination with the useful properties such as high strength, very low creep, excellent corrosion and weather resistance, high-temperature service capability, and good electrical properties. The commonest epoxy resins employed for pultrusion are systems based on bisphenol-A (BPA). Curing reaction with cross-linking agents or hardeners results in the transformation of linear epoxy resins to three-dimensional cross-linked thermosets. Mostly amines and acid anhydrides act as the cross-linkers. Compared to the UP and VE resins, epoxy pultrusion is relatively challenging. The rate of polymerisation of epoxy resins is relatively lower than that of the UP resins. Characteristically, the gelation (described in Section 2.4.2) of UP resins occurs at about 10 % – 30 % of monomer conversion compared to 40 % and above for the epoxy resins. As a result, in the case of epoxy pultrusion, the gelation region shifts further towards the die exit resulting in increased pulling forces. Furthermore, the conversion rate of the monomer determines the pultrusion line speed [2]. Although the selection of the right temperature profile and the formulation improves the reaction kinetics, pultrusion of epoxy necessitates significant know-how.

The resin formulation may contain other additives like low profile fillers, e.g. calcium carbonate, which help to lower material costs and improve surface quality; aluminium trihydroxide, a flame retardant; anti-foaming agents to minimise the void content; wetting agent to increase wettability of the reinforcements; accelerators to accelerate reaction kinetics and mould release agents, which effectively reduce the force necessary to pull the material through the die. Although the additives mentioned impart specific functionality to the pultruded profile, those additives can be optional. However, mould release additive is inevitable in the pultrusion process.

2.2.3 Mould release agents

Whenever two materials come into contact, the attractive force between their molecules influences the interaction between each other. The adhesion and moulding are therefore close to each other. Adhesion is a permanent phenomenon in which two components bind together to create a useful functional product, whereas the moulding is a temporary adhesive process in which the product takes the shape of the mould through interactions with its surface [39]. In other words, during the moulding process, the (pre)polymers in liquid or semi-solid form encounters the mould surface and solidify. Thermosets with its reactive groups tend to bond to the mould surface, especially to the metal surfaces having high surface energies resulting in mould sticking [40–44]. The continuous build-up of stuck resin causes mould fouling demanding mould cleaning or in worst cases mould damage.

Mould release agents prevent the matrices from sticking on to the mould surface by either reducing the surface energy of the mould or by forming an intermediate layer between the mould and the moulded component which undergoes cohesive failure during the demoulding process [45]. Therefore, the mould release agents are one of the essential ingredients for any composite moulding. Mould release agents are the compounds that contain chemical groups such as alcohol phosphates, fatty amines, fatty acid esters, fluorocompounds, silicones, and waxes. *Wypych* [46,47] describes in detail the release agents and their mechanism of action and lists comprehensively the release agents that are available in the market.

Depending on the application method, mould release agents fall into two categories: external mould release and internal mould release (IMR). External mould release agents are applied directly on the surface of the mould and can be non-permanent or semi-permanent depending on the need to withstand the process conditions. In general, external mould release agents are suitable for batch processes that permit their application between the moulding cycles.

On the other hand, pultrusion is a continuous process and demands a release agent that should be effective throughout the production time. IMRs, mixed as an integral ingredient in the resin formulation, favour the continuous build-up of the interfacial layer and is therefore more common in the pultrusion process. IMRs are increasingly used also in batch processing techniques such as resin transfer moulding as well as in the processing of bulk moulding compounds and sheet moulding compounds [48–50]. The mechanism of action of IMRs is similar like external mould release in a way that IMRs also forms a weak boundary layer between the mould surface and the part, which is susceptible to cohesive failure during part removal. *Karbhari* [51] in his paper reviewed that the mechanism behind the formation of the interfacial layer could be due to the migration of IMRs to the surface of the composite or the change in solubility of the IMR between the uncured and the cured state of resin causing it to become incompatible at the surface and forming a surface level molecular separation layer. The mechanism may, however, depend upon the type and chemical composition of IMR, processing temperature, mould surface chemistry and the polymer type processed [46]. Utilising an IMR that is incompatible with a selected die (mould), fibre sizing, or resin formulation will result in an unsuccessful process and deterioration in the composite's performance [52,53]. Therefore, the selection of right IMR becomes crucial, as it directly impacts the properties and the quality of the composite and the productivity of the process by easing the release of the components. In pultrusion, this indeed means the reduction of the resistive forces.

2.3 Resistive forces during pultrusion

As mentioned earlier in Section 1.2, resistive forces arise as the fibre-matrix moves through the pultrusion line. *Price* [54] categorised the resistive forces from fibre creel to the die entrance as *collimation force* and within the heated die as *bulk compaction force* and *temperature-induced force*. The bulk compaction force relates to the mechanical forces arising due to the compaction of unrestrained impregnated reinforcements entering the geometrically confined die cavity. Within the heated die, the temperature induces thermal expansion and viscosity changes due to polymerisation of the resin formulation. This results in the fibre-matrix to exert temperature-induced forces on the die wall. In other words, the forces arising inside the pultrusion die are the outcome of friction and viscous

drag between the fibre-matrix and the die wall. In addition to these two forces, *Bibbo* and *Gutowsky* [55] identified the resin backflow within the die also contribute to the resistive forces. The pulling device must exert an equivalent force in the opposite direction to facilitate the pultrusion process. Equation 2.1 expresses the generalised form of the total pulling force, independent of profile geometry, exerted on the puller [56]:

$$\vec{F}_{pull} = \vec{F}_{coll} + \vec{F}_{comp} + \vec{F}_{vis} + \vec{F}_{fric} \quad (2.1)$$

where F_{pull} is the total pulling force; F_{coll} , the collimation force; F_{comp} , the compaction force; F_{vis} , the viscous drag; and F_{fric} , the frictional force.

Figure 2.5 presents schematically the force components and the zones at which they arise. From the schematic, one infers that the fibre-matrix undergoes various physicochemical transformations from the die entry to die exit and the parameters such as fibre compaction, permeability, rheology of the resin formulation and surface energy directly influence the force components [6,26,57–61]. Therefore, understanding pultrusion die dynamics demand a collective knowledge of those physicochemical parameters and the underlying phenomena. Section 2.4 reviews in detail the relevant literature on these parameters and their effects on the process.

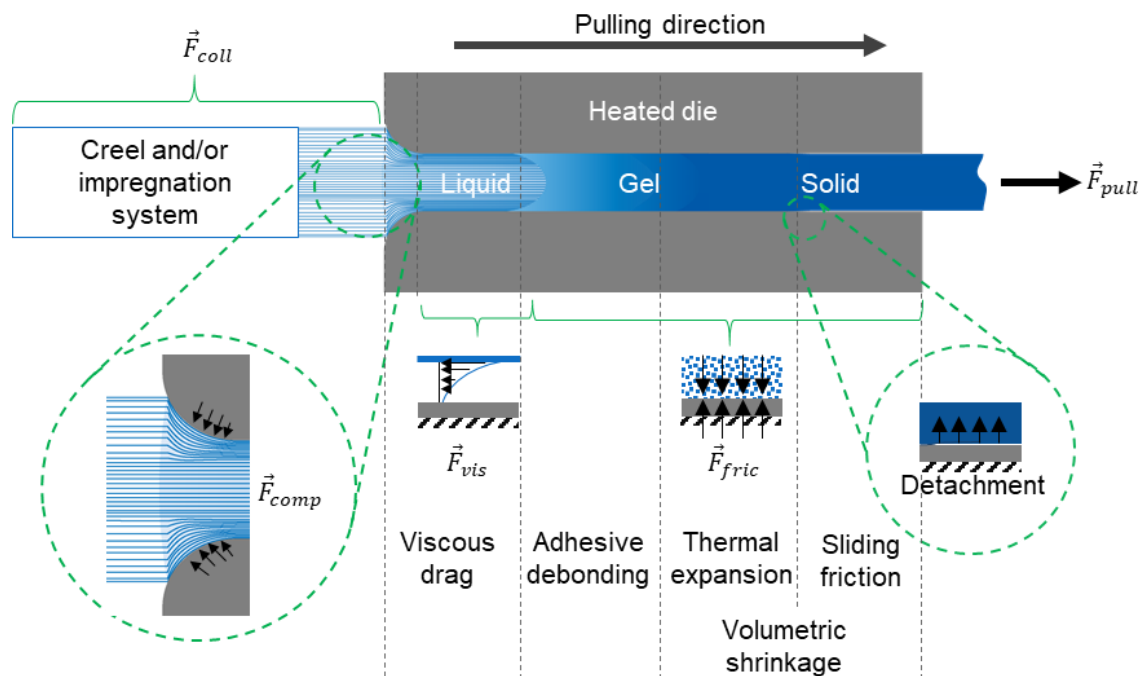


Figure 2.5: Pultrusion die dynamics (resin phases and force components).

Recalling the elements of the total pulling force, the compaction force F_{comp} arises because of fibre-matrix compaction in the tapered entry segment of the die where the resin formulation is in the liquid phase. In the literature, the Equation 2.2 represents F_{comp} mathematically.

$$\vec{F}_{comp} = \iint_{A_1} p \sin \theta dA_1 \quad (2.2)$$

where p is the compaction pressure exerted on the tapered segment of the die wall; θ , the taper angle; and A_1 , the surface area of the tapered segment of the die.

Once the fibre-matrix enters the straight segment of the die, viscous drag on the thin liquid fibreless resin layer between the moving fibre-matrix and the stationary die wall result in viscous forces because of the difference in the velocity profile across the thickness of the thin fibreless resin layer. Most of the literature [6,62–65] consider the resin flow until gelation follows plane Couette flow in this layer. Therefore, the force component F_{vis} is generalised using the equation,

$$\vec{F}_{vis} = \frac{v_{pull}}{\lambda} \iint_{A_2} \eta(\alpha, T) dA_2 \quad (2.3)$$

where v_{pull} is the pulling speed; λ , the thickness of the thin resin layer; η , temperature (T) and degree of cure (α) dependent viscosity; and A_2 , the die surface area of the viscous region, i.e. until gelation.

The studies [57,64,66–69] report various theoretical and experimental approaches to determine the resin layer thickness λ . Further, the thin resin film may not be present in the regions where the fibres directly contact the die wall. *Ástroöm et al.* [70] propose plausible mathematical expressions to determine λ .

After the gelation, the resin flow becomes more elastic than viscous, leading to the domination of frictional forces over viscous drag. The published studies thus generalise the frictional component F_{fric} using the equation,

$$\vec{F}_{fric} = \iint_{A_3} \mu_k (p_n + \sigma_{adh}) dA_3 \quad (2.4)$$

where μ_k is the coefficient of kinetic friction between the moving composite profile and the die wall; p_n , the normal contact pressure exerted by the profile against die wall; σ_{adh} , the adhesive strength between the gelled matrix and the die wall; and A_3 , the surface area of the die in the frictional region.

In ideal cases, the frictional forces start to vanish once the profile detaches from the die surface caused by cure shrinkage. Nevertheless, in practical situations, friction-free sliding depends on “pilling” (powdery resin substance adhering to the profile surface due to mould fouling) free pultrusion.



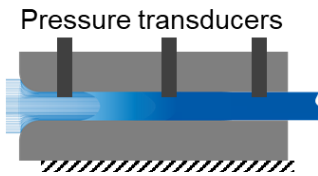
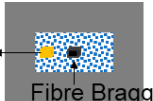
Safonov et al. [71] review the literature published on components of the pulling forces and their individual contributions to the total pulling force. They summarised in their review that there exists no explicit agreement between the publications regarding the relevance of the contributions of the individual components to the total pulling force, i.e. in some cases viscous forces were dominant whereas in others the frictional forces. The underlying causes have to be, however, investigated based on the material processed, processing parameters and the profile geometry.

Pulling force measurements

Measuring pulling force in pultrusion facilitate to understand and control the progress of the pultrusion process. Literature reports different approaches that aimed to measure the pulling force experimentally. Table 2.1 lists the methods practised to measure the pulling force inline during the pultrusion process. Measuring the power consumed by the puller remains one of the simplest and straightforward approaches compared to the methods

listed in Table 2.1. Nevertheless, the force calculated from the power consumption does not provide any scientific insight into the process. Therefore, measurement of total resistive forces using force transducers mounted directly on the frame on which the pultrusion die slides (on-die force measurement) became favourable choice [27,53,54,67,69,72]. Alternatively, *Li et al.* [26,68] utilised the mat tracer method to measure the forces using short cut fibre mat (CFM) reinforcements inserted periodically in between the continuous reinforcement stacks. The CFM locally increased the fibre volume fraction and showed an increase in the force as it moves inside the die. They traced the position of the CFM inside the die using the length of the inserted mat and the speed of pultrusion, and in turn calculated the forces at different positions along the die length.

Table 2.1: State-of-the-art inline pulling force measurement methods.

Measurement methods	Schematic representation	References
On-die force measurement		[27,53,54,67,69,72]
Mat tracer		[26,68]
In-die pressure measurements		[57,73,74]
Integrated sensors		[58,59,75,76]

Further, integrating pressure gauges (in-die pressure measurement) at specific points along the die allowed to measure the normal pressure exerted by the fibre-matrix on the sensor [57,73,74]. Indeed, such construction resembles slit rheometer [77]. Interpolating the results between the measuring points using the rheological and thermo-chemical behaviour of the resin formulation allows to predict the forces along the length of the die. However, this becomes challenging on changing the line speed or the process variables since it demands new interpolation models for each parameter change, say for example, different resin formulations. Other methods include the use of integrated sensors such as fibre optic sensors, strain gauges and force sensing resistors (FSR) that integrates into the pultrusion profile [58,59,75,76]. Such systems provided insight into temperature profile, internal stresses in the pultrusion profile and the curing behaviour of the resin. However, the shear stress caused by the internal stress difference across the cross-section of the fibre-matrix mass inside the die cavity decreases the reliability of such sensors to measure

the stresses at fibre-matrix-die wall interface. Additionally, once the resin cures, the sensors remain within the solid profile body and therefore may not reflect the frictional forces between the die and the composite.

Apart from the above discussed inline methods, studies report offline measurement approaches that aimed to pre-determine the force components. *Li et al.* [26] developed a special tool to measure the friction coefficient between the fibre-matrix and tool surface. They connected the tool to a universal testing machine to record the forces and in turn, calculated the kinetic friction coefficient. *Krämer et al.* [78] proposed a method and a fixture to measure the release force required to demould a cured resin sheet. The method is relevant for batch processes like resin transfer moulding or compression moulding to test the effectiveness of the release agents used. *Bjekovic et al.* [49] report a similar approach to characterise the release agents. In addition to the experimental characterisation, many investigations attempted to model the pultrusion process, including the pull force modelling. *Safonov et al.* [71] presents a detailed review of the literature on mathematical modelling of pultrusion. On the other hand, per se, both experimental investigations and mathematical modelling of pulling force demand knowledge on the characteristic behaviour of the fibre-matrix combinations being processed.

2.4 Material behaviour and characterisation

Manufacturing of high-performance composites requires exhaustive knowledge about the characteristics of fibre-matrix combinations employed and their process-specific behaviours. A vast amount of literature reports the behaviour of the reinforcements, temperature-induced physicochemical changes of the matrix and the interaction between the pultrusion die and the fibre-matrix in the pultrusion process. The following sections review the literature relevant to the aim of this thesis.

2.4.1 Reinforcement behaviour

During the manufacturing of fibre reinforced composites using advanced manufacturing techniques, two central parameters of interest concerning the reinforcements are the compaction of the fibres within the reinforcing structure and the permeability of the reinforcements. The following sections review the widespread methodologies adopted in the publications to characterise these two parameters.

Fibre compaction

The fibre volume fraction and orientation of reinforcing fibres in a composite are crucial since the mechanical properties of the composite directly depend on them. Generally, the reinforcing fibre network undergoes compaction during the composite consolidation in the processes that apply pressure on the reinforcements. The fibre volume fraction of the consolidated composite, in turn, depends on the level of compaction of the reinforcing fibre network achieved in the process. Therefore, knowledge of the relationship between the amount of compaction and fibre volume is of interest to the composite processors.

During compaction of the fibre network, two essential phenomena occur that directly affect the compaction of the wet reinforcements. They are the (viscous) flow of resin in the fibre network and the (elastic) deformation of the fibre network. The viscous flow generates pressure within the reinforcements, whereas the elastic deformation results in the generation of stresses in the fibre network. The resin pressure together with the stresses

in the fibre network balance the compaction pressure applied transverse to the laminate plane, and is mathematically represented as,

$$p = \sigma + p_r \quad (2.5)$$

where p is the applied pressure; σ , the stresses in the fibre network; and p_r , the resin pressure.

The pressure exerted by the resin flow is a function of permeability (described in the following section) of the reinforcements. Nevertheless, as mentioned above, both the resin pressure and the stresses in the fibre network depends on the fibre volume fraction. Gutowski [79] proposed a model (Equation 2.6) that describes the relationship between the stresses in the fibre network and the fibre volume fraction.

$$\sigma = \frac{3\pi E}{\beta^4} \frac{\sqrt{\frac{\varphi_f}{\varphi_0}} - 1}{\left(\sqrt{\frac{\varphi_{max}}{\varphi_f}} - 1\right)^4} \quad (2.6)$$

where σ is the stress or pressure applied in the direction transverse to the laminate plane (which is equivalent to the stresses experienced by the fibre network); E , the bending stiffness of the fibre; β , a constant (span length/span height) for the fibre network (for unidirectional laminate it is the scale of fibre waviness); φ_f , the fibre volume fraction; φ_0 , the initial fibre volume fraction at no applied load; φ_{max} , the maximum possible fibre volume fraction (0.785 for a square and 0.907 for a hexagonal packing).

Although the Gutowski's model was developed for the compression moulding, *Kim et al.* [80] adopted the model to measure the compressibility of different configurations of the fibrous reinforcements particularly to address the closed injection pultrusion process. The investigations realised the measurement of the compaction pressure by compressing the reinforcing layers transversely. They also tested the dry fibres having different fibre orientations. The effect of fibre stiffness on compressibility has a strong dependence on fibre orientation. For example, with the unidirectional rovings, the required compaction pressure was two-fold less compared to fibres oriented perpendicular to each other. Further, the paper reported that lubricated (i.e. wet) fibres compact easily compared to the dry fibres.

In an another approach [81], the dry glass rovings were pulled through copper tubes having different lengths to measure the compaction force. This experiment closely represents the pultrusion process. In the experiment, the fibre compaction was determined using the relation,

$$p = \frac{(F_2 - F_1)\mu}{(L_2 - L_1)\pi D_{tube}} \quad (2.7)$$

where F is the respective measured forces using the tubes of two different lengths; L , the respective lengths of the tubes; D_{tube} , the diameter of the tubes; and μ , the friction coefficient (assumed to be 0.6) between glass fibres and metal.

The effect of process parameters like temperature, viscosity of the resin formulation, and pulling speed on the fibre compaction pressure was also reported [82–86]. The investigations described that the increase in viscosity of the resin formulation increases fibre compaction pressure. *Sharma et al.* [58] analysed the effect of die inlet geometry on the fibre compaction pressure. The analysis considered three different inlet geometries: wedge, parabolic and round with different angles, foci and radius respectively. Their results show that the wedge-shaped inlet exerted more pressure than the other two. Steeper the angle of entrance geometry, less is the compaction pressure. Similarly, increasing foci or radius of the entrance resulted in less compaction pressure.

The studies describe that the pressure rise due to the fibre compaction occurs only up to the end of the tapered segment of the linear pultrusion die. Once the reinforcements pass the tapered entrance, the pressure exerted on the die wall influenced by fibre volume fraction remains constant, as the fibre volume fraction does not change in the straight segment of the die [87]. Figure 2.6 shows the schematic of a typical fibre compaction zone at the entrance of a pultrusion die.

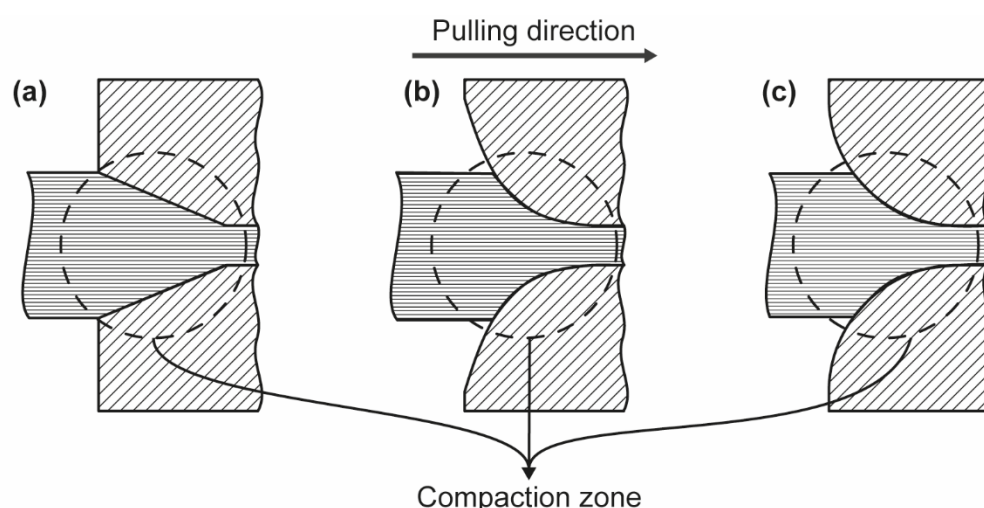


Figure 2.6: Schematic illustration of the compaction zone of a typical pultrusion die with – (a) tapered, (b) parabolic, and (c) rounded entrance geometry.

Permeability and resin flow

The permeability of a reinforcement is the ease with which a fluid flow through its fibre networks. The concept of permeability originates from geology and hydrology research related to the resistance against pressure-driven fluid flow through beds of isotropic porous sand. *Darcy* [88] proposed an empirical approach (Equation 2.8) to measure the permeability of such porous media.

$$v_{fluid} = -\frac{K}{\eta} \nabla P \quad (2.8)$$

where v_{fluid} is the flow velocity; K , the permeability of the medium; η , the viscosity of the fluid and ∇P , the pressure gradient.

Darcy's law serves as a foundational model of fluid flow through a porous medium and therefore the field of composites also widely adopts it to describe fluid flow through the

fibre reinforcements. The resin flow in composites during consolidation follows two different mechanisms: percolation flow and shear flow illustrated in Figure 2.7 [89]. Typically the percolation flow mechanism describes the flow in thermoset composites and the shear flow describes the flow in thermoplastic composites [90]. The permeability of the fibrous reinforcements and the resin flow, however, depends on the fibre volume fraction.

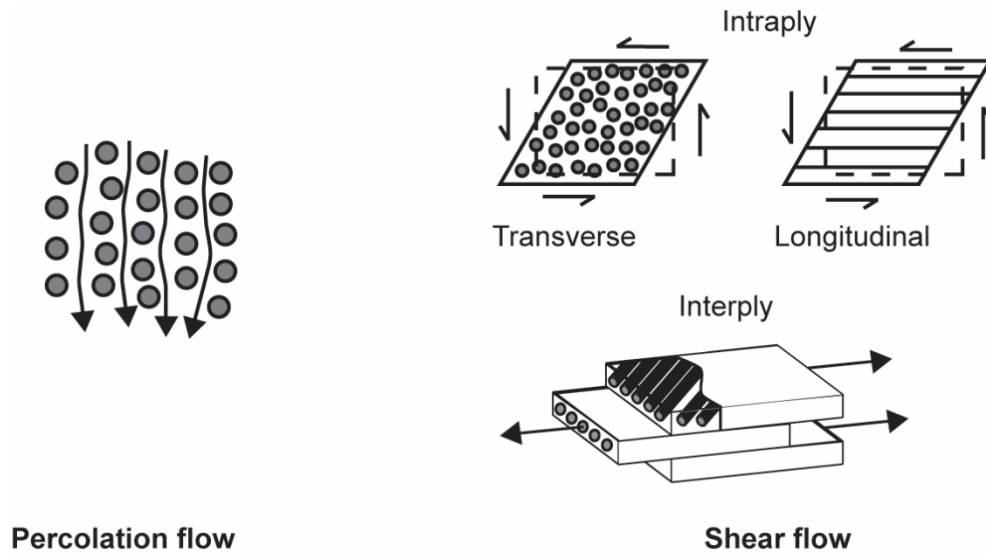


Figure 2.7: Resin flow mechanisms during composite processing (redrawn from [89]).

The fibrous reinforcements are generally anisotropic. Therefore, the permeability K , in Darcy's model is better represented as a symmetric second-order tensor [91]. Many investigations have proposed models and experimentally estimated the permeabilities in the longitudinal and transverse direction to the fibre orientation. One of the widely used models for estimating the permeability is the Kozeny-Carman relation. However, Gebart [92] claims that the applicability of the Kozeny-Carman relation is limited to the UD tows in which the transverse flow is constricted than the longitudinal flow due to the close packing of the fibres. That is, the transverse permeability cannot be greater than zero above the maximum possible fibre volume fraction ϕ_{max} . He, therefore, developed an improved model for longitudinal and transverse permeability of UD laminates (Equation 2.9) based on Kozeny-Carman equation.

$$K_{xx} = \frac{8r_f^2 (1 - \phi_f^2)}{c \phi_f^2}$$

$$K_{yy} = K_{zz} = C_1 \left(\sqrt{\frac{\phi_{max}}{\phi_f}} - 1 \right)^{2.5} r_f^2 \quad (2.9)$$

where K_{xx} is the permeability in the fibre direction; K_{yy} and K_{zz} , the permeability in the directions transverse to the fibre direction; r_f , the radius of the fibre; c , the dimensionless shape factor which depends on both the fibre arrangement and fibre volume fraction; C_1 , the model constant which depends on the fibre arrangement (i.e. quadratic or hexagonal arrangement). Gebart's model showed good agreement with his resin transfer moulding experiments.

Many of the literature that dealt with thermosetting composite manufacturing processes including resin transfer moulding, vacuum processing, filament winding and pultrusion considered the resins in their liquid phase as a Newtonian fluid with low Reynolds number until gelation [6,93]. This assumption allowed the authors to adopt the popularly used Gutowski's method for fibre compaction, Kozeny-Carman and/or Gebart's methods for permeability and Darcy's model for resin flow to represent the respective phenomena. Equations 2.5 through 2.9 allow the estimation of compaction force for a given fibre-matrix combination, fibre volume fraction and processing conditions. The established methods facilitate the prediction of compaction force close to the practical conditions. Therefore, this work utilises the existing literature for understanding the compaction phenomena and later for interpretation of the experimental results.

2.4.2 Characteristic analysis of resin formulation

The resin formulation (matrix) undergoes physicochemical changes during composite consolidation. The thermosets consist of monomers or oligomers that chemically bond together to form a cross-linked polymer. The monomers are stable chemical molecules that do not participate in polymerisation reaction until the system acquires critical energy (i.e. the activation energy) required to trigger the polymerisation. Upon acquiring the critical energy, depending on the kind of monomer molecules, the monomers react with each other to form cross-linked high molecular weight compounds. In other words, as the polymerisation progress, the liquid resin transforms from liquid to a solid material. The transformation is attributed to the change in viscosity and density during the curing reaction. The change in viscosity depends on the degree of cure, which is the measure of the level of conversion of the monomers into high molecular weight compounds. For successful processing, understanding these two inter-related properties, commonly termed as kinetics and chemo-rheology, therefore becomes indispensable.

Further, because the matrix interacts with the mould surface in the pultrusion process, the curing kinetics, chemorheology and the surface energy of the matrix, especially epoxies, are of interest for this thesis. The following sections describe the theoretical background and review relevant literature that deals with the characterisation of curing kinetics, chemorheology and interfacial surface free energy of the epoxy resin systems.

Curing kinetics

There are many techniques used to monitor the kinetics of the cure of thermosets such as Dynamic Scanning Calorimetry (DSC), Fourier transform infrared spectroscopy (FTIR), dielectric measurements and rheokinetic measurements. Among others, DSC is the most popular and extensively used technique in the determination of kinetic parameters and kinetic equations of curing thermosets. The DSC technique measures the rate of heat generated during a chemical reaction. The underlying assumption in DSC kinetic measurements is that the change in heat flow is proportional to the change in the extent of reaction, mathematically represented as,

$$\frac{d\alpha}{dt} = \frac{1}{H_{tot}} \frac{dH_t}{dt} \quad (2.10)$$

where dq/dt is the rate of heat generated during curing reaction; α , the degree of monomer conversion; $d\alpha/dt$, the rate of conversion. In other words, the degree of conversion at any

given time t , is the ratio between the heat of reaction H_t until the time t , and the total heat of reaction H_{tot} until the completion of the curing [94], i.e.,

$$\alpha = \frac{H_t}{H_{tot}} \quad (2.11)$$

Both H_t and H_{tot} can be directly calculated from the DSC data by integrating the area under the heat flow curve (Figure 2.8).

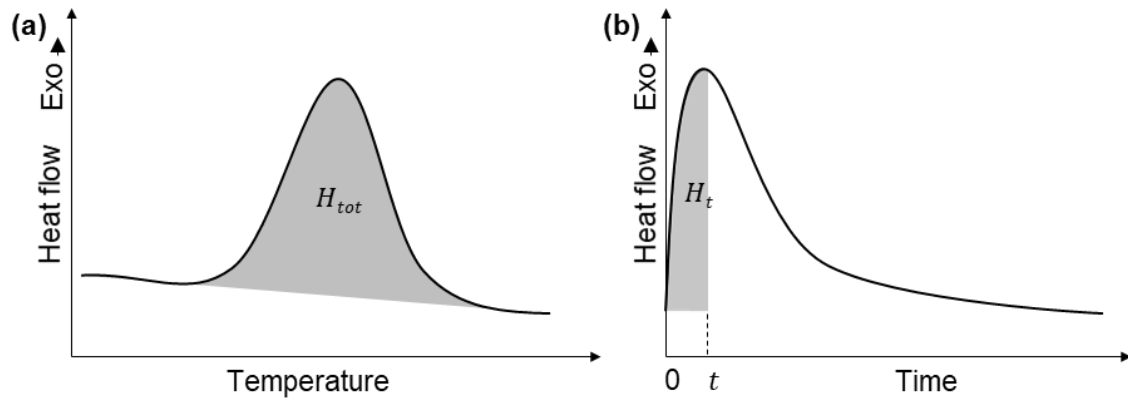


Figure 2.8: Schematic of typical DSC curves showing the area under the exothermic peaks H_{tot} and H_t up to time t : (a) dynamic temperature scan, (b) isothermal scan.

Several empirical models describe the dependence of the degree of cure on time and temperature for various thermosets. Many of these models are based on an autocatalytic model firstly proposed by *Kamal and Sourour* [95,96]. The literature [97–99] report that the Kamal-Sourour (KS) model (Equation 2.12) adequately describes the epoxy cure kinetics.

$$\frac{d\alpha}{dt} = (k_1 + k_2\alpha^m)(1 - \alpha)^n \quad (2.12)$$

and,

$$k_i = A_i \exp\left(-\frac{E_i}{RT}\right) \quad (2.13)$$

where k_i is the Arrhenius terms with a corresponding pre-exponential factor A_i and activation energy E_i ; m and n , the reaction order constants; R , the universal gas constant; and T , the absolute temperature.

A series of isothermal or dynamic scans using DSC allow generating experimental kinetic data suitable for fitting the empirical model represented in Equation 2.12. Isothermal scans allow a more straightforward regression of data. However, during isothermal scans, particularly for high-temperature measurements, a significant heat might not be detected before the sample reaches thermal equilibrium at the initial segment of the measurement leading to missing data. Therefore, dynamic scans at different heating rates are more suitable in such cases.

Alternative approaches to model-based methods, like KS model, include model-free methods like Friedman, Ozawa-Flynn-Wall, Kissinger-Akahira-Sunose and Vyazovkin. Their approach utilises isoconversional values to determine the kinetics of the reaction assuming reaction rate at a constant value of conversion is only a function of temperature [100–103].

Numerous investigations reported the curing kinetics of the resin systems used explicitly for pultrusion. Table 2.2 lists a few of the relevant studies that investigated the epoxy resin systems and the kinetics model utilised to predict the degree of cure in the pultrusion process.

Table 2.2: List of kinetic models for predicting the degree of cure in epoxy pultrusion.

Model	Kinetic relation	References
First order model	$d\alpha/dt = k(1-\alpha)$	[77,104,105]
KS model	$d\alpha/dt = (k_1+k_2\alpha^m)(1-\alpha)^n$	[97–99]
n^{th} order model	$d\alpha/dt = k(1-\alpha)^n$	[6,106–109]

Rheology

The rheological analysis captures information about temperature-dependent modulus, and phase transitions of reacting thermosets (referred to as chemorheology [110]). Because of their curing nature (i.e. transformation from viscous liquid to viscoelastic solid), the rheological experiments for thermosets generally utilise parallel plate rheometer. During the test, the resin formulation placed in between the plates experiences strain as the plates move relative to each other. The possible mode of the test can be rotational or oscillatory. For thermosets of initially relatively low viscosity and curing to a solid, the oscillation mode is a preferred measuring technique [111]. The advantage of the oscillatory test is that it allows measurement of the storage modulus (G') and loss modulus (G'') in addition to the viscosity of the curing mass. Here G' describes the elastic character and G'' describes the viscous character of a viscoelastic material.

A viscoelastic material responds to the applied strain or stress function with a time lag. The following equations define typically the applied shear strain or shear stress as a function of time in a rheometer [111].

$$\gamma(t) = \gamma_A \cdot \sin(\omega t) \quad (2.14)$$

$$\tau(t) = \tau_A \cdot \sin(\omega t) \quad (2.15)$$

where γ_A is the strain amplitude; τ_A , the stress amplitude and ω , the angular frequency. For viscoelastic materials, on pre-setting the strain function $\gamma(t)$, the stress function will have a phase lag, δ , resulting in

$$\tau(t) = \tau_A \cdot \sin(\omega t + \delta) \quad (2.16)$$

The phase lag will always be a value between 0° and 90° (i.e. $0 < \delta < \pi/2$ rad). An ideally elastic material responds without phase lag ($\delta = 0^\circ$) and an ideally viscous fluid with phase lag ($\delta = 90^\circ$). From these values, the complex shear modulus G^* can be calculated as,

$$G^* = G' + iG'' \quad (2.17)$$

where i is the imaginary unit and according to Hooke's law,

$$G' = \frac{\tau_A}{\gamma_A} \cos \delta$$

$$G'' = \frac{\tau_A}{\gamma_A} \sin \delta \quad (2.18)$$

The chemorheological profiles for a typical thermoset generally show that $G' < G''$ during the early stages of the cure, indicating low conversion of monomers. As the polymerisation proceeds, the polymerising chains lengthen with increasing cross-linking density resulting in a change in both G' and G'' until reaching a crossover/gelation point (where $G'(\omega) = G''(\omega)$). The gelation point refers to the time or temperature that results in full connectivity or initial formation of an infinite network through a polymer sample (Figure 2.9). The viscosity profiles also reveal changes during the cure, as thermosets show rapid increase in their viscosity during gelation.

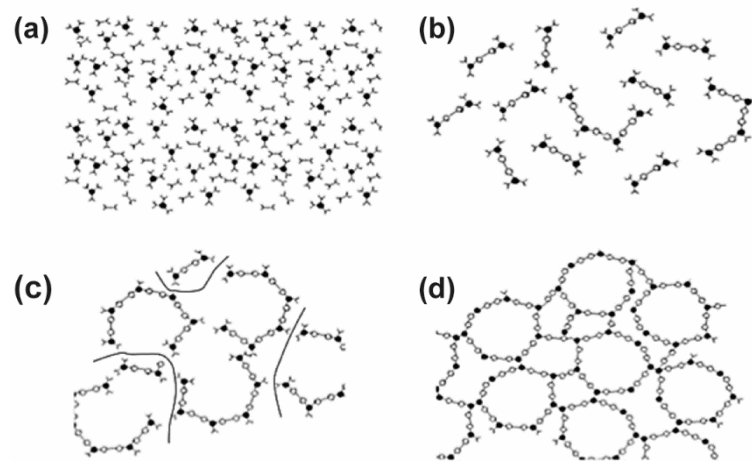


Figure 2.9: Schematic representation of cross-linking phenomena during the curing of thermosets: (a) monomer stage, (b) linear growth and branching (c) gelling incomplete cross-linked network, (d) fully cured thermoset [112].

Rheology is a useful tool for evaluating the gelation point of thermosets. Published investigations propose several approaches to determine the gelation point: (1) the crossover point of G' and G'' , (2) the point where shear viscosity approaches infinity (i.e. $\eta \rightarrow \infty$) and (3) the point at which the ratio G''/G' (or $\tan \delta$, the loss factor) is independent of the frequency of oscillation of the parallel plates. The crossover point approach is valid for the stoichiometrically balanced systems. In other words, for the stoichiometrically balanced systems, at the gelation point, the $\tan \delta$ reaches unity. Upon reaching the condition $G' > G''$, the matrix do not show any apparent flow behaviour [110,113].

The oscillatory measurements, using Newton's law, also allow calculating complex viscosity η^* of the curing thermosets using the relation

$$\eta^* = \frac{\tau(t)}{\dot{\gamma}(t)} \quad (2.19)$$

where $\dot{\gamma}$ is the shear rate.

Equation 2.20 represents complex viscosity mathematically

$$\eta^* = \eta' - i\eta'' \quad (2.20)$$

The real and imaginary parts of the Equation 2.20 relate to the loss and storage modulus as $\eta' = G''/\omega$ and $\eta'' = G'/\omega$. Further, modulus of the complex viscosity is given by

$$|\eta^*| = \sqrt{\eta'^2 + \eta''^2} \quad (2.21)$$

Cox-Merz empirical rule [114] claims that the modulus of the complex viscosity, $|\eta^*|$, and the steady-state viscosity, η , of a thermoset are equivalent at steady-state shear conditions in the viscous region [115,116], i.e.,

$$|\eta^*(\omega)|_{\omega \rightarrow 0} = \eta(\dot{\gamma})|_{\dot{\gamma} \rightarrow 0} \quad (2.22)$$

Several investigations report the chemo-rheological models for the thermosets. *Halley et al.* [110] present a comprehensive review of the chemo-rheological models in their paper. Since the viscosity development of the resin formulations depends on the type of chemical reactions between the species involved and the temperature. Further, there exists no universal model which describes the rheological behaviour of all thermosets. Nevertheless, many studies report Equation 2.23 well represents the chemorheology of a two-component epoxy system relevant to this work [94,106,117,118].

$$\eta = \eta_{\infty} \exp\left(\frac{E_{\eta}}{RT} + K_{\eta}\alpha\right) \quad (2.23)$$

where η_{∞} and K_{η} are the empirical constants; E_{η} , the activation energy of the viscous flow; R , the gas constant, and T , the absolute temperature.

Surface free energy

Understanding the surface energy of the resin formulations is vital for successful composite processing. The interaction between resin formulation and fibre surface is one of the deciding factors that determine the mechanical properties of the formed composite. Similarly, the interaction between the moulding die surface and the resin formulation impacts the surface characteristics of the moulded composite [39]. Although both the interactions are analogous, one prefers good adhesion between fibre and the matrix at the end of the moulding cycle. Conversely, after moulding, the moulded part must separate easily from the mould. Methodically estimating the surface free energies or surface tension of the individual materials used in a process reveals the level of interaction between the interacting components.

For the materials like epoxy, the surface energy changes as the polymerisation progress [119,120]. The change in surface energy also depends on temperature [121]. In addition, the presence of mould release further influences the surface energy changes [39]. Literature reports the use of the sessile drop method [122] and the Wilhelmy plate method [123] to measure the contact angle and the surface tension of the resin formulations. These methods can also be employed to characterise the surface free energies of the metal (mould) surfaces [121,124,125]. Figure 2.10 schematically illustrates the contact angle

formed by a sessile droplet on a solid surface and the liquid lamella formed around the Wilhelmy plate.

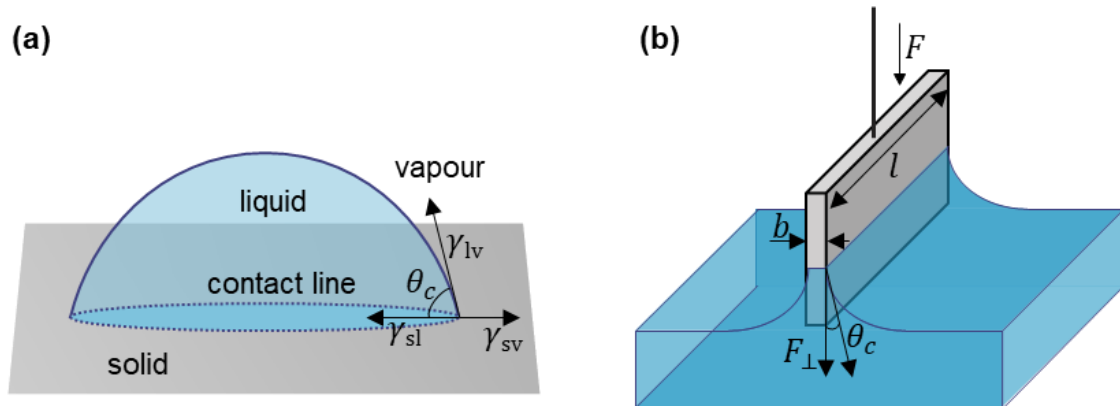


Figure 2.10: Schematic illustration of – (a) contact angle formed by sessile liquid droplet with a solid surface and (b) liquid lamella on the Wilhelmy plate.

Young [126] described that the mechanical equilibrium of three interfacial tensions defines the contact angle of a liquid drop on a solid surface. Mathematically, the interactions are related as,

$$\gamma_{lv} \cos \theta_c = \gamma_{sv} - \gamma_{sl} \quad (2.24)$$

where γ_{lv} is the liquid-vapour; γ_{sv} , the solid-vapour; and γ_{sl} , the solid-liquid interfacial tensions respectively and θ_c represents Young's contact angle.

An optical goniometer can be employed to measure the contact angle of a sessile droplet directly [127]. The instrument consists of a horizontal table on which the solid test specimen can be placed. An objective or a camera equipped with protractor observes the metered volume of the liquid droplet of interest placed on the solid surface. The contact angle of the liquid droplet can be hence directly measured from the image captured using the camera. A 0° contact angle means a complete spreading/wetting of the solid surface by the liquid. The wetting property decreases with increasing contact angle.

On the other hand, the Wilhelmy plate method utilises a chemically inert metal plate, with defined dimensions, mounted to a precise weighing balance. The plate is immersed into and raised from the liquid of interest during the measurements. The weighing balance measures the buoyancy force that the plate experience during the immersion and raising of the plate. From the buoyancy force experienced by the plate, the surface tension of the liquid can be calculated using the relation,

$$\gamma_{lv} = \frac{F_{\perp}}{L_{WP} \cos \theta_c} \quad (2.25)$$

where F_{\perp} is the vertical component of the buoyancy force experienced by the Wilhelmy plate; and L_{WP} , the contact surface length (i.e. $2l+2b$ in Figure 2.10 (b)) of the Wilhelmy plate.

Estimation of the surface free energies of the resin formulations and the die wall facilitates the calculation of work of adhesion (W_A) using Young-Dupré equation,

$$W_A = \gamma_{lv}(1 + \cos \theta_c) \quad (2.26)$$

The measurement of work of adhesion provides insight into the phenomena of adhesion of the polymerising resin to the die wall and the effect of mould release to hinder the adhesion during pultrusion.

2.5 Conclusion of the state-of-the-art

The sections reviewed above, in general, the literature published on the pultrusion process, fibre-matrix combinations employed in the pultrusion and more specifically, the resistive forces and their measurement techniques. Additionally, the literature review on the characterisation of the reinforcements and the resin formulations further aids in understanding the physicochemical phenomena of the pultrusion process.

Inference from the reviewed literature reveals that in the pultrusion process, since the pulling force remains as a quantifiable feedback, the measurement of resistive forces is essential to gain scientific knowledge about the process. A summary of the critical analysis of the relevant information and knowledge gathered from the literature review follows herewith.

Several authors developed methods to investigate the phenomena occurring in the pultrusion and proposed specific models for the process. The methods and models, however, possess limitations since the individual studies considered only partially the multi-physical nature of the process. The generalised models that considered even detailed thermo-chemical and thermo-mechanical phenomena only validated the numerically calculated resistive forces based on the results from the analytical characterisation of the resin formulations. For example, the state-of-the-art pulling force model utilises the chemo-rheological model of the resin formulation, based on rheometric data to calculate viscous drag (F_{vis}). However, such models are by no means precise enough to model the flow near the die wall, but only seek to illustrate the viscous behaviour qualitatively at the die wall. This is because the models considered a constant viscous resin film thickness between the die wall and the moving fibre-matrix and have not considered the degree of direct interaction of the fibres in the fibre-matrix-die wall interface.

Further, the kinetic friction coefficient considered in the literature to calculate frictional forces (F_{fric}) were either specific or arbitrary. However, the friction depends not only on the surface-normal pressure exerted by the fibre-matrix caused by the temperature-induced thermal expansion but also on the multiple factors such as die surface roughness, presence of release agents, the concentration of release agents, the effectiveness of release agent, presence of low-profile additives and level of pilling. Pultrusion being a complex process, requires intricacy to model each phenomenon occurring in the process, in turn, demanding experimental methods to validate the developed models.

On the other hand, the experimental techniques that are available to characterise the process through the measurement of resistive forces possess challenges in quantifying the stresses at the fibre-matrix-die wall interface along the entire length of the die, which is essential to understand, for example, the effectiveness of mould release. State-of-the-art approaches mostly measure the pulling forces inline utilising pressure transducers at specific points (in-die pressure measurement) along the die length, as reported in [74,77], or measure the overall pulling force using a force transducer (on-die force measurement)

mounted at the end of a freely sliding die in the pulling direction [27]. The in-die pressure measurement method, however, records discontinuous data requiring data interpolation between the measured points that may not be accurate enough. Even increasing the number of measuring points continue to possess the problem and economic challenges. On the other hand, although the on-die force measurement method is relatively simple and economical, measuring the detailed profile of the resistive forces along the die length is not possible. Other alternative approaches, as reviewed in [7], use force sensing resistors or optical fibres as a sensory reinforcement in parallel to the reinforcing fibres, which later will be an integral part of the composite. This, however, possess disadvantages such as artificially increasing reinforcement or filler content. Additionally, such sensors are not suitable in an environment containing compliant wet fibrous reinforcements to measure resistive forces between the die wall and the fibre-matrix. Further, as the matrix solidifies and the consolidated profile contracts away from the die wall, the frictional forces between the profile and the die wall may not be measurable with integrated sensors [59,76].

In addition to the process parameters, the presence of process additives in the resin formulation like IMR significantly affects the resistive forces [52]. The techniques described earlier generally allow measuring the effects on the overall pulling force caused by the IMR. However, the position along the die length at which the IMR effectively acts and its amplitude are still not quantifiable. On the other hand, the state-of-the-art analytical and numerical models available for pultrusion process do not adequately address the problem. It is because most of the thermo-mechanical and chemo-rheological models used to model the pultrusion process do not include all the parameters that impact the pulling force. For example, the change in concentration of IMR in the resin formulation may not affect the cure rheology of the resin formulation. However, the change in surface energy and surface quality in the presence of IMR affects the shear force exerted by the fibre-matrix within the pultrusion die. It will take a very complex model to include all the issues and to address all the effects. Nevertheless, there are no methods available to date that can validate such models experimentally.

In brief, the following are the shortcomings of the state-of-the-art methodologies:

- Limited possibilities exist to quantify the stresses at the fibre-matrix-die wall interface at each of the infinitesimal segments along a pultrusion die.
- Introducing additional measuring aids (such as CFM) along with the reinforcements to measure the local forces influence measurements because of change in the multi-physics of the process.
- Integrated sensor measurements, unfortunately, do not reflect the surface interaction phenomena between the fibre-matrix and the die wall.
- Pressure gauge measurements at specific points along the die length are insufficient to monitor the phenomena occurring at each of the infinitesimal segments along the die length.
- Available methodologies do not sufficiently address to test the effectiveness of IMRs in the process.
- Full scale inline pulling force measurements may not be economical because of the need for large quantity of material and resource intensiveness.

Nevertheless, the works published by several researchers through the years is of great interest to the present work. This review endeavoured to compile the relevant studies conducted on specific issues and phenomena that interact in the pultrusion process and permitted in developing further strategies and to integrate them into the concepts pursued in this research work. Furthermore, the review shows that die dynamics is a vital phenomenon and the core of the pultrusion process. The limitations of the state-of-the-art methodologies mentioned above and deficiency in the experimental methods to quantify the die dynamics necessitates the development of a methodology that quantify the process phenomena during the consolidation of fibre-matrix within a pultrusion die. Therefore, this research work aims to develop and validate a new cost-efficient offline methodology to investigate and quantify the die dynamics of a thermoset pultrusion accounting the multi-physics nature of the process. Further, this work pursues to utilise the developed methodology to pre-determine the process settings for a given fibre-matrix combination.

3 Objectives and approach

The review of the literature reveals that the available state-of-the-art methodologies to investigate the pultrusion process do not sufficiently consider the physicochemical phenomena occurring within a pultrusion die. In particular, the process models developed based on the data obtained through different pulling force measurement techniques (described in Section 2.3) and the rheokinetic data of the resin systems have not included the impact of process additives, for example, the IMR. Thus, so far, the existing methodologies have not investigated and quantified the die dynamics of the pultrusion considering holistically the process, geometrical and material parameters involved in the process. Additionally, the existing experimental techniques demands a resource intensive full-scale pultrusion line.

3.1 Research hypothesis

In principle, in any process, the physical quantities define the process phenomenon. Literature, therefore, adopts pulling force to define the (process) die dynamics of the pultrusion. Besides, in a rotating system torque is the measure of the force that makes an object to rotate about an axis. Therefore, transforming the linear motion in pultrusion to a system with rotational motion permits to measure the resistive forces (described previously in Chapter 2) as torque. Chapter 4 describes in detail the methodology adopted in this work for the transformation. Considering the nature of the pultrusion process and the underlying physics of the process, this work proposes following research hypotheses to quantify the pultrusion die dynamics using the rotational system:

1. The thermo-mechanical and chemo-rheological phenomena occurring within a pultrusion die in a pultrusion process and in a system in which the fibre-matrix wound on a core rotating about its axis in a sealed annular volume between the core and a hollow cylindrical die are analogous.
2. The shear and normal forces exerted by the fibre-matrix, rotating within the annular volume of the coaxial cylinders, on the fixed outer cylinder is continuously measurable as torque.
3. The process, geometrical and material parameters have similar effect on the forces that arise in pultrusion and rotating core processes.
4. The torque experienced over time by the fixed outer cylinder in the rotating system is equivalent to forces experienced by a pultrusion die along its length in pultrusion.

3.2 Objective and scope of the thesis

This work establishes a new offline experimental methodology to analyse the die dynamics through a physical replication of the pultrusion process. The following objectives realise the goal of this work:

1. Develop a new offline method and an apparatus to measure equivalent of the resistive forces in a pultrusion die in terms of torque.
2. Development of measurement process and investigate the process variables.
3. Study the effect of process, geometrical and material parameters on the resistive forces and establish a die dynamics model.

4. Validate the new method against pultrusion through experimental measurements of pulling force on a lab-scale pultrusion line.

Chapters 4 – 8 address the research objectives and verifies the proposed hypotheses. A new apparatus developed and fabricated to facilitate the experimental measurements allows characterising the die dynamics. Chapter 4 describes in detail the new methodology, hereinafter called as “rotating core method”, and the apparatus, hereinafter called as “Die Dynamics Simulator (DDS)”. Chapter 5 details the development and optimisation of the torque measurement process using the newly developed apparatus. Investigation of thermal, chemo-rheological and interfacial energy properties of the resin formulation is necessary to examine, analyse and understand the physicochemical changes of the resin formulation that occur in the process. Chapter 6 discusses the curing kinetics, rheological characteristics and surface energetics of the resin formulations used. Chapter 7 presents the conducted parametric studies using the apparatus to verify the general applicability of the new method to represent the pultrusion process. Chapter 8 presents the validation and comparison of the new methodology with the results obtained from a lab-scale pultrusion line.

To maintain focus on the primary objectives of the work and adhere to budgetary constraints, the scope of this investigation concentrates on isothermal processing of epoxy-glass fibre system in pultrusion and rotating core method. Further, to simplify the problem of investigation and to validate the proposed method, the research work focuses on analysing pultrusion die dynamics while pultruding a rectangular thin composite profile.

3.3 Thesis methodology

As described in the previous sections, the measurement of different resistive forces that arise within the pultrusion die poses many challenges. The existing inline measurement techniques possess limitations not only to measure the resistive forces along the entire length of the die, but also at the specific zones of interest, for example in the gelation region. This is because, the force measurement along the length of a pultrusion die (i.e. in a linear process) requires a sensor network which records data at each position along the die’s length. In other words, the entire surface of the die cavity should act as a sensor. However, such a complex network is impractical and not economical.

On the other hand, transforming linear process into a rotational process allows to record the forces arising at each instance of time over the course of polymerisation as torque. Thus, transformation of the operational coordinate simplifies and overcomes the need for complex sensor network in the die. Therefore, within the scope of this research work, an offline rotating core approach has been developed which is more effective in measuring the resistive forces continuously as torque. Figure 3.1 schematically illustrates the principle behind the transformation of the pultrusion process to the rotating core method (i.e. from a linear system to a rotational system). The symbols F_{pull} and F_{die} in Figure 3.1 denotes total pulling force and sum of resistive forces arising in the straight segment of the pultrusion die respectively. The symbol M denotes the torque experienced by the cylindrical die in the rotating core method.

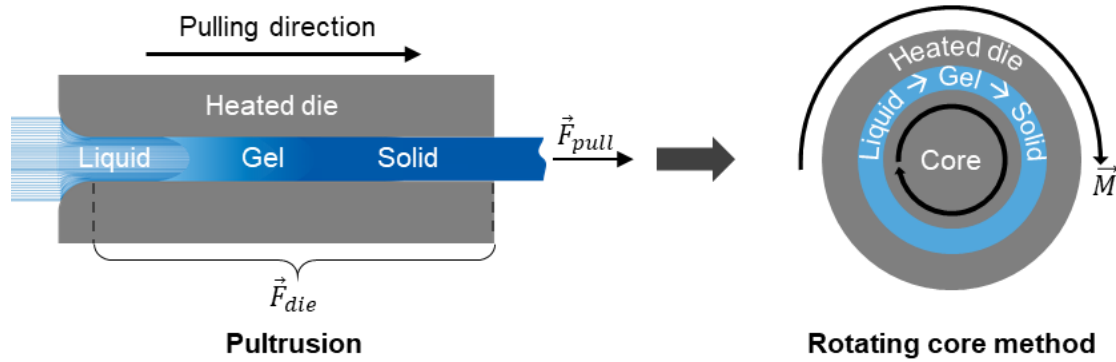


Figure 3.1: Transformation from linear motion to rotational motion.

The experiments verify the transformed hypothetical model using the apparatus (DDS) developed explicitly for the purpose. In the rotating core method, impregnated roving (utilising filament winding technology [128]) wound on a solid core is introduced into a heated die mounted on a torque transducer. As the core wound with fibre-matrix rotates about its axis, the DDS records the torque, temperature of the die and the rotational speed of the core. The recorded data permits to investigate the dynamics of the process including the progress of polymerisation. Further, experiments conducted varying the parameters like die temperature, the rotational speed of the core, diameters of the die and the core, resin formulation, and fibre volume fraction allow to study their effects on the die dynamics. In parallel, pultrusion experiments conducted with similar parameters favour the validation of the results from the rotating core method. The following flow diagram (Figure 3.2) represents the approach and the overall steps adopted to achieve the goal of this work.

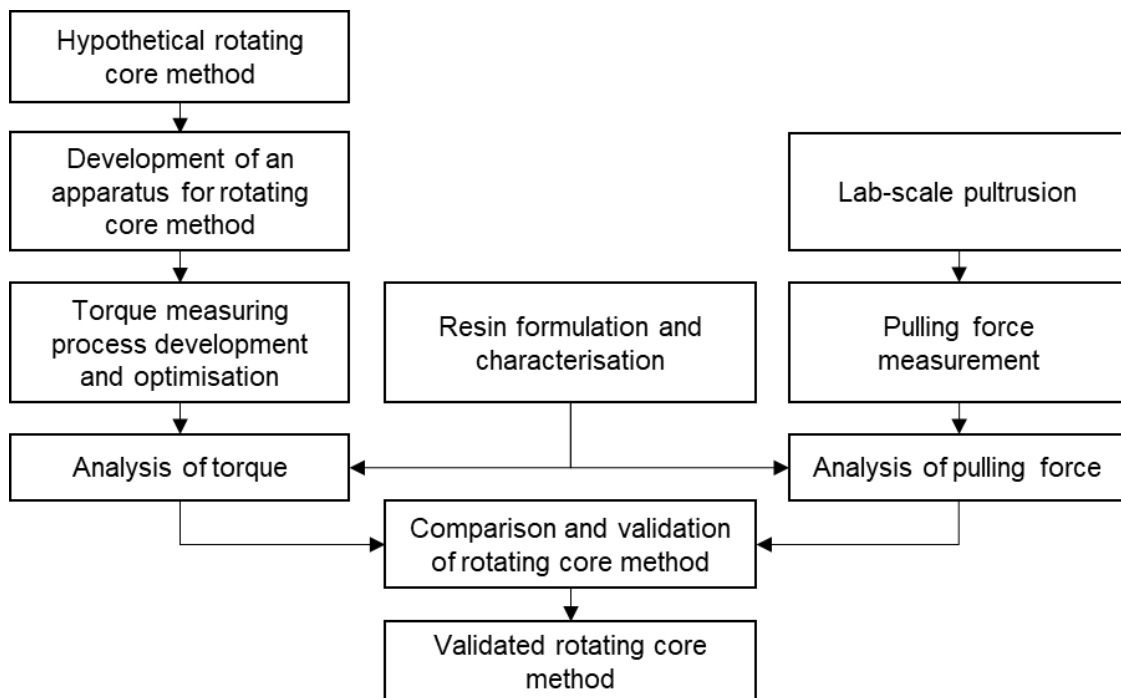


Figure 3.2: Flow diagram representing the approach of the thesis.

4 Development of rotating core method

This chapter describes the theoretical aspects considered for the development of the rotating core method and the adopted design strategies for the development of DDS. The sections elucidate implemented analytical approaches that facilitate the transformation of the linear pultrusion system to a rotational system as well as to theoretically prove the equivalence of both the systems. Further descriptions include, the theoretical aspects considered for the definition of hardware and software requirements to fabricate the DDS. The approaches permitted systematic development of the apparatus for the measurement of die dynamics.

4.1 Rotating core method

The rotating core method is an offline process analysis technique. The technique pragmatically simulates the phenomena occurring inside the straight segment of a pultrusion die (Hypothesis 1). In a typical pultrusion process, the fibre-matrix has a linear motion (flow) in the straight segment of the pultrusion die. The principle behind the rotating core method is the transformation of this linear motion of the material to rotational motion, conserving all the transport phenomena of a thermoset pultrusion process.

Principally the rotating core method consists of a cylindrical core and a stationary hollow cylindrical die coaxial to one another (Figure 4.1). The difference between the die's inner radius and the core's outer radius creates an annular gap between them. The annular gap serves to introduce the fibre-matrix within its volume along the length. The core acts as a drive to rotate the fibre-matrix along the die wall. Upon heating the cylindrical die, the resin formulation inside the annulus polymerises resulting in a tubular composite.

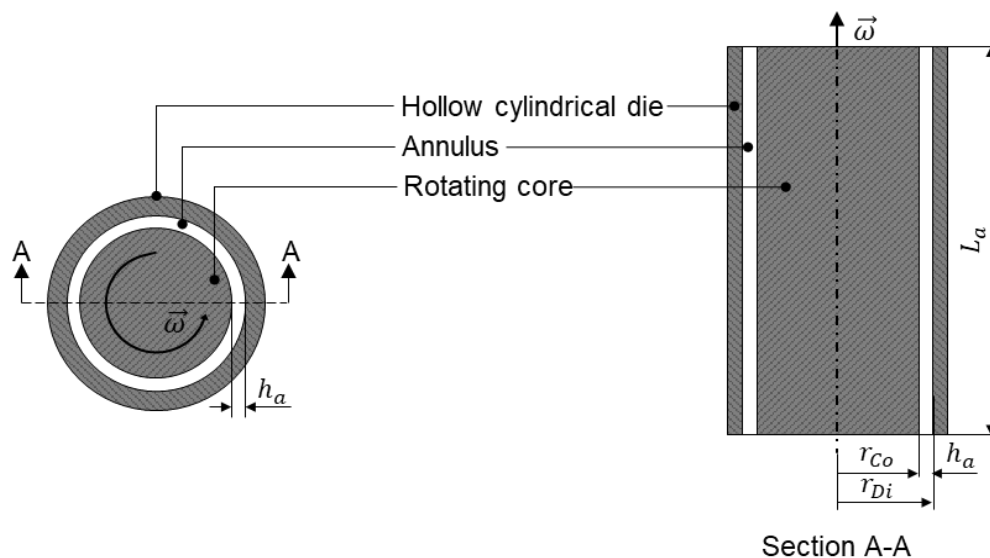


Figure 4.1: Schematic of the cylindrical die and core setup in the rotating core method.

The notations r_{Co} and r_{Di} denote the radius of the core and the inner radius of the die respectively, h_a and L_a denote the thickness and length of the annular ring, respectively and ω denotes the angular velocity.

4.1.1 Representation of pultrusion in linear cartesian coordinates

A generic representation of a simple rectangular profile in the straight segment of a rectangular die cavity is shown in Figure 4.2. Considering the dimensions of the cavity in the cartesian coordinates, the symbols L , w and h denote the cavity's length, width, and thickness respectively. The length extends along the x-axis, the width along the y-axis and the thickness along the z-axis. In Eulerian frame of reference, impregnated reinforcements enter the straight segment of the die at the position x_0 and the consolidated composite profile exits the die at x_L at a pulling velocity v_{pull} . On the time scale, the impregnated reinforcements enter the die at t_0 and the profile exits the die at time t_L . Thereby the residence time of the fibre-matrix within the die cavity is Δt ($\Delta t = t_0 - t_L = L / v_{pull}$).

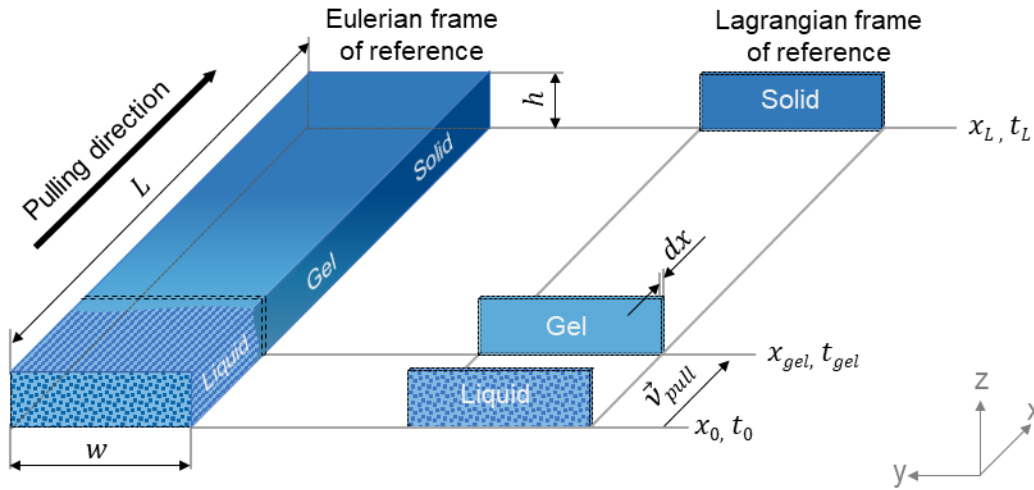


Figure 4.2: Generic representation of a simple rectangular profile in an Eulerian and a Lagrangian frame of reference in the cartesian coordinates.

On the other hand, observing the profile in a Lagrangian frame of reference, for the given time Δt , an infinitesimal fibre-matrix parcel of length dx moves from x_0 to x_L at a velocity v_{pull} (an analogous to plug flow reactor). As a result of polymerisation, during its motion, the matrix component within the infinitesimal material parcel transforms from viscous liquid to a viscoelastic solid. Throughout its motion within the die cavity, the moving infinitesimal material parcel exerts resistive forces on the stationary die wall because of the molecular momentum (i.e. due to viscosity and friction). Recalling the forces from Section 2.3, they can be grouped into viscous (until gelation) and frictional forces (post gelation). Therefore, the total resistive force (F_{die}) that the straight segment of the die experience is

$$\vec{F}_{die} = \vec{F}_{vis} + \vec{F}_{fric} \quad (4.1)$$

or represented in the tensor form as

$$\vec{F}_{die} = \iint \tau_{ij} dA_{sr} \quad (4.2)$$

where τ_{ij} are the directional stress components and A_{sr} , the surface area of the rectangular die cavity. The indices i and j specify the orientation of the surface upon which it is acting and the direction in which the stress component acts, respectively. Considering the

unidirectional (velocity driven) flow of material in the straight segment of the pultrusion die in the cartesian coordinates (Figure 4.2), Equation 4.2 reduces to

$$F_{die} = 2 \left(\int_0^L \int_0^w \tau_{yx} dy dx + \int_0^L \int_0^h \tau_{zx} dz dx \right) \quad (4.3)$$

where applies (from Section 2.3)

$$\tau_{ix} = \begin{cases} \eta \frac{v_{pull}}{\lambda} & , \text{ for } \eta < \eta_{gel} \\ \mu_k (p_n + \sigma_{adh}), & \text{ for } \eta \geq \eta_{gel} \end{cases} \quad (4.4)$$

4.1.2 Transformation from the linear system to a rotational system

Transforming the infinitesimal material parcel (shown in Lagrangian frame of reference in Figure 4.2) from the cartesian coordinates to cylindrical coordinates results in a system shown in Figure 4.3. In the new system, $d\theta$ is equivalent to the infinitesimal length dx , L_a is equivalent to the $2(w + h)$ of the material parcel, and h_a an equivalent of h (ideally $h/2$ because only the hollow die acts as heat source) of the material parcel in the cartesian coordinates, respectively. When the material parcel revolves around the axis of the cylinder at an angular velocity ω , the path of revolution creates an annular ring.

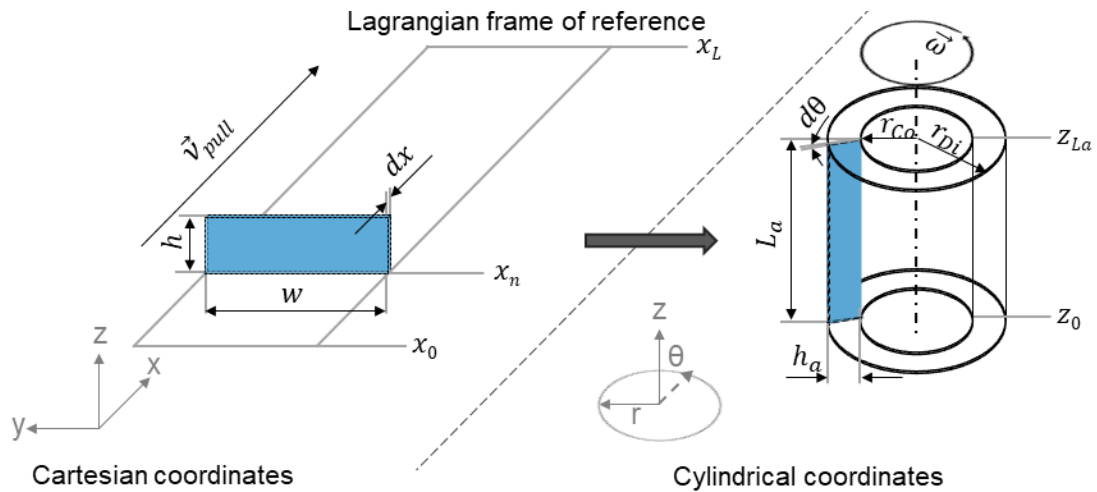


Figure 4.3: Schematic representation of transformation of the infinitesimal width of fibre-matrix from the linear cartesian to rotational cylindrical coordinates.

To establish the relation between the linear and rotational systems and to simplify the problem during the transformation of linear motion to the rotatory motion, following assumptions (1–12) needs to be defined:

1. The die and core are always coaxial to one another.
2. The mass of resin and fibre present inside the annulus does not change during the process.
3. There is no slip between the fibre-matrix and the rotating core.
4. No-slip condition is applicable at the die wall until gelation.
5. The viscous resin holds stable Couette flow (in the fibreless resin layer) until gelation.
6. There are no inter-fibre movements between the fibres present in the annulus.

7. The radial and axial flow of resin formulation during rotation are negligible.
8. The tangential flow of resin formulation within the fibre bed is negligible compared to that in the fibreless resin layer.
9. The temperature of the die wall and the resin layer close to the die wall are always equal.
10. Heat flow in the radial direction across the annular cross-section is uniform.
11. Heat flow in the axial direction is negligible.
12. Degree of cure of the resin formulation at the beginning of the process is negligible.

The assumptions mentioned above puts the system into a condition to have pure circumferential flow within the annulus. Therefore, the transformed rotational system is analogous to a concentric cylinder rheometer with rotating inner cylinder. The following chapters discuss the verification of the above assumptions through analytical and experimental characterisations.

When the core rotates, the angular displacement of the fibre-matrix inside the annular ring generates momentum flux. As a result, the fibre-matrix exerts resistive forces on the surface of the stationary cylindrical die wall. However, because of the rotational motion, the die wall experience a moment of the momentum flux (i.e. torque) about the rotational axis (Figure 4.4). Mathematically the torque is expressed as

$$\vec{M}_{cdie} = \vec{r}_{Di} \times \vec{F}_{cdie} \quad (4.5)$$

where M_{cdie} is the torque the cylindrical die experience; F_{cdie} , the tangential force (momentum flux) acting on the inner die wall.

If the volume of fibre-matrix in the annulus equals the volume of the annulus, then the outer radius of the fibre-matrix r_{rf} approaches the die's inner radius r_{Di} (i.e. $r_{rf} \approx r_{Di}$). In ideal conditions, if the fibres are completely wet, a fibreless resin layer of thickness λ appears at the interface between the die wall and the fibre-matrix. Therefore, the flow in the annular volume (i.e. in the fibreless resin layer) resembles planar Couette flow between parallel plates (as reported in [129]).

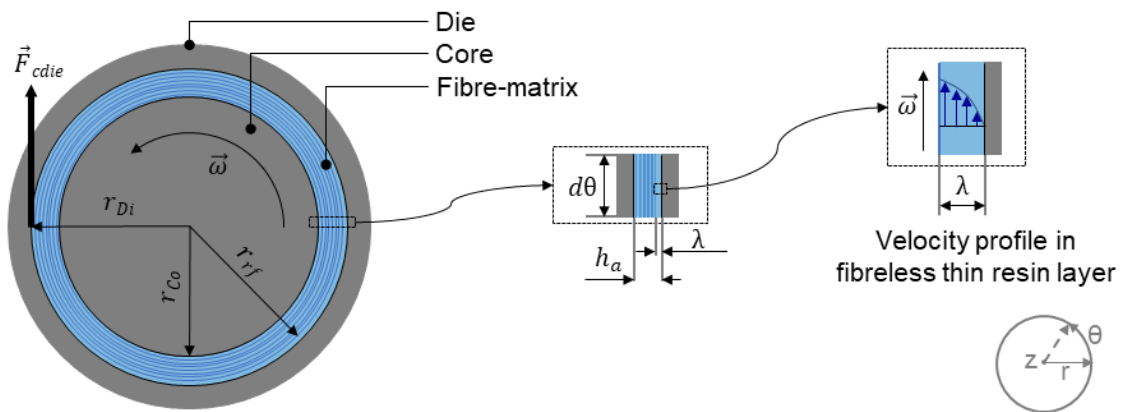


Figure 4.4: Illustration of torque exerted by the rotating fibre-matrix on the die wall and planar Couette flow as well as the resin velocity profile in the thin fibreless resin layer between moving fibre-matrix and the stationary die wall in the die-core setup.

Because the flow is a planar Couette flow and the force vector is always perpendicular to the radius vector, Equation 4.5 can be rewritten using Equation 4.2 and 4.3 as

$$M_{cdie} = r_{Di} \int_0^{L_a} \int_0^{2\pi} \tau_{r\theta} dA_{sc} \quad (4.6)$$

where applies

$$\tau_{r\theta} = \begin{cases} \eta \frac{\omega r_{Di}}{\lambda} & , \text{ for } \eta < \eta_{gel} \\ \mu_k(p_n + \sigma_{adh}) & , \text{ for } \eta \geq \eta_{gel} \end{cases} \quad (4.7)$$

Equations 4.6 and 4.7 show that the torque depends on material and process parameters: angular velocity ω of the core; inner surface area A_{sc} of the cylindrical die; inner radius r_{Di} of the die; thickness λ of the thin fibreless resin layer; viscosity η of the resin formulation; kinetic friction coefficient μ_k between the die wall and the composite profile; the normal pressure p_n exerted by the fibre-matrix on the die wall; and the adhesive strength σ_{adh} between the gelled matrix and the die wall. Consequently, the torque depends on the filament diameter (i.e. radius r_f), fibre volume fraction φ_f , process temperature T , degree of cure α of the resin formulation and the surface roughness R_a of the die and the core. The secondary parameters like chemical shrinkage coefficient of resin formulation as well as the coefficient of thermal expansion of filaments, resin formulation, core, and die also influence the torque. The dependence of the torque on the above parameters is detailed in Chapter 7.

Equation 4.6 is valid for one revolution of the fibre-matrix in the annular ring. Further, as per the assumptions mentioned above, at any instant of time t , the physical properties of each infinitesimal material parcel (in tangential and axial direction) in the annular volume are identical. Therefore, the force (i.e. torque) exerted by each of them on the die wall is equal. Consequently, the net torque at any given point of time is the algebraic sum of the torque experienced by the die at each point on its wall surface. Hence, mathematically the torque is represented as

$$\sum_t M_{cdie} = r_{Di} \sum_t \tau_{r\theta} A_{sc} , \text{ at any instant of time } t \quad (4.8)$$

In other words, the net torque becomes purely a function of time and therefore

$$\sum_{t=t_0}^{t=t_L} M_{cdie} = r_{Di} \sum_{t=t_0}^{t=t_L} \tau_{r\theta} A_{sc} \quad (4.9)$$

Hence, measuring the torque experienced by the cylindrical die throughout the course of polymerisation of the resin formulation permits to continually monitor the forces exerted by the fibre-matrix on the die wall. The force can be calculated by rearranging Equation 4.9 and applying on Equation 4.5 as

$$\sum_{t=t_0}^{t=t_L} F_{cdie} = \frac{1}{r_{Di}} \sum_{t=t_0}^{t=t_L} M_{cdie} \quad (4.10)$$

From Equations 4.3, 4.9 and 4.10, the average total resistive force F_{die} experienced by the straight segment of a pultrusion die and the total resistive force ΣF_{cdie} from rotating core method can be equated as

$$F_{die} = C \sum_{t=t_0}^{t=t_L} F_{cdie} \quad (4.11)$$

The dimensionless constant C relates the forces measured in both the processes independent of the geometry of the dies and the measurement parameters. Here,

$$C = \frac{A_{sr}}{d_p t_L A_{sc}} \quad (4.12)$$

where d_p is the number of data points recorded per unit time in the rotating core method. Selecting suitable geometrical and process parameters, thus permits the rotating core method to measure the equivalent of the forces that a pultrusion die experiences.

4.2 Development of an apparatus to quantify die dynamics

As described earlier, the rotating core system is an analogous to a rotational rheometer. However, the existing standard rheometers are specifically designed to measure only the viscosity of fluids. Consequently, they possess limitations to simulate the pultrusion die dynamics considering the impact of reinforcements on the process. Their further limitations include inability to handle reinforcement structures in the annular gap, low rated torque sensors (in mN m range), as well as inability to measure torque in the frictional regime (i.e. post gelation) of the pultrusion process. Therefore, quantification of the die dynamics using the rotating core method demands the development of a new apparatus (DDS) capable of continuously measuring the torque throughout the composite consolidation process. Based on these necessities, the key requirements of the DDS considered within the scope of this work include:

1. An annular gap with defined geometry between a cylindrical core and a hollow cylinder.
2. A sealed annular volume to prevent the flow of material into or out of the annular volume.
3. A drive to rotate the core.
4. A heating device to supply heat energy to the hollow cylinder.
5. A torque sensor to measure the torque exerted by the revolving fibre-matrix on the inner wall of the hollow cylinder.
6. Temperature sensors to monitor the temperature of the system during the measurement process.
7. A speed sensor to monitor the speed of revolution of the core.
8. A data acquisition system to collect the torque, temperature and speed measured during the process.
9. Control units to control the temperature of the heaters and rotational speed of the drive.
10. A data processing and storage device.
11. A software interface to interact with the control units and data acquisition devices.

4.2.1 Design strategy

Substantiation of the validity of the assumptions considered under Section 4.1.2 demands the adoption of specific design strategies while designing the components for the DDS. The following sections discuss the adopted primary design strategies for the die-core system used in this study.

Die and core geometry

The flow between rotating concentric cylinders vary from circular Couette flow to wavy vortex flow depending on the rotational Reynolds number of the system [130–132]. The rotational Reynolds number for the fluid rotating between the concentric cylinders (with a stationary outer cylinder) can be calculated using the relation

$$Re = \frac{\rho\omega r_i(r_o - r_i)}{\eta} \quad (4.13)$$

where Re is the Reynolds number; ρ , the density of the fluid; ω , the angular velocity of the core; r_i , the radius of the core; r_o , radius of the stationary hollow cylinder; and η , the viscosity of the fluid.

The critical Reynolds number for the flow (in an annulus with a stationary outer cylinder) to deviate from Couette flow is 99.53 [133]. Therefore, according to the assumption 5 mentioned above, operation within the planar Couette flow regime demands the selection of suitable geometrical parameters for the die and the core. The rotational Reynolds number for the systems considered in this work, calculated using the data obtained from viscosity (0.6 Pa s) measurements (Chapter 6) and the considered rotational velocity (0.1 – 0.45 rad s⁻¹), is less than 0.0001. In addition to the flow behaviour, other requirements to be considered, while choosing the die and core geometry, include the size of the torque sensor, electric drive for driving the core, heaters for heating the die, and the ability to utilise the reinforcing materials generally employed for pultrusion.

Predicated on the above requirements, to demonstrate the functionality of DDS for quantification of die dynamics, two cylindrical dies with an inner radius of 11 mm and 5.5 mm are chosen. Further, to study the effects of thickness variation of the composite on the die dynamics, annular gaps of 1 mm and 2 mm are chosen. Consequently, cores with 10 mm and 9 mm radii are used in combination with the die having 11 mm inner radius. For the die having 5.5 mm inner radius, cores with 4.5 mm and 3.5 mm radii are chosen.

For the experiments, at least 100 mm effective annular volume length (L_a) is chosen to minimise the errors caused by the local deviations in the fibre orientation of the windings (Section 5.4.1). Figure 4.5 shows the schematic of the cross-sections and the minimum overlapping length of the die-core assemblies utilised in this work. Further, rotational flow in an annulus of finite length may generate dissimilar flow behaviour at the annular volume's edges [133]. On the other hand, as discussed above, the systems considered in this work has rotational Reynolds number much below the critical Reynolds number, maintaining the planar Couette flow condition. Therefore, the significance of edge (at z_0 and z_{L_a}) effects on the measured torque is considered negligible.

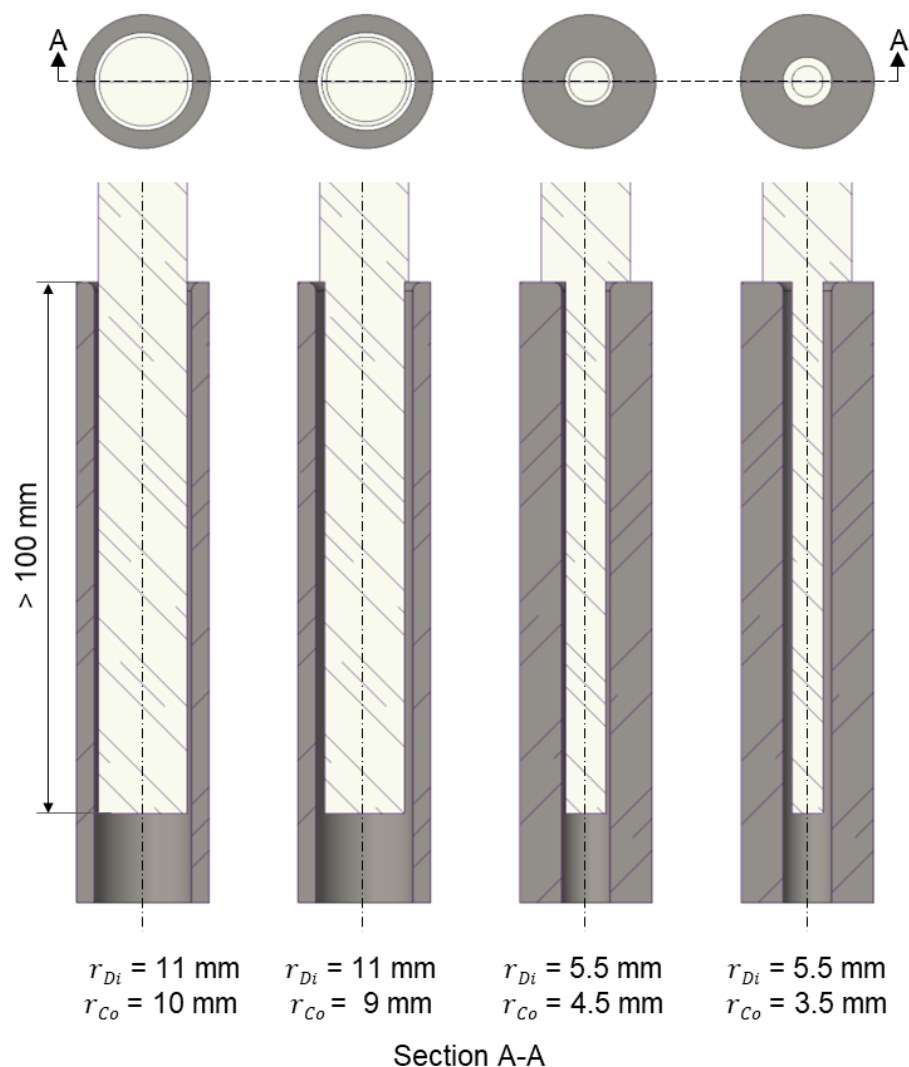


Figure 4.5: Schematic of the cross-sections of the die-core assembly with different radii and annular thicknesses utilised in this work.

Further, utilisation of a two-part die (like typical pultrusion dies) would favour easy preparation before the measurement and easy cleaning after the measurement cycle. However, a two-part die demands an excellent precision fit so that the assembled parts fit together without any transverse cross-sectional mismatch of the die walls. The mismatch of the walls in the direction perpendicular to that of the rotation, even by few micrometres, would hinder the flow of the resin, damage the fibres and certainly would lead to erroneous measurements. Hence, based on the above requisites, a one-part tubular die is favoured over the two-part die.

A tubular die allows the introduction of the core with the fibre-matrix only in the axial direction of the die (i.e. by push-in mechanism). A tapered or rounded entry in the die is, therefore, necessary to facilitate a smooth introduction of the fibre-matrix into the co-created annular volume. Therefore, based on the results from *Sharma et al.* [134,135], a rounded entry edge (with a 2 mm fillet radius) is chosen.

Furthermore, measurement of temperature of the die wall is mandatory to monitor the heat flow in the die-core system. A cavity drilled in the die wall, thus, serves to directly integrate a thermocouple (Figure 4.6).

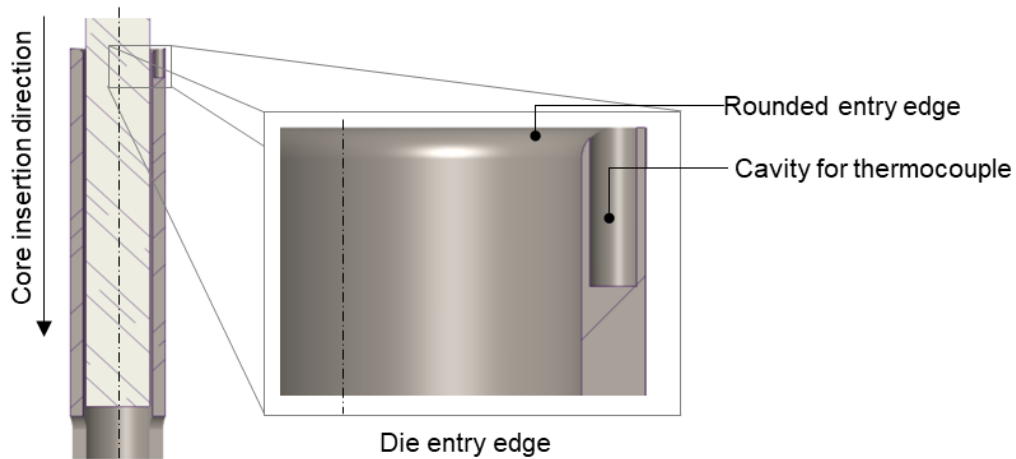


Figure 4.6: Cross-section of the die-core assembly showing rounded entry edge and the cavity for a thermocouple.

Sealing rings

The amount of fibre-matrix present inside the annular volume must not change during the process so that the DDS emulates the straight segment of a pultrusion die. Introduction of two sealing rings at the ends of the annular volume ensure the prevention of material flow out of the annular volume (Figure 4.7). However, the sealing rings could positively influence the torque because of additional friction. Therefore, the sealing rings are designed to have a conical outer cross-section which results in a minimum contact with the die surface and hence minimise the friction.

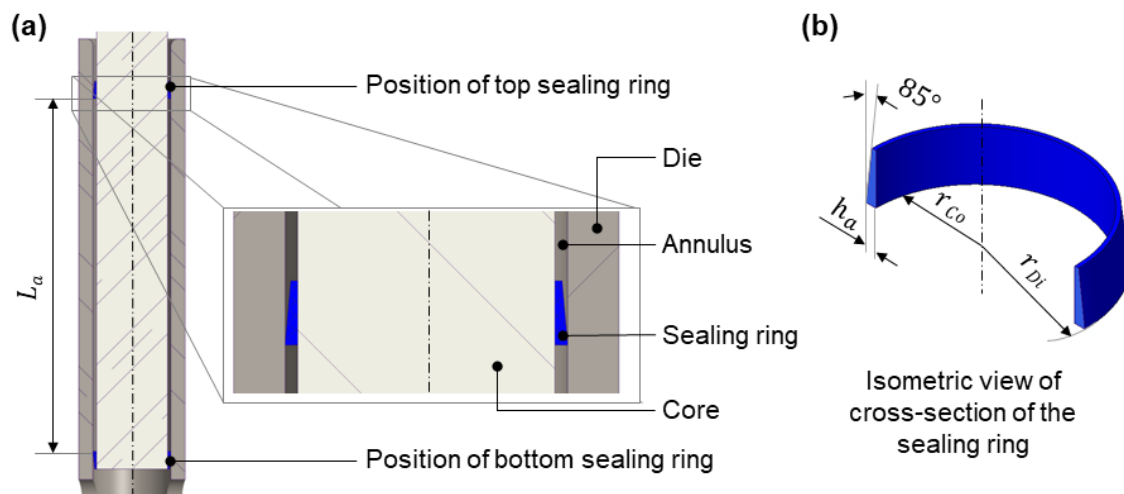


Figure 4.7: Cross-section of – (a) the die-core arrangement with sealing rings and (b) isometric view of the sealing ring.

In contrast, the cylindrical inner cross-section of the sealing rings guarantees a maximum contact area with the core's surface. As a result, due to the larger contact surface area, the friction between the core and the ring will be higher than that between the die and the

ring which ensure the rotation of the rings together with the core. The sealing rings are made of POM (polyoxymethylene) considering its excellent tribological and chemical resistance characteristics [136].

Surface roughness of the die and the core

The surface roughness of the die wall and the core is one of the primary factors that could affect the torque experienced by the die wall as well as the relative movement of fibre-matrix with respect to the die wall and the core. However, the relative movement between the core and the fibre-matrix is not preferred. In other words, the fibre-matrix must co-rotate together with the core to satisfy the no-slip condition defined earlier. On the other hand, the introduction of any fixing medium (like rings or pins) would geometrically and thermally contaminate the annular volume, and the system is no more comparable to the straight segment of the pultrusion die. These requirements demand the selection of suitable roughness for the die wall and the cores' surface.

A smooth die wall together with a rough core surface (i.e. $R_{a,die} \ll R_{a,core}$) would result in a lower coefficient of friction between the die wall and the fibre-matrix compared to the core and the fibre-matrix. Consequently, a mechanical interlocking effect appears between the core and the fibre-matrix. Through this effect, the fibre-matrix mechanically adheres to the core's surface. Therefore, the solid cores were manufactured by turning and finally sanded to have surface roughness values between ($R_{a,core}$) 0.821 μm and 1.102 μm . The inner die walls were finished by internal turning and finally honed to have surface roughness values between ($R_{a,die}$) 0.089 μm and 0.096 μm . The roughness of the core surface is, therefore, an order of magnitude higher than that of the die wall. For comparison, typical pultrusion dies have cavity surface roughness from (R_a) 1 μm to 2 μm [2]. Hence, the effect of roughness on the torque experienced by the cylindrical die becomes relatively insignificant. This work, thus, does not focus on the effect of surface roughness on the die dynamics which is recommended for future studies. Figure 4.8 shows the dies and cores with the sealing rings employed in this work.

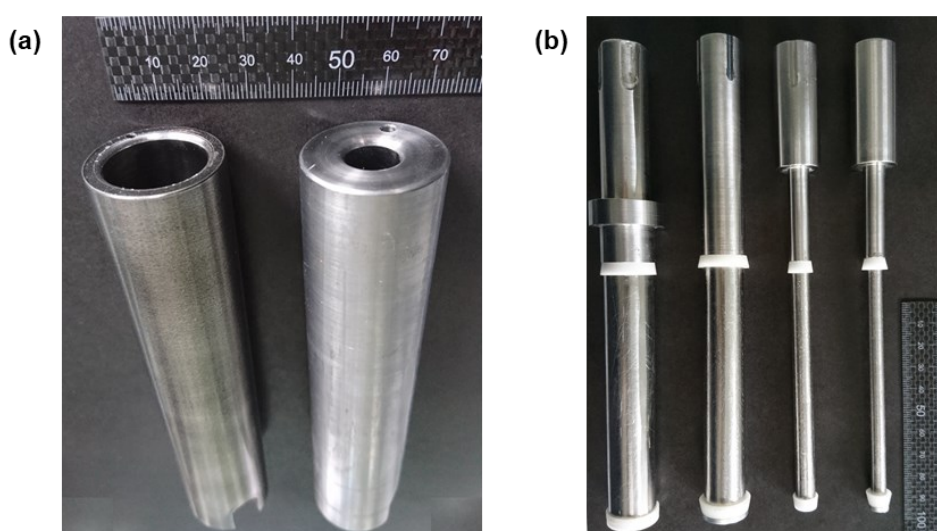


Figure 4.8: The dies and cores utilised in this work: (a) dies with inner radius 11 mm and 5.5 mm (left to right); (b) cores with radius 10 mm, 9 mm, 4.5 mm and 3.5 mm with respective sealing rings (left to right).

4.2.2 Hardware setup

The hardware setup of the DDS consists of structural, electrical, and electronic components. Figure 4.9 shows the concept of the DDS developed to quantify the die dynamics of an isothermal pultrusion process.

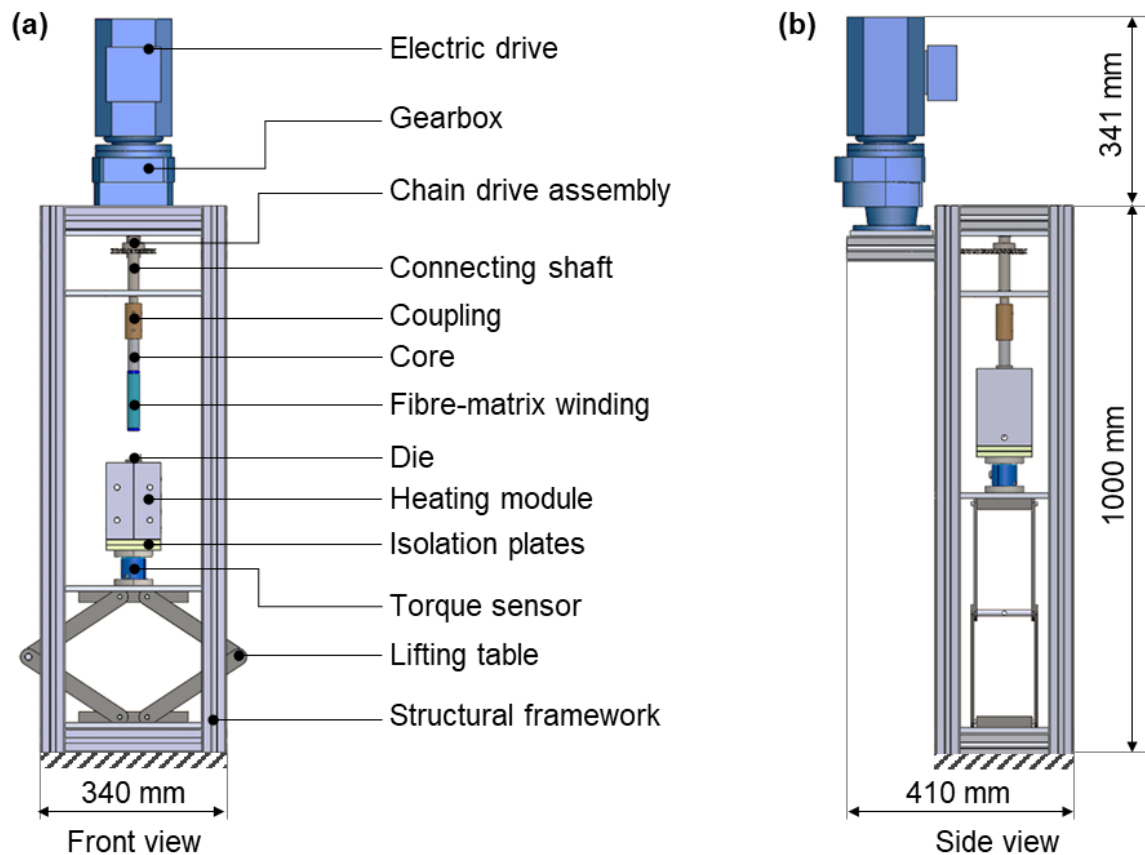


Figure 4.9: Concept of the DDS for quantifying the die dynamics of an isothermal thermoset pultrusion process – (a) front view with the lowered lifting table and (b) side view with the raised lifting table.

The DDS comprises of a metal structural framework to which the functional components are mounted. The die together with the heating module and the torque sensor is mounted on a lifting table. The lifting table serves to raise and lower the die assembly, which allows the die to be pushed on to the core. A set of four precision sliding guides ensure the prevention of horizontal out of plane movements of the lifting table, so that the axial centres of the die and the core lie precisely on the same vertical axis. The lifting table can be lowered up to 250 mm from the raised (or measuring) position to ease mounting and removal of the core from the drive. The lifting table is electrically operated using a 12 V DC electric drive.

The heating module (Figure 4.10) consists of two aluminium blocks fastened together. The two-part concept facilitates the ease of die-core removal and better thermal contact to the die. A cavity in the middle of the heating module allows to insert the die into the heating module. The cavity and the die are machined to have ISO H7/h6 tolerance [137] which ensures excellent surface contact between the die and the heating module. Holes drilled on to the walls of the heating modules allow the integration of up to four electric heaters

and two thermocouples into the heating module. An additional hole at the bottom of the heating module specially serves for the insertion of the die locking pin. The locking pin locks the die to the heating module against the axis of rotation of the core. The heating module, separated through two isolation plates, is mounted on the torque sensor.

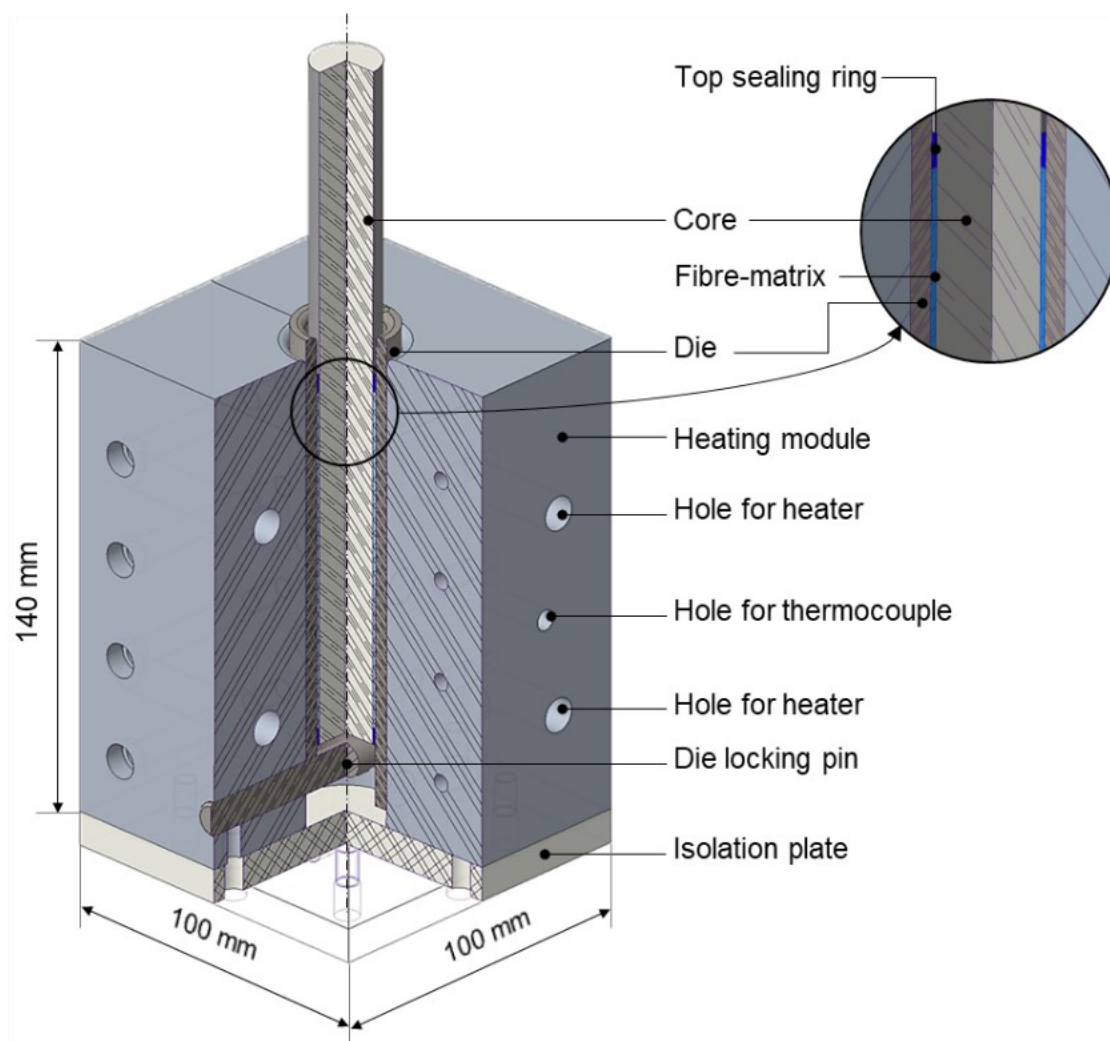


Figure 4.10: Heating module assembly offset-section showing the die and core arrangement within the heating module and magnification showing fibre-matrix between the die and core.

On the top section of the DDS, a connecting shaft, mounted on the same vertical axis as that of the core, connects the core to the driving unit. The core and the connecting shaft are coupled through a screwed coupling. The driving unit comprises of a chain drive assembly, gearbox and an electric drive. The DDS uses the electric drive, and a gearbox unit (G22C DM80GC4 TW) purchased from KEB Antriebstechnik GmbH, Schneeberg, Germany. The drive assembly comprises a 3 - phase alternating current motor and a spur gear assembly with a capacity to generate up to 111 N m peak torque. The variable frequency inverter KEB Combivert F5 – BASIC controls the rotational velocity of the drive. The rotational velocity of the electric drive changes in proportion to the input signal voltage (0 – 10 V DC) supplied to the variable frequency inverter. The structural components, the

heating module, the dies, the cores, and the sealing rings are manufactured and assembled in-house at DITF Denckendorf.

4.2.3 System control and data acquisition setup

The schematic of the data acquisition, data processing and visualisation and the control systems, shown in the Figure 4.11, permit to measure the process parameters torque, rotational velocity and temperature on the DDS as well as to control the rotational velocity of the drive.

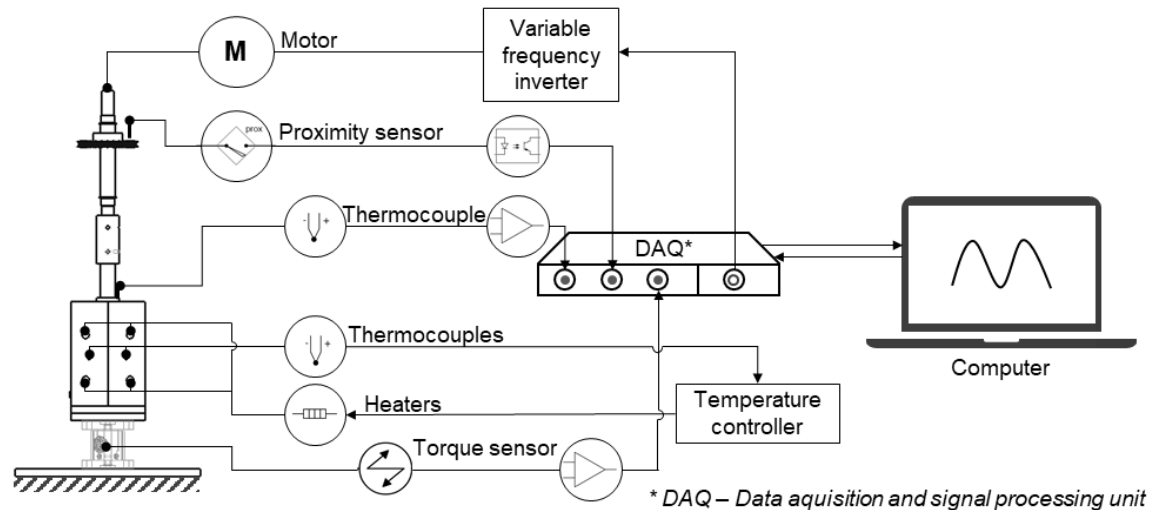


Figure 4.11: Schematic setup of data acquisition, processing and visualisation systems as well as control systems in DDS.

The DDS utilises a reactive non-rotating strain gauge-based torque sensor (DF-30) purchased from Lorenz Messtechnik GmbH, Alfdorf, Germany, to measure the torque exerted by the fibre-matrix on the die. The torque sensor has a rated torque of 20 N m. A sensor amplifier (LCV/U10) also purchased from Lorenz Messtechnik GmbH is used to amplify the torque sensor signal to normed voltage signal (± 10 V DC) that can be read through the data acquisition unit. Two thermocouples of Type J integrated into the heating module provide the real-time temperature feedback to the PID temperature control modules GEFRAN 400 from Gefran SPA, Provaglio d'Iseo (BS), Italy, which control the heaters. A PT100 thermocouple integrated into the die wall measures the temperature of the die.

An inductive proximity sensor mounted in the vicinity to the sprocket wheel of the chain drive assembly gives pulsed output signals to count the number of teeth per unit time. This in turn permits to calculate the rotational velocity of the core.

The (DAQ) data acquisition and the signal processing unit USB-6008 purchased from National Instruments Inc., Austin, USA, facilitates to receive the signals from torque sensor, thermocouple in the die wall, and the proximity sensor simultaneously. The multifunctional input-output device USB-6008 has the provisions for eight analogue signal input channels and two analogue signal output channels. Three of the eight input channels are used for collecting torque, rotational velocity, and temperature signals. One of the two

analogue output channels is used to control the rotational velocity of the electric drive by supplying control voltage to the variable frequency inverter.

The variable frequency inverter is programmed in such a way that the control voltage signal of 0 V DC corresponds to 0 rpm and +5 V DC corresponds to 8 rpm rotational speed of the core respectively. This facilitates the operation of the electric drive at variable rotational velocity. The visualisation and the processing of the acquired data and controlling the electric drive velocity is realised by connecting the USB-6008 to a personal computer.

4.2.4 Software interface

A new user interface program is developed using the *Visual Basic .NET* to connect data acquisition unit with the signal processing unit. The program utilises National Instruments' dynamic link library to establish communication between a personal computer and the USB-6008. The user interface is designed in a modular way to allow integration of more accessible extensions in the future. As shown in Figure 4.12, the user interface comprises the following modules:

1. An input module to define,
 - a. the data storage location and filename.
 - b. the rotational velocity of the core.
 - c. the geometrical parameters of the die and the core.
2. A real-time data visualisation module to visualise torque, rotational speed, and the temperature.
3. A control module to start, stop and reset the measurement process.
4. A test module to test the rotational velocity of the electric drive.
5. An advanced settings module to define the frequency of measurement and the calibration parameters.

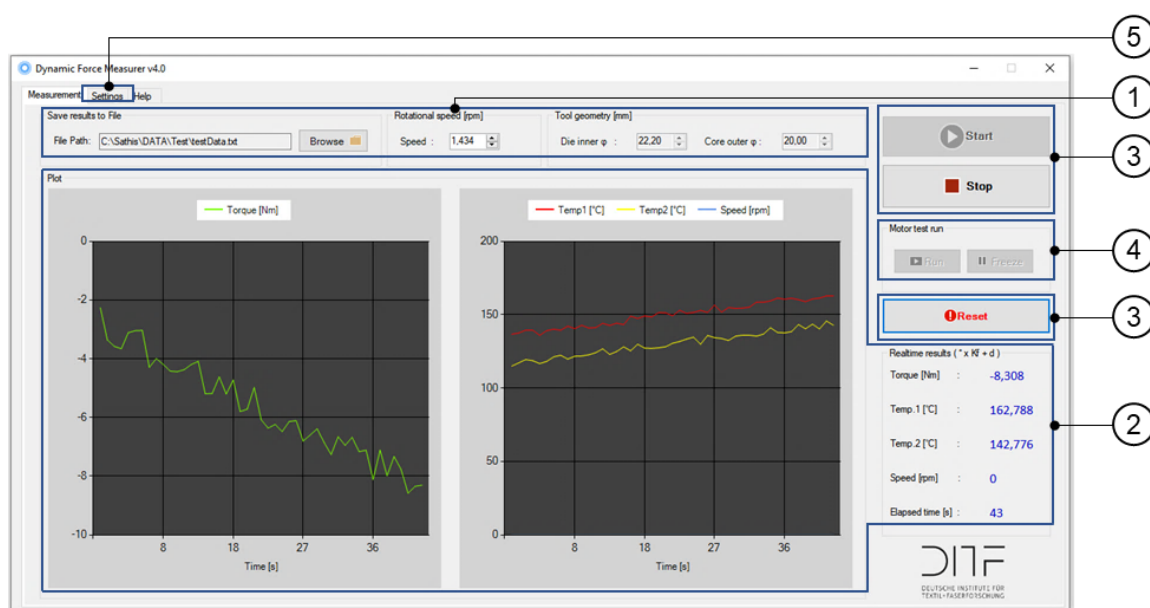


Figure 4.12: The user interface of the DDS and its modules.

The data collected are stored into a text file of ASCII TEXT format. The text file contains the measurement data, including the input variables like geometrical parameters of the die

and core, the set rotational velocity of the core as well as the frequency of measurement. The measured torque, temperature and rotational speed values are stored in a column separated format to ease the processing of the data later using data processing tools such as Microsoft Excel. Figure 4.13 shows the DDS apparatus and its components developed as a part of this work.

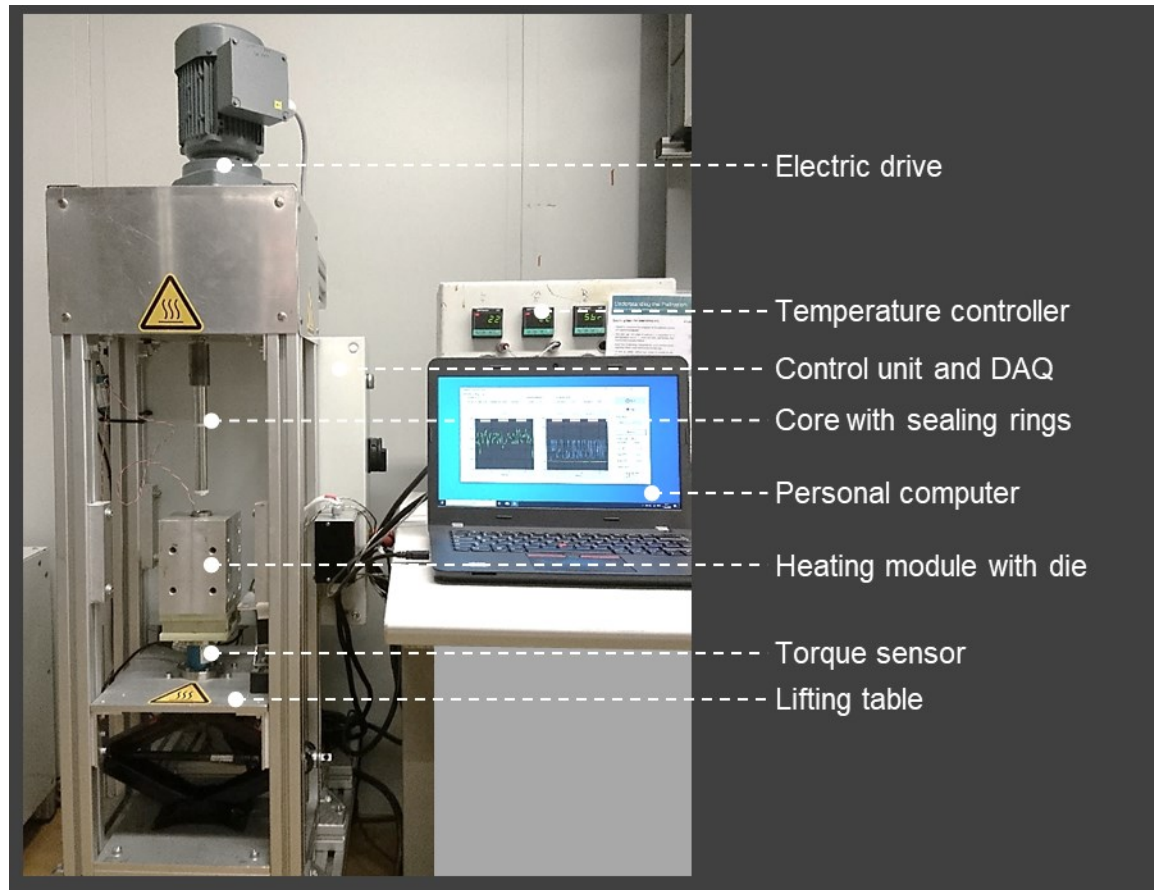


Figure 4.13: The DDS apparatus and its components.

4.2.5 Calibration of DDS

Calibration steps were performed to verify the validity of the data obtained from the developed DDS apparatus. The input variables temperature and speed of the DDS were calibrated to identify the deviation from the set values and accordingly include a correction factor. The output variable torque was calibrated to identify the baseline torque (i.e. the torque exerted by the core mounted with sealing rings and without the fibre-matrix) at different operating (temperature and speed) conditions and to exclude the resulting baseline torque from the measurements with fibre-matrix.

Calibration of heating unit

The temperature of the die has to be exactly regulated to control the polymerisation of the resin formulation during the torque measurements. Therefore, calibration of the temperature of the die was carried out to identify the deviation from the set temperature. The temperatures of the heating module and the die were measured separately and plotted against time (Figure 4.14). From the measured temperature data, the error fraction e_T between set and the actual temperature of the die can be calculated as

$$e_T = \left| \frac{T_{set} - T_{cdie}}{T_{set}} \right| \quad (4.14)$$

The temperature error fraction for the heating system amounts to approx. 6 %. Albeit the expected excellent surface contact of the die and the heating module, the difference in the temperatures would have resulted because of the thermal contact resistance attributed to surface roughness between them. Direct integration of heaters in the die would minimise the temperature difference from the set value. On the other hand, the set temperature of the heating module in the current setup could include the correction factor (i.e. $T_{heating\ module} = T_{cdie} e_T$) to compensate the temperature error. Therefore, in this work, the later approach was adopted. For example, for a required die temperature of 120 °C, the set temperatures $T_{heating\ module}$ of the heaters were 127 °C.

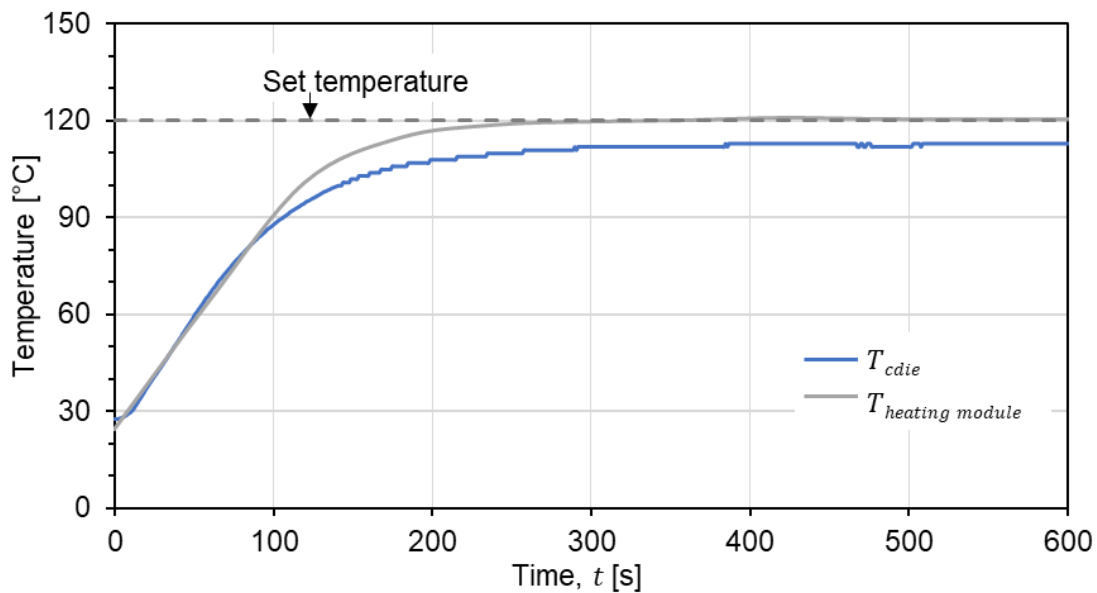


Figure 4.14: The temperature difference between the set temperature and the heating module and die temperatures.

Calibration of electric drive

The rotational speed of the drive controls the surface velocity of the fibre-matrix wound on the core. The dependence of the measured torque on the surface velocity v_s (where $v_s = \omega r_{Di}$) of the fibre-matrix (from Equation 4.7) demands strict control of the rotational speed of the core. The calibration procedure involved measuring the angular speed of the core using a pre-calibrated tachometer while varying supplied control voltage U_{cv} to the variable frequency inverter. Figure 4.15 shows the linear dependency of the angular velocity of the core on the control voltage signal supplied to variable frequency inverter. Using the relation between the control voltage and the core's angular velocity, the control voltage necessary for the desired surface velocity can be calculated using

$$U_{cv} = \frac{v_s}{10.206r_{Di}} \quad (4.15)$$

The above relationship is built into the user interface program of DDS to facilitate the selection of desired surface velocity during the measurements.

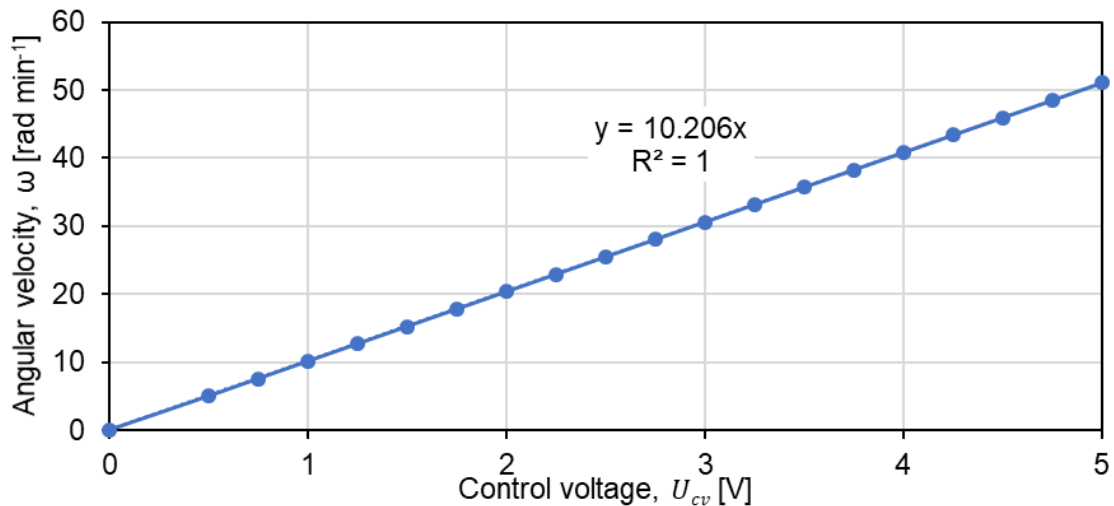


Figure 4.15: Linear relationship between the control voltage and the angular velocity of the core on DDS.

Torque sensor calibration

Calibration procedures have been carried out to ensure the reliability and the repeatability of the employed torque sensor. The aberrations created during the assembly of DDS such as eccentricity in the axis of the core, non-uniform stresses (because of different thermal expansion coefficients) created in the components, and the axis of orientation of the die and the core would cause parasitic effects on the torque transducer. As a consequence, after the introduction of the core into the die, even the stationary core (i.e. $\omega = 0 \text{ rad s}^{-1}$) would apply parasitic forces on the torque transducer. Hence, a calibration procedure was carried out after assembling the components of the DDS apparatus.

Further, calibration procedure involves measuring the torque with varying parameters such as die temperature and the rotational velocity of the core, with the sealing rings mounted core (without fibres). Figure 4.16 shows the recorded baseline torque without fibre-matrix (i.e. empty annular gap).

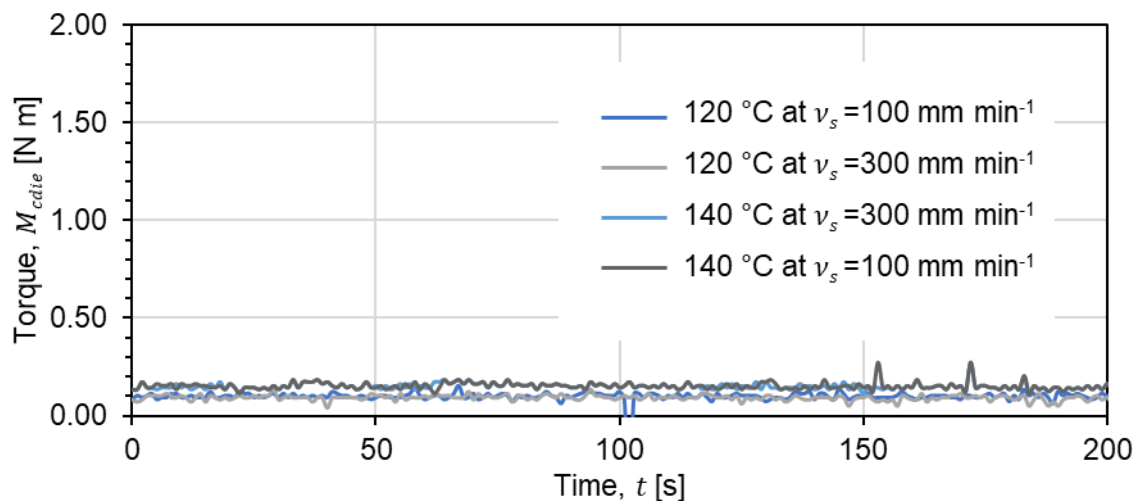


Figure 4.16: Torque measured at various temperatures and angular speeds with the 10 mm radius core and sealing rings on the DDS.

The mean torque measured with stationary core is 0.082 ± 0.025 N m amounting to a 0.43 % zero-error for the rated torque of 20 N m of the sensor. Therefore, the zero-error of the torque sensor is considered insignificant for the measurements. Nevertheless, the deviation is implemented into the data acquisition program. A similar observation is made for the measurements carried out after allowing the core (10 mm radius) to rotate with the sealing rings in the die. The torque was recorded at die temperatures of 120 °C and 140 °C with 100 mm min⁻¹ and 300 mm min⁻¹ sealing ring surface speeds.

The mean torque for the system at 140 °C is observed to be marginally higher than that for the measurements at 120 °C. An increase in the diameter of the sealing rings because of thermal expansion would have created more compression against the die wall leading to marginal increase in torque. Nevertheless, the errors are mathematically nullified during the data processing of the measured torque.

4.3 Conclusion of the development of the rotating core method

An offline rotating core method is developed to quantify the die dynamics of a thermoset pultrusion process considering the physicochemical characteristics of the process. The theoretical derivations based on the literature data show that the resistive forces experienced by the pultrusion die is a consequence of the physicochemical changes in the fibre-matrix within the die (Equation 4.3). Transforming the linear pultrusion system into a rotational system and extending the analytical derivations to the rotating core system (Equation 4.6) shows that the physicochemical changes (i.e. the phenomena) occurring inside a pultrusion die and in the annular volume of the DDS are analogous. The mathematical expressions thus allow to substantiate the hypothesis 1 which states that the phenomena occurring in both the processes are equivalent. In addition to that, the experimental results presented in the following chapters further verify the hypothesis.

Furthermore, based on the principles of the rotating core method, DDS was developed and fabricated to quantify the torque exerted by the rotating fibre-matrix on the cylindrical die wall. The developed apparatus, DDS, allow empirical simulation of the phenomena occurring inside a pultrusion die during a thermoset pultrusion process. Systematic design strategies were adopted during the fabrication of the DDS to ensure the realisation of the rotating core method. Nonetheless, the standardisation of the rotational core method and the DDS are comprehended by establishing measurement procedures and systematically studying the impact of process and material parameters on the measured torques.

5 Measurement process development for DDS

This chapter details the development of experimental procedures to measure the die dynamics using the developed rotating core methodology and the DDS. The challenges addressed include the identification and quantification of the parameters influencing the measurements carried out on the DDS. Further, the preliminary investigations enable the selection of materials and the definition of the process window. A systematic analysis of the influence of the preparatory process and material parameters on the measured torque permits to establish measurement procedures for die dynamics quantification.

5.1 Materials used

As described in the previous chapters, this work focuses on validating and demonstrating the applicability of the rotating core method to quantify the die dynamics of an isothermal pultrusion process. The resin system used within this work to demonstrate the functionality of the DDS is a two-component BADGE (Bisphenol-A-di-glycidyl ether) epoxy resin with an amine curing agent. The factors considered for the choice of the resin system include the ability to process using open bath impregnation, and low emission of volatile organic compounds. The amine-based curing agents provide advantages over the acid anhydrides: higher reactivity without catalysts even at temperatures lower than 150 °C and insensitivity to humidity [138].

The epoxy resin EPIKOTE™ Resin MGS® LR285 and the curing agent EPIKURE™ Curing Agent MGS® LH286 from Hexion Speciality Chemicals Inc., Esslingen a. N., Germany, suits for all the experiments conducted in this work. The relatively slow curing nature of the EPIKOTE™ Resin MGS® LR285 with EPIKURE™ Curing Agent MGS® LH286 infusion resin system, compared to standard pultrusion resin systems, facilitates to clearly identify and distinguish different regimes during the course of polymerisation (Section 7.4). Nonetheless, the utilisation of DDS can be extended to other standard pultrusion resin formulations as well. The mixing mass fraction of the resin to the curing agent employed is 100:40. Table 5.1 lists the properties of the resin and the curing agent.

Table 5.1: Properties of the resin and the curing agent employed in this work [139].

Designation	Type	Density [g cm ⁻³]	Viscosity at 25 °C [Pa s]	Mix viscosity at 25 °C [Pa s]
EPIKOTE™ Resin MGS® LR285	Resin	1.18 – 1.23	0.6 – 0.9	0.6
EPIKURE™ Curing Agent MGS® LH286	Curing agent	0.94 – 0.97	0.06 – 0.1	

UD (Unidirectional) E-glass direct rovings from P-D Glasseiden GmbH Oschatz, Oschatz, Germany, were used as reinforcement material for the DDS and pultrusion experiments. The glass rovings had a sizing preparation compatible with the epoxy resin system. Table 5.2 lists the properties of the E-glass roving used in this work.

Table 5.2: Properties of the glass rovings used [140].

Designation	Filament diameter [μm]	Linear density of the roving [tex]	Tensile strength [cN tex ⁻¹]
EC 14-600-350	14	600	45.0

A preliminary screening study, conducted by Roy [141] investigated the surface energy characteristics and the compatibility of various IMRs with the selected resin system. Based on the results of this study, the release agent showing best release properties and minimal impact on the mechanical properties of the composite is used for the experiments within this work. In addition to the IMR, an external mould release is additionally applied to the components of the DDS which come into contact with the resin. Table 5.3 lists the properties of the release agents used in this study.

Table 5.3: Properties of the release agents used [142,143].

Designation	Type	Manufacturer	Viscosity at 30 °C [Pa s]	Density [g cm ⁻³]
PAT® 656/B3R	IMR	E. und P. Würtz GmbH & Co. KG, Bingen a. R., Germany	0.5-1.0	1.01
Aqua Release 250	External mould release	Jost Chemicals GmbH, Laudenbach, Germany	-	1.0

5.2 Development of measurement process for DDS

The process steps that allow the utilisation of DDS to measure the torque have been established and the parameters that influence the measurement data have been identified. Based on the identified process variables, preparatory investigations were conducted to define the process window for the given set of process and material variables. The experimental procedure to quantify die dynamics using the DDS involves steps illustrated in Figure 5.1. The following sections detail the measurement methodology developed for the DDS.

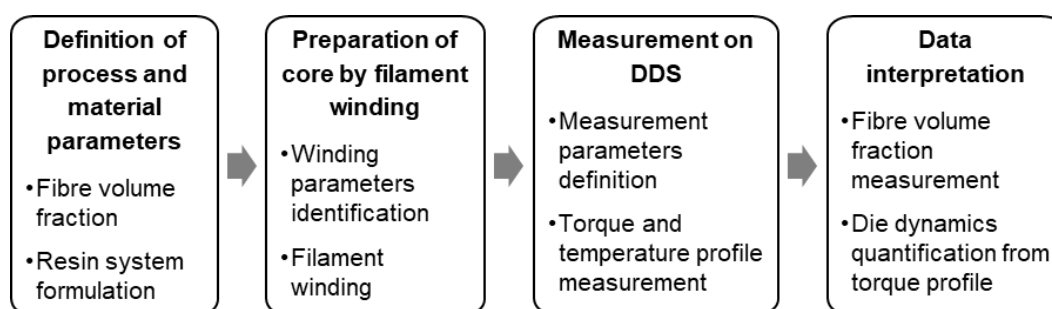


Figure 5.1: Experimental steps involved in quantifying die dynamics using the rotating core method.

5.2.1 Fibre volume fraction determination

Recalling from Chapter 2, the fibre volume fraction of a composite profile is one of the prime factors that directly influence the pulling force in pultrusion. Similarly, the fibre volume fraction in the annular volume affects the torque measured on the DDS. For a comparative analysis, the fibre volume fraction, for both the systems (pultrusion and offline measurement through DDS) should be equal. To have similar fibre volume fraction, it is necessary to calculate the achievable fibre volume fraction in the annular volume of the selected system. Mathematically, the fibre volume fraction in the annular volume is given by

$$\varphi_{fa} = \frac{V_{roving}}{V_{annulus}} \quad (5.1)$$

with

$$V_{roving} = L_{roving} A_{roving} = L_{roving} \frac{T_{tex}}{\rho_f} \frac{1}{10^6} \quad (5.2)$$

$$V_{annulus} = L_a \pi (r_{Di}^2 - r_{Co}^2) \quad (5.3)$$

where φ_{fa} is the calculated fibre volume fraction in the annular volume; V_{roving} , the volume of the roving in mm^3 ; $V_{annulus}$, the volume of the annulus in mm^3 ; L_{roving} , the length of the roving in mm; A_{roving} , the cross-sectional area of the roving (i.e. $T_{tex}/10^6 \rho_f$) in mm^2 ; T_{tex} , the linear density of the roving in tex; and ρ_f , the density of the fibre in g mm^{-3} .

Equations 5.1 to 5.3 show that for a fixed annular volume, the fibre volume fraction is a function of the length of the roving present inside the annular volume i.e. the length of the roving wound on the core. Therefore, to achieve a desired fibre volume fraction, the length of the roving required to be wound on the core can be calculated as

$$L_{roving} = \frac{\varphi_{fa} L_a \pi (r_{Di}^2 - r_{Co}^2) \rho_f \cdot 10^6}{T_{tex}} \quad (5.4)$$

Additionally, as a second verification factor, the weight of the roving to be wound can be calculated knowing the roving length and the linear density of the roving as

$$m_{roving} = \frac{T_{tex} L_{roving}}{10^6} \quad (5.5)$$

where m_{roving} is the mass of the roving in g.

The volume of the resin formulation, V_{resin} (in mm^3), required for the given fibre volume fraction and annulus geometry can thus be calculated as

$$V_{resin} = V_{annulus} - V_{roving} \quad (5.6)$$

5.2.2 Preparation of the core with impregnated fibres

The DDS uses impregnated rovings wound on a core as the input material for the torque measurements. To wind the impregnated rovings on a core, the preparation procedure employs filament (hoop) winding technique. For this, the preparatory steps have been

developed which utilises a 4-axis filament winding machine X-Winder Model 4X-23 from X-Winder LCC, Ohio, USA, to prepare the fibre-matrix wound core. As attachments, a pneumatic brake and a tension meter were mounted to the winding machine to control and measure the tension of the wound roving inline during winding.

Figure 5.2 shows the 4-axis filament winding machine and its components employed to prepare the core. In the winding process, a parallel wound spool supplies the roving. The dry roving from the spool passes through the pneumatic brake, several guiding rollers, the impregnation bath, a set of squeeze rollers, and a tension meter. Subsequently, the delivery head winds the impregnated rovings on the rotating core. The impregnation bath contains the resin formulation. As the roving passes through the squeezing rollers, the rollers squeeze the excess resin out of the roving and facilitate better penetration of resin into the fibre bundle. In the winding setup, the core remains stationary and rotates about its axis. In contrast, the winding unit (from spool to the delivery head) translates to-and-fro along the axis of the core to wind the roving along the length of the core. The direction of rotation of the core (i.e. the direction of winding) is chosen to be same as the direction of rotation of core during the measurement on the DDS. This prevents the unwinding of the roving from the core during the torque measurement process on the DDS.

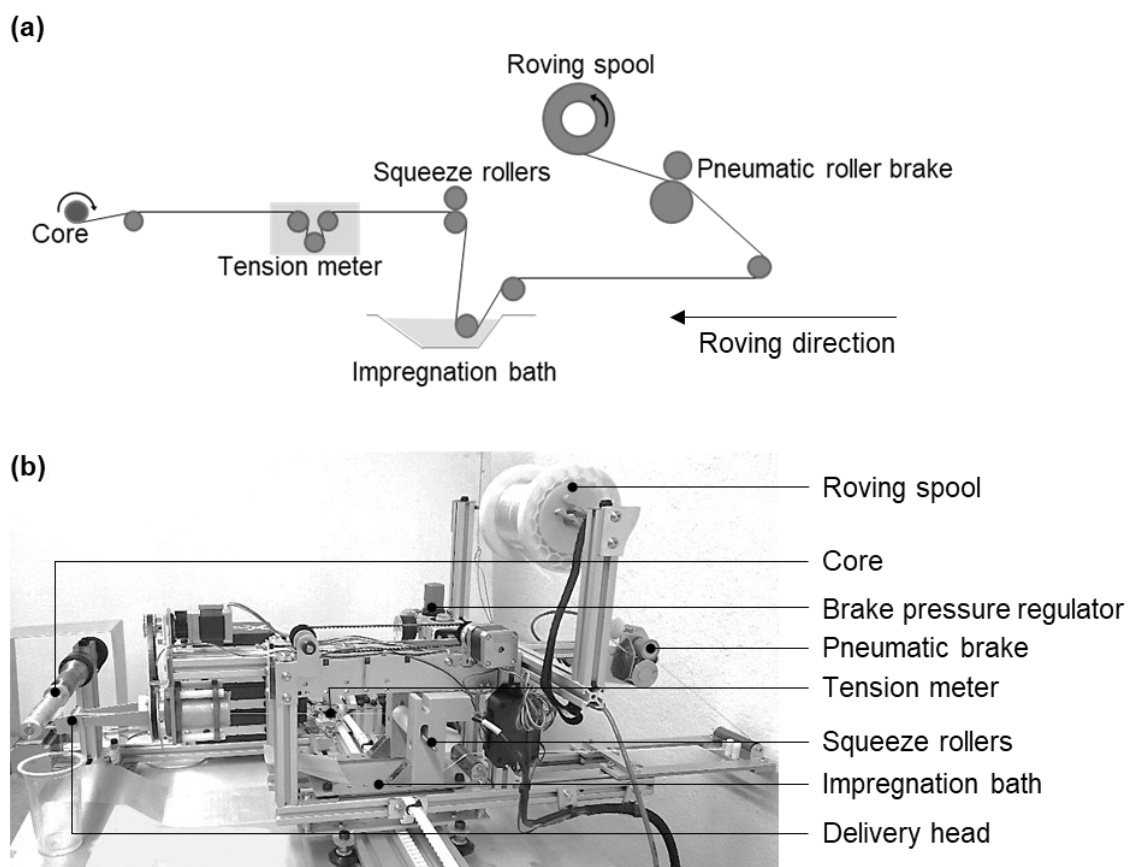


Figure 5.2: Preparation of pre-impregnated fibre wound core using a 4-axis filament winding machine: (a) schematic representation of the fibre path from the spool to the core; (b) filament winding machine and its components.

The filament winding machine operates using the common purpose G-code (numerical control programming language) [144]. The application program X-Winder Designer 2.0

facilitates the generation of G-code with the input variables roving width, type of winding, winding angle, length of winding, number of layers and the diameter of the core. The generated G-code can be edited to match the requirements, for example, the start and stop position and the number of layers, using a text file editor such as Notepad++ [145]. Figure 5.3 shows the delivery head and a 10 mm radius DDS core being wound with the impregnated roving.

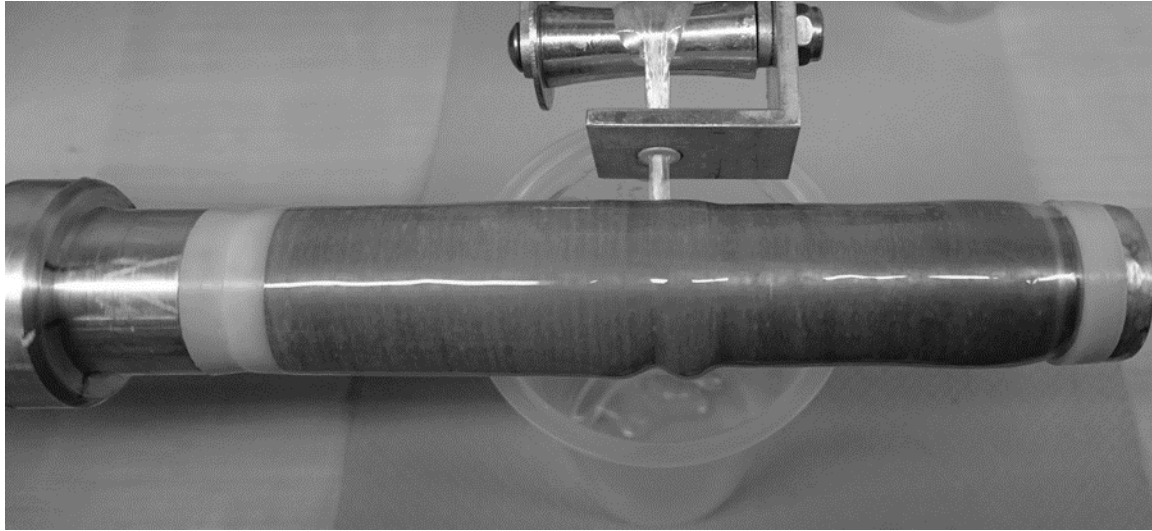


Figure 5.3: The delivery head and a 10 mm radius DDS core being wound with impregnated roving.

Filament winding parameters

To wind the rovings on the DDS core, in a way that the wound filaments represent the morphology of filaments in a profile pultruded out of rovings (represented in Figure 4.2), the following conditions need to be satisfied:

1. A winding angle θ_w of approx. 0° (0° refers to the plane perpendicular to the rotational axis of the core) and,
2. Uniform distribution of the filaments across the annular volume.

The rotational speed (i.e. the winding speed) of the core and the translational speed of the winding unit decides the angle of winding [128,146]. Therefore, controlling the winding speed of the core and the traverse speed of the winding unit allows controlling the winding angle and the distribution of fibres across the annular volume. A winding angle of 0° is not feasible with the filament winding technique since the winding unit traverse always creates a winding angle larger than 0° . The winding angle for the given set of core and winding parameters can be calculated as

$$\theta_w = \tan^{-1} \left(\frac{60 v_w}{2\pi r_{Co} U_w} \right) \frac{180}{\pi} \quad (5.7)$$

where v_w is the traverse speed of winding unit in mm s^{-1} ; and U_w , the winding speed of the core in rpm (revolution per minute). Equation 5.7 shows that the winding angle θ_w is a function of traverse speed of winding unit v_w , winding speed of the core being wound U_w , and the radius of the core r_{Co} . However, the radius of the core increases with the number

of wound layers increases. Mathematically, the radius of the core at n^{th} layer can be calculated using

$$r_{Co,n} = r_{Co,n-1} + h_{roving} \quad (5.8)$$

where h_{roving} is the thickness of the roving after winding on the core in mm and n , the layer number (a positive integer). Therefore, for a constant winding angle, the winding speed of core decreases in proportion to the increase in the number of layers. The total number of layers required to wind the calculated length of roving L_{roving} within the annular length L_a over the core of radius r_{Co} is given by

$$n = \frac{L_{roving} \sin \theta_w \tan \theta_w}{L_a} \quad (5.9)$$

Equations 5.7 and 5.9 allow to calculate the minimum achievable winding angles for the given fibre volume fraction and number of layers. Table 5.4 lists the possible winding angles for the chosen die-core systems (Section 4.2.1) with the glass roving having 600 tex linear density. Further, the fibre volume fractions of 0.61 and 0.56 are chosen accordingly to be comparable with the pultrusion experiments discussed in Chapter 8. Although single layer winding of the entire roving length L_{roving} was possible, a minimum of 4 layers was chosen for two reasons: (1) to avoid the slippage of wound fibres from its position due to compaction of the overlapping fibres; and (2) to facilitate the integration of thermocouples between the layers which measure the heat flow across the thickness of the wound fibre-matrix.

Further, Table 5.4 shows that calculated deviations in the fibre orientation in the wound core are comparable to that observed in UD pultruded profiles (up to 4° for CFRP [147] and more than 5° for GFRP [148]).

Table 5.4: The possible winding angles for the annular length of 100 mm in combination with listed parameters.

Fibre volume fraction φ_{fa} [-]	Number of layers n [-]	Core radius r_{Co} [mm]	Annulus thickness h_a [mm]	Possible winding angle θ_w [$^\circ$]
0.61	4	10	1	1.16
0.61	8	9	2	1.19
0.61	4	4.5	1	1.68
0.61	8	3.5	2	1.78
0.56	4	10	1	1.21
0.56	8	9	2	1.24
0.56	4	4.5	1	1.75
0.56	8	3.5	2	1.84

Knowing the possible winding angles, Equations 5.7 and 5.9 allow to calculate the required winding unit traverse speed and the winding speed of the core with the increasing thickness of the fibre-matrix. Since the variables v_w and U_w are interdependent, selection of initial winding speed is necessary to calculate the varying winding speed with increasing

core radius. Considering the factors such as the deceleration and acceleration of winding unit while changing the translational direction, ability to complete the winding well within the pot-life of the resin system as well as to facilitate complete wetting of the filaments with the resin formulation, an initial winding speed of 30 rpm was chosen. Figure 5.4 shows the selected winding parameters to wind the cores with the filament orientations listed in Table 5.4. The initial winding speed of 30 rpm resulted in the traverse speeds shown in Figure 5.4 (a).

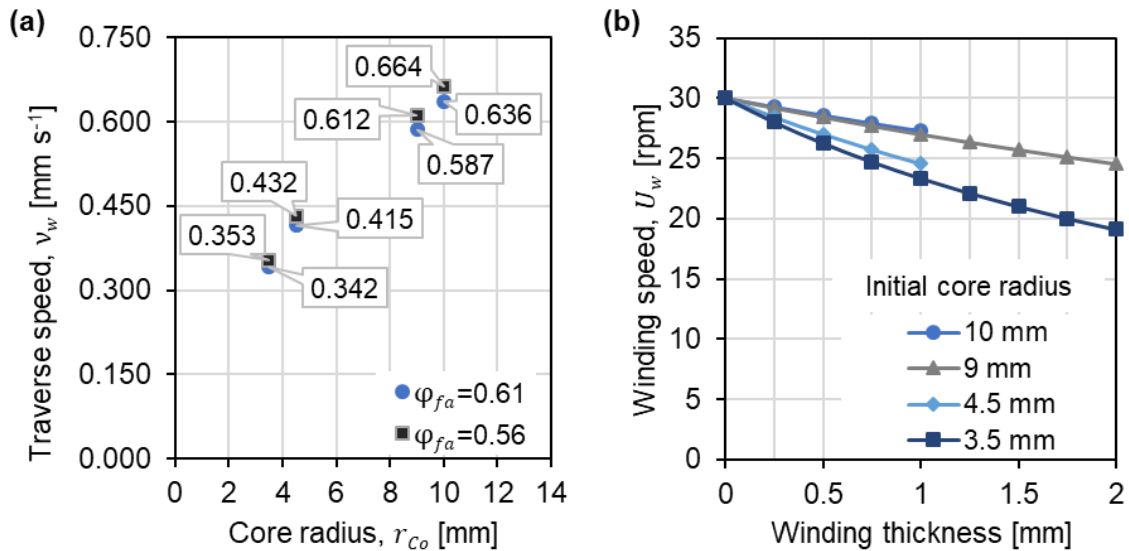


Figure 5.4: Selected winding parameters: (a) the traverse speeds of winding unit for various initial core radii at fibre volume fractions $\varphi_{fa} = 0.61$ and $\varphi_{fa} = 0.56$; (b) the decreasing winding speed with increasing winding thickness.

As inferred from Figure 5.4 (a), the traverse speed increases with the increasing core radii and the fibre volume fraction. At a constant traverse speed, the winding speed decreases quadratically with the increasing thickness of the wound fibre-matrix (Figure 5.4 (b)).

Roving tension

In the winding process, the roving passes through multiple guiding rollers, impregnation bath and squeezing rollers and therefore experiences axial stress. The axial stress in the roving exerts radial compaction pressure on the core and the subsequent wound layers. Consequently, the filaments from the outermost layer may radially displace (i.e. slip) into the previous inner layer due to the compaction. The final diameter of the fibre-matrix on the wound core, therefore, depends on the roving tension.

A tension meter (Type: TSB1-500-15) of 5 N capacity from Hans Schmidt & Co. GmbH, Waldkraiburg, Germany, mounted on to the winding machine (shown in Figure 5.2) was used to monitor the roving tension inline during the winding process. A pneumatic rubber roller brake, mounted on to the winding machine, applied pressure on the roving surface perpendicular to the axis of the roving. A pressure regulator was used to control the applied pressure by varying the air pressure in the brake. The roving tension with set brake pressure was recorded using a USB-6008 data acquisition module and a personal computer. A user interface has been developed using *Visual Basic .NET* to connect the personal computer with the data acquisition system for recording the winding tension data.

From the roving's axial tension, the radial compaction pressure on the core and the subsequent layers can be calculated using

$$p_{cn} = \sum_{i=0}^n \frac{F_{roving}}{W_{roving} r_{Co,i}} \quad (5.10)$$

where p_{cn} is the compaction pressure on the n^{th} layer in MPa; F_{roving} , the roving tension in N; and W_{roving} , the spread width of the wound roving in mm. The spread width of the roving used in this work was measured as 4 mm. On assuming an elliptical roving cross-section and hexagonal packing (with 90.8 % filling) of the circular filaments in the roving, the thickness of the layer is approximated by rearranging the mathematical relation to calculate area of an ellipse (i.e. $A = h W \pi/2$, here h and W represents the minor and major axis of the ellipse respectively) as,

$$h_{roving} = \frac{1}{0.908 \frac{\pi}{2} W_{roving}} A_{roving} = \frac{1}{0.908 \frac{\pi}{2} W_{roving}} \frac{T_{tex}}{\rho_f 10^6} \quad (5.11)$$

Using Equation 5.11, the calculated wound thickness of the 600 tex roving utilised in this work amounts to 0.0414 mm (i.e. 41.40 μm). However, this is an idealisation, and in practice, the actual thickness (or the aspect ratio) of the roving may deviate from the calculated one. This is because of the influence of various material and processing parameters, one among them being axial tension. From the conditions above, it is inferred that the traverse speed of the winding unit creates overlap on the windings. The number of overlaps is inversely proportional to the traverse speed of the winding unit. Hence, while calculating the radius of the n^{th} layer, the number of possible overlaps should be included.

Figure 5.5 (a) shows the mean axial tension with different applied brake pressures. Figure 5.5 (b) shows the calculated total compaction pressure on the cores calculated using Equation 5.10 with increasing applied brake pressure.

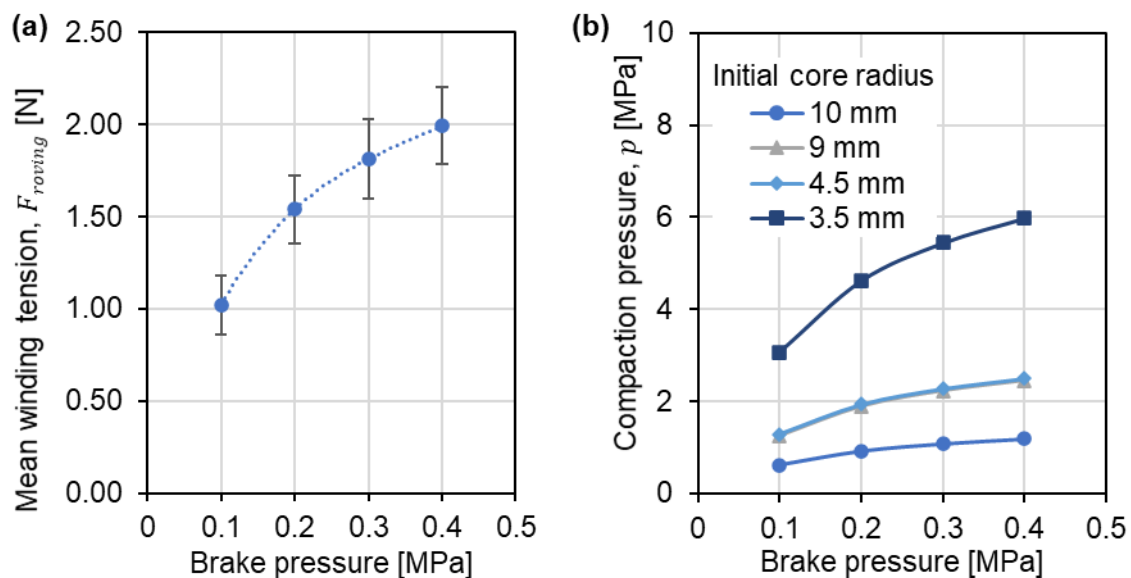


Figure 5.5: Effect of increasing brake pressure on (a) the mean winding tension, and (b) the calculated total compaction pressure on the core.

The measured roving axial tension increases as the square of the applied brake pressure. Consequently, the compaction pressure on the core also increases with increase in applied brake pressure. The core with least diameter experiences the highest compaction pressure, as shown in Figure 5.5 (b). The raise in the calculated compaction pressure on the core is directly proportional to the thickness of the windings.

The final diameters of the core with wound fibre-matrix were measured after allowing the matrix to cure. Figure 5.6 and Figure 5.7 show the effect of applied brake pressure on the change in the final diameters of the cured samples wound according to the parameters listed in Table 5.4.

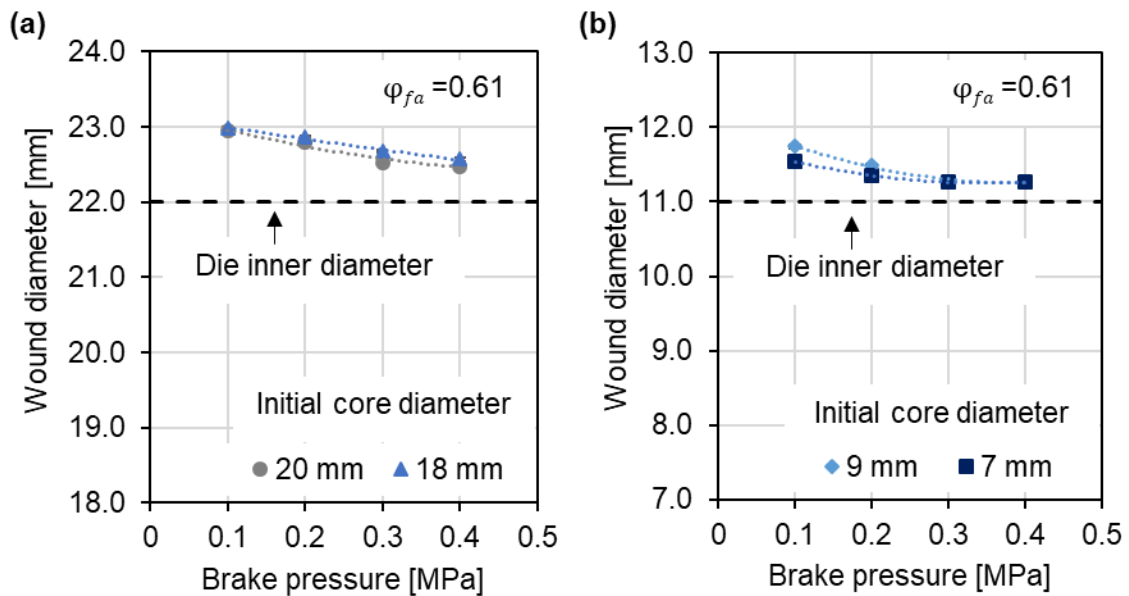


Figure 5.6: Final diameter of the cores wound for $\varphi_{fa} = 0.61$ with increasing applied brake pressure: (a) 20 mm and 18 mm cores; (b) 9 mm and 7 mm cores.

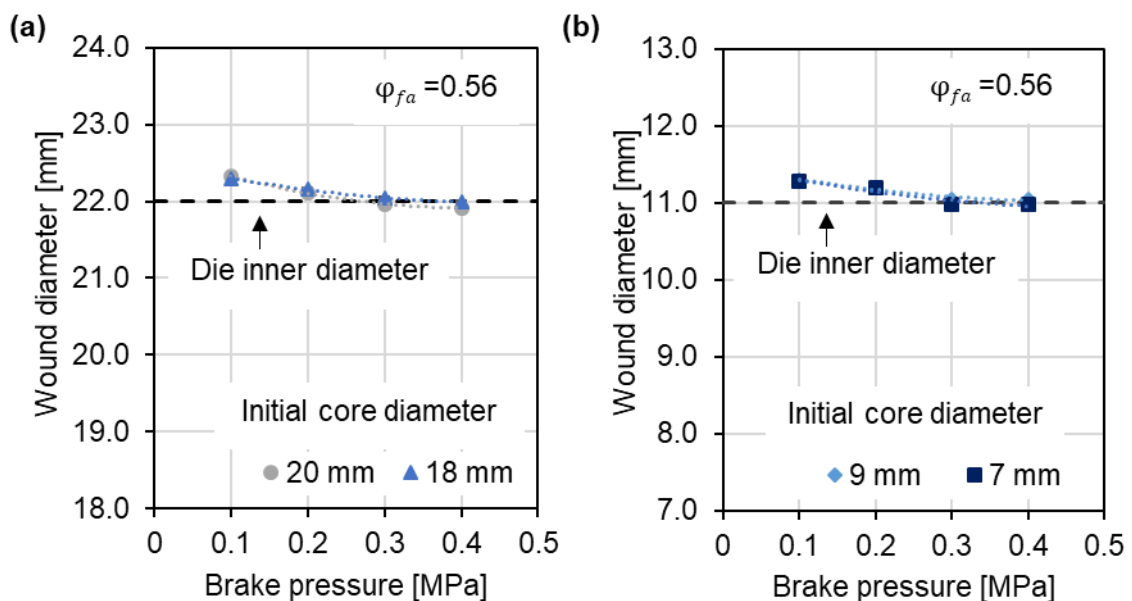


Figure 5.7: Final diameter of the cores wound for $\varphi_{fa} = 0.56$ with increasing applied brake pressure: (a) 20 mm and 18 mm cores; (b) 9 mm and 7 mm cores.

As the axial tension of the roving increases, a decrease in the final winding diameter is observed. The final diameters of the wound cores for the annular fibre volume fraction of 0.56 are smaller than that of the cores wound for the annular fibre volume fraction of 0.61. The reduction in the total length of the rovings wound on the cores and the number of overlaps in the windings for lesser annular fibre volume fraction results in a smaller diameter.

The final winding diameters for all the samples wound for the annular fibre volume fraction of 0.61 as well as the samples wound with applied brake pressures less than 0.3 MPa for annular fibre volume fraction of 0.56 are larger than that of the respective die inner diameters. The larger winding diameters are the result of the presence of resin film between the filament layers and low compaction of the fibre-matrix during winding. Because of the larger winding diameters, further compaction of the fibre-matrix is expected while pushing in the wound core into the die for torque measurements. In other words, like in pultrusion process where the compaction occurs in the entry segment of the die, in the DDS the reinforcement is partially compacted during winding and the final compaction occurs at the rounded edge of the DDS die while the core is being inserted into the die.

Increasing the applied brake pressure beyond 0.4 MPa for samples of $\varphi_{fa} = 0.61$ would further compact the winding. However, winding tensions above 1.8 N, squeezed out more resin from the inner layers due to the increased compaction force. This consequently results in higher fibre volume fraction in the inner layers. Further, the winding tension above 1.8 N caused problems when removing the cured composite samples from the core.

The core samples wound with brake pressures ≥ 0.3 MPa for $\varphi_{fa} = 0.56$ have smaller wound diameters than the die inner diameter. Consequently, a core diameter smaller than the inner diameter of the die results in a thin gap between the die wall and the windings. This is, however, not preferred for the torque measurements, since the normal pressure on the die wall may significantly be reduced as a result of smaller diameters.

5.2.3 Torque measurement on DDS

The die wall experiences torque when the wound core rotates inside the die. Preparatory steps for the DDS experiments involve the definition of the measuring parameters such as measurement frequency, temperature of the die and the rotational velocity of the core. The die is preheated to the set temperature (like in pultrusion process) so that the wound fibre-matrix experience the temperature as soon as they contact the die wall. Subsequently, the wound core is mounted to the drive system of the DDS through the coupling (described in Section 4.2.2). Immediately after mounting the core to the drive system, the measurement process is set to begin so that the data acquisition begins even before the insertion of the core into the pre-heated die. The core is allowed to rotate while the lifting table is being raised to the measuring position. As the lifting table raises along the axis of the core, the die mounted in the heating module slides vertically over the rotating core wound with fibre-matrix. The lifting table should be raised until the die covers the top edge of the top sealing ring. The free end of the wound roving has to be tucked-in into the previous layer at the end of the winding process to prevent the end from slipping while the die slides over the fibre-matrix. Figure 5.8 shows the DDS at the core mounting position and torque measuring position.

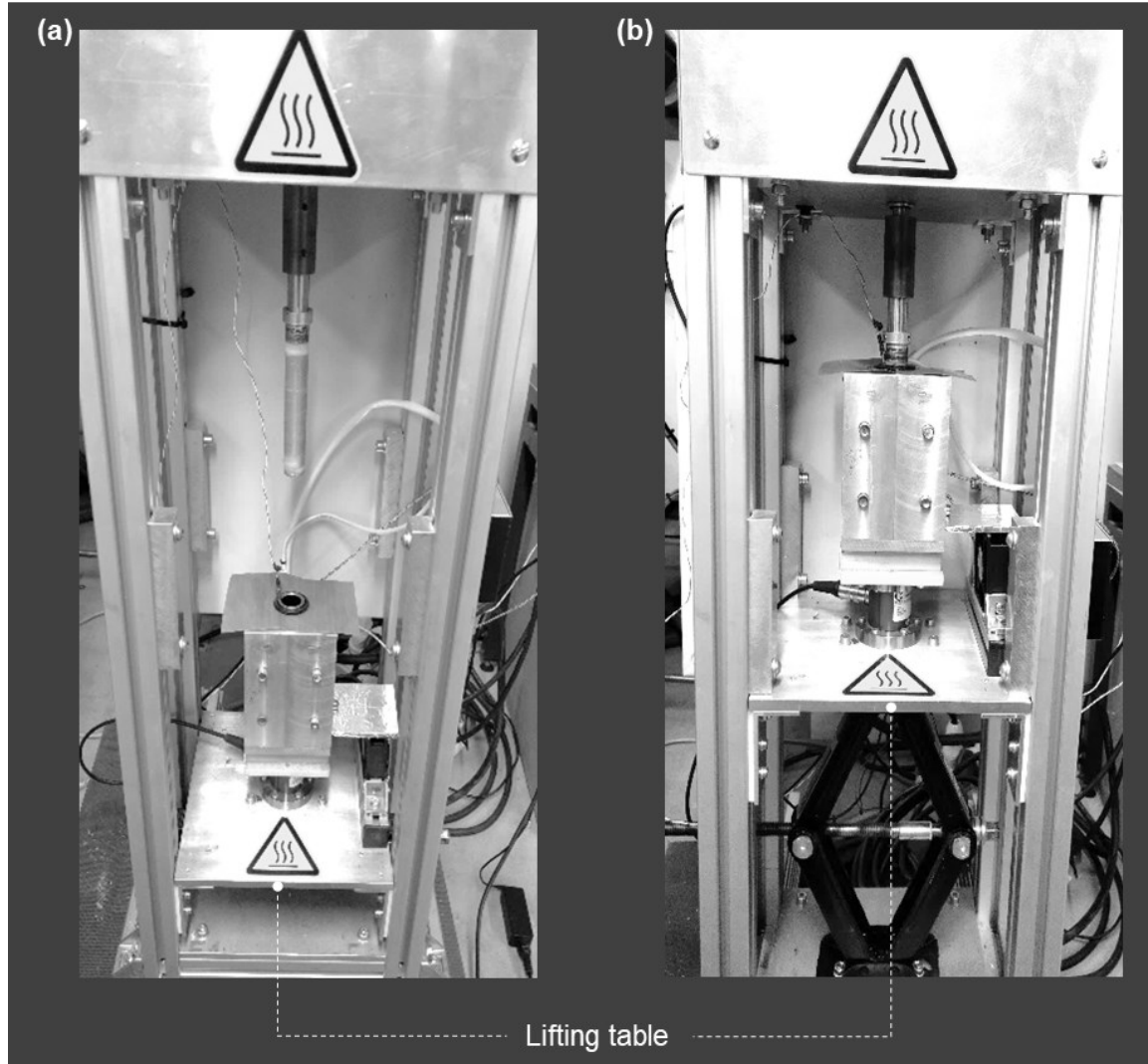


Figure 5.8: DDS at (a) the core mounting position with lowered lifting table and (b) the measuring position with raised lifting table.

The period of measurement depends on the rate of polymerisation of the used resin formulation. Alternatively, the time of measurement can be selected based on the length of the pultrusion die and the line speed of the pultrusion of interest. At the end of a measurement cycle, the lift table is lowered to the mounting position to facilitate the removal of the core from the DDS together with the cured composite. Further, the cured composite is removed from the core and is weighed. From the measured weight of the tube, the previously calculated fibre volume fraction can be validated using the relation

$$\varphi_{c,DDS} = \frac{m_{roving}}{\rho_f} / \left(\frac{m_{roving}}{\rho_f} + \frac{m_{c,DDS} - m_{roving}}{\rho_{resin}} \right) \quad (5.12)$$

where $\varphi_{c,DDS}$ is the fibre volume fraction of the composite; $m_{c,DDS}$, the mass of composite in g; and ρ_{resin} , the density of the cured matrix in g mm^{-3} .

The deviation between $\varphi_{c,DDS}$ and φ_{fa} is observed to be negligible and in principle will be equal if there were no flow of resin out of the annular volume during the measurement. Therefore, measuring the weight of the cured composite is used as a measure to validate

the effectiveness of the sealing rings. The data acquired during the measurement process were stored in a text file, as described in Section 4.2.3. For the further visualisation and results interpretation, the data were processed using the program Microsoft Excel.

Figure 5.9 shows a characteristic torque and temperature measured on DDS. The data measured is for the die-core system having r_{Di} of 11 mm and r_{Co} of 10 mm. The measurement temperature was 120 °C and the fibre volume fraction of the composite is 0.61. The resin formulation contained a mass fraction of 3 phr IMR in addition to the resin and the curing agent.

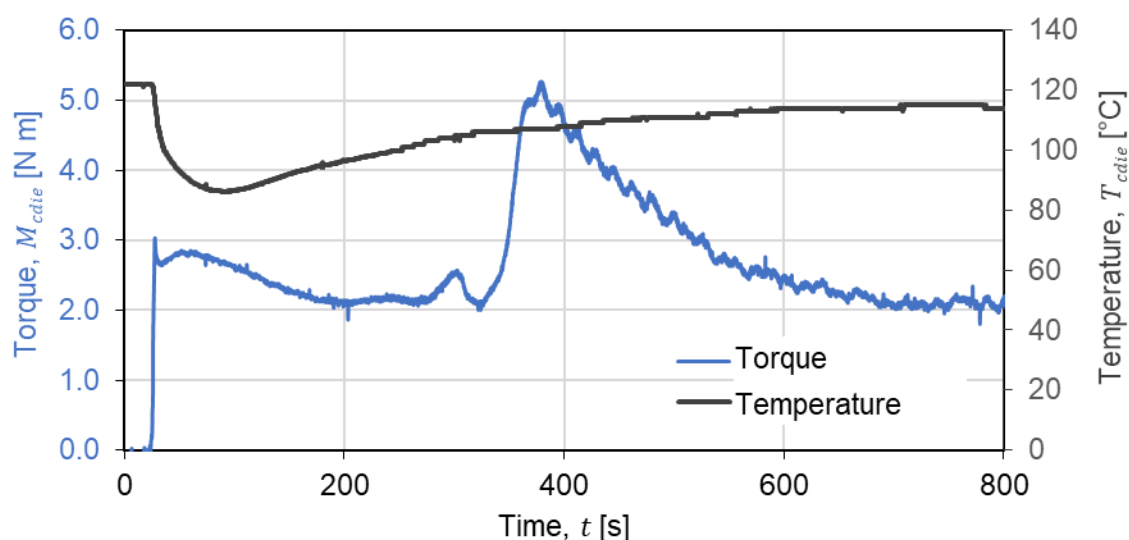


Figure 5.9: Characteristic torque and temperature data measured on the DDS.

Figure 5.9 shows that the rate of change of torque can be observed as the polymerisation of the resin formulation progresses. An initial increase in the torque up to 3 N m is observed until the completion of the core insertion. Simultaneously, a fall in die wall temperature is also observed. Further experiments were carried out to evaluate the temperature and torque behaviour while varying the process and material parameters.

5.2.4 Temperature measurement in winding layers

As observed from Figure 5.9, the temperature of the die decreases from the set temperature of 120 °C to 82 °C once the wound core was introduced into the die. Since the wound core was at ambient temperature (about 21 °C) initially, as soon as the fibre-matrix encountered the die, the heat flow from the die to fibre-matrix cause the fall in the temperature of the die. Nevertheless, the temperature measured using the thermocouple integrated into the die wall may deviate from the actual temperature near the die wall. To measure the real temperature of the fibre-matrix which is in direct contact with the die wall and through-thickness heat flow in the wound layers, further experiments were conducted by integrating thermocouples between the layers of the windings (Figure 5.10). The temperature measurements were carried out using unsheathed fine gauge Type-K thermocouples having wire diameters of 50 μm purchased from Omega Engineering Inc., Deckenfronn, Germany [149].

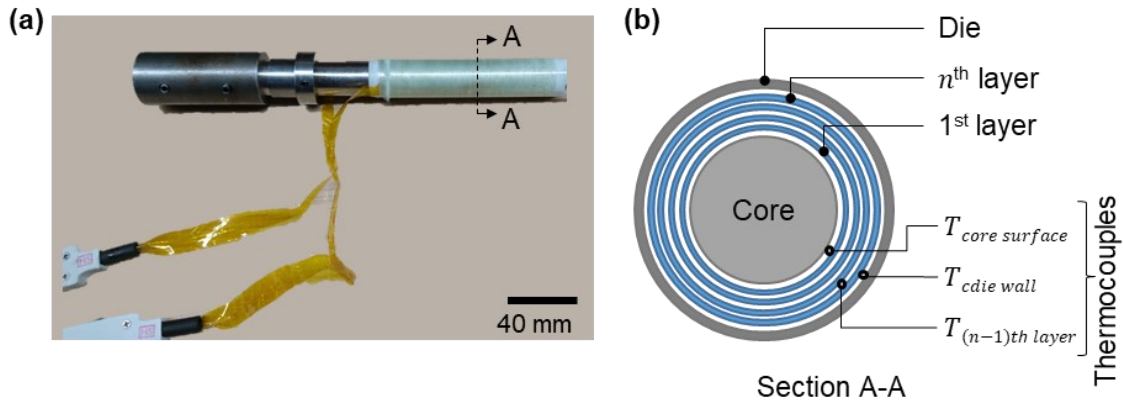


Figure 5.10: Thermocouples integrated during filament winding in between the layers of the windings, the die and the core – (a) Photograph of the core with thermocouples and (b) schematic illustration of the position of the thermocouples in the winding cross-section.

The increase in filler content inside the annular volume due to the introduction of thermocouples is negligible due to their fine diameter. The wires of the thermocouples are isolated using Kapton tapes outside the windings to favour better handling. The thermocouples were connected to the data acquisition device ALMEMO® 2890-9 from Ahlborn Mess- und Regelungstechnik GmbH, Holzkirchen, Germany, using the connectors ALMEMO® ZA 9020-FS [150]. Thermocouples were integrated between the core surface and the first layer, between the n^{th} (last) layer and the $(n-1)^{\text{th}}$ layer as well as between the n^{th} layer and the die inner surface, respectively. Because of the short length of the thermocouple wires, the temperature measurements were carried out with stationary cores (i.e. $\omega = 0 \text{ rad s}^{-1}$). Figure 5.11 shows the temperature profiles measured using the integrated thermocouples.

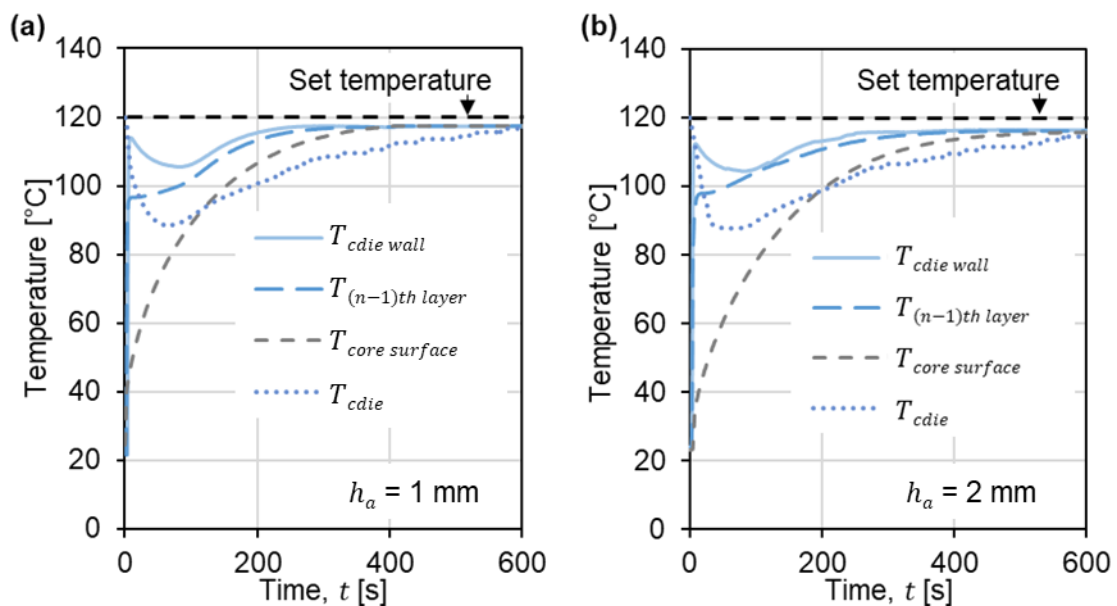


Figure 5.11: Temperature profiles measured with integrated thermocouples at set die temperature of 120 °C: measurements with die having 11 mm inner radius and (a) annular gap of 1 mm, and (b) annular gap of 2 mm.

Interpretations from Figure 5.11 show that the temperature at the die wall, $T_{cdie\ wall}$, measured using Type-K thermoelement integrated between the n^{th} layer and the die wall, deviates from the temperature, T_{cdie} , measured using the PT100 thermoelement integrated into the die. It can be assumed that is because the die transfers heat to the fibre-matrix and the fibre-matrix receives heat from the die. Until the core insertion process is complete, the top section of the die continually receives fresh fibre-matrix, which was at ambient temperature, resulting in an exponential decrease in the temperature. Once the insertion process is complete, the heat flow in the through-thickness direction of the fibre-matrix further decreases the temperature of the die. Since the reaction time of the PID temperature controller of the heaters lags the rate of the heat flow into the fibre-matrix, an increase in temperature is observed only after 70 s. Nevertheless, the temperature profile measured directly on the die wall using the Type-K thermocouple and the integrated PT100 thermoelement in the die, allowed to calculate the rate of change of temperature difference $d(\Delta T)/dT$. This is used later in the estimation of the curing kinetics of the resin system in DDS (Section 7.3).

The measured temperature profile further shows the influence of the winding thickness on the rate of temperature change. The thicker the winding, the slower is the heat flow through the thickness. The core reaches its maximum temperature (118 °C) at about 400 s with the 1 mm thick winding, whereas it took about 600 s with the 2 mm winding. From the above temperature measurements, the temperature profile of the layers in between the die and the core can be mathematically predicted (Figure 5.12) using the equation

$$T_i = T_{cdie\ wall} - i \left(\frac{T_{cdie\ wall} - T_{core\ surface}}{n} \right) \quad (5.13)$$

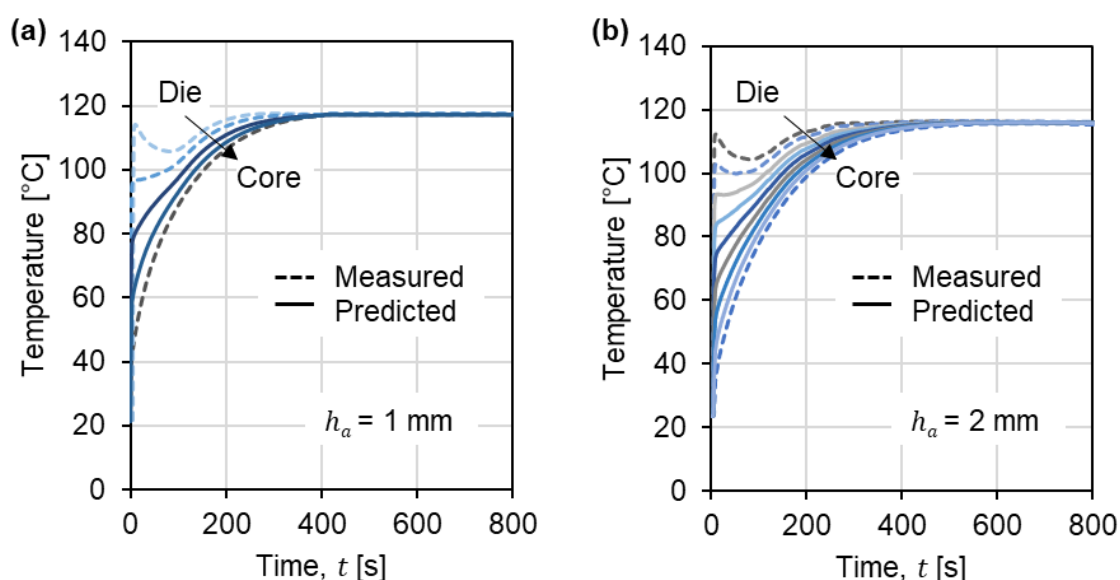


Figure 5.12: Predicted temperature profiles of the in-between layers for the windings in an: (a) annular gap of 1 mm, and (b) annular gap of 2 mm.

Thermal expansion of the core

From the temperature measured on the core surface and in the windings, the thermal expansion of the core and the fibre-matrix can be calculated (using Equation 5.14) to assess the effect of temperature induced expansion of the core on the torque evolution.

$$\Delta A = A 2\alpha_T \Delta T \quad (5.14)$$

where ΔA is the change in cross-sectional area due to thermal expansion; A , the initial cross-sectional area; α_T , the thermal expansion coefficient of the material; and ΔT , the temperature change in the material. For the calculations, the coefficient of thermal expansion of the core ($16.5 \times 10^{-6} \text{ m m}^{-1} \text{ K}^{-1}$) and the fibre-matrix ($5.4 \times 10^{-6} \text{ m m}^{-1} \text{ K}^{-1}$ for E-glass filaments and $55 \times 10^{-6} \text{ m m}^{-1} \text{ K}^{-1}$ for epoxy) reported in literature [151–153] has been used. Figure 5.13 shows the relative change in the cross-sectional area of the core for different annular gaps with respect to the cross-sectional area of the fibre-matrix winding with increasing temperature. The plot shows that the change in cross-section of the core with respect to the cross-section of the fibre-matrix increases linearly with temperature. The maximum cross-sectional change of the core is about 1.85 % of the cross-section of the fibre-matrix having 1 mm thickness (in case of 10 mm radius core at 140 °C). A maximum increase of 1.55 % in the cross-section is observed at the core surface temperature of 120 °C. Comparing the Figure 5.9, Figure 5.12 and Figure 5.13, the relative change in cross-sectional area of the core up to 1.5 % takes place in the regime where the resin formulation is in liquid state (described in Section 7.3). In this regime the thermal expansion of the entire system increases the internal pressure in the annular volume. Since the resin formulation behaves like a Newtonian fluid in the liquid state, the change in the drag force on the die wall due to increase in the pressure in the annular region is considered negligible. The change in the cross-sectional area of the core due to thermal expansion in the gelation regime of the matrix and beyond is therefore, less than 0.05 %. Hence, the effect of thermal expansion of the core on the torque evolution is not considered within the scope of this research work. Nevertheless, the effect may be verified in the future, for example, with dilatometric experiments.

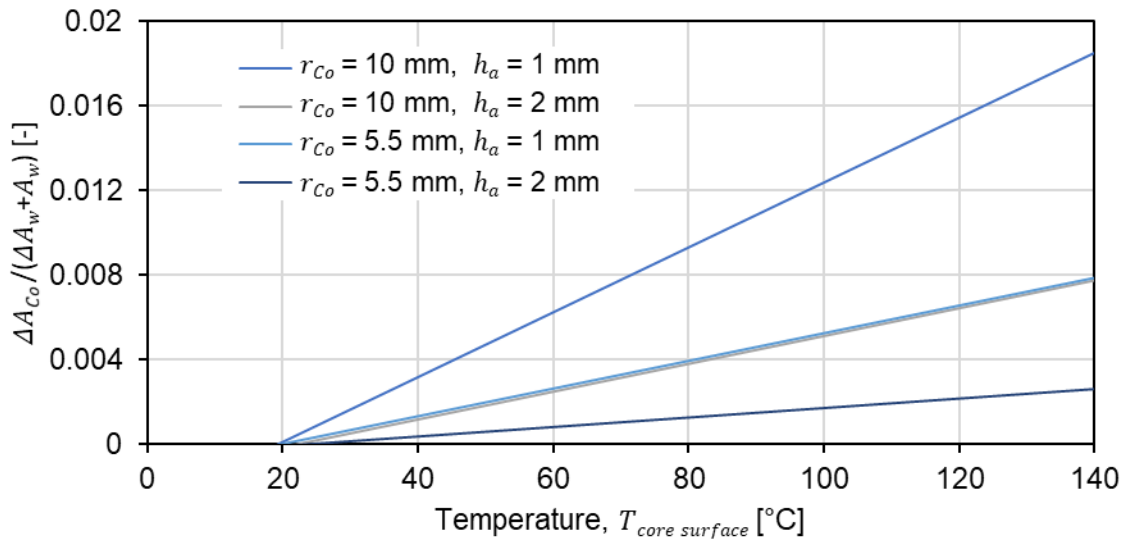


Figure 5.13: Relative change in the cross-sectional area of the core (ΔA_{Co}) with respect to the cross-sectional area of the fibre-matrix (A_w) with increasing temperature for different core radius (r_{Co}) and annular gaps (h_a).

5.3 Influence of preparatory process variables on torque measurements

Initial experiments with wound dry fibres were carried out to measure the baseline torque in the absence of resin formulation. For the experiments, the wound cores were first

introduced into the pre-heated die and subsequently the measurement process was triggered. Figure 5.14 shows the recorded torque plotted against the period of measurement for 11 mm radius die with an annular gap of 1 mm at a set die temperature of 120 °C.

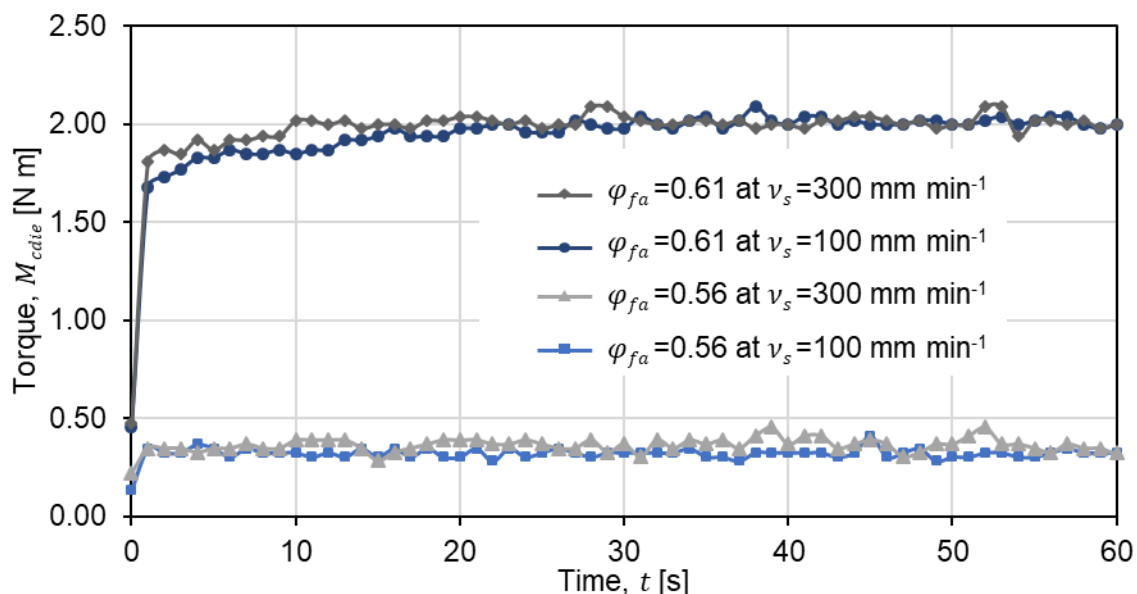


Figure 5.14: Torque measured with varying core rotational velocity and fibre volume fractions in the 11 mm radius die with dry fibres wound at 0.3 MPa applied brake pressure on 10 mm radius core.

The measurement was carried out for about 1 min after which there no changes observed in the slope of the measured torque. Increase in the measured baseline torque is observed with increasing fibre volume fraction. An increase in 5 % fibre volume fraction increased the measured torque to about 82 %. The higher torque for the core with higher fibre volume fraction is the result of compaction of the winding having a larger diameter than the die inner diameter (Figure 5.6). However, the change in the measured torque with the change in rotational velocity of the core could not be observed.

Subsequently, experiments were carried out with the impregnated roving windings to investigate the effect of process and material parameters on the torque evolution. Chapter 7 details the results of the parametric study and therefore in this section only the effect of preparatory process parameters, i.e. the winding tension and the fibre volume fraction, are discussed.

Further torque measurement experiments were conducted to analyse the influence of winding tension and fibre volume fraction on the initial torque. Figure 5.15 shows the effect of varying winding tension and the change in the fibre volume fraction on the measured initial torque. The measurements were carried out with die having 11 mm inner radius at an annular gap of 1 mm at the die temperature of 120 °C. The increase in the initial torque during the core insertion phase for the windings wound with less winding tension is higher compared to the windings wound with high winding tension (Figure 5.15 (a)). The higher initial torques are the consequence of the higher compaction due to larger diameters of the windings wound at low winding tensions. Further, during the experiments, visual

observations revealed that the amount of resin squeezed out at the rounded entry edge of the die was higher for the cores wound with less winding tension.

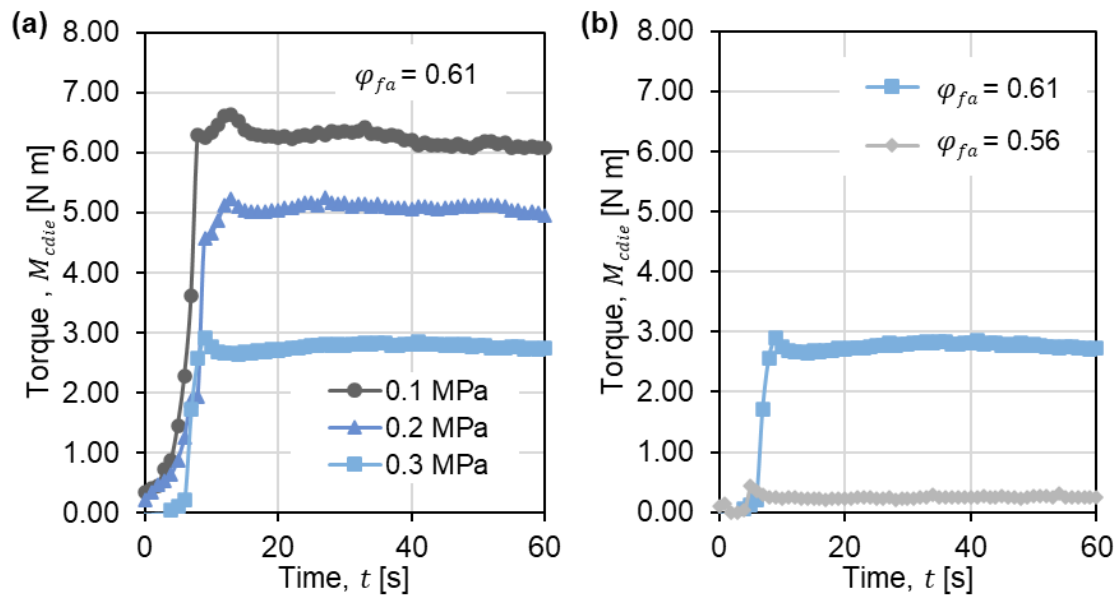


Figure 5.15: Torque measured with impregnated fibre windings: change in the initial torque with (a) varying applied brake pressure during filament winding for $\varphi_{fa} = 0.61$; and (b) varying fibre volume fraction with 0.3 MPa applied brake pressure during filament winding.

Since in the winding process, the low winding tensions exert low compaction force on the inner layers of the windings, the amount of resin squeezed out from the inner layers is also less. As a result, the cores wound with less winding tension has more resin than the one wound with high winding tension. When the die slides over the wound core, the constrained volume of the die squeezes the excess resin out of the windings thus, exerting a proportional compaction pressure to the volume of excess material present in the windings (Figure 5.16).

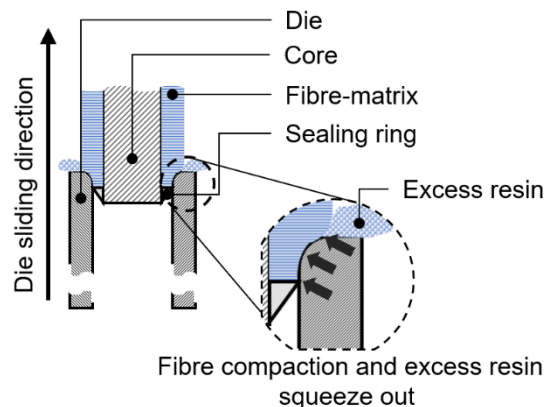


Figure 5.16: Schematic illustration of fibre compaction and excess resin squeeze out at the rounded entry edge of the die during the core insertion phase.

The cores with a fibre volume fraction of 0.56 exerted significantly lower torque compared to the cores with a fibre volume fraction of 0.61 (Figure 5.15 (b)). This is again due to the fact that the relatively smaller wound diameters of the core (shown in Figure 5.7)

consequently resulted in less compaction. In that case, interesting to observe is that the DDS could also be used to estimate the equivalence of compaction force (F_{comp}).

5.4 Optical evaluations

Optical microscopy of the samples allows to analyse the effect of the core preparatory process parameters on the morphology of the samples including the fibre orientation and distribution, the fibreless resin layer thickness and its homogeneity as well as fibre volume fraction. In this work, scanning electron microscopy and optical microscopy techniques were employed to evaluate the surfaces and the cross-sections of the samples. The samples were investigated using a Hitachi TM-1000 tabletop scanning electron microscope from Hitachi High-Technologies Corporation, Tokyo, Japan and Keyence VHX-2000 optical microscope from Keyence Corporation, Osaka, Japan. For the analysis of the cross-section of the samples, the cylindrical samples from DDS measurements were cut into half along their length (i.e. L_a), resulting in a semi-cylindrical tubes having approx. 20 mm length, and embedded in the sample mounting resin EpoFix from Struers GmbH, Willich, Germany. The embedded samples were further turned and polished as per the guidelines described (method F for composites) in [154].

5.4.1 Influence of winding tension

The surfaces of the composite samples (without any post-processing) after the DDS measurements were investigated using the scanning electron microscope. Figure 5.17 shows the micrographs of the surfaces of the samples wound with different winding tensions.

Visible differences in the orientation of the fibres are inferred from the micrographs. The black spots observed in the micrograph are the matrix present on the sample's surface. The samples wound with an applied brake pressure of 0.1 MPa (Figure 5.17 (a1)) has high undulations compared to the other two samples wound with 0.2 MPa (Figure 5.17 (b1)) and 0.3 MPa (Figure 5.17 (c1)) applied brake pressures, respectively. To quantify the fibre orientation and its distribution, the micrographs were subjected to image analysis. An open-source image processing software ImageJ [155] was used to estimate the orientations and their distribution of the fibres in the samples. The software classifies the orientations with colour codes and outputs the histogram of the orientations and the gaussian distribution of the calculated orientations.

Figure 5.17 (a2 - c2) displays the micrographs with overlaid colour codes generated by ImageJ for different fibre orientation for the respective samples in Figure 5.17 (a1 - c1). Figure 5.17 (a3 - c3) shows the histogram of the orientations of the fibres and their distribution. From Figure 5.17 (a3) a broad distribution in the fibre orientations ranging from -30° to $+15^\circ$ is observed. The reason for the wide deviation in the fibre orientation is related to the high degree of compaction undergone by the fibres during core insertion from their as wound state. A high degree of compaction resulted in the generation of wrinkled fibre architecture. As the winding tension increases, the distribution in the fibre orientation narrows down with increased 0° orientations. The observations correlate well with the diameter measurements presented in Section 5.2.2.

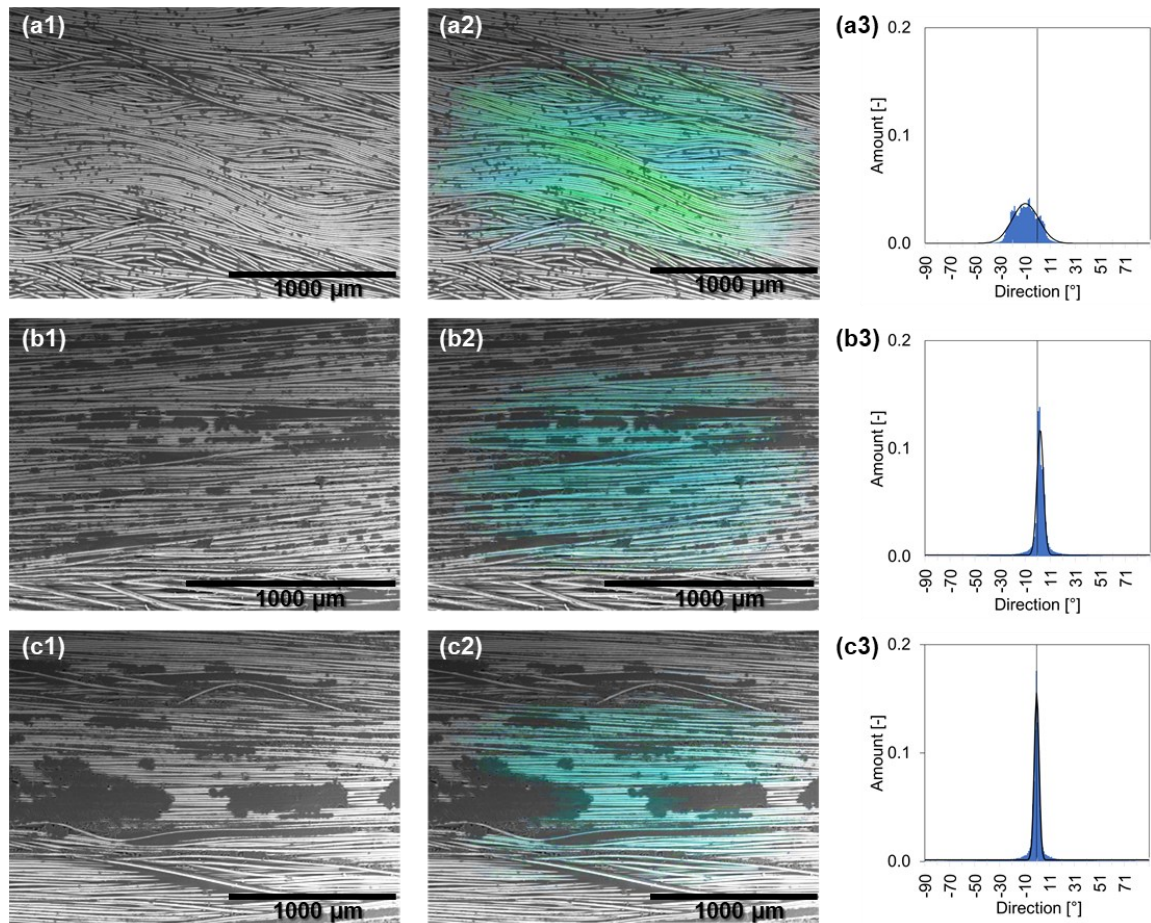


Figure 5.17: Scanning electron micrographs of the surface of composite samples from DDS wound with varying winding tensions: micrographs of samples wound with (a1) 0.1 MPa, (b1) 0.2 MPa and (c1) 0.3 MPa applied brake pressure; (a2), (b2) and (c2) respective micrographs analysed for the fibre orientation showing colour-coded orientations (cyan = 0° , blue = $+\theta$ and green = $-\theta$) and; (a3), (b3) and (c3) respective distribution of fibre orientation.

5.4.2 Through-thickness resin flow

Analysis of the radial or through-thickness flow of the resin during the measurement was realised by winding the last (n^{th}) layer of the samples with coloured resin formulation. The longitudinal cross-sections of the wound samples from three different measurement procedures: as wound and cured samples, samples cured in the die with stationary core and sampled cured in the die with rotating core, were investigated under an optical microscope (Figure 5.18). For the experiments, samples containing 8 winding layers were prepared for the annular gap of 2 mm.

Since under the visible light conditions, the colour difference between the layers was not distinguishable, in particular for the samples cured in the die, the micrographs were processed using an open-source image processing software GIMP [156]. The colour channel mixer feature of the software permits to filter the red, green and blue (RGB) components of the colours in their respective channels. Since the colour used for the last layer was orange, filtering all the other colours except red component resulted in the images shown in Figure 5.18 (a2 – c2) respectively.

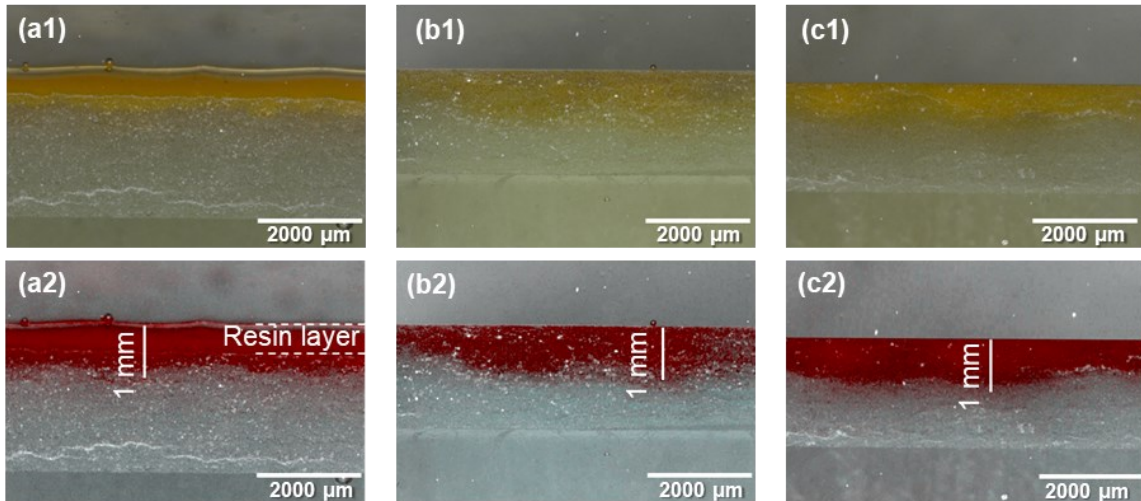


Figure 5.18: Micrographs of the coloured samples: (a1) as wound-cured, (b1) cured in the die with stationary core, and (c1) cured in the die with rotating core; (a2 - c2) respective colour filtered images.

Figure 5.18 (a2) shows a thick layer (approx. 0.5 mm) of cured fibreless resin on the last wound layer. During winding, the excess resin in the previous wound layers gets squeezed out because of compaction and remain on the surface of the last wound layer unless otherwise externally removed such as using doctor blades. The thickness of the coloured resin together with the last wound layer is about 1 mm. From Figure 5.18 (a2) inference can be made that, in the as wound samples, there is no penetration of resin into the $(n-1)^{th}$ layer. During the core insertion procedure, the excess resin present on the sample and within the windings gets squeezed out as illustrated in Figure 5.16.

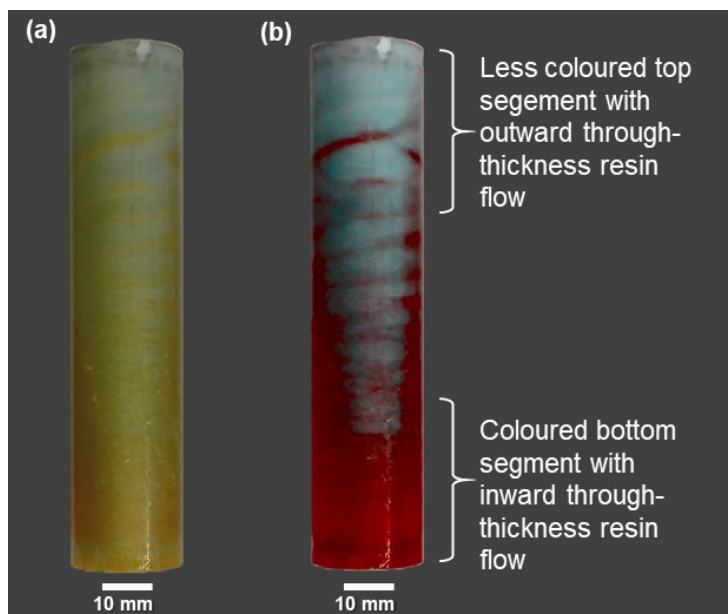


Figure 5.19: Images of the sample cured on a stationary core showing colour gradient from bottom to top of the sample – (a) photograph and (b) colour filtered photograph.

However, as observed from Figure 5.18 (b2) the resin from the outer layer penetrates the inner layers. The penetration of resin into the inner layers is observed only at the bottom segment (i.e. at the die entry end) of the winding (Figure 5.19). Beyond the initial entry distance of about 15 mm, the excess resin from the outer layer is squeezed out resulting in no observable through-thickness inward flow of resin. The compaction induced outward flow of resin from the inner layers wash out most of the coloured resin from the outer layer in the top segment of the winding, leaving a less coloured surface as observed in Figure 5.19. The optical evaluations thus conclude that the radial or through-thickness flow and the axial flow of the resin occur only during the insertion procedure. Such a phenomenon is comparable to the pultrusion process where the backward flow of resin occurs only at the tapered entry segment of the pultrusion die.

5.4.3 Fibre distribution

The winding process might influence the fibre distribution across the cross-section of the sample due to the compaction of the fibres caused by winding tension. However, as discussed in Section 5.2.2, it is preferred to have uniform distribution of fibres across the cross-section of the windings to better represent the fibre architecture in the pultruded profiles. Therefore, the longitudinal cross-sections of the samples cured in the die with rotating core were investigated under a scanning electron microscope to analyse the fibre distribution across the winding cross-section. Figure 5.20 shows the micrograph of the cross-section of the samples. The fibre distribution across the cross-section of the samples containing 0.61 fibre volume fraction (Figure 5.20 (a) & (b)) is uniform or in other words, the fibres were not displaced towards the core. However, the samples with 0.56 fibre volume fraction (Figure 5.20 (c)) shows a biased fibre distribution in which the fibres were displaced more towards the core resulting in a thick fibre-free resin layer of about 70 μm on the die side of the sample. Further issues observed with the samples having 0.56 fibre volume fraction are presented in Chapter 7.

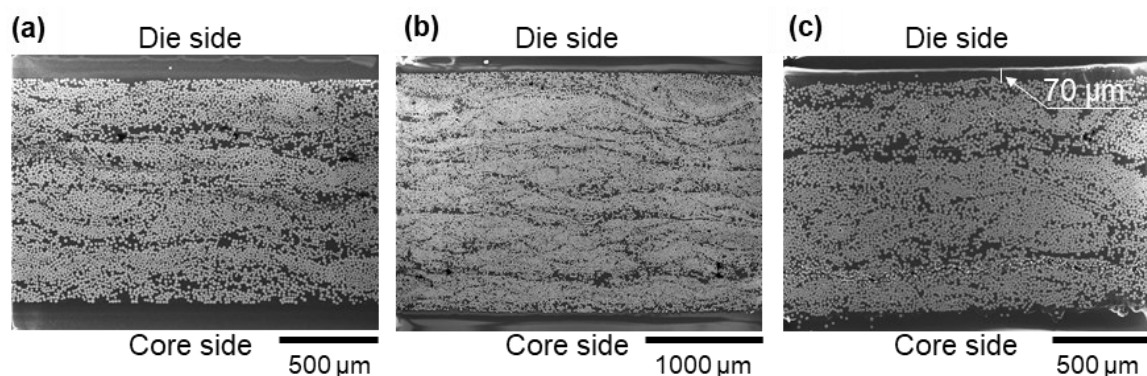


Figure 5.20: Scanning electron micrographs of longitudinal cross-section of the samples: (a) with $\varphi_{fa} = 0.61$ and $h_a = 1$ mm, (b) with $\varphi_{fa} = 0.61$ and $h_a = 2$ mm, and (c) with $\varphi_{fa} = 0.56$ and $h_a = 1$ mm.

Comparing the above microscopic evaluations with the results discussed in the section 5.4.2, the compaction of the wound layers during core insertion in DDS (in the case of samples having 0.61 fibre volume fraction) distributes the fibres uniformly across the cross-section of the sample. On the other hand, since the compaction of the samples having 0.56 fibre volume fraction is negligible (Figure 5.15 (b)), the fibres in the sample

hold the same architecture that they took during the winding process. Only the excess resin present on the outer surface of the windings is wiped out during the core insertion leaving a thick fibreless resin layer.

5.4.4 Resin layer thickness

As discussed in the previous chapters, the fibreless resin layer between the die surface and the moving fibre-matrix directly influence the viscous drag. Recalling Equation 2.3, increase in the fibreless resin layer thickness decreases the viscous drag. The resin layer thickness for a regular triangular packaging of fibres is expressed as [70],

$$\lambda = r_f \left(\sqrt{\frac{2\pi}{\sqrt{3}\phi_f}} - 2 \right) \quad (5.15)$$

Using Equation 5.15, for the filaments used in this work, the samples having a fibre volume fraction of 0.56 and 0.61 would result in a fibreless resin layer thickness of 7.632 μm and 6.14 μm , respectively. The resin layer thickness is however not constant throughout the cross-section since the fibre packaging within the rovings and their architecture inside die cavity favour the fibres to directly encounter the die wall or move away from the die wall. Therefore, in practical cases, microscopic investigation of the cross-section of the cured composite would give the realistic resin layer thickness. Hence, the sample cross-sections were investigated using a scanning electron microscope.

Figure 5.21 shows a micrograph of a sample having 0.61 fibre volume fraction. Interpretation of the micrograph reveals the variation of the resin layer thickness along the length of the sample. The distance between the fibre surfaces and the sample edge were measured using the image analysis software ImageJ. From the measured data, the distribution of resin layer thickness was calculated (Figure 5.21 (b)). The calculated mean thickness of the resin layer is $7.147 \pm 4.382 \mu\text{m}$.

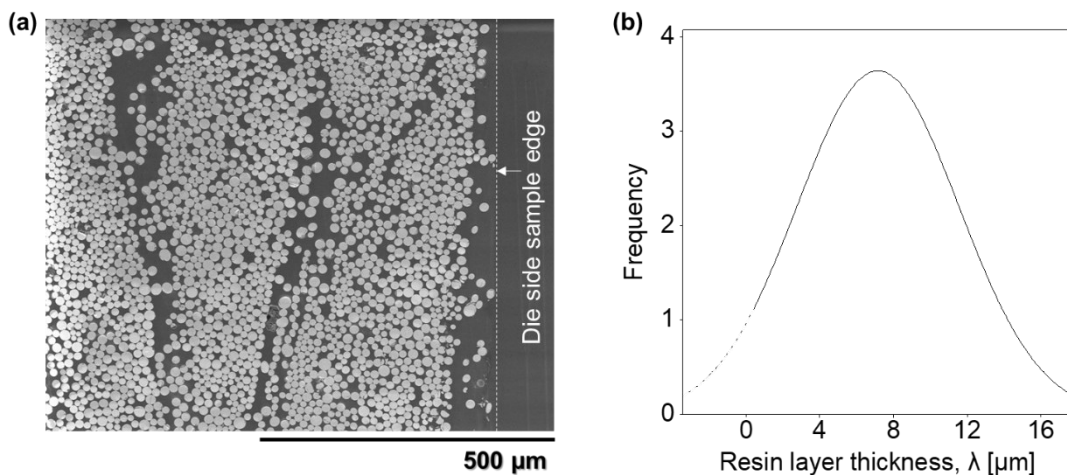


Figure 5.21: (a) Scanning electron micrograph showing resin layer thickness between the die wall and the outer edge of the sample at $\phi_{fa} = 0.61$ and (b) the gaussian distribution of resin layer thickness.

5.5 Conclusion of measurement process development

The sections of Chapter 5 described the established torque measuring procedure including core preparation using filament winding process. For the experimental evaluation of the rotating core method, a glass fibre-epoxy system has been utilised in the experiments. Investigations were conducted to identify and define the limiting variables of the rotating core method using different preparatory process parameters that influence the torque measurement. The results reveal that the DDS can be utilised to continuously measure the torque evolution using fibre-matrix wound on a solid core. The observed variation in the torque throughout the measurement time (described in Section 5.2.3) shows that the torque experienced by the die in DDS is a result of physicochemical changes experienced by the fibre-matrix in the annulus. This verifies the research hypothesis 2 proposed in Chapter 3. Detailed investigative results of torque evolution behaviour with various process and material parameters are discussed in Chapter 7.

Additionally, the observations made from the evaluation of temperature profile of the windings facilitate the determination of curing kinetics of the resin formulation in the DDS. The evaluation on winding tension and its influence on the measured torque permits to calculate the compaction of the fibre-matrix in the entry segment of the die. The optical evaluations revealed the relationship between the fibre orientation and the winding parameters. Roving tension of about 1.8 N in the winding process is found to be optimal for having approx. 0° orientation of the fibres in the windings during torque measurement on DDS. This represents fibre orientation in a pultruded profile. Assessment of the resin film thickness explicitly verifies the assumption 5 (described in Section 4.1.2) on the flow behaviour of the resin formulation in the viscous state. The deviations in the measured fibreless resin layer thickness reiterates the need for the empirical methods over the hitherto numerical models which uses constant λ to calculate the forces in the viscous region. Further, the investigations on through-thickness resin flow in the radial direction and axial direction confirms the assumptions 7 and 8.

6 Characterisation of properties of resin formulation

The polymerisation behaviour of the resin formulation and its property evolution is the most important physicochemical phenomenon among those driving the morphological changes in a composite material under given processing conditions. Investigation of the resin properties, therefore, is highly relevant for the analysis of the manufacturing process. Specific to this work, the resin formulation characterisation facilitates the adoption of suitable design strategy and selection of process parameters and enable interpretation of the results obtained from the DDS measurements and pultrusion experiments. In particular, the analysis of the evolution of temperature-dependent chemo-rheological properties and the surface energetics of the utilised resin formulation are highly relevant for this work. This is because the morphological changes in the resin formulation mostly drives the forces that act on the die wall. This chapter, therefore, describes the experiments conducted to determine the curing kinetics, rheological properties and the surface energetics of the resin formulations.

6.1 Resin formulations

The resin formulation contains epoxy resin, amine curing agent and the IMR described in Chapter 5. Table 6.1 lists the formulations prepared for the experiments and their nomenclature.

Table 6.1: Resin formulations and their nomenclature.

Sample nomenclature	Resin formulation		
	Resin fraction [-]	Curing agent fraction [phr]	IMR fraction [phr]
Resin	100	-	-
Curing agent	-	100	-
IMR	-	-	100
REF	100	40	-
E+IMR0.5	100	40	0.5

The digits at the end of E+IMR denotes the respective fraction of IMR in the formulation (e.g. E+IMR0.5 contain 100 parts resin, 40 phr curing agent and 0.5 phr IMR in the formulation). The formulations were prepared at the ambient temperature.

6.2 Curing kinetics determination using DSC

Invariably, most of the thermosets undergo exothermic chemical reaction during the curing process in which low molecular weight monomers polymerise from a liquid state to a rubbery and finally into a solid state. Covalent crosslinks formed during the curing process leads to the change in the state of the resin formulation. Recalling the theoretical description of the phenomena from Section 2.4.2, the rate of conversion and extent of curing in terms of the degree of monomer conversion is given by the Equation 2.10 and 2.11 respectively. The relation shows that the rate of curing is proportional to the rate of change of heat in the resin formulation. DSC experiments permit to record the heat flux

that occurs due to the polymerisation reaction of the resin formulation. Therefore, DSC experiments were conducted to measure the heat flux of the resin formulations. The experiments, however, did not use reinforcing fibres with the assumption that the fibres do not influence the curing kinetics of the resin formulation except acting as a heat sink.

The standard DSC measurement procedure involves in containing a small quantity of the material sample in a shallow crucible placed on a heat flux plate. An empty crucible placed on a second heat flux plate acts as a reference so that the differential heat measured is only due to the thermal behaviour of the material sample itself [157]. Mass of the material sample required for DSC experiments typically varies between 10 - 20 mg. A pre-calibrated Mettler Toledo DSC 3+ instrument was employed in this work for the DSC experiments. Since the polymerisation reaction can occur even at ambient temperatures for the resin formulations used, the DSC experiments were conducted immediately once the mixtures were prepared to minimise the effects caused by early polymerisation reactions.

To facilitate the determination of curing kinetics, both isothermal and dynamic scans were conducted. The isothermal runs were conducted for at least 200 min at temperatures 100 °C, 120 °C, and 140 °C, respectively. The dynamic scans were performed from 0 °C to 250 °C at 1 K min⁻¹, 2 K min⁻¹, 5 K min⁻¹, and 10 K min⁻¹ heating rates. Figure 6.1 shows the specific heat flow measured in the DSC experiments. As discussed in Section 2.4.2, the peaks in the curve is the result of the exothermic heat generated due to the polymerisation. For all the samples a second run was performed after the first run to analyse the residual heat of reaction – an estimation of post-cure kinetics. The samples were rapidly cooled back to 0 °C at 50 K min⁻¹ between the runs. None of the samples showed observable exothermic peaks during the second run since above a critical cross-linking density, the reaction becomes more diffusion-controlled [112] making the reaction insensitive to the measurements.

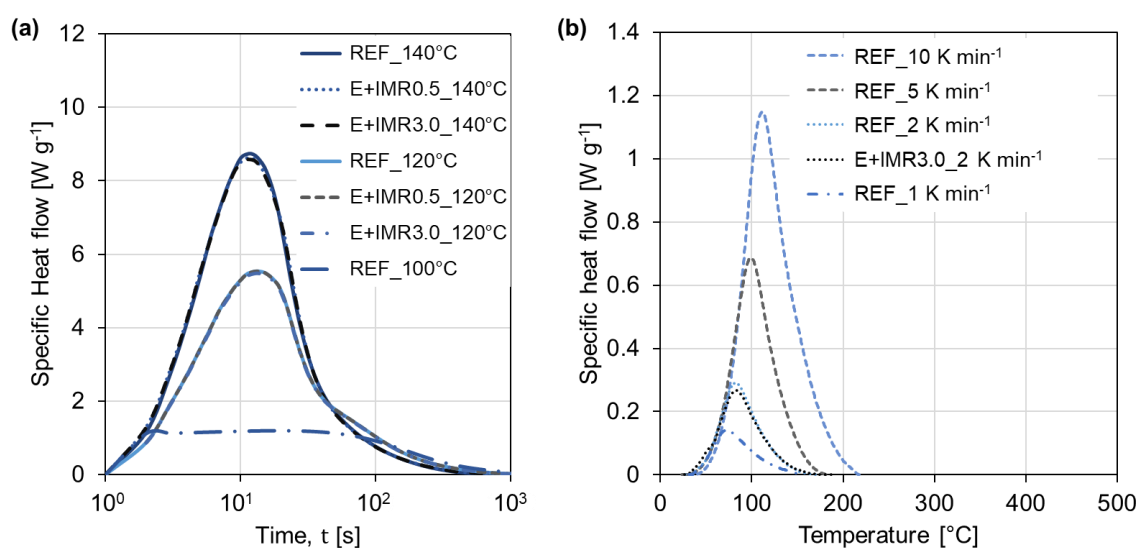


Figure 6.1: Specific heat flow measured in the DSC experiments for various resin formulations – (a) Isothermal runs at different temperatures, and (b) dynamic scans of samples using various heating rates.

The specific heat flow measured during isothermal runs (Figure 6.1 (a)) for the samples show that the presence of IMR does not significantly change the reaction kinetics. Nevertheless, initial measurement points may not well reflect the true heat of reaction due to the thermal shock caused by rapid heating of the sample from ambient temperature to test temperature. The dynamic scans, however, provide an advantage in this case because the sample heats up according to the selected temperature ramp. Yet, like the isothermal measurements, no observable difference in the total heat of reaction is detected for the samples with and without IMR (Figure 6.1 (b)). Therefore, only the REF samples were further analysed at various heating rates in the dynamic scan experiments.

The degree of conversion α and the rate of conversion $d\alpha/dt$ are calculated as per the procedure described in Section 2.4.2. Figure 6.2 shows the calculated degree of conversion and the rate of conversion of the resin formulations at various isothermal temperatures.

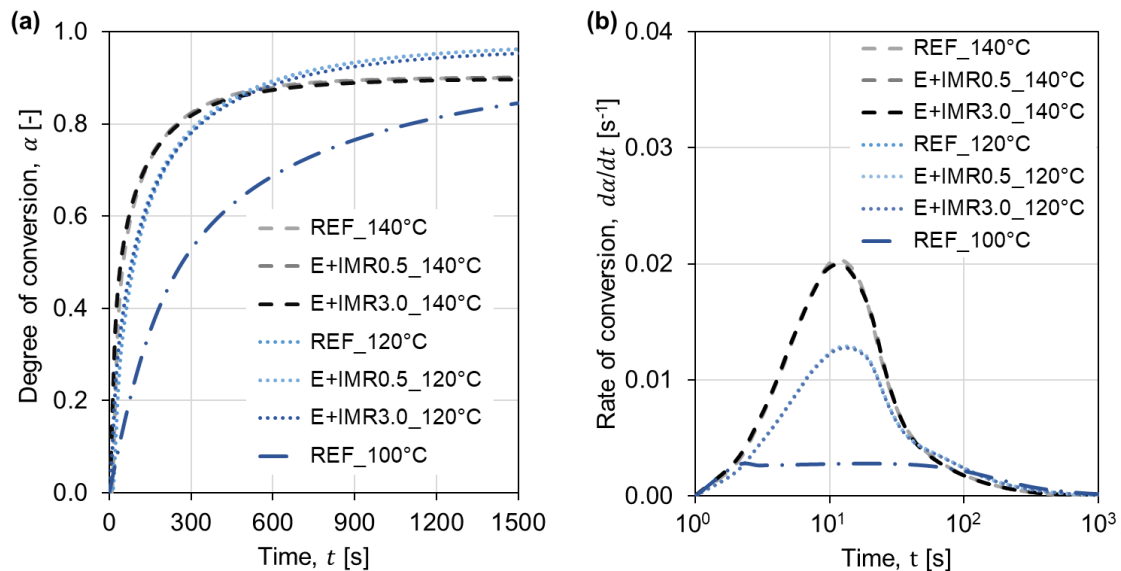


Figure 6.2: Calculated curing behaviour of the resin formulations – (a) degree of cure and (b) rate of curing.

The presence of IMR in the resin formulations does not alter the rate of conversion and the degree of conversion of the resin formulations. In other words, the IMR used in this study neither accelerates nor inhibits the polymerisation reaction. The degree of conversion curves shows that the conversion at 100 °C reaches a maximum of about 0.84 in 1500 s, whereas the conversion at 120 °C and 140 °C reaches a maximum of about 0.92 and 0.89 for the same period respectively. Comparing the rate of conversion at different test temperatures reveals that increasing the test temperature increases the conversion rate. However, at the temperature of 140 °C, the rate of conversion is higher than that of 120 °C only until about 500 s, after which the rate of conversion becomes negligible for 140 °C sample. Such a phenomenon is a result of vitrification, where the glass transition temperature T_g of the cured resin becomes higher than that of curing temperature T_{cure} . Beyond the vitrification point, the reaction becomes diffusion-controlled and therefore the rate of conversion becomes sluggish in nature [158].

Most importantly, the objective of the DSC experiments conducted within the scope of this work is to determine the curing kinetic parameters of the used resin formulations. Therefore, the above experimental data are used to establish curing kinetic models.

The sigmoidal shape of the rate of conversion curves (Figure 6.2 (b)), where the rate of conversion rapidly increases from zero to its maximum at the initial stage, suggests an autocatalytic nature of the reaction [95,159]. As described in Chapter 2, KS model (Equation 2.12) well represents the autocatalytic reaction kinetics of epoxy-amine resin systems. Therefore, the KS model was used to fit the da/dt vs α curves. The curve fitting was realised using the Netzsch Kinetics Neo[®] software from Erich NETZSCH GmbH & Co. Holding KG, Selb, Germany [160]. Figure 6.3 (a) shows the da/dt vs α curves fit with KS model. The software further features fitting the KS model with dynamic scan results (Figure 6.3 (b)) and multi-step temperature data.

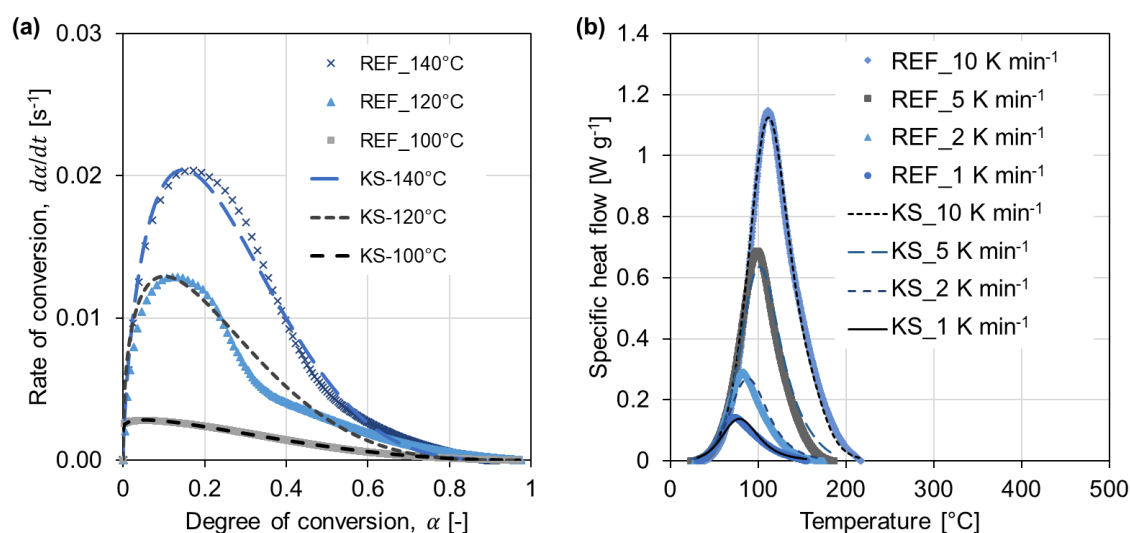


Figure 6.3: Curve fitting of KS model to the experimental DSC data – (a) isothermal runs data and (b) dynamic scan data.

The kinetic parameters determined by the curve fitting are listed in Table 6.2. The reaction follows a 2.62 order reaction which is the sum of the reaction order constants m and n .

Table 6.2: Kinetic parameters determined from curve fitting DSC experimental data using KS model.

m [-]	n [-]	k1		k2	
		A ₁ [min ⁻¹]	E _{a1} [J mol ⁻¹]	A ₂ [min ⁻¹]	E _{a2} [J mol ⁻¹]
0.37	2.25	2.73x10 ⁵	5.80x10 ⁴	3.92x10 ²	3.59x10 ⁴

The cure kinetics parameters permit to calculate the temperature-dependent conversion behaviour of the resin formulations in the rheometer, DDS and pultrusion experiments.

6.3 Rheological behaviour analysis using rheometer

The analysis of temperature-dependent rheology reveals the viscosity development and the gelation time of the resin formulations. As described in Section 2.4.2, rheological

experiments were conducted in an oscillatory mode using parallel plates. The experiments utilised an MCR 301 rheometer from Anton Paar Germany GmbH, Ostfildern, Germany. Due to the adhesive nature of the epoxy resin formulations, disposable trays and plates were used for the measurements. The top plates had a diameter of 25 mm and were made of aluminium.

Since there is a risk that a higher strain rate ruptures the gelling matrix, lower strain rates ensure the intactness of the forming gel and would result in measuring “true” gelation time. Therefore, the rheological measurements were performed at an angular frequency of 1 Hz with 1 % angular strain in the material. The gap between the plates was selected to be 1 mm to minimise the temperature gradient within the sample. Like for the DSC experiments, the resin formulations were prepared immediately preceding the measurement process to minimise the effects from pre-measurement polymerisation. Since the experiments on DDS and pultrusion cannot be performed without the IMR due to the die seizure risk, only the formulations containing IMR were analysed for their rheological properties. For the measurements, about 5 ml of sample was placed on the bottom plate at 20 °C. After lowering the top plate to the measurement position, the excess resin squeezed out of the gap was wiped out to minimise the impact of the edge effects on the strain. A Peltier element equipped in the rheometer heated the bottom plate from 20 °C to the measuring temperature of 100 °C, 120 °C and 140 °C for various experiments respectively. The software Rheoplus v3.41, that controls the rheometer also features the calculation of loss modulus G'' and storage modulus G' from the applied strain and the measured torque. The complex viscosity can be calculated further from the calculated loss and storage modulus using the relations described in Section 2.4.2. Figure 6.4 shows the complex viscosity development of the resin formulations at various test temperatures. As the test temperature increases, the development of viscosity of the samples advance.

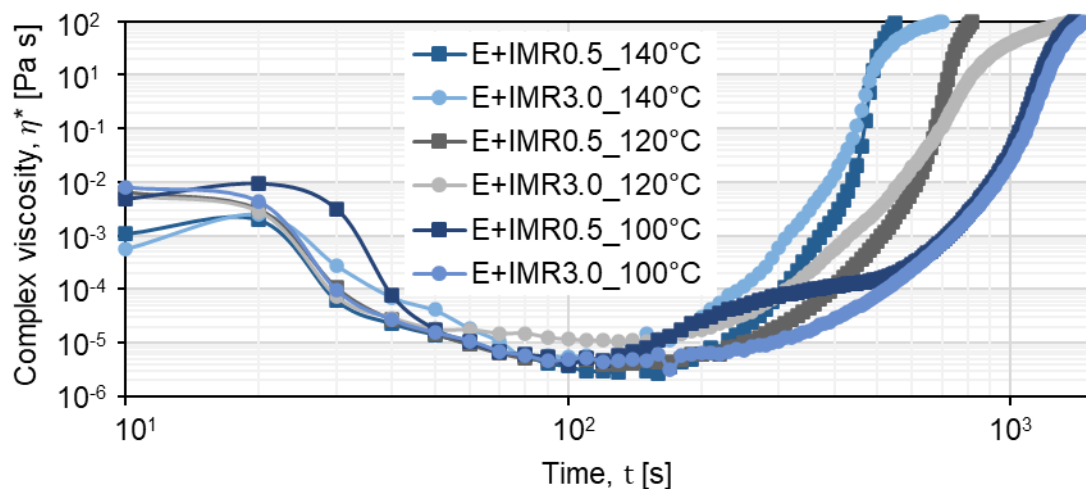


Figure 6.4: Viscosity development of the resin formulations measured at various temperatures

Interesting to note is that, although the IMR in the resin formulations has not affected the cure kinetics, a visible impact on the viscosity development could be observed. The rate of viscosity development of the formulations containing 3.0 phr IMR was higher until a specific time at test temperatures 120 °C and 140 °C. A cross-over point could be observed for both the samples at about 680 s and 480 s at test temperatures 120 °C and

140 °C respectively. Beyond the cross-over point, the rate of viscosity development of the samples slowed down compared to the samples containing 0.5 phr IMR. A pronounced decrease in the viscosity development rate could be observed for the sample tested at 120 °C. A possible reason for this effect could be the interaction of the IMR with the testing plates. At a higher degree of conversion of the resin formulation, formation of IMR interphase between the test plates and the sample could have resulted in the decrease in measured torque in the rheometer and hence the viscosity. However, at 100 °C test temperature, a converse phenomenon could be observed where the rate of viscosity development of formulations containing 0.5 phr IMR is higher than that of the one containing 3.0 phr IMR.

The rheometer measurements, in addition to the viscosity development behaviour, provide information on the gelation time of the cross-linking polymers. Chapter 2 described the theoretical aspect of the gelation. The gelation time was determined from the cross-over points of the calculated storage and loss modulus (i.e. the time at which $G' = G''$). Figure 6.5 (a) shows the estimated gelation time for the resin formulations having varying concentration of IMR at various test temperatures. Since the temperature profile in the rheometer and the DSC experiments vary due to different heating setups employed, the degree of conversions during the rheometer experiments have to be calculated from the curing kinetics parameters using KS model discussed earlier. Figure 6.5 (b) shows the calculated degree of conversion of the resin formulations in rheometer experiments at the respective gelation time.

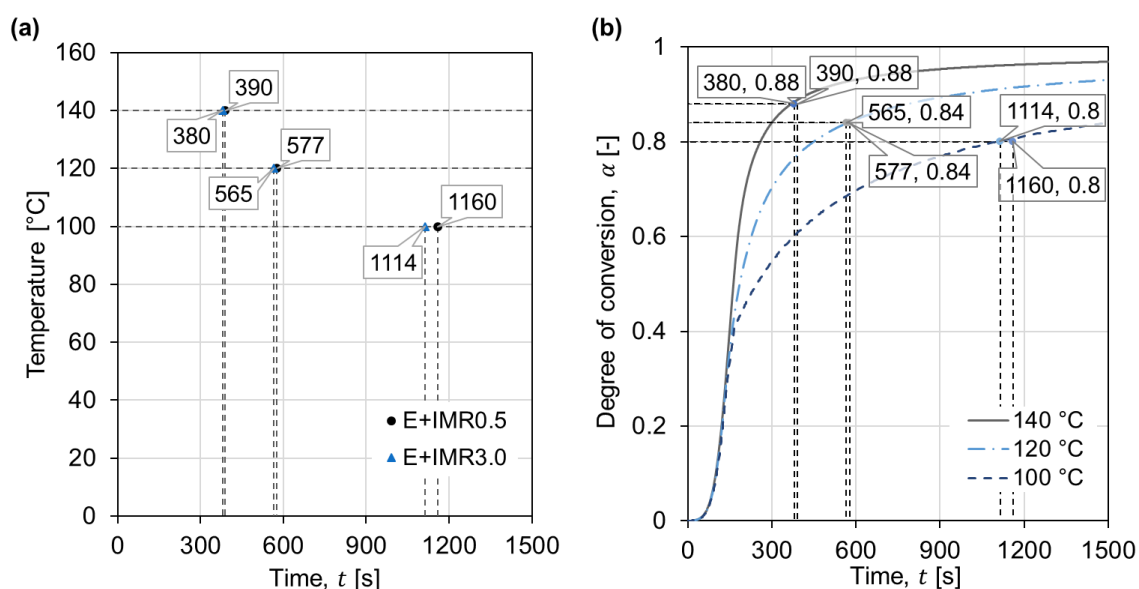


Figure 6.5: (a) Gelation time estimated from the cross-over point of the storage and loss modulus data and (b) degree of conversion estimated from the curing kinetics for the respective gelation time.

In correlation with the curing kinetics, increasing the process temperature reduces the time required for the resin formulation to undergo gelation. Increasing the IMR concentration marginally reduce the gelation time. However, the degree of conversion for both E+IMR0.5 and E+IMR3.0 samples are almost the same at gelation. The results confirm that the presence of IMR at the selected concentration do not alter the gelation process

significantly. Nevertheless, the reason for the difference in viscosity development between the samples with varying IMR concentration has been further analysed in the perspective of interaction of IMR with the testing plates (i.e. interfacial surface energy).

6.4 Surface energy analysis

The surface energy analysis of the materials provides information about the interaction of the materials with its environment. The environment can be a gas, a liquid or a solid which the material encounter. Section 2.4.2 detailed the theoretical background of the surface free energy of materials and the methods to quantify the surface energy. An important aspect specific to this work within the scope of surface energy analysis is to quantify the interaction of resin formulations to the die surface. In particular, the change of surface free energy of the resin formulation in the presence of IMR.

The surface energy or surface tension of the resin formulations and the individual components of the formulation were estimated employing a tensiometer (DCAT 25 from DataPhysics Instruments GmbH, Filderstadt, Germany) using the Wilhelmy plate method described in Section 2.4.2. The Wilhelmy plate utilised was made of iridium-platinum alloy designated as PT11 by the manufacturer [161]. The tests were carried out at a controlled environment having 20 °C temperature and 65 % relative humidity. The tensiometer measures the forces that act on the Wilhelmy plate during immersion and recession of the plate from the liquid. From the measured forces, the surface tension can be calculated using the Wilhelmy equation (Equation 2.25). Figure 6.6 shows the surface tensions of the resin formulations and their components calculated using Wilhelmy equation.

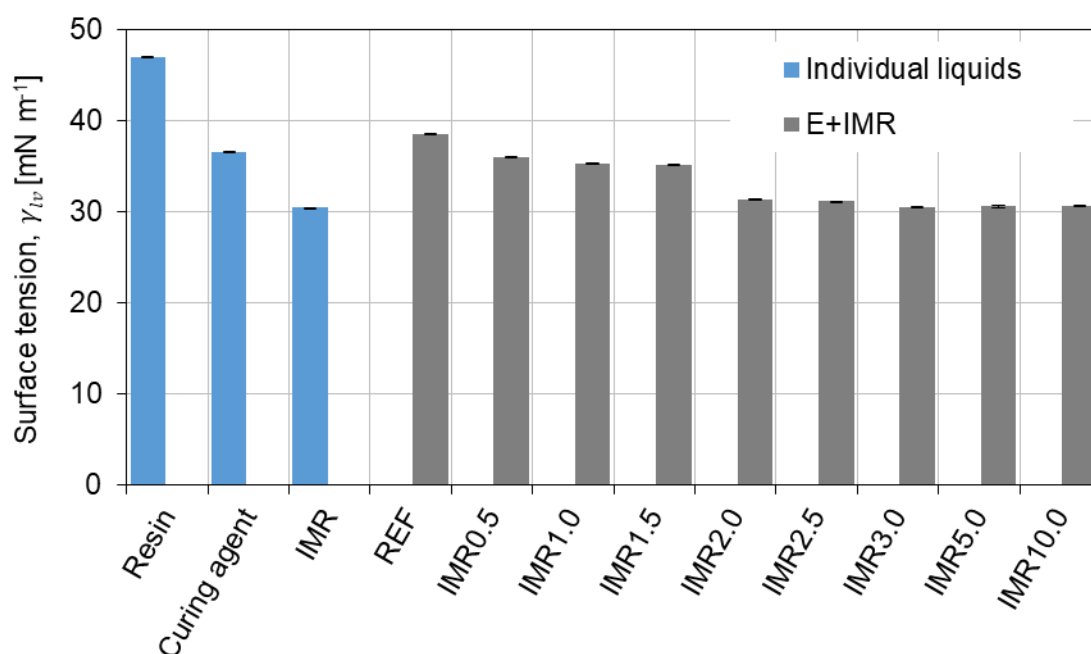


Figure 6.6: Surface tension of the resin formulations and their components measured using the Wilhelmy plate method.

The surface tension of the IMR used in this work is measured about 30 mN m⁻¹. However, the surface tensions of the resin and the curing agent are much higher than that of the IMR. The REF samples, a mixture of resin and the curing agent, has surface tension

between its individual components. In other words, mixing the curing agent with the resin reduces the surface tension of the resin. Adding IMR to the resin formulation further reduces the surface tension. The surface tension of the formulation with 0.5 phr of IMR reduces the surface tension of the mixture without IMR from approx. 38 mN m^{-1} to 34 mN m^{-1} , which is about 10.5 % reduction. Increasing the concentration of IMR in the formulations further reduces the surface tension. An IMR concentration of 3 phr in the formulation decreased the surface tension almost equal to that of the pure IMR. Increasing the concentration of IMR above 3 phr showed no significant change in the surface tension of the formulations. The results conclude that the presence of IMR modifies the interaction of the resin formulations with the surface they encounter. Furthermore, the results show that the IMR has more affinity towards the die surface compared to the resin and the curing agent. This may enhance the likelihood for the formation of an interface layer between die surface and the resin formulation. However, the temperature dependence of the surface tension could not be measured using the tensiometer due to the reactive nature of the resin formulation.

Assessment of the temperature-dependent surface interaction of the resin formulations was realised using a contact angle goniometer (OCA 25 from DataPhysics Instruments GmbH). Sessile drop method described in Section 2.4.2 was used to measure the contact angle of the resin formulation droplets placed on a thoroughly cleaned heated steel die surface. The resin formulation droplets were generated using an automated pumping system that generates equal volume ($5 \mu\text{l}$) of the droplets for each experiment. The steel die was pre-heated to the test temperature before placing the droplets on its surface. Test temperatures selected for the experiments were $20 \text{ }^\circ\text{C}$, $80 \text{ }^\circ\text{C}$, $120 \text{ }^\circ\text{C}$, and $140 \text{ }^\circ\text{C}$. The contact angle between the steel die surface and the droplet was measured 10 s after the placement of the droplet to ensure that the droplet attains the set temperature and remain stable. The measured contact angle and the calculated work of adhesion for the resin formulations at different test temperatures are shown in Figure 6.7.

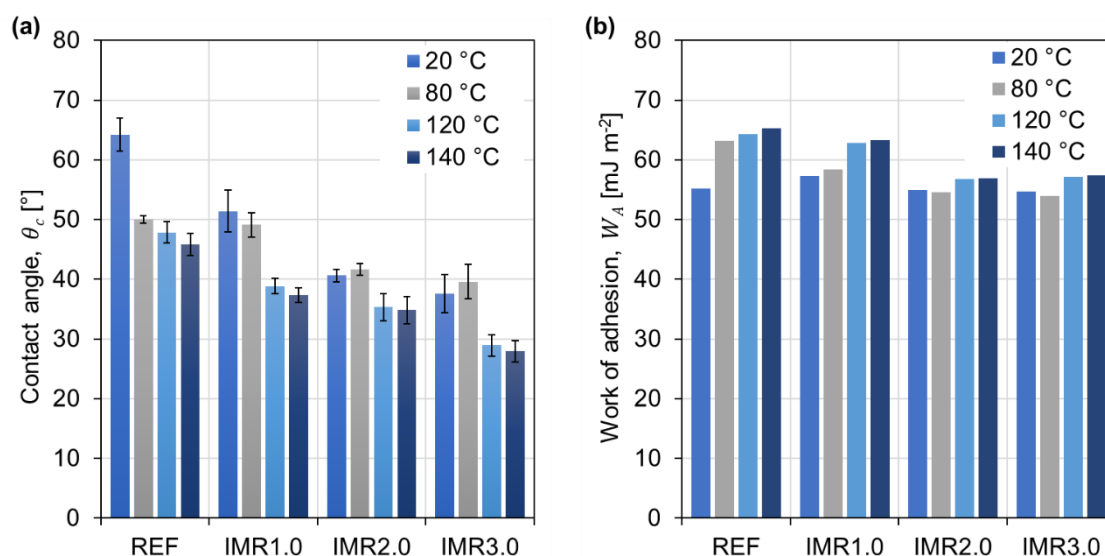


Figure 6.7: (a) Contact angles of the resin formulation droplets with the steel die surface at different temperatures measured using contact angle goniometer and (b) work of adhesion calculated from the contact angle and surface tension measurements.

Comparing the contact angles at different test temperatures shows that the increasing temperature decreases the contact angle. The temperature-induced reduction in the viscosity of the resin formulation could be a reason for the reduction in the contact angle. Nevertheless, the increasing concentration of IMR in the resin formulation decreases the contact angle. Therefore, at higher concentration of IMR, a better wetting of the die surface can be achieved. The calculated work of adhesion (using Equation 2.26) shows that the increase in the concentration of IMR increases the work of adhesion until 2 phr and above which no observable changes in the work of adhesion could be noticed. A similar trend is observed at all tested temperatures.

From the results of the surface energy measurement, the following inferences can be drawn:

- The presence of IMR in the resin formulation modifies the surface energy of the resin system.
- Increasing the concentration of IMR decreases the surface tension of the resin formulations.
- The effect of IMR on the surface energy modification is observed at all the tested temperatures.

Although the results are applicable in the pre-gelation regime of the resin formulations, the inferences can be used to understand the interaction of the cured (i.e. post-gelation) matrix with the die surface.

6.5 Conclusion of resin formulation characterisation

The experimental characterisation of the resin formulations enabled to determine their curing kinetics, rheological behaviour and the surface energetics. The DSC experiments show that the presence of IMR do not alter the curing kinetics of the resin formulations investigated. From the rheology measurements, the gelation time of the resin formulation is determined which permits to distinguish the viscous and frictional force components of the resistive forces. The curing kinetics and the rheological properties of the resin formulations allow the selection of suitable time scale for the DDS measurements which would be comparable to the pultrusion measurements.

Further, the surface energy characterisations show that the presence of IMR significantly affects the adhesion of the curing resin formulation to the die surface and in turn the demoulding forces. The results would permit to further assess the physicochemical phenomena occurring during the course of polymerisation of the resin formulation in the DDS and pultrusion experiments.

7 Experimental investigation on torque evolution

One of the primary objectives of this work is to verify the wider applicability of the newly developed rotating core method for the quantification of pultrusion die dynamics. The DDS measurements, therefore, must reflect the effect of process and material parameters that affect the pultrusion die dynamics. This chapter details the parametric study conducted on the DDS and presents the results of the analysis of the torque evolution behaviour while varying investigation parameters. Further, the use of statistical methods that facilitate experimental design and the result analysis are presented.

7.1 Experimental design

In the pultrusion process, the primary parameters that affect the die dynamics include temperature profile of the die, pulling speed, fibre volume fraction and the resin formulation. Generally, pultrusion utilises specific die cavity geometry in accordance with the composite profile geometry. For given material and process parameters, the pulling force scales proportionally to the surface area of the die cavity (Equation 2.2 to 2.4). Therefore, for the parametric investigation, in addition to the process and material parameters mentioned above, the DDS measurements include geometrical parameters: the thickness of the windings and the radius of the die. At least two values for each selected parameter were tested for their impact on torque evolution. Table 7.1 lists the parameters with their respective values selected for the experiments. The chosen trial space is based on the properties of the resin formulations detailed in Chapter 6 and the succeeding pultrusion experiments discussed in Chapter 8.

Table 7.1: List of parameters studied and the selected trial space.

Parameters		Unit	Sample nomenclature prefix	Trial space		
Process	Die temperature, T_{cdie}	°C	T	120	140	-
	Surface velocity, v_s	mm min ⁻¹	V	100	200	300
Geometric	Die radius, r_{Di}	mm	R	11	5.5	-
	Annular gap, h_a	mm	H	1	2	-
Material	Fibre volume fraction, ϕ_{fa}	-	FV	0.56	0.61	-
	IMR concentration	phr	IMR	0.5	1.5	3.0

Since the parametric study analyses six parameters with at least two values each, the number of experiments required to identify the effect of each parameter and their interaction with the other parameters demands a minimum of 64 sets of experiments. For a better representation of the measured data, each set of experiment should be repeated at least thrice resulting in a minimum of 192 experiments. Adding more values to the trial space further increases the number of experiments. Although such full factorial experiments would help to understand the effect of each individual parameter and their influence on the measured torque, considering the available resources, statistical Design of experiments (DOE) method was implemented to reduce the number of experiments.

DOE is a statistical tool which allows to systematically establish the relationship between factors affecting a process and the output of that process. Using DOE, a full factorial design or fractional factorial design can be implemented. The full factorial design includes all the parameters with their test values of interest and the combination of each set. The advantage of the full factorial design is that the effect of each individual parameter and their influence on the output variable can be experimentally determined. On the other hand, a fractional factorial design tests all the parameters and their values with only the selected number of combinations. The interaction between the parameters and their effects on the output are statistically related [162]. In this work, 1/4th fractional factorial design is used to analyse the influence of process parameters on the torque measured on the DDS. For the implementation of DOE and the result analysis, the statistical software Minitab® 18 was used [163]. The software permits to generate the test sets and the order in which the experiments have to be conducted.

Table 7.2 lists the test sets generated using the DOE software Minitab® 18. The 16 sets of experiments listed were repeated at least thrice to assess the repeatability of the torque-time behaviour. The experimental sets were assigned names based on the nomenclature prefix defined in Table 7.1 together with their respective values. For example, the name T120-V100-R11-H1-FV0.56-IMR0.5 denotes the sample that was tested at 120 °C with a 100 mm min⁻¹ surface velocity of the fibre-matrix in a die with an inner radius of 11 mm at an annular gap of 1 mm with a fibre volume fraction of 0.56 and IMR concentration of 0.5 phr.

Table 7.2: List of test set generated using DOE.

Test set	Test set nomenclature
1	T120-V100-R5.5-H1-FV0.61-IMR3.0
2	T140-V100-R5.5-H2-FV0.61-IMR3.0
3	T120-V300-R5.5-H2-FV0.61-IMR3.0
4	T140-V300-R5.5-H1-FV0.61-IMR3.0
5	T120-V300-R11-H1-FV0.56-IMR0.5
6	T140-V300-R11-H1-FV0.61-IMR0.5
7	T120-V300-R11-H1-FV0.61-IMR0.5
8	T120-V100-R11-H2-FV0.61-IMR3.0
9	T140-V100-R11-H1-FV0.61-IMR3.0
10	T120-V300-R11-H1-FV0.61-IMR3.0
11	T140-V300-R11-H1-FV0.61-IMR3.0
12	T140-V200-R11-H1-FV0.61-IMR3.0
13	T120-V300-R11-H2-FV0.61-IMR3.0
14	T120-V300-R11-H1-FV0.56-IMR3.0
15	T140-V300-R11-H1-FV0.61-IMR1.5
16	T140-V100-R11-H1-FV0.61-IMR0.5

7.2 Parametric study on DDS

The investigations with the various process, material and geometric parameters were conducted to determine their effect on torque evolution within the die. The process,

material and the geometric parameters were varied during the experiments according to the test plan established using DOE method. The torque measurement experiments were conducted according to the procedure described in Section 5.2.3. The results of all the torque measurement experiments are presented in Appendix A.

7.2.1 Process parameters

For a given fibre volume fraction and the profile geometry, the temperature and the pulling speed are the two primary control parameters in the pultrusion process. Because the curing kinetics of the resin formulation depends on the temperature and the rate of heat transfer in the resin formulation, the pulling speed and temperature profile of the die dictates the degree of conversion. In other words, increasing the pulling speed demands an increase in temperature to attain the same degree of conversion of the resin formulation. But the confined pultrusion die length limits the pulling speed that would achieve a reasonable degree of conversion within the die cavity for a set temperature profile suitable for the resin formulation.

On the other hand, unlike pultrusion, the principle of operation of DDS makes it independent of the die length limitations. Therefore, DDS permits to process the material at any temperature independent of the angular velocity. For the parametric analysis, as listed in Table 7.1 the cores wound with fibre-matrix were tested at the temperatures 120 °C and 140 °C with the fibre-matrix surface velocities (i.e. at r_{rf}) of 100 mm min⁻¹, 200 mm min⁻¹, and 300 mm min⁻¹, respectively while keeping the other parameters constant.

Effect of die temperature

Figure 7.1 shows the measured torque-time curve for the above-mentioned parameter variations. Observing Figure 7.1, an increase in the process temperature does not show apparent differences in the measured torque at the initial stage of the measurements until 200 s. However, the rate of change of torque advances with increasing die temperature beyond 200 s.

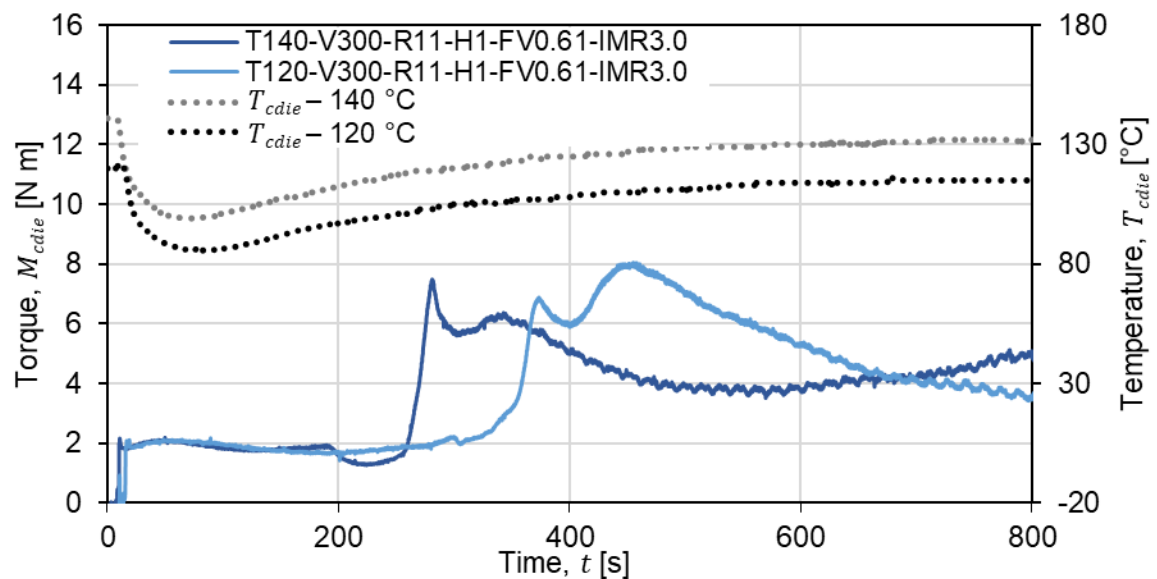


Figure 7.1: Characteristic torque-time curves measured at $T_{die} = 120$ °C and 140 °C.

Increasing the process temperature increases the rate of conversion (Figure 6.2) which in turn increases the viscosity of the resin formulation. Since the measured torque is proportional to the viscosity of the resin formulation (from Equation 4.6), increasing the process temperature advances the rate of change of measured torque. The faster curing of resin formulation processed at 140 °C results in narrow and advancing peaks of the torque compared to the one processed at 120 °C. In other words, at higher temperatures gelation and solidification of the resin formulation shifts towards lower times.

In the pultrusion process, the above phenomenon results in the reduced viscous region (i.e. viscous drag) within the die. Therefore, increasing the temperature of the die keeping all the other parameters constant, decreases the contribution of viscous force component and increases the contribution of frictional force component to the total pulling force.

Effect of process speed

In the DDS, changing the rotational velocity of the wound core alone does not affect the degree of cure. This allows studying the impact of change in the processing speed on the torque evolution. Similar to the change in process temperature, the change in surface velocity of the rotating fibre-matrix does not show an observable effect on the measured torque until the cure induced viscosity of the resin formulation increases (Figure 7.2). This is because, as mentioned in Chapter 2, most of the epoxy resin systems behave as Newtonian fluids.

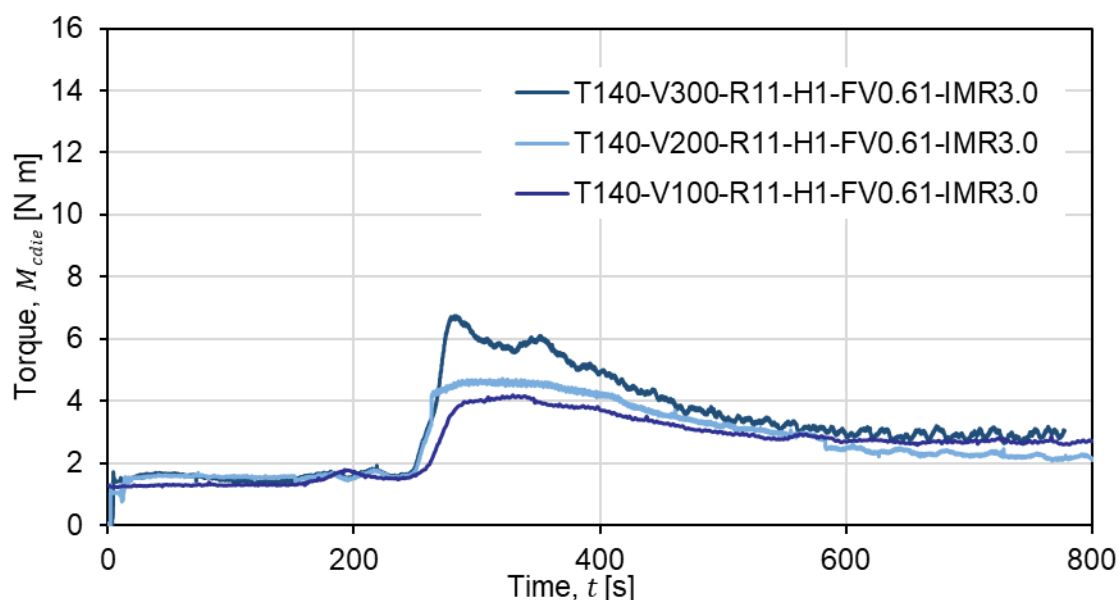


Figure 7.2: Characteristic torque-time curves measured at surface velocities $v_s = 100 \text{ mm min}^{-1}$, 200 mm min^{-1} , and 300 mm min^{-1} .

Further, as described in Section 4.1.2, the shear rate in the DDS follows simple shear principle in which the shear rate is directly proportional to the surface velocity. Until the formation of cross-linked networks (Figure 2.9 (c)), the viscosity of the resin decreases with an increase in temperature because of increased molecular mobility. Therefore, increasing the strain rate (i.e. the surface velocity) marginally affect the shear stress and hence the measured torque (from Equation 2.19). Once the gelation of resin formulation begins, the increase in cure induced viscosity leads to an exponential increase in the

measured torque. Figure 7.2 shows that the peak torque measured at a surface speed of 300 mm min^{-1} of the fibre-matrix is about 7 N m whereas that for the 100 mm min^{-1} is 40 % less. The increase in torque should, therefore, be coupled to both increase in strain rate (i.e. three times more) and the cure induced viscosity effects. A similar trend is observed between the samples with surface speeds 100 mm min^{-1} and 200 mm min^{-1} .

Further, unlike a peak observed in the case of 300 mm min^{-1} sample, a plateau is detected after the maximum torque for both the samples with the surface speeds of 100 mm min^{-1} and 200 mm min^{-1} . In the post-gelation zone, where the material behaves more elastic than viscous, such behaviour is attributed to the strain rate dependent stress in the samples. At lower strain rates, the gelled resin formulation deforms at a lower rate possessing a lower rate of change of stress in the material. On the other hand, at the higher strain rates, the higher rate of deformation of the cross-linked networks possess a higher rate of change of stress. *Siviour et al.* [164] review the phenomena behind the strain rate dependency of stress evolution in polymers.

Based on the above results, considering a pultrusion process with increasing pulling speed, for a similar degree of conversion of resin formulation, the pulling force increases proportionally. This again validates the theoretical considerations given by Equations 2.3 and 4.6.

7.2.2 Geometrical parameters

The geometrical parameters, the thickness of the fibre-matrix as well as the area of contact between the fibre-matrix and the die surface, would affect the resultant torque measured on the DDS. To quantify the effect of the geometrical parameters stated above on the torque evolution, experiments were conducted with varying core and die geometries. Based on the experimental design, the test set was selected such that the torque measurement investigates the effect of both contact area and the thickness of the samples respectively while holding the other parameters constant.

Effect of die surface area

The torque measurement on DDS using the dies with the inner radii of 11 mm and 5.5 mm in combination with the cores of radius 9 mm and 3.5 mm , respectively facilitated to investigate the effect of contact area between the fibre-matrix and the die surface on the torque evolution. Both the dies had equal outer diameter as shown in Figure 4.5. Because of the equal outer diameters of 15 mm , the wall thickness of the dies translates to 4 mm and 9.5 mm for 11 mm and 5.5 mm die inner radii, respectively.

The difference in the wall thickness results in different thermal masses for the dies. That is, the die with thicker wall possess higher thermal mass compared to that with a thinner wall. Consequently, the heat flow into the fibre-matrix is different for both the samples. The difference in the heat flow is observed from the measured temperatures of the respective dies. Thus, because of the temperature differences, for the smaller diameter samples, a shift in the rate of change of torque (i.e. rate of conversion of resin formulation) towards left in the torque-time curve is observed. However, in a pultrusion process, the dimensioning of the pultrusion die has to consider such effects to achieve the desired degree of conversion at a given pulling speed and temperature profile of the die.

Figure 7.3 shows the temperature of the die together with the resultant torque measured over time with varying die-core geometry. As discussed above, the thermal loss during core insertion phase of the thicker die is observed to be minimal compared to the thinner die. In addition to the die wall thickness, the volume of the material introduced into the die with 11 mm inner radius is 122 % higher than that for the die with an inner radius of 5.5 mm. Consequently, the amount of heat flow increases leading to decrease in the temperature of the thinner die at a higher rate compared to the thicker die. The difference in the heat flow between the two samples resulted in the varying rate of conversion and hence the torque.

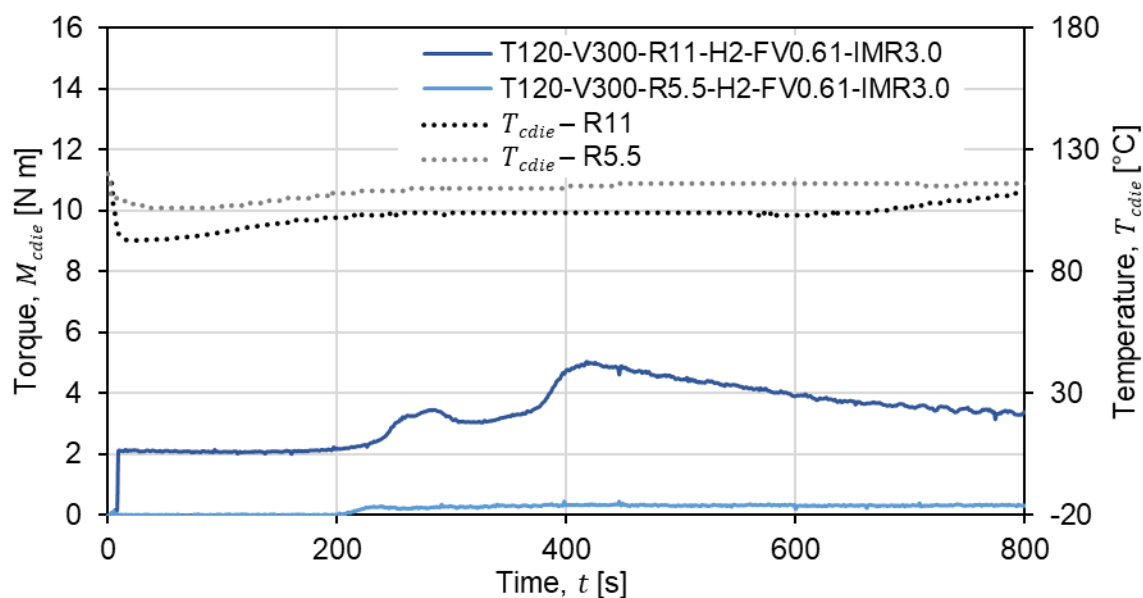


Figure 7.3: Typical torque-time curves for varying die-core geometry.

Comparing the peak resultant torques for both the samples, the sample with 5.5 mm outer diameter shows a peak torque of about 0.26 N m at 235 s. Whereas, the sample with 11 mm outer diameter exhibits peak torque of 4.89 N m at 426 s although the contact area of the later sample is twice that of the former sample. The reason behind the large variation is attributed to the low initial compaction torque (described in Section 5.2.4) exhibited by the smaller diameter sample during the core insertion phase. However, normalising the compaction torque of the smaller diameter sample equivalent to the larger diameter sample would result in peak torque of 2.38 N m. This is about 51 % variation between the peak torques and is proportional to the contact area. The inference demands a careful selection of the winding parameters for the core preparation process to achieve comparable measurements within DDS experiments.

Further, the results show that like in pultrusion process, the compaction of the fibre-matrix in the compaction zone of the die significantly influence the shear stress exerted by the fibre-matrix on the die wall in the straight segment of the die. As described earlier in Chapter 2, the compaction of fibre-matrix in the pultrusion process is influenced by the fibre volume fraction, viscosity of resin formulation, the geometry of the profile and the entrance geometry of the die. In addition to the above-mentioned parameters, in the DDS, the winding tension in the preparation process also influences the compaction of the wound fibre-matrix.

Effect of winding thickness

The effect of part thickness on the torque evolution behaviour was investigated by using cores with different diameters. Unlike in the pultrusion process, where the change in profile thickness demands change in the geometry of the cavity and hence the contact area of the fibre-matrix, in DDS the thickness of the part (i.e. winding) can be varied by varying the diameter of the solid core. Varying merely the diameter of the core facilitates constant contact surface area between the rotating fibre-matrix and the die wall. Thus, the effect of change in part thickness can be investigated without the influence of the contact surface. The experiments utilised the die having 11 mm inner radius in combination with cores having 10 mm and 9 mm outer radius resulting in the winding thickness of 1 mm and 2 mm respectively. Figure 7.4 shows the temperature and torque measured over time for varying winding thickness.

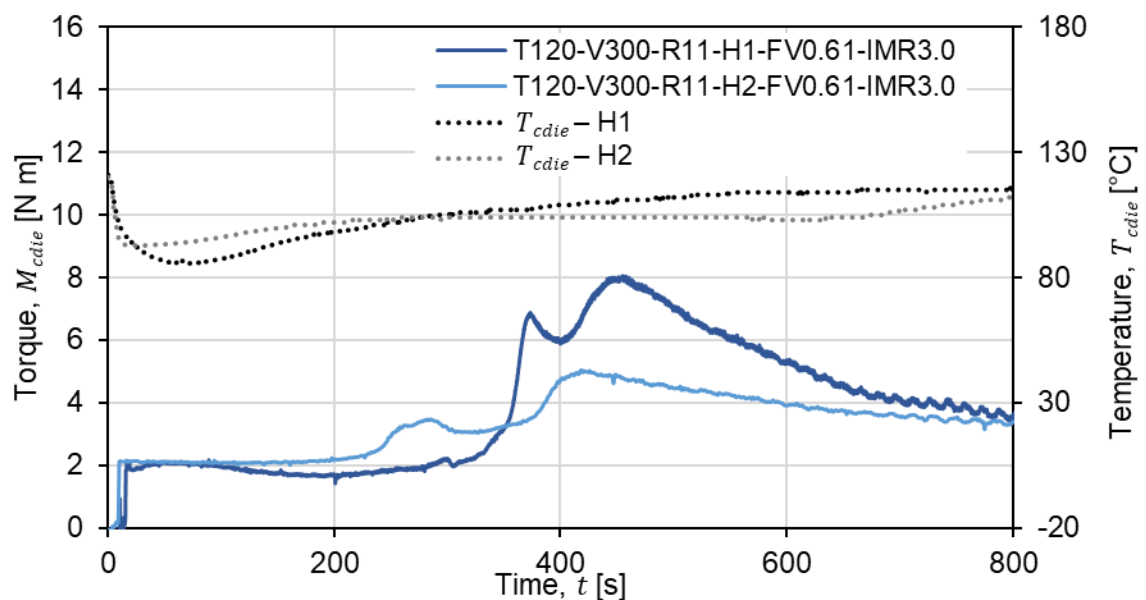


Figure 7.4: Typical torque-time curves for varying winding thickness.

Because of the poor thermal conductivity of the fibre-matrix, the through-thickness rate of heat flow from the die wall to the core surface for the thicker sample would be less compared to the thinner sample. Sample temperatures investigated with integrated thermocouples verifies the heat flow rate in the samples (Figure 5.12). Accordingly, although the rate of decrease in the temperature at the beginning is higher, the reversal of temperature change for the thicker sample is higher (93 °C) compared to the thinner sample (85 °C). In consequence, the degree of conversion of resin formulation of the surface of thicker samples precedes the thinner sample. The effect of the higher degree of conversion of the resin formulation at the surface of the thicker samples results in the higher measured torque up to about 350 s of the measurement. However, the temperature of the 1 mm winding exceeds the 2 mm winding at about 280 s which accelerate the rate of conversion of the resin formulation. Consequently, beyond 350 s, the measured torque of the thinner samples exceeds the thicker samples.

On the other hand, 2 mm samples unlike 1 mm samples, shows a broad distribution of torque. As the thickness of the sample increases, the temperature-induced degree of

conversion at the initial phase of the process in the layer farther from the die wall would be relatively low compared to that close to the die wall. The solidified surface layers will subsequently resist the normal pressure exerted, due to thermal expansion of the inner layers, by the sample against the die wall. This would result in lower shear stress at the die-sample interface. Such phenomena, however, are not substantial with thinner samples. Therefore, thinner samples exert higher shear forces in a shorter time. Conversely, the thicker samples exert relatively lower shear forces over a longer period. In other words, the gelation in the layer close to the core surface occurs in a shorter period for thinner samples whereas the thicker samples would need a longer period. A similar phenomenon was reported by the *Baran et al.* [165] in their pultrusion process simulation in which they studied the effect of profile thickness on the pulling force. From the DDS measurements, it is observed that the difference in total torque measured over 800 s between the samples with varying sample thickness is negligible. However, the contribution of viscous and frictional components to the total shear force varies as the sample thickness varies. Thicker samples exert more frictional force because of the faster surface gelation compared to the thin samples.

7.2.3 Effect of fibre volume fraction

The fibre volume fraction is one of the primary parameters that affect the pulling force in the pultrusion process. Therefore, understanding the effect of fibre volume fraction on the torque evolution behaviour becomes essential to quantify the die dynamics. As the amount of reinforcing fibres increase, the thickness of the fibreless resin layer decreases resulting in increased velocity driven viscous drag. Additionally, the probability of contact friction between the die surface and the fibres increases with increasing fibre volume fraction increasing the contribution of the frictional forces to the total shear force. To investigate the effect of fibre volume fraction on the torque evolution, fibre volume fractions 0.61 and 0.56 were selected – a typical range for an open bath pultrusion process. Figure 7.5 (a) shows the characteristic torque-time curves measured with varying fibre volume fractions.

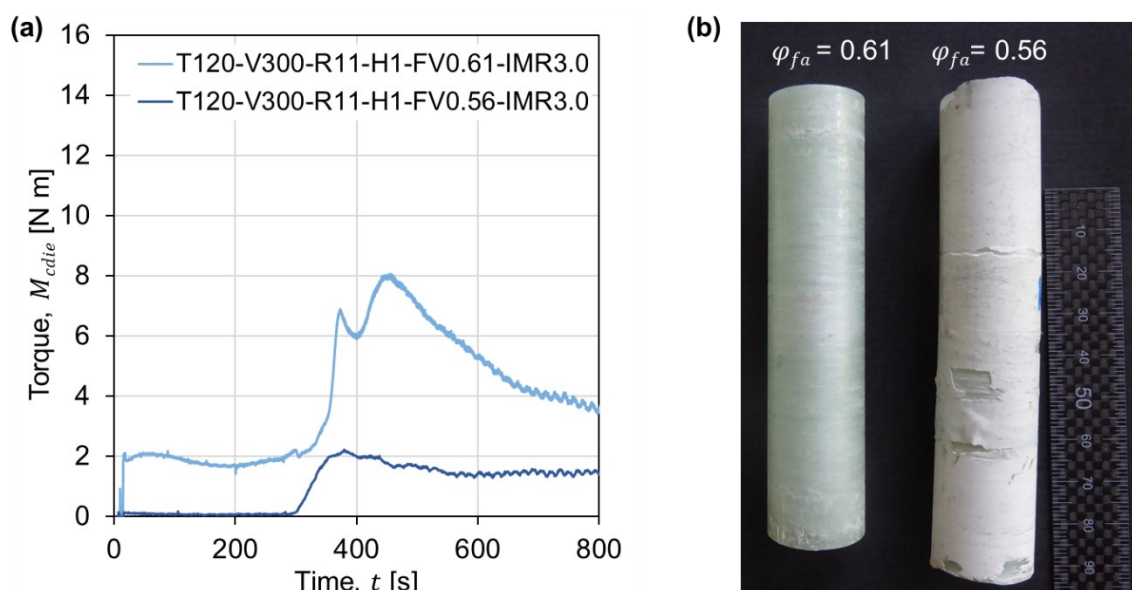


Figure 7.5: (a) Torque-time curve for varying fibre volume fraction and (b) photographs of the cured samples from respective DDS measurements.

Comparing the torque-time curves in Figure 7.5 (a), the samples having 0.56 fibre volume fraction experiences very low compaction during the core insertion phase. Because of lower compaction, the torque exerted by the sample on the die wall remains lower compared to the sample with 0.61 fibre volume fraction. Similar applied brake pressure utilised for both samples (0.61 and 0.56 fibre volume fraction) during winding of the core results in relatively smaller diameter windings for the sample with 0.56 fibre volume fraction. Consequently, the samples do not experience fibre compaction during core insertion phase. Further, the smaller wound diameters increase the fibreless resin layer thickness (Figure 5.20 (c)). This would have led to the reduction in the shear stress exerted by the resin layer on the die wall. Nevertheless, at about 300 s of the measurement, a noticeable progressive increase in the rate of change of torque is observed. Unlike, the samples with 0.61 fibre volume fraction, the samples with 0.56 fibre volume fraction exhibit a relatively flat curve after reaching the peak torque. Observing the surface of the cured sample (Figure 7.5 (b)) reveals the presence of a thick cured matrix layer with few fractures in between. The fractured resin rest caused by pilling would have increased the friction between the die wall and the rotating sample resulting in the flat nature of the curve post-gelation.

Mathematically normalising the torque-time curve of the sample with 0.56 fibre volume fraction to match the initial compaction experienced by the sample with 0.61 fibre volume fraction would result in peak torque of about 4 N m. Nevertheless, the peak torque is still 50 % lesser than that for the sample with 0.61 fibre volume fraction (about 8 N m). However, after normalisation, the total torque measured over 800 s for the samples with 0.56 fibre volume fraction is 11 % less compared to the other, though, from Equation 5.14, a decrease in the fibre volume fraction by 5 % would decrease the viscous drag by about 19.5 %. As described in Chapter 2, because of stochastic nature of the pultrusion process and the complex chemo-rheological and thermo-mechanical coupled phenomena occurring within the pultrusion die, the semi-empirical relations require experimental validation to precisely define the process dynamics.

7.2.4 Effect of internal mould release

Mould release agents are one of the crucial components of the pultrusion resin formulation. As literature specify, there is no universal mould release that functions effectively with all resin formulations and all processing conditions. Yet, a specific release agent has a critical concentration to be effective with a selected resin formulation and the process temperatures. This has been proven with the surface energy measurement results presented earlier in Chapter 6. The concentrations of IMR in the resin formulation chosen for the DDS measurements, based on the surface energy measurement results, are 0.5 phr, 1.5 phr and 3.0 phr. The resin formulations were prepared as per the recommendation of the release agent supplier which states that the release agent must be mixed into the epoxy resin before the amine curing agent is introduced into the mixture. The reason behind the mixing procedure is that the amine curing agent has more affinity towards the epoxy resin compared to the release agent. Therefore, mixing the release agent ahead of curing agent helps in the formation of micelles like structure in which the release agent surrounds the epoxy molecules and thereby preventing its interaction with die surface. However, such hypotheses need validation and are beyond the scope of this work.

The torque-time curve measured using the cores prepared with the resin formulation containing varying concentration of release agent is shown in Figure 7.6 (a).

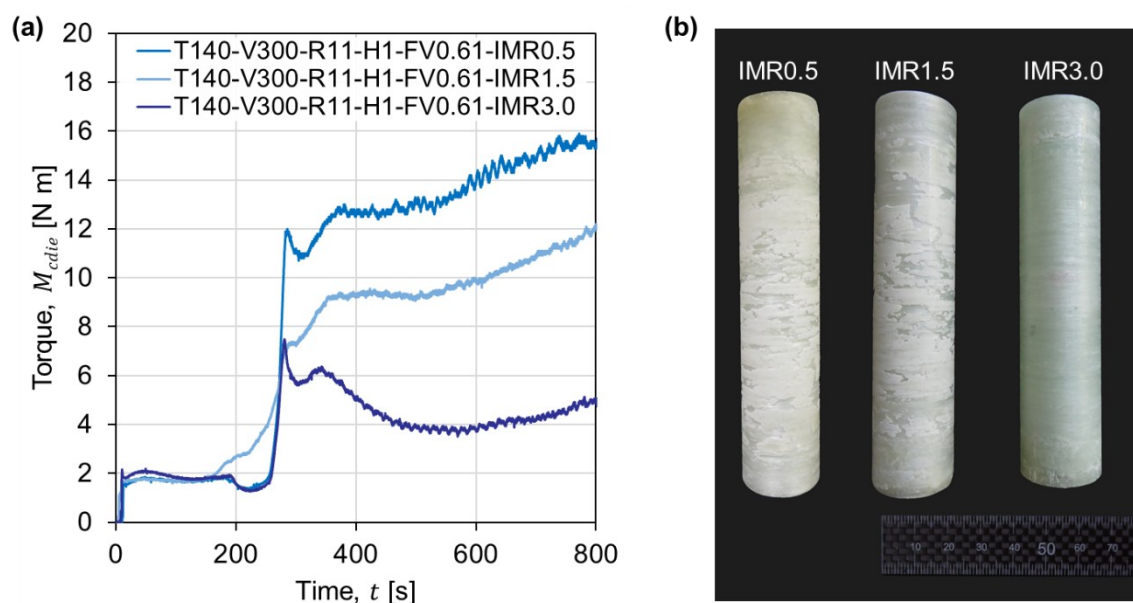


Figure 7.6: (a) Measured torque-time curves of the samples with varying IMR concentration in the resin formulation and (b) photographs of the cured samples with respective IMR concentrations.

Inferences from the torque-time show that concentration of the IMR directly affect the die dynamics. At low conversion levels of the resin formulation, there is no observable variation in the behaviour of the measured torque. Once the formation of cross-linking networks begins (at about 180 s), the rate of change of torque can be observed. At about 290 s, the samples with resin formulations containing 0.5 phr IMR exerts highest shear force whereas the samples with 3.0 phr IMR applies least shear force on the die wall. Interesting to note that is the peak torque is not just caused by the thermal expansion of the bulk but also due to the adhesion of the curing matrix to the die wall. The results, therefore, reiterates that the pulling force models should include the work of adhesion which indeed depends on the effectiveness of the IMR. Beyond reaching the peak torque at about 290 s, the measured torque drops to about 8 % in case of samples with 0.5 phr IMR. Subsequently, the measured torque progressively increases until the end of the experiment. A similar trend is observed for the samples with 1.5 phr IMR but at relatively lower torque levels.

Conversely, the samples having 3.0 phr IMR show a successive decrease in the measured torque. Unlike the other two samples, the torque-time curve for the sample containing 1.5 phr IMR shows a progressive increase in the torque beginning 180 s. The plausible reason for such behaviour could be the formation of stable cross-linked networks. That is, the formed polymer networks do not undergo strain-induced rupture. At lower IMR concentrations the rupture would have occurred because of adhesion of the part of the resin to the die surface and at higher IMR concentrations the slip between the gelling networks would result in a strain-induced rupture. The observations postulate that there exists a critical concentration of IMR that would hinder the gel rupture. Nevertheless, the hypothesis needs further validation.

Observing the photographs of the samples Figure 7.6 (b), the samples that had a lower concentration of IMR in the resin formulation contains thin layers of matrix depositions on their surface. Further, during the experiments once the sample was removed from the die, a powdery resin substance was found in the die and on the sample surfaces. The powdery substance and the irregular matrix surface on the samples is the result of pilling caused by the poor separation of the matrix from the die surface. From the inferences, scenarios illustrated in Figure 7.7 is proposed to understand the effect of mould release concentration. At the initial phase of the measurement process during which the degree of conversion of the resin formulation is negligible, the shear forces are purely viscous (Figure 7.7 (a)). Once the resin formulation reaches a phase illustrated in Figure 2.9 (c), the migration of IMR towards the die wall (Figure 7.7 (b)) result in one of the two following scenarios:

1. Quantity of IMR in the interphase is below the critical concentration or,
2. Quantity of IMR in the interphase is equal to or above the critical concentration.

Scenario 1 does not prevent the adhesion of the matrix on to die wall resulting in the formation of the adhered matrix layer. As the core continues to rotate, the shear forces exerted by the bulk fibre-matrix on the adhered matrix layer leads to a cohesive failure within the itself (Figure 7.7 (c)). The cohesive failure within the cured matrix increases the friction between the fractured surfaces resulting in further increase of the measured torque. With increasing friction “grinding” of the adhered matrix results in the powdery substance.

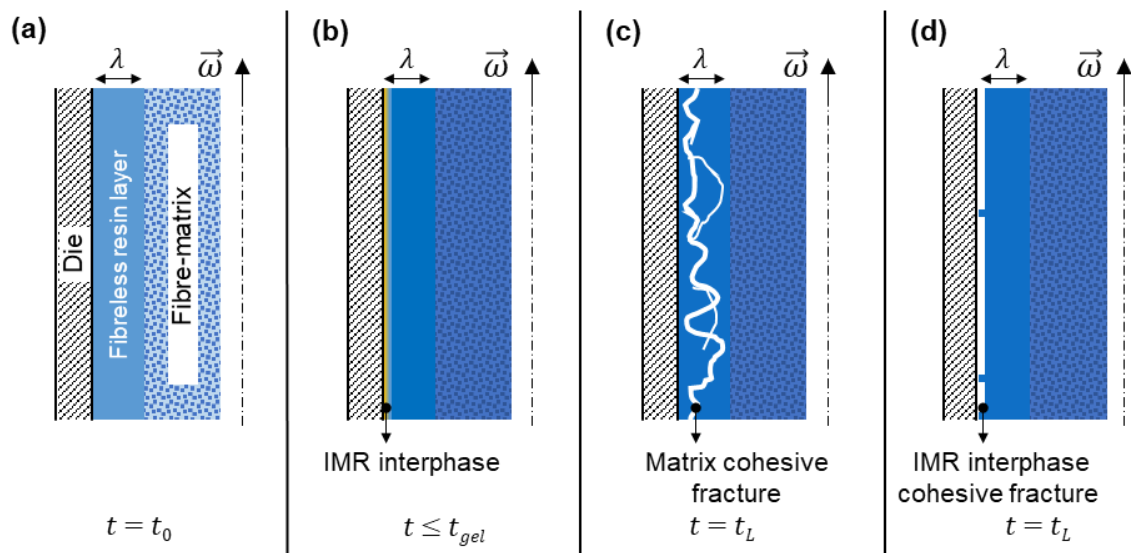


Figure 7.7: Schematic illustration of phenomenon taking place during polymerisation at the die wall-resin film interface in the DDS: (a) as introduced fibre-matrix; (b) formation of IMR interphase in the fibreless resin-film; (c) scenario of cohesive fracture within cured matrix; and (d) scenario of cohesive fracture in IMR interphase.

On the other hand, if the scenario 2 becomes valid, the adhesion of the matrix on to the die wall is prevented by the IMR interface leading to cohesive fracture within IMR interphase (Figure 7.7 (d)). Cohesive fracture of the IMR interphase would lead to a lubricating effect minimising the shear force and hence measured torque. Nevertheless,

depending on the effectiveness of the IMR, a combination of both the scenarios are also probable.

7.3 Viscous and frictional components estimation

Estimation of the contribution of viscous and the frictional components of the shear stress to the measured torque is realised using the cure kinetics and rheological data of the resin formulation. The curing kinetics parameters determined from the DSC measurements (Section 6.1) facilitate the calculation of the degree of conversion of the resin formulation for the temperature profile measured in the DDS and in the rheometer experiments. Further, the rheological measurements of the resin formulation reveal the gelation point (i.e. the time at which $G'' = G'$). The degree of conversion at the gelation point determined from the rheological measurements is calculated from the degree of conversion plot as shown in Figure 7.8.

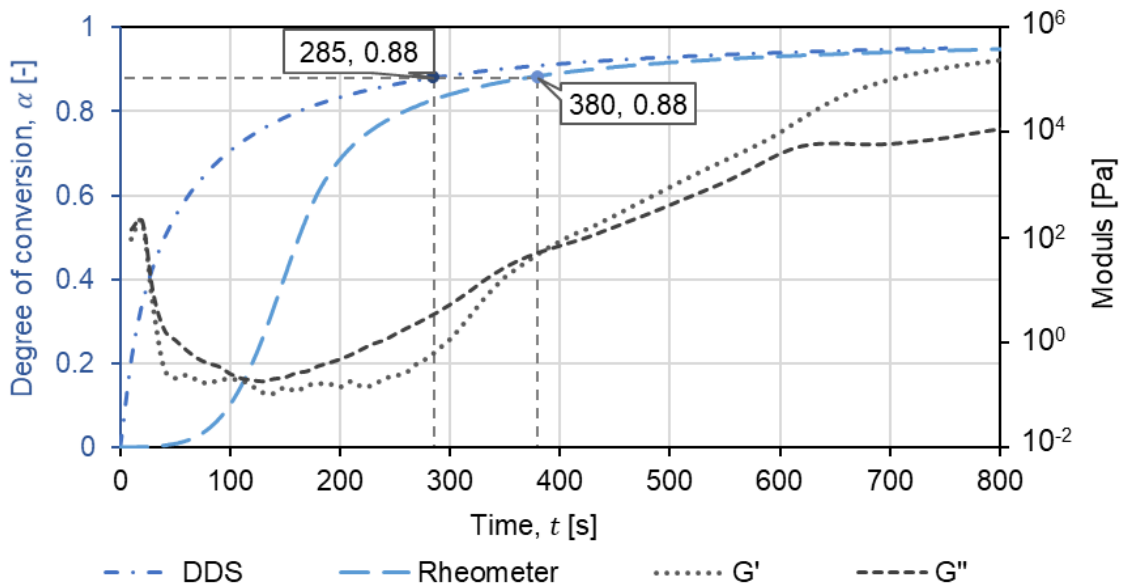


Figure 7.8: Gelation point determination for DDS measurements from the degree of conversion determined at the gel point on the rheometer (measurement temperature 140 °C).

Extrapolating the degree of conversion identified for the rheometric data to the ordinate allows identifying the time at which the resin formulation acquires an equivalent degree of conversion in the DDS measurements. As illustrated in Figure 7.8, the degree of conversion at gelation is 0.88 for the measurements carried out at 140 °C. A similar approach can be used for the other temperature variations (presented in Appendix B).

The rate of conversion of the resin formulation is observed to be slower on the rheometer compared to that on DDS. The slower conversion rate in the rheometer is attributed to the measurement procedure adopted for the viscosity measurements. During the viscosity measurements in the rheometer, the resin formulations were heated from the ambient temperature to the measurement temperature. Whereas, in DDS the windings were introduced into a preheated die. Consequently, for the above case shown in Figure 7.8 the gelation point in the rheometer is 380 s, whereas in the DDS the gelation point is reached

much ahead at 285 s. Nevertheless, the degree of conversion for both the process became equal at about 800 s.

Because the measured torque is the result of viscous drag and the frictional forces (according to Equation 4.6) exerted by the fibre-matrix on the die wall, applying the gelation point determined from the procedure described above on the torque-time curve permits to define the separation line between the viscous and frictional component in the measured torque. Figure 7.9 shows the identified viscous and frictional zones in the torque-time curve separated by the gelation line. The shaded region in the graph represents the beginning and the end of the gelation process.

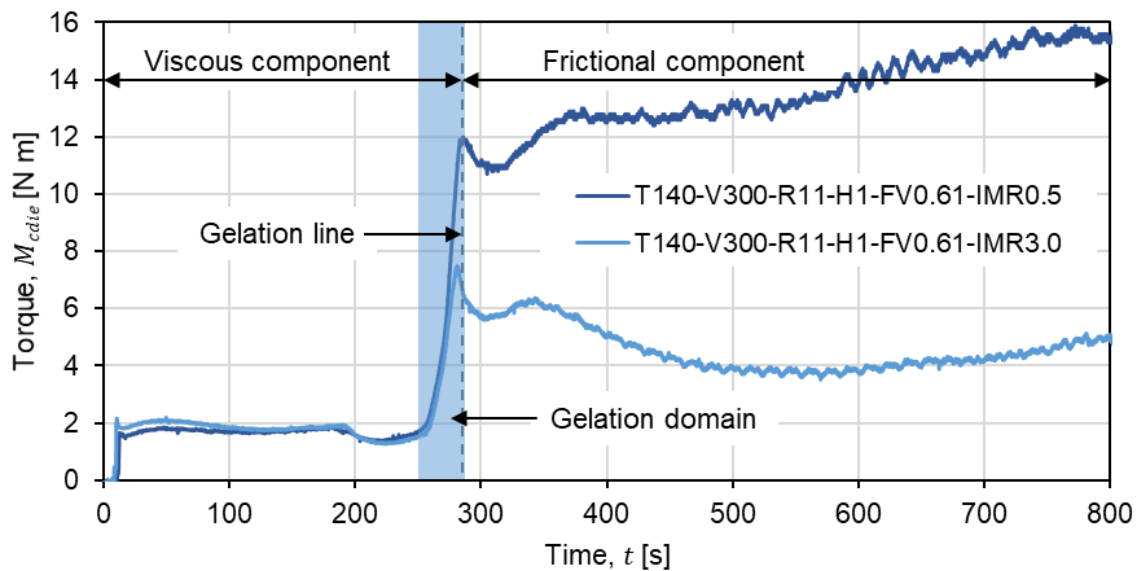


Figure 7.9: Typical viscous and frictional zones in the torque-time curve separated by the gelation line.

The determination of viscous and frictional domains in the torque-time curve allows identifying the physicochemical phenomena influencing the dynamics of the process. Using the data, it would be possible to categorise the effect of each process, geometric and material parameters on the torque evolution behaviour and hence the die dynamics.

7.4 Die dynamics model

The parametric investigations of the torque evolution behaviour in the DDS measurements allow to establish a generalised model for the torque-time relationship. Figure 7.10 illustrates the established torque-time relationship model. The torque-time curve can be split into six distinguishable zones as shown in Figure 7.10. The torque evolution behaviour in each zone is influenced by one or more parameters. The following sections describe each zone and the parameters that influence the size and shape of the torque-time curve within the respective zone.

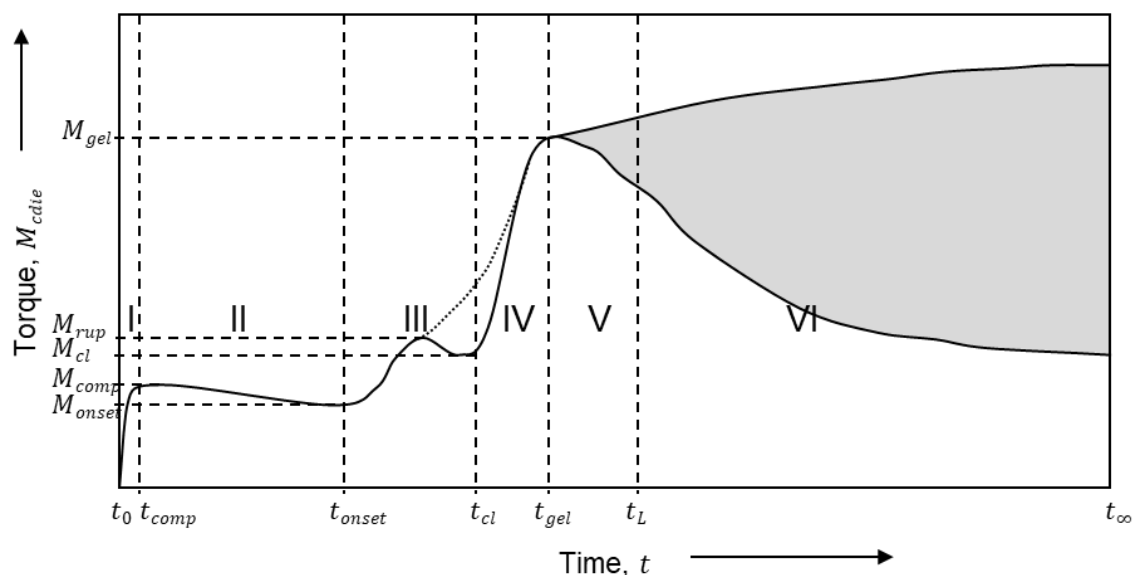


Figure 7.10: Torque-time relationship model for the tested fibre-matrix system.

Zone I

Zone I can be identified as the compaction zone. The rate of change of torque is proportional to the compaction pressure the fibre-matrix undergo. The torque in this zone is influenced by the initial viscosity of the resin formulation, fibre volume fraction and the core preparation parameters (i.e. the winding tension). Increase in the viscosity and the fibre volume fraction increases the maximum torque, whereas an increase in winding tension reduces the observed peak torque in this zone. Additionally, the geometry of the die entrance would affect the compaction and hence the torque evolution. The width of the zone, denoted by t_{comp} , is defined by the core insertion rate and the length of the core. The torque measured in this zone is, however, not influenced by the die temperature and the IMR concentration. Furthermore, the torque evolution in the following stages of the process is directly coupled to the initial compaction of the fibre-matrix. For a given fibre volume fraction, resin formulation viscosity and the die entrance geometry, F_{comp} could be calculated from the M_{comp} , provided the impact of fibre orientation on the compaction is known.

Zone II

Zone II can be identified as the viscosity reduction zone in which a negative rate of change of torque is observed. The decreasing torque is the result of temperature-induced viscosity reduction of the resin formulation. As the temperature of the fibre-matrix increases the viscosity decreases due to increased molecular mobility within the resin formulation. A decrease in the torque is observed until the ordinate value denoted by M_{onset} . Within this zone, varying the shear rate marginally affects the torque behaviour because the viscosity effect is more pronounced than the shear rate induced stress variations.

The width of the zone II depends on the conversion rate of the resin formulation which again is a function of the temperature. In other words, the higher the processing temperature or rate of conversion of the resin formulation, the lesser will be the t_{onset} .

Zone III

The gelling networks begin to cross-link thereby increasing the density and the viscosity of the resin formulation (Figure 2.9 (c)). As a result, the torque increases exponentially with time. For the resin formulations investigated in this work, the degree of conversion reaches above 0.8 at the t_{onset} . As the cross-linking density increases, the following two possible scenarios can be described in this zone:

Scenario 1: The shearing of the cross-linking networks in the fibreless resin region caused by the relative motion of the fibre-matrix to the die wall would rupture the gelled networks. The presence of sufficient IMR in between the forming networks may further positively influence this phenomenon. The torque necessary to rupture the gelling networks is denoted by M_{rup} . Consequently, the torque evolution follows the continuous line illustrated in zone III of Figure 7.10 resulting in a hump-shaped curve. Most of the torque-time curve observed in this work show such behaviour.

Scenario 2: The cross-linking density becomes much high so that the gelled matrix withstands the shearing of the networks. The concentration of IMR might also influence the stability of the gelling network as described in Section 7.2.4. In this case, the torque evolution follows the dotted line illustrated in zone III of Figure 7.10.

The results show that the concentration of IMR present on the die surface increases or the development of an IMR interphase occurs within this zone. If scenario 1 is valid, stable gelled networks begin to form only towards the end of this zone. M_{cl} and t_{cl} (here the subscript cl denotes cross-linking) denote the respective ordinate and abscissa for the end of the zone III.

Zone IV

Zone IV is where the coupling of chemo-rheological and thermo-mechanical behaviour of the gelled matrix dominates. As the gelled networks interconnect with each other, the viscosity of the resin formulation increases exponentially and in parallel, the temperature-induced volumetric expansion of the bulk fibre-matrix exerts normal pressure on the die wall. The coupled effect exponentially increases the shear stress on the die wall leading to a proportional increase in the measured torque. Additionally, if the curing matrix adheres to the die surface, the work necessary for the cohesive fracture of the resin film further increases the torque. As a result, overall maximum torque (M_{gel}) is observed in this zone. The rate of change of torque in this zone is influenced by the cross-linking rate and density, IMR concentration and the thermal expansion coefficient of the fibre-matrix.

Zone V

Zone V defines where further cross-linking of the gelled network induces shrinkage resulting in the separation of the fibre-matrix surface from the die wall reducing the measured torque. However, if the adhesion dominates the separation, a scenario illustrated in Figure 7.7 (c) becomes valid and the torque increases further due to the friction between the cured part and the die wall. Typically, zone V marks the end of a pultrusion process and therefore the width of the zone is denoted as t_L .

Zone VI

Zone VI is an extension of the zone V and is valid only for the rotating core methodology. The shaded region represents the effectiveness of the separation of the part from the die wall and hence is a measure of the effectiveness of the IMR. Depending on the effect of IMR, the torque curve follows a path within the shaded region. The top boundary represents mould sticking and fouling, whereas the bottom boundary represents an effective release of the part from the die.

7.5 Statistical analysis on process parameter interactions

The parametric investigations discussed in the previous sections permit to analyse the effect of individual parameters on the die dynamics (i.e. torque evolution behaviour). However, the interaction of the individual parameters with each other is not obvious since the experimental procedure adopted a fractional factorial experimental design. Statistical techniques, analysis of the variance (ANOVA) and the Pareto standardised effects plot, facilitate to determine the interaction and the significance of individual parameters and their effects on the torque. The features integrated with the software Minitab® 18 were used to perform statistical analysis of the experimental results.

For the statistical analysis sum of the shear stress exerted by the fibre-matrix on the die wall for a measurement period of 800 s was calculated from the measured torque using the relation

$$\tau_{r\theta,800s} = \sum_{t=0}^{t=800} \frac{M_{cdie}}{2\pi r_{Di}^2 L_a} \quad (7.1)$$

The mean shear stress calculated for the individual test set is shown in Figure 7.11.

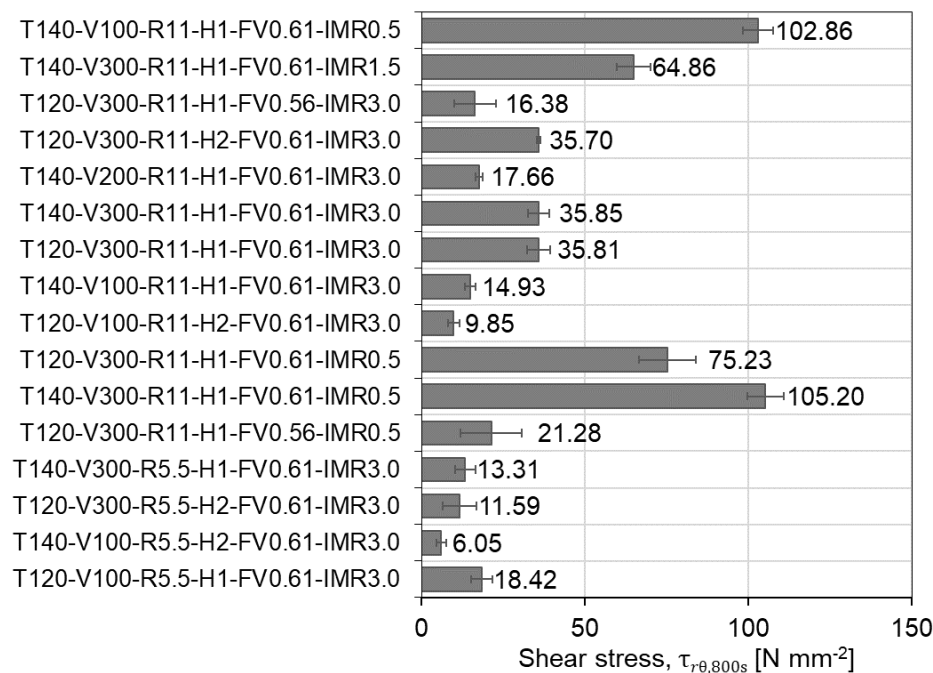


Figure 7.11: Sum of the shear stress calculated from the measured torque for a measurement period of 800 s.

The analysis of variance of the calculated shear stress determines whether at the preferred statistical confidence level (here 95 %), the individual test sets are all part of the entire test set or fall outside of the considered test sets. The procedure compares the variance between the means of the test sets and the variance within the test sets. The variance analysis further enables to plot a Pareto plot (Figure 7.12) with the standardised effects of individual parameters and their interaction on the response variable (sum of shear stress). The standardised effects are t-statistics that test the null hypothesis that there are no significant effects. The Pareto plot contains the absolute values of the standardised effects from the largest effect to the smallest effect. The chart also plots a vertical reference line, based on the selected confidence level, to indicate which effects are statistically significant. From the Pareto plot, one can determine the magnitude and the importance of the effects of the parameters on the response variable. On the Pareto plot, bars that cross the reference line are statistically significant [163].

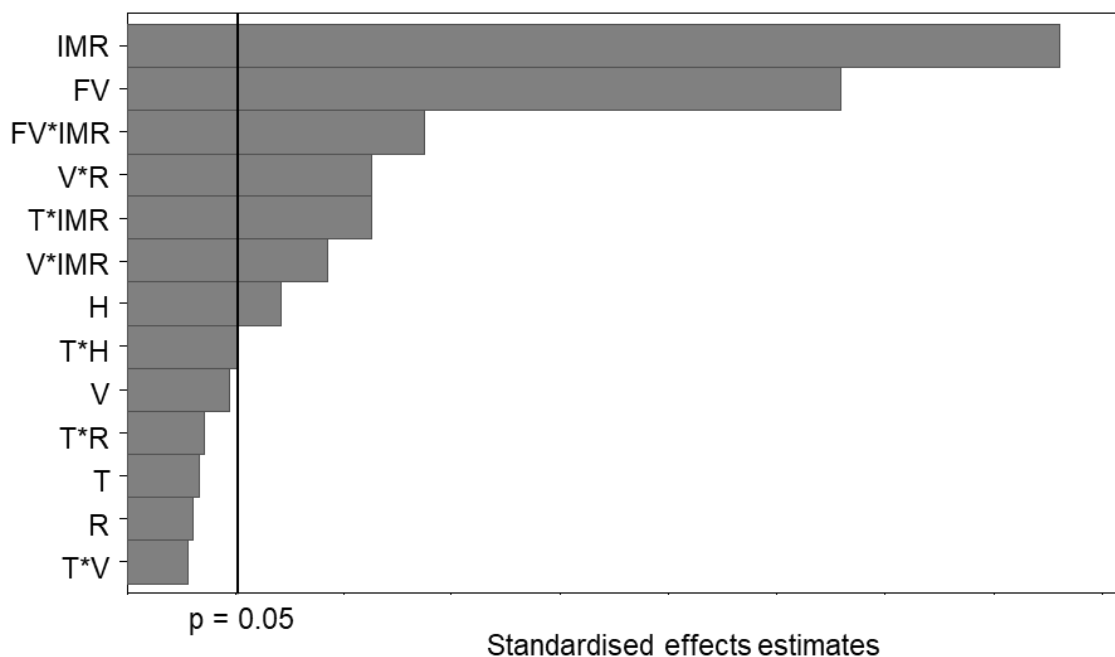


Figure 7.12: Pareto plot of the standardised effects of the parameters on the calculated shear stress.

The Pareto plot shows that the effect of parameters IMR concentration, fibre volume fraction, and winding thickness are statistically significant. The two-way interactions between fibre volume fraction and the IMR concentration, surface velocity of the fibre-matrix and IMR concentration, temperature and the IMR concentration, as well as the surface velocity of the fibre-matrix and inner radius of the die also show statistical significance. However, the parameters temperature, surface velocity of the fibre-matrix, and die inner radius alone do not show statistical significance on the calculated shear stresses. Comparing the results presented in Figure 7.11, the sum of shear stress over a measurement interval of 800 s do not vary while varying the temperature or surface velocity. Since the shear stress calculation is geometry independent, the effect of variation of the die radii neutralises. The statistical analysis makes it obvious that within the tested samples IMR concentration shows the most significant effect on the torque evolution behaviour. The fibre volume fraction plays the second most critical role.

The regression model generated from the regression analysis of the calculated shear stresses is given by

$$\begin{aligned} \tau_{r\theta,800s} = & -1081 + 4.03 T - 0.173 V + 3.56 R + 160.4 H + 1205.9 FV \\ & + 186.3 IMR - 0.00163 T * V - 0.0731 T * R - 1.323 T * H \\ & - 0.507 T * IMR + 0.03354 V * R + 0.0429 V * IMR - 253.7 FV \\ & * IMR \end{aligned} \quad (7.2)$$

Here the shear stress is a function of the tested parameters. The model has a standard deviation of 5.004 MPa from the shear stress calculated from the experimental data. The regression model facilitates to analyse the variation in the response variable (i.e. the shear stress) while varying the process, material and geometrical parameters. The centre points utilised for the analysis are T=130 °C, V=200 mm min⁻¹, R=8.5 mm, H=1.5 mm, FV=0.585, IMR=1.5 phr. Figure 7.13 shows the contour plots of the fitted mean shear stresses generated on Minitab® 18 using Equation 7.2 at various parameter combinations.

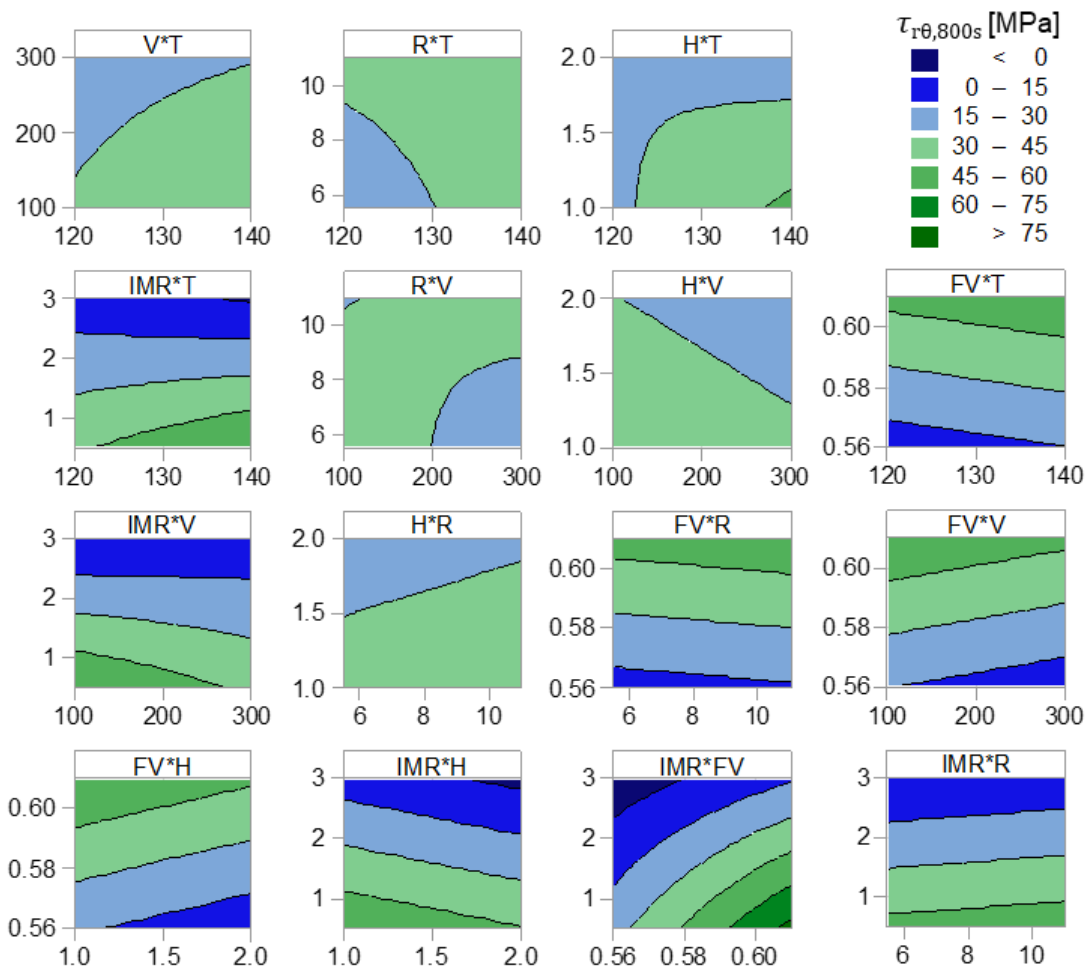


Figure 7.13: Contour plots of the shear stresses ($\tau_{r\theta,800s}$) at various parameter combinations.

(Axis to be read as: ordinate*abscissa. e.g. V*T in graph title denotes velocity in ordinate and temperature in abscissa).

The contour plots show that the calculated total shear stress linearly vary while varying fibre volume fraction in combination with sample thickness, contact area, die temperature,

and shear strain. However, the shear stress exhibits non-linear character while varying fibre volume fraction with the IMR concentration. On the other hand, varying IMR concentration with strain rate and temperature has a shifting shear stress response from non-linear at lower IMR concentrations to a linear response at higher IMR concentration in the resin formulation. The two-way interactions between contact area and the temperature, shear strain respectively and between the sample thickness and the temperature show a higher order relation with the total shear stress. The results expose the complex multi-physics nature of the process dynamics.

Nevertheless, analysing the shear stress for shorter measurement intervals may display different trends because, as described in Section 7.4 each of the parameters affects the measured torque differently at different zones of the torque-time curve. For example, until t_{gel} , IMR does not significantly influence the shear stress and hence the measured torque.

7.6 Conclusion of torque evolution behaviour investigation

The parametric study conducted on the DDS validates the possibility to utilise the rotating core method and the DDS to evaluate the die dynamics with various process, material and geometrical parameters. Further, application of statistical methods DOE and ANOVA enabled the systematic execution of the experimental procedures and the analysis of the results obtained from the experiments.

The experimental results show the dependency of the torque experienced by the DDS die on process, material and geometrical parameters. On the other hand, the torque evolution is attributed to the evolution of stresses within the fibre-matrix during the consolidation. Therefore, changing the parameters affect the stresses within the fibre-matrix and in-turn the torque evolution. Hence, the mathematical relation expressed in Equation 4.6 is validated through experimental observations. This verifies the research hypothesis 3 with respect to the rotating core method.

The curing kinetics and rheological parameter estimations enable the identification of the viscous and the frictional components of the measured torque. Furthermore, from the parametric analysis and the resin formulation characterisation, a six zonal die dynamics model is developed for the system studied. The established model, thus, can be used to experimentally quantify the forces illustrated in Figure 2.5.

The statistical analysis revealed that the presence of IMR significantly influences the measured total torque compared to the other parameters studied. Conversely, the effect of the temperature of the die and the rotational velocity of the core on the evolved total shear stress over 800 s of measurement period are statistically insignificant at 95 % confidence level. Further, the statistical regression model allows to visualise the dependency of the process dynamics on the multi-parameter interactions. Knowledge gained from the detailed parametric evaluations allows to compare and further validate the rotating core method with the pultrusion process.

8 Validation of rotating core method using pultrusion

Application of the rotating core method for the quantification of the pultrusion die dynamics necessitates validation of the results obtained from the DDS measurements against the pultrusion measurements. Further, mapping the die dynamics, measured as torque evolution on the DDS, to the pultrusion die dynamics involves the transformation of the rotational system back into the linear system. This chapter, therefore, describes the pultrusion experiments carried out to determine the pulling force that arises while pultruding glass fibre rovings with the resin formulations described in Chapter 5. Comparison of the results obtained from both the systems facilitates to verify the proposed empirical pulling force-torque evolution model.

8.1 Bench-scale pultrusion

The experiments utilised a custom-built lab-scale pultrusion line for the measurement of pulling forces. Figure 8.1 shows the core components of the lab-scale pultrusion line: the heating platens and a pultrusion die mounted on a sliding rail; a force transducer; and a line speed tachometer. Apart from the core components shown, the line is equipped with a fibre creel, a resin bath, roving guides and a cleat type tractor puller similar to the schematic shown in Figure 2.1.

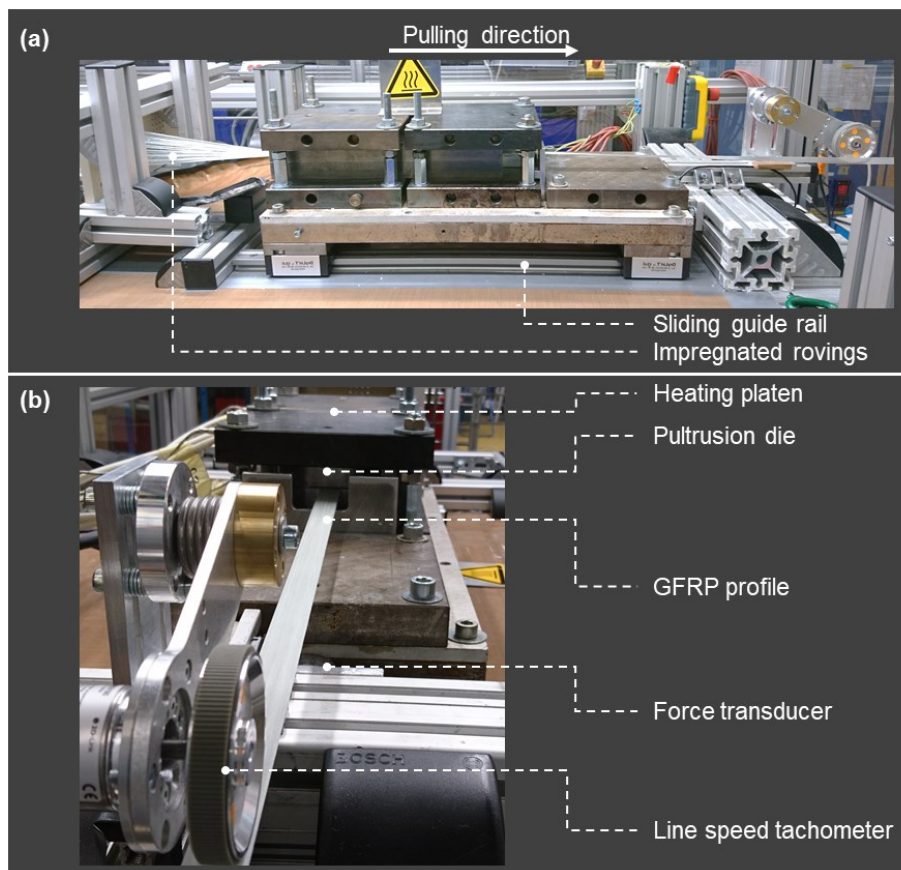


Figure 8.1: Core components of the bench-scale pultrusion line – (a) side view and (b) front view.

The heating platens and the die assembly were mounted on the sliding linear guide rails separated by an isolation plate with a metal base. The sliding guide rails were fixed on to a height-adjustable table that enables to match the height of the centre-plane of the die to the plane of the tractor puller. A force transducer with a rated maximum force of 50 kN (from Hottinger Baldwin Messtechnik GmbH, Darmstadt, Germany) was mounted to the table in such a way that the metal base of the isolation plate compresses the transducer during pultrusion as the whole assembly slides freely on the sliding rails. The force data acquisition was realised by connecting the force transducer to a USB-6008 through a signal amplifier MVD2510 (from Hottinger Baldwin Messtechnik GmbH). The acquired data was recorded on a personal computer using a user interface programmed on *Visual Basic .NET*. The temperature of the heating platens was controlled by the PID temperature control modules with real-time temperature feedback from Type J thermocouples integrated into the heating platens.

Considering the limitation of the resources, a suitable pultrusion die that was already available at DITF Denkendorf was utilised for the pultrusion experiments. Figure 8.2 shows the schematic of the cross-section and the dimensions of the pultrusion die used in this work. The die has a length of 350 mm and a cavity cross-sectional area of 20 x 0.5 mm². The surface roughness of the die cavity varied between $R_a = 0.99 \mu\text{m}$ to $1.19 \mu\text{m}$ along its length. The selected die also has a comparable profile geometry adopted in DDS. Further, because of its thin cross-section the effect of temperature gradient across the cross-section of the fibre-matrix would be minimised. During the experiments, the die was mounted between the top and bottom heating platens as shown in Figure 8.2. The top and bottom heating platens clamped the die in place during the pultrusion.

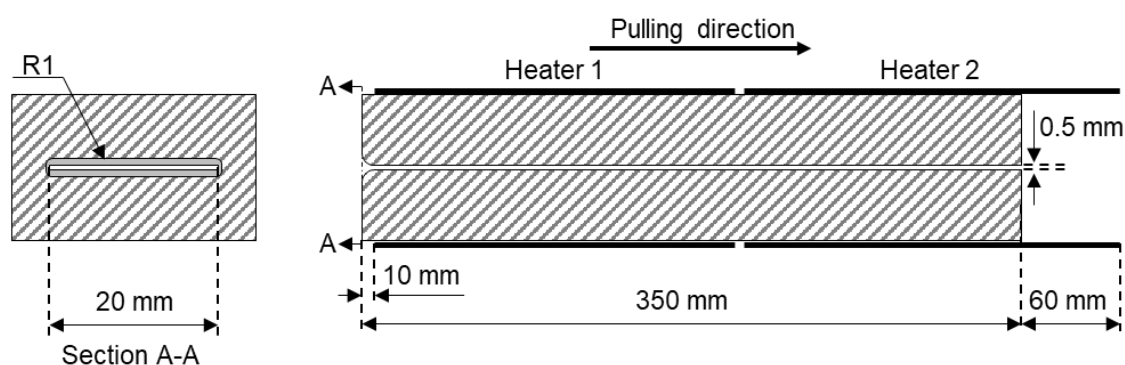


Figure 8.2: Schematic of the cross-section and the dimensions of the pultrusion die used for the pultrusion experiments.

8.1.1 Fibre volume fraction

The number of glass fibre rovings (listed in Table 5.2) required for the pultrusion experiments were determined based on the required fibre volume fraction. The relation between the cross-section area of the die cavity and the idealised cross-section area of the rovings permits to determine the number of rovings required for a specified fibre volume fraction and is mathematically expressed as

$$\varphi_f = \frac{A_{roving}}{A_{die}} = \frac{1}{A_{die}} \frac{n_r T_{tex}}{\rho_f \cdot 10^6} \quad (8.1)$$

where φ_f is the fibre volume fraction in the pultrusion die; A_{die} the cross-sectional area of the pultrusion die in mm^2 ; n_r , the number of rovings required for the specified fibre volume fraction.

From the above relations using 24 rovings will result in 0.56 fibre volume fraction and 26 rovings will result in 0.61 fibre volume fraction. During the experiments, it was not possible to achieve fibre volume fractions beyond 0.61. This is because adding even one more roving (i.e. $\varphi_f = 0.64$ with 27 rovings) resulted in enormous pulling force and consequently fibre bundles ruptured. Although higher fibre volume fractions are typical for the round cross-sectional and thicker profiles, the thin geometry of the cavity used in this work does not allow increasing the fibre volume fraction beyond 0.61.

8.1.2 Temperature profile measurement

The temperature profile inside (T_{pdie}) the die cavity during the pultrusion of the fibre-matrix is one of the important data that facilitate the determination of the temperature-dependent degree of conversion of resin formulation within the die. The temperature measurement was realised by employing a thin thermocouple wire of 0.4 mm diameter. The thermocouple, which was 10 m long, was pulled in parallel to the rovings into the die during the pultrusion experiments. One end of the wire acted as a thermocouple, whereas the other end was connected to the data acquisition device ALMEMO® 2890-9 using the connectors ALMEMO® ZA 9020-FS. Figure 8.3 shows the temperature profile measured in-line during the pultrusion experiments at the desired temperatures and line speeds. The residence time (Δt) of the fibre-matrix depicted on the figure illustrates time for which the thermocouple remained in the die.

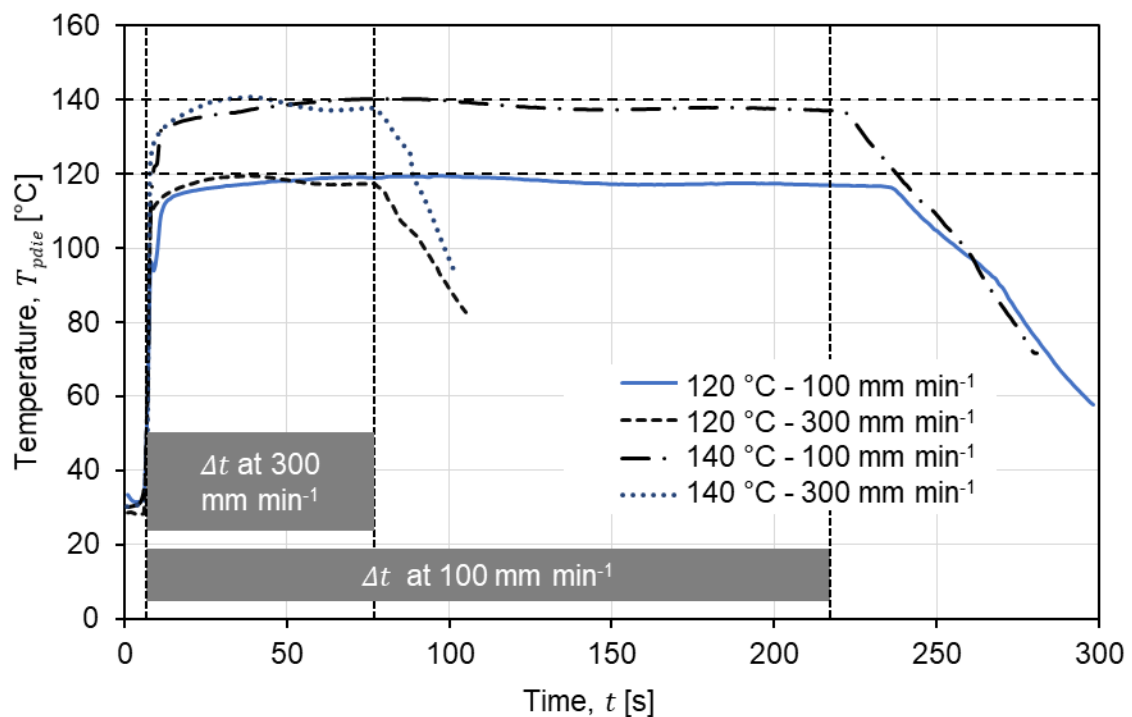


Figure 8.3: Temperature profile measured in-line during the pultrusion experiments at 120 °C and 140 °C at the pulling velocities 100 mm min^{-1} and 300 mm min^{-1} respectively.

The temperature of the fibre-matrix increases exponentially as they enter the pre-heated die. Within the die, the measured temperature profile shows a hump beyond which the temperature remains almost constant until the profile exits the die. The hump-like appearance in the temperature curve could be because of the minor temperature differences between the front and the rear heating platens. The temperature of the profile decreases rapidly as it exits the die. The rate of decrease in temperature after the die exit is observed to be higher in the experiments conducted at 140 °C because of the temperature difference between the pultruded profile exiting the die and the ambient temperature. Applying the measured temperature profile to the curing kinetics model allows the calculation of the degree of conversion of the resin formulation within the pultrusion die.

8.1.3 Pulling force measurement

The pulling forces were measured during the pultrusion experiments conducted on the lab-scale pultrusion line. The process and material parameters were varied in the trial space listed in Table 7.1. The fixed die geometry limited the change in the geometrical parameters for the pultrusion experiments. Experiments conducted with further variations in geometrical parameters on the pultrusion line would have amplified the validity of rotational core method for the quantification of die dynamics rather than increasing further insights into the model. Nevertheless, the results obtained from the pultrusion experiments within the trial space permits to compare and establish a relationship between the rotational core method and the pultrusion.

The pultrusion experiments were carried out uninterruptedly beginning with a lower concentration of IMR (i.e 0.5 phr) in the resin formulation and subsequently increasing the IMR concentration, unless a die seizure occurred in between. The procedure allows to minimise the error in the measured forces caused by the presence of IMR residue on the surface of the die from the previous experiments. For every change in the parameter, die purging was adopted to clean the residues present inside the die cavity. Nevertheless, in case of die seizure, the die was opened and cleaned, and the further experiments began again from the preparation procedures (i.e. redrawing rovings into the die and reheating).

Figure 8.4 shows the characteristic pulling forces recorded during the pultrusion experiments (more results are shown in Appendix C). The experimental datasets follow the same nomenclature listed in Table 7.2 excluding the radius and the thickness parameters. The irregular waviness observed on the pulling force curve is because of the stick-slip phenomena of the fibre-matrix within the die and is typical for a pultrusion process [57]. Apart from the waviness, the pulling force remains constant throughout the experiment within the selected set of parameters. Accumulation of powdery substance at the die exit and on the pultruded profile surface was observed with the experiments conducted using the resin formulation containing 0.5 phr IMR concentration. This could be because of the pilling caused by the adhesion of the resin to the die surface at a low concentration of IMR. The effect is similar to that observed during the DDS experiments described in Section 7.2.4. The effect is more pronounced with the profiles which had 0.56 fibre volume fraction. Increased resin film thickness (λ) at lower fibre volume fraction would have increased the pilling effect. However, at IMR concentration of 3.0 phr, the generation of powdery substance diminished.

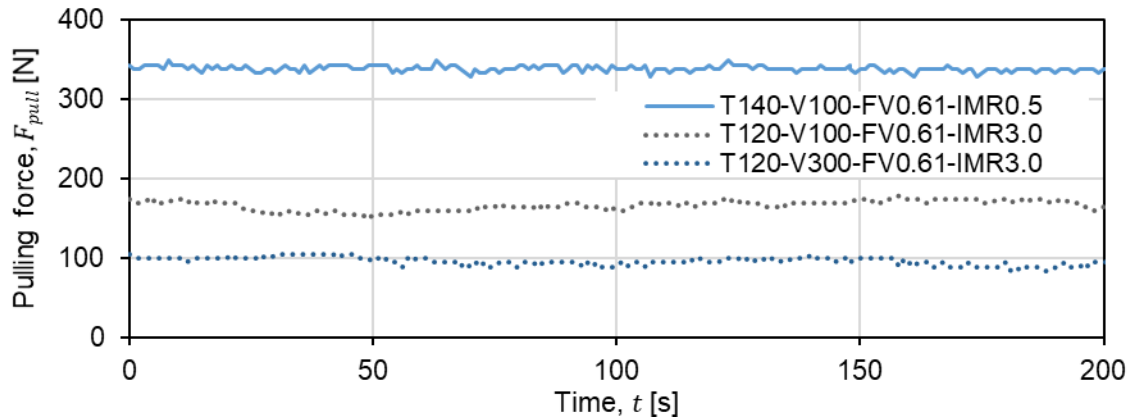


Figure 8.4: Characteristic pulling force measured in-line during the pultrusion with the varying process and material parameters

Figure 8.5 shows the mean pulling force measured during the pultrusion experiments for all datasets. Inference from the average pulling force reveals the following trend:

- Increasing die temperature increases the total pulling force.
- Increasing line speed decreases the total pulling force.
- Increasing fibre volume fraction increases the total pulling force.
- Decreasing IMR concentration in the resin formulation increases the pulling force.

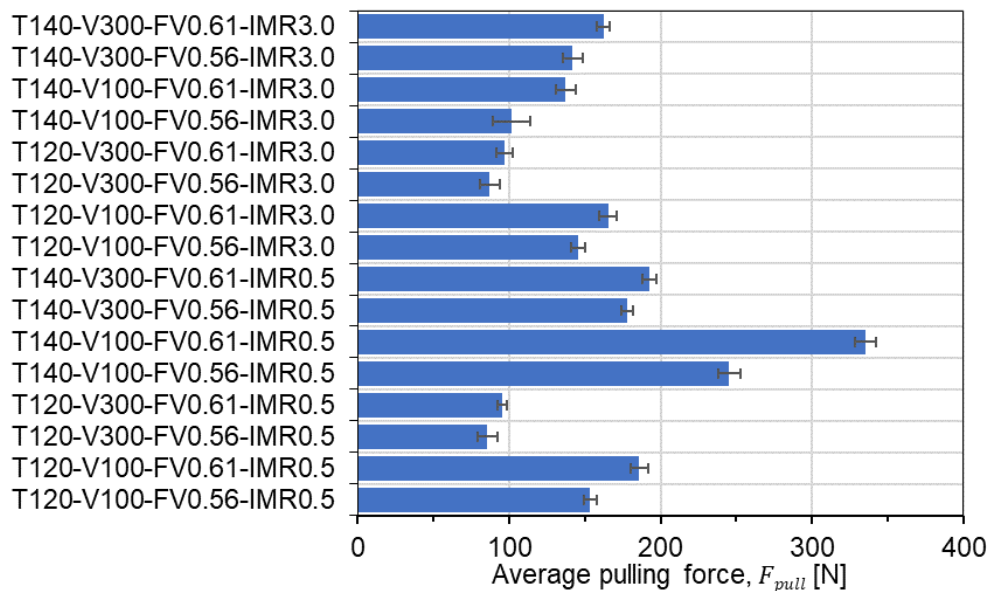


Figure 8.5: Average pulling force measured during the pultrusion experiments with the varying process and material parameters.

The observed trends while varying the process parameters (temperature and line speed) is linked to the degree of conversion of the resin formulation within the die cavity. Increasing the die temperature accelerates the rate of conversion of the resin formulation resulting in achieving a higher degree of conversion within the die cavity at given residence time. However, increasing the line speed have a converse effect since the residence time of the fibre-matrix within the die cavity reduces upon increasing the line speed. As a result, less conversion is achieved within the die cavity. During the experiments, only the sample

sets pultruded at 140 °C die temperature and 100 mm min⁻¹ line speed exited the die in a solid state. All the other samples were sticky and got squeezed between the cleats in the tractor puller leaving the impressions of the cleats on the profile.

The trends observed with the pulling force while varying the material parameters (i.e. fibre volume fraction and the IMR concentration) must be understood in combination with the process parameters. Increasing the IMR concentration decreases the pulling force. However, this is true only if the resin formulation undergoes gelation within the die cavity. If the residence time is not long enough for the resin formulation to undergo gelation, the effect of IMR is not pronounced. Nevertheless, the effect of fibre volume fraction is independent of process parameters at short residence times at which the resin formulation remains viscous. In other cases, increasing the fibre volume fraction increases the pulling force because of increase in normal pressure on the die wall.

8.2 Comparison and validation of the pulling force models

The torque measured on the DDS must be expressed as force to compare and map the results from the rotating core method and the pultrusion process. Since the DDS measurements, unlike pultrusion, do not depend on the length of the die, the measurements can be carried out for an infinite time. Additionally, the thermal history of the material in the DDS measurements and the pultrusion measurements are not similar. This posed a challenge while selecting the data range (i.e. time limits) from the DDS measurements that equates to the data from the pultrusion process. Nevertheless, the degree of conversion determined for both the process would serve as a common factor based on which the data range from DDS could be selected for the comparison. The curing kinetics of the resin formulation permits to calculate, like that for the DDS measurements described in Section 7.3., the degree of conversion that resin formulations have undergone within the pultrusion die. Figure 8.6 shows the calculated degrees of conversion achieved for a 210 s residence time of the fibre-matrix in the pultrusion die and the time required (t_{calc}) for the equivalent degree of conversion on the DDS. Similarly, the time required to achieve degrees of conversion with other residence times can be determined.

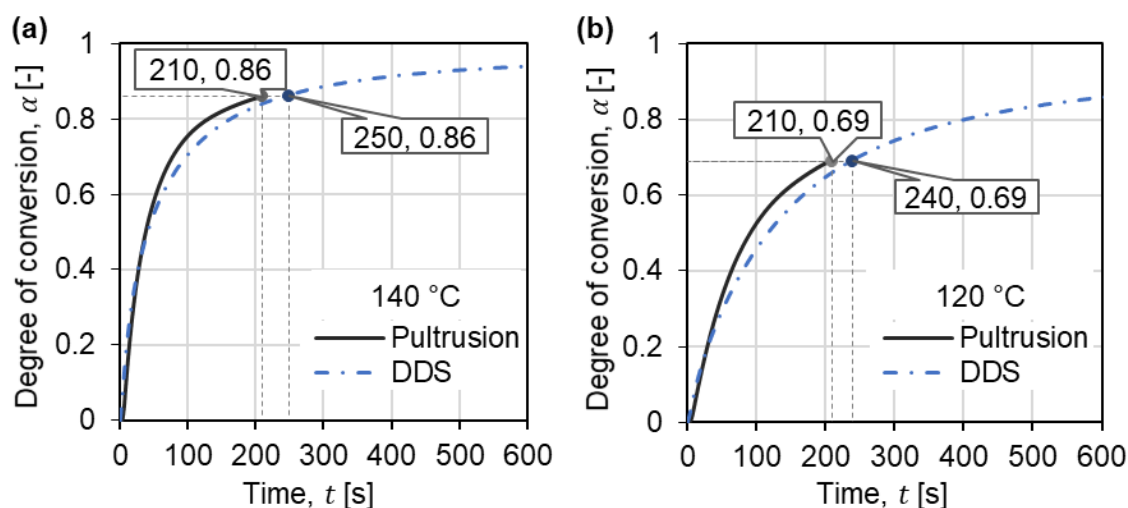


Figure 8.6: Calculated degrees of conversion for a residence time of 210 s in the pultrusion die and the respective time required for the equivalent degree of conversion on DDS at die temperatures of – (a) 140 °C and (b) 120 °C.

Applying the identified time limits from the above procedure to Equation 4.10 facilitates to calculate the total force exerted by the fibre-matrix on the die wall in DDS. Further, from Equation 4.11, the force exerted for a surface area of the DDS die equivalent to that of pultrusion die can be calculated. Figure 8.7 shows a typical lower and upper limit in the torque-time curve considered for the calculation of the force equivalence between the DDS measurements and the pultrusion experiments.

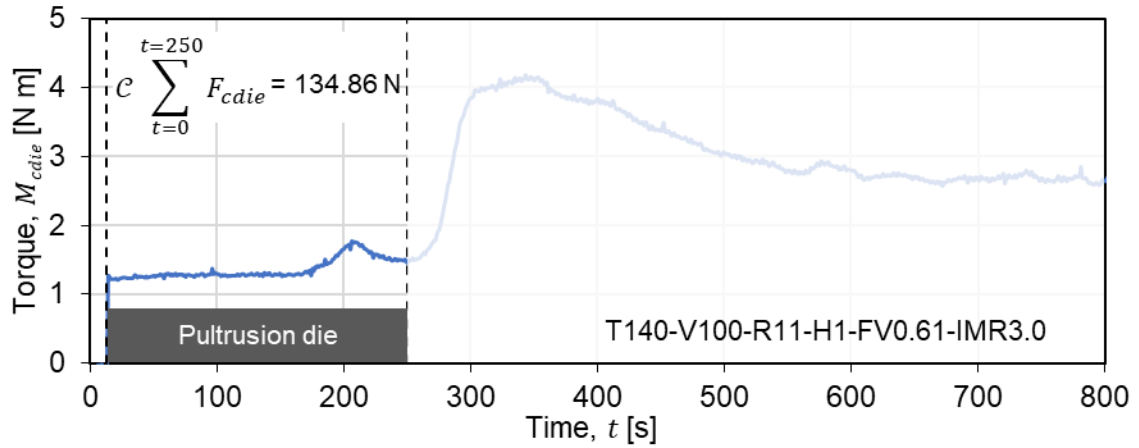


Figure 8.7: Typical lower and upper limits of the torque-time curve considered for the calculation of the force equivalence between DDS and pultrusion.

Table 8.1 lists the measured forces from the pultrusion and the DDS experiments. The data used for the calculations, for the case of DDS, are from the experiments that used the annular gap of 1 mm (i.e. H1 samples).

Table 8.1: Comparison of measured forces from pultrusion and DDS measurements.

Sample set	Pultrusion				DDS			Mean deviation [%]
	Residence time Δt [s]	Degree of cure α [-]	Mean pulling force F_{pull} [N]	Std. Dev [N]	Time t_{calc} [s]	Measured mean force F_{die} [N]	Std. Dev [N]	
	T140-V300-FV0.61-IMR3.0	70	0.67	162.21	4.27	88	158.15	
T140-V300-FV0.61-IMR0.5	70	0.67	192.59	4.72	88	194.94	6.58	1.22
T140-V100-FV0.61-IMR3.0	210	0.86	137.38	6.52	250	134.86	4.04	-1.83
T140-V100-FV0.61-IMR0.5	210	0.86	335.5	7.09	250	318.12	7.04	-5.89
T120-V100-FV0.61-IMR3.0	210	0.69	165.23	5.99	240	152.19	18.45	-7.89
T120-V300-FV0.61-IMR3.0	70	0.42	97.08	5.28	89	94.18	4.72	-2.99
T120-V300-FV0.61-IMR0.5	70	0.42	95.49	2.99	89	86.33	5.56	-9.16
T120-V300-FV0.56-IMR0.5	70	0.42	85.47	7.97	89	52.7	18.4	-38.34
T120-V300-FV0.56-IMR3.0	70	0.42	87.11	6.59	89	39.67	14.29	-54.46

However, the sample sets T120-V300-FV0.56-IMR0.5 and T120-V300-FV0.56-IMR3.0 show significant deviation in the calculated forces. The sample sets containing a fibre volume fraction of 0.56 show large deviations in the calculated forces. The reason for significantly lesser forces measured on DDS is attributed to the diameter of the fibre-matrix windings that were used for the measurements. As discussed in Section 7.2.3, the smaller diameter windings resulted in significantly lower compaction forces during the core insertion phase. Additionally, the thicker fibreless resin layer of the samples reduces the viscous drag further (Figure 5.20 (c)).

On the other hand, the lower fibre volume fraction in the pultrusion process does not affect the pulling force because of the higher entropy of the fibres. Unlike in the windings used for DDS, in the pultrusion process, the fibres are not constrained and therefore are equally distributed across the cross-section of the die cavity. The distribution of fibres across the cross-section of the die cavity increases the probability that the fibres encounter the die wall. Consequently, the fibreless resin layer thickness in the pultrusion process is less compared to that of the DDS sample. The scanning electron micrographs of the cross-section of the pultruded profiles shown in Figure 8.8 (a) and (b) confirms the fibre distribution within the profile.

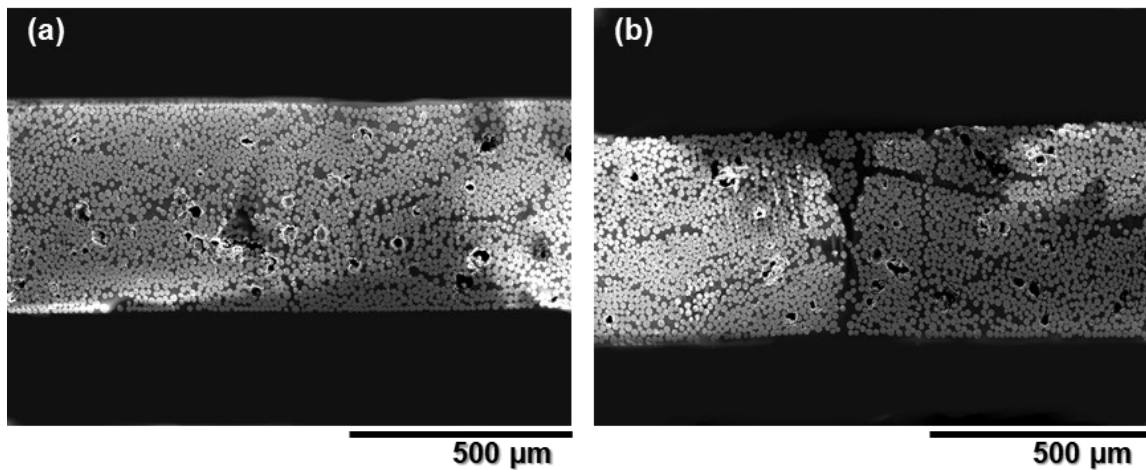


Figure 8.8: Scanning electron micrographs of the cross-section of the pultruded profiles with fibre volume fraction (a) $\varphi_f = 0.61$ and (b) $\varphi_f = 0.56$.

The calculated forces from the DDS measurements show that the developed rotating core method well represents the pultrusion process. Albeit, the pulling force model, given by Equation 4.1, does not include the compaction pressure (which is M_{comp} in terms of torque) experienced by the fibre-matrix in entry segment of the die, the experimental results show that the inclusion of compaction pressure is necessary to calculate the force equivalence between the processes. This is because the compaction force acts as the baseline force to which the subsequent temperature-induced viscous and frictional forces sums upon. Nevertheless, one can calculate the individual components of the forces by identifying the required time limits.

Further, the experimental results show that the measurement of compaction of fibre-matrix in the rounded/tapered entry segment of the die and the friction caused by the fibres that encounter the die wall further distinguishes rotating core method to quantify die dynamics from the standard coaxial rotating viscometers.

8.3 Conclusion of rotating core method validation

Pultrusion experiments carried out to measure pulling forces using a similar process and material parameters that are used in DDS measurements, facilitate the validation of the rotating core method. The parameter variations show a similar trend in the pulling forces observed with the DDS samples. Inferences show that the presence of release agent in the resin formulation decrease the pulling force. However, due to the length limitation of the pultrusion die, contribution of frictional forces to the pulling forces could not be observed. Nevertheless, the curing kinetic parameters facilitate the determination of the degrees of conversion that the resin formulations have undergone at various processing conditions in both the pultrusion and DDS.

Comparing the forces measured using the DDS, for the same degrees of monomer conversion, the samples with higher fibre volume fraction show a good correlation with that of the pultrusion. The observed pulling force results verify the research hypothesis 4. In particular, the stresses exerted by the fibre-matrix on the die wall in both pultrusion and rotating core processes are identical for higher fibre volume fraction tested within the scope of this work. However, the research hypothesis 1 which states the identical phenomena in both the process does not hold true at lower fibre volume fractions in the DDS. Additional experiments with varying roving tension during the core winding for the DDS experiments with lower fibre volume fractions would be necessary to fully verify the hypothesis 4.

9 Summary and future scope

The main concluding remarks extracted from the current work are summarised in this chapter. Additionally, recommendations for future work are suggested.

9.1 Summary

The literature review conducted on the pultrusion process and its modelling show that there has been always an immense interest in understanding the pultrusion die dynamics and its impact on the characteristics of the pultruded profile. Analysis of the pulling force remains one of the core subjects in evaluating the die dynamics. The contributions of multiple physical characteristics of the resistive forces to the total pulling forces were identified and the respective mathematical models were proposed. Nevertheless, the experimental validation of the models remained a challenge because of the continuous, stochastic and multi-physical nature of the pultrusion process. This work, therefore, devised a novel offline rotating core method to continuously measure the resistive forces that arise because of the changes in the thermo-chemical stresses within the moving fibre-matrix during their consolidation within a pultrusion die.

The transformation of the linear flow of the material in the pultrusion process to a rotational motion allow to continuously measure the resistive forces in terms of torque. Conserving the transport phenomena of the pultrusion process in the rotating core method permits to develop a system analogous to the process. The newly developed rotating core method and the model verifies the time dependent stress evolution within the pultrusion die. The design and development of the DDS facilitated to realise the experimental evaluation of the resistive forces in terms of torque. Design strategies such as the selection of die-core geometry, sealed annular volume, and integration of thermocouple have been adopted for the fabrication of the DDS. The design strategies enable the pragmatic simulation of the process occurring within the pultrusion die on the DDS.

The newly developed rotating core method necessitates the identification and definition of the limiting variables that could be used to evaluate the die dynamics. The operating procedures have been established which involves the preparation of the fibre-matrix core by filament winding and measuring the torque using the prepared core on the DDS. The influence of the preparatory process parameters, in particular the winding tension, on the torque evolution behaviour has been analysed. It is found that the winding tension and the fibre volume fraction influence the fibre orientation in the fibre-matrix winding during the torque measurement. Winding tension of about 1.8 N for a fibre volume fraction of 0.61 results in fibre orientation that are suitable for the measurement of die dynamics on DDS. The analysis of through-thickness flow on the resin formulation into the wound layers suggests that there is a backflow of resin in the initial compaction phase during the introduction of the core into the die. The effect, however, fades in the later stage of the measurement process. This correlates well with the pultrusion process, as reported in literature. Further, microscopic analysis of the cross-sections of the consolidated windings enable the determination of the fibreless resin layer thickness. It is found that there exists a fibreless resin layer between the die wall and the moving fibre-matrix. However, the thickness of the resin layer varies along the length of the composite with very high standard

deviations (i.e. $7.147 \pm 4.382 \mu\text{m}$) suggesting such deviations must be considered in the mathematical models with an error factor.

The characterisation of the resin formulations for their curing kinetics, rheological behaviour and the surface free energies facilitate the evaluation of the torque evolution behaviour. In particular, the effect of presence of IMR and its concentration on the die dynamics could be evaluated based on the analytical characterisation results. The determined curing kinetic parameters and the rheological behaviour show that the resin formulation used in this work reach gelation at a monomer degree of conversion of about 0.86. However, the degree of conversion at gelation also depends on the processing temperature. Further, the surface energy analysis at various temperatures show the dependency of the work of adhesion of the resin formulations on the processing temperature. The work of adhesion increases with the temperature which however depends on the concentration of the IMR present in the resin formulation. IMR concentration of 3.0 phr in the resin formulation reduces the surface tension by about 21 % compared to the resin formulation without IMR.

Further, parametric investigations conducted analyse the effect of the process, material and geometrical parameters on the die dynamics (i.e. in terms of torque evaluation behaviour). Statistical tools facilitated the experimental design. The key conclusions of the parametric evaluations show that the resistive force evolution depends on all the parameters studied: processing temperature, shear strain, fibre volume fraction, presence of IMR and its concentration, the surface contact area of the fibre-matrix with the die and the thickness of the fibre-matrix. Based on the results of the parametric analysis, a process dynamics model is developed. The model identified six zones in the torque-time curve, which are influenced by the individual parameters described above or the interactions between them. Statistical analysis of the results shows that the presence of IMR has a dominating effect on the total shear stress calculated from the measured torque. The regression model generated using statistical analysis reveal the relationship between the evolving stresses and the interaction between the parameters studied. Further, from the determined curing kinetic parameters and the rheological measurements of the resin formulations, the viscous and the frictional components of the measured torque could be determined using the gelation time.

The results of the rotating core method are validated using the pultrusion experiments. Pulling forces were measured while pultruding a rectangular GFRP profile using the same materials used for the DDS measurements on a lab-scale pultrusion line. The results show that the pulling force is proportional to the die temperature and the fibre volume fraction and inversely proportional to the pulling velocity and the IMR concentration in the resin formulation. The temperature profile measurements in the pultrusion experiments allow the determination of the degree of cure that the fibre-matrix undergo within pultrusion die. Using the temperature-dependent degree of cure as a common parameter, the forces measured for the respective degrees of conversion in the pultrusion process and DDS experiments are compared to validate the pulling force model of the rotating core method. The results show that the pulling forces derived from the torque measurements on the DDS are comparable with that measured on the pultrusion line. The deviations between the pulling forces of the two systems are statistically insignificant (at 95 % statistical confidence level) for higher fibre volume fractions. However, for fibre volume fractions of

0.56, the force measured on the DDS deviated more than 38 % than that of forces measured on the pultrusion line. The deviations could be attributed to the smaller diameters of the windings (Section 5.2.2) caused by the higher winding tension and the hence resulted compaction of the fibre-matrix in the DDS die.

9.2 Future scope

The research findings presented in this work show that the novel rotating core method approach for the quantification of the pultrusion die dynamics is comprehensive and that further enhancements may be implemented over it. Several identified scopes for improvement are described in the following.

The effect of roving winding tension on the torque evolution behaviour and hence the die dynamics could be further investigated. Especially at low fibre volume fractions the forces measured on DDS show high deviations compared to that of the pultrusion. Low winding tension (i.e. less than 1.8 N) may produce relatively bulky fibre-matrix windings and hence would minimise the observed deviation. This would allow on the one hand to extend the applicability of the DDS for low fibre volume fractions and on the other hand to identify the limitations of the rotating core method with respect to the fibre volume fraction.

Further, the effect of surface properties (for example, surface roughness and surface chemistry) of the DDS die on the torque evolution behaviour could be investigated. This would improve the precision of the rotating core method and hence the predicted die dynamics. In addition, it would enhance the expediencies of the rotating core method particularly to understand the interaction of different resin formulations with different die surfaces.

The effect of thermal expansion of the core on the torque evolution behaviour was assumed to be negligible in this work. Investigations to quantify the effect of core's thermal expansion on the torque evolution behaviour would enhance the accuracy of the developed model. Alternatively, utilisation of a thermally isolated core may be considered.

Furthermore, integration of pressure sensors in the DDS die would allow to quantify the pressure changes that occur during polymerisation and hence their contribution to the forces at different phases of the matrix. Integration of thermocouples and dielectric sensors in the fibre-matrix windings to monitor the degree of cure online during polymerisation would abridge the necessity for offline DSC measurements.

Within the scope of this work, the forces measured through DDS experiments are validated against that of the pultrusion experiments. However, the validation are performed only for the degree of conversion (up to a maximum of 0.86) of the resin formulations. Further experiments, for example using a longer pultrusion die or at lower pulling speeds, compared to the one utilised in this work, would result in higher degree of conversion within the die. On the other hand, to perform experiments with equivalent low surface speeds on the DDS, the electric drive of the DDS has to be replaced (possibly with a synchronous motor). This is because the present drive possesses limitation to rotate at low speeds at high torques.

This work focused on investigating the isothermal pultrusion process dynamics using the novel rotating core method. Nevertheless, the rotating core method could be further

extended to investigate non-isothermal pultrusion processes through modification of the energy supply and control systems of the DDS. For example, by utilising induction-based heating systems or alternative energy sources like microwave or ultraviolet radiations. The modification may also allow to study thermoplastic matrix materials.

Furthermore, investigations on the effect of fibre type (for example, carbon fibres) or fibre architecture (for example, the surface veils and woven fabrics) on the die dynamics are envisaged as the continuation of this work.

Bibliography

- [1] L. Hollaway, *Polymer composites for civil and structural engineering*, Springer Science & Business Media, Dordrecht, 2012.
- [2] T. Starr, *Pultrusion for engineers*, Woodhead Publishing Ltd, Cambridge, 2000.
- [3] Lucintel LLC, *Pultrusion Market Report: Trends, Forecast and Competitive Analysis*, (2019). <https://www.lucintel.com/pultrusion-markets.aspx> (accessed September 6, 2019).
- [4] 5M s.r.o, *Composite pultruded profiles*, (2020). <https://www.5m.cz/en/products/kompozitni-profil> (accessed November 30, 2020).
- [5] Röchling SE & Co. KG, *Röchling SE & Co. KG*, (2020). <https://www.roechling-industrial.com/industries/renewable-energies/wind-energy/materials-for-wind-turbine-blades/spar-caps-for-wind-turbines> (accessed November 30, 2020).
- [6] R. Gorthala, J. Roux, J. Vaughan, Resin flow, cure and heat transfer analysis for pultrusion process, *J. Compos. Mater.* 28 (1994) 486. <https://doi.org/10.1177/002199839402800601>.
- [7] J.E. Sumerak, J.D. Martin, Pulse of pultrusion: Pull force trending for quality and productivity management, *Polym. Polym. Compos.* 1 (1993) 199A-210A.
- [8] J. Ramôa Correia, Pultrusion of advanced fibre-reinforced polymer (FRP) composites, in: *Adv. Fibre-Reinforced Polym. Compos. Struct. Appl.*, Woodhead Publishing Ltd, Cambridge, 2013: pp. 207–251. <https://doi.org/10.1533/9780857098641.2.207>.
- [9] S. Epple, C. Bonten, Production of continuous fiber thermoplastic composites by in-situ pultrusion, in: *AIP Conf. Proc.*, American Institute of Physics Inc., 2014: pp. 454–457. <https://doi.org/10.1063/1.4873820>.
- [10] A. Luisier, P.-E. Bourban, J.-A.E. Månson, Reaction injection pultrusion of PA12 composites: process and modelling, *Compos. Part A Appl. Sci. Manuf.* 34 (2003) 583–595. [https://doi.org/10.1016/S1359-835X\(03\)00101-5](https://doi.org/10.1016/S1359-835X(03)00101-5).
- [11] K. Chen, M. Jia, H. Sun, P. Xue, Thermoplastic Reaction Injection Pultrusion for Continuous Glass Fiber-Reinforced Polyamide-6 Composites, *Materials (Basel)*. 12 (2019) 463. <https://doi.org/10.3390/ma12030463>.
- [12] A. Zoller, P. Escalé, P. Gérard, Pultrusion of Bendable Continuous Fibers Reinforced Composites With Reactive Acrylic Thermoplastic ELIUM® Resin, *Front. Mater.* 6 (2019) 290. <https://doi.org/10.3389/fmats.2019.00290>.
- [13] A. Brack, H. Janssen, C. Brecher, Manufacturing of Miniaturized Thermoplastic FRP Components Using a Novel Reaction Injection Pultrusion Process, in: *SAMPE Seattle 2017*, Seattle, 2017.
- [14] A. Brack, *Kontinuierliche Herstellung von miniaturisierten Endlosprofilen aus thermoplastischen Faserverbundkunststoffen*, RWTH Aachen, 2018. <https://doi.org/10.18154/RWTH-2019-01520>.
- [15] D.H. Kim, W. Il Lee, K. Friedrich, A model for a thermoplastic pultrusion process

- using commingled yarns, *Compos. Sci. Technol.* 61 (2001) 1065–1077. [https://doi.org/10.1016/S0266-3538\(00\)00234-7](https://doi.org/10.1016/S0266-3538(00)00234-7).
- [16] B.T. Åström, R.B. Pipes, A modeling approach to thermoplastic pultrusion. I: Formulation of models, *Polym. Compos.* 14 (1993) 173–183. <https://doi.org/10.1002/pc.750140302>.
- [17] J.A. Larock, H.T. Hahn, D.J. Evans, Pultrusion Processes for Thermoplastic Composites, *J. Thermoplast. Compos. Mater.* 2 (1989) 216–229. <https://doi.org/10.1177/089270578900200304>.
- [18] B.T. Åström, Development and application of a process model for thermoplastic pultrusion, *Compos. Manuf.* 3 (1992) 189–197. [https://doi.org/10.1016/0956-7143\(92\)90082-6](https://doi.org/10.1016/0956-7143(92)90082-6).
- [19] G. Bechtold, S. Wiedmer, K. Friedrich, Pultrusion of Thermoplastic Composites - New Developments and Modelling Studies, *J. Thermoplast. Compos. Mater.* 15 (2002) 443–465. <https://doi.org/10.1177/0892705702015005202>.
- [20] B.J. Devlin, M.D. Williams, J.A. Quinn, A.G. Gibson, Pultrusion of unidirectional composites with thermoplastic matrices, *Compos. Manuf.* 2 (1991) 203–207. [https://doi.org/10.1016/0956-7143\(91\)90141-3](https://doi.org/10.1016/0956-7143(91)90141-3).
- [21] Y. Ruan, J.C. Liu, D.C. Chesonis, L.A. Carvell, Development of a two-dimensional thermal model for the steady state thermoplastic pultrusion process, *Sampe.* (1992) 1432–1444. <https://ui.adsabs.harvard.edu/abs/1992sampeymp.1432R/abstract> (accessed August 24, 2018).
- [22] N. Svensson, R. Shishoo, M. Gilchrist, Manufacturing of Thermoplastic Composites from Commingled Yarns-A Review, *J. Thermoplast. Compos. Mater.* 11 (1998) 22–56. <https://doi.org/10.1177/089270579801100102>.
- [23] M. Milwich, Thermoplastic braid pultrusion, in: *Proc. ICCM, 2009*. <http://www.iccm-central.org/Proceedings/ICCM17proceedings/Themes/Manufacturing/MANUFACTURING TECH/INT - MANUF TECH/IC3.2 Milwich.pdf>.
- [24] M.S. Irfan, N. Shotton-Gale, M.A. Paget, V.R. Machavaram, C. Leek, S. Wootton, M. Hudson, S. Helmsmans, F.N. Bogonez, S.D. Pandita, G.F. Fernando, A modified pultrusion process, *J. Compos. Mater.* 51 (2017) 1925–1941. <https://doi.org/10.1177/0021998316666653>.
- [25] S. Strauß, A. Senz, J. Ellinger, Comparison of the Processing of Epoxy Resins in Pultrusion with Open Bath Impregnation and Closed-Injection Pultrusion, *J. Compos. Sci.* 3 (2019) 87. <https://doi.org/10.3390/jcs3030087>.
- [26] S. Li, L. Xu, Z. Ding, L.J. Lee, H. Engelen, Experimental and Theoretical Analysis of Pulling Force in Pultrusion and Resin Injection Pultrusion (RIP)-Part I: Experimental, *J. Compos. Mater.* 37 (2003) 163–189. <https://doi.org/10.1106/002199803028676>.
- [27] D. Srinivasagupta, S. Potaraju, J.L. Kardos, B. Joseph, Steady state and dynamic analysis of a bench-scale injected pultrusion process, *Compos. Part A Appl. Sci. Manuf.* 34 (2003) 835–846. [https://doi.org/10.1016/S1359-835X\(03\)00182-9](https://doi.org/10.1016/S1359-835X(03)00182-9).
- [28] M. Connolly, M. Brennan, CFD Modeling of the Closed Injection Wet- Out Process For Pultrusion Definition of Process Challenge, in: *9th World Pultrusion Conf., EPTA, 2008*.

- [29] K. Jansen, D. Weidler, M. Hoffmann, Method and device for the production of a plastic profile, US8066922, 2011.
- [30] E. Witten, V. Mathes, M. Sauer, M. Kühnel, Composites Market Report 2018 - Market developments, trends, outlooks and challenges, 2018. https://www.avk-tv.de/files/20190118_avk_ccev__marktbericht_2018_final_2.pdf.
- [31] M.U. Witt, M. Milwich, G.T. Gresser, M. Hammer, J. Knippers, Bio-Pultrusion of Façade-Profiles from Sustainable Materials, in: Mater. Sci. Forum, 2015: pp. 1033–1038.
- [32] X. Peng, M. Fan, J. Hartley, M. Al-Zubaidy, Properties of natural fiber composites made by pultrusion process, J. Compos. Mater. 46 (2012) 237–246.
- [33] J.D.H. Hughes, The carbon fibre/epoxy interface—A review, Compos. Sci. Technol. 41 (1991) 13–45. [https://doi.org/10.1016/0266-3538\(91\)90050-Y](https://doi.org/10.1016/0266-3538(91)90050-Y).
- [34] H.F. Wu, D.W. Dwight, N.T. Huff, Effects of silane coupling agents on the interphase and performance of glass-fiber-reinforced polymer composites, Compos. Sci. Technol. 57 (1997) 975–983. [https://doi.org/10.1016/S0266-3538\(97\)00033-X](https://doi.org/10.1016/S0266-3538(97)00033-X).
- [35] D. Ratna, Handbook of Thermoset Resins, ISmithers, Shawbury, UK, 2009.
- [36] S. Mazumdar, Composites manufacturing: materials, product, and process engineering, CRC press, Boca Rotan, 2001.
- [37] B. Ellis, others, Chemistry and technology of epoxy resins, Springer, Dordrecht, 1993.
- [38] C. May, Epoxy resins: chemistry and technology, Marcel Dekker, Inc., New York, 2018.
- [39] D.E. Packham, Mould Sticking , Fouling and Cleaning, Report 150, Rapra Technology Ltd., Shropshire, 2002.
- [40] M. Nakazawa, Mechanism of adhesion of epoxy resin to steel surface, 1994.
- [41] R.G. Schmidt, J.P. Bell, Epoxy Adhesion To Metals, Adv. Polym. Sci. 75 (1986) 33–71. <https://doi.org/10.1007/BFb0017914>.
- [42] T. Semoto, Y. Tsuji, K. Yoshizawa, Molecular understanding of the adhesive force between a metal oxide surface and an epoxy resin, J. Phys. Chem. C. 115 (2011) 11701–11708. <https://doi.org/10.1021/jp202785b>.
- [43] E.H. Andrews, N.E. King, Adhesion of epoxy resins to metals - Part 1, J. Mater. Sci. 11 (1976) 2004–2014. <https://doi.org/10.1007/BF02403348>.
- [44] J. Bouchet, A.-A. Roche, The Formation of Epoxy/Metal Interphases: Mechanisms and Their Role in Practical Adhesion, J. Adhes. 78 (2002) 799–830. <https://doi.org/10.1080/00218460213836>.
- [45] B.J. Briscoe, S.S. Panesar, Aliphatic esters as mould release agents for polyurethanes; the role of interface morphology, J. Phys. D. Appl. Phys. 19 (1986) 841–856. <https://doi.org/10.1088/0022-3727/19/5/016>.
- [46] G. Wypych, Handbook of antiblocking, release, and slip additives, ChemTec Publishing, Toronto, 2005.

- [47] A. Wypych, *Databook of Antiblocking, Release, and Slip Additives*, ChemTec Publishing, Toronto, 2014. <https://books.google.de/books?id=aMFCQO8zqWkC>.
- [48] G.W. Critchlow, R.E. Litchfield, I. Sutherland, D.B. Grandy, S. Wilson, A review and comparative study of release coatings for optimised adhesion in resin transfer moulding applications, *Int. J. Adhes. Adhes.* 26 (2006) 577–599. <https://doi.org/10.1016/j.ijadhadh.2005.09.003>.
- [49] R. Bjekovic, K. Piotrowicz, Epoxy resin and release agents part I: Influence of external and internal release agents on the adhesive properties of epoxy resin, *J. Appl. Eng. Sci.* 13 (2015) 45–50. <https://doi.org/10.5937/jaes13-7210>.
- [50] M.V. C. SERRÉ, R. ERRE, Behavior of internal mold release agent during BMC thermosets composites cure and aging, *J. Mater. Sci. Lett.* 20 (2001) 1989–1991.
- [51] V.M. Karbhari, Effect of internal mold release agent on the cure and property variation in resin transfer molding composites, *J. Materials Sci. Lett.* 17 (1998) 2061–2062.
- [52] E. Lackey, J.G. Vaughan, P. Talbot, B. Burnham, *Effects of Mold Release Additives on Pultrusion Processing and Properties*, The University of Mississippi Composite Materials Research Group, Mississippi, 2001.
- [53] E. Lackey, J.G. Vaughan, P. Talbot, B. Burnham, Experimental Examination of the Effects of Internal Mold Release Agents for Pultrusion Processing, in: *CFA Compos.*, 2000.
- [54] H.L. PRICE, S.G. CUPSCHALK, Pulling Force and Its Variation in Composite Materials Pultrusion, in: 1984: pp. 301–322. <https://doi.org/10.1021/ba-1984-0206.ch018>.
- [55] M.A. Bibbo, T.G. Gutowski, Analysis of the Pulling Force in Pultrusion, in: *Annu. Tech. Conf. - Soc. Plast. Eng.*, 1986: pp. 1430–1432.
- [56] G.L. Batch, C.W. Macosko, A computer analysis of temperature and pressure distributions in a pultrusion die, in: 42nd Annu. Conf. Expo'87, 1987: p. 1987.
- [57] D. Srinivasagupta, J.L. Kardos, B. Joseph, Analysis of pull-force in injected pultrusion, *J. Adv. Mater.* 38 (2006) 39.
- [58] D. Sharma, T.A. McCarty, J.A. Roux, J.G. Vaughan, Pultrusion die pressure response to changes in die inlet geometry, *Polym. Compos.* 19 (1998) 180–192. <https://doi.org/10.1002/pc.10089>.
- [59] K.S. Raper, J.A. Roux, J.G. Vaughan, E. Lackey, Permeability impact on the pressure rise in a pultrusion die, *J. Thermophys. Heat Transf.* 13 (1999) 91–99. <https://doi.org/10.2514/2.6405>.
- [60] E. Lackey, J.G. Vaughan, An Analysis of Factors Affecting Pull Force for the Pultrusion of Graphite/Epoxy Composites, *J. Reinf. Plast. Compos.* 13 (1994) 188–198. <https://doi.org/10.1177/073168449401300301>.
- [61] A. Atarsia, R. Boukhili, Effect of Pulling Speed on the Sizes of the Liquid, Gel and Solid Zone During Thermoset Pultrusion, *J. Reinf. Plast. Compos.* 19 (2000) 1493–1503. <https://doi.org/0803973233>.
- [62] P. Carlone, G.S. Palazzo, Viscous pull force evaluation in the pultrusion process by a finite element thermo-chemical rheological model, *Int. J. Mater. Form.* 1 (2008)

- 831–834. <https://doi.org/10.1007/s12289-008-0264-0>.
- [63] S.M.M. Moschiar, M.M.M. Reboredo, J.M. Kenny, A. Vázquez, Analysis of pultrusion processing of composites of unsaturated polyester resin with glass fibers, *Polym. Compos.* 17 (1996) 478–485. <https://doi.org/10.1002/pc.10636>.
- [64] S.M. Moschiar, M.M. Reboredo, H. Larrondo, A. Vazquez, Pultrusion of epoxy matrix composites: Pulling force model and thermal stress analysis, *Polym. Compos.* 17 (1996) 850–858. <https://doi.org/10.1002/pc.10678>.
- [65] M. Giordano, L. Nicolais, Resin flow in a pultrusion process, *Polym. Compos.* 18 (1997) 681–686. <https://doi.org/10.1002/pc.10320>.
- [66] P. Carlone, G.S. Palazzo, Computational Modeling of the Pulling Force in a Conventional Pultrusion Process, *Adv. Mater. Res.* 772 (2013) 399–406. <https://doi.org/10.4028/www.scientific.net/AMR.772.399>.
- [67] I. Baran, Modelling the Pultrusion Process of Off Shore Wind Turbine Blades, Technical University of Denmark, 2014.
- [68] S. Li, L. Xu, Z. Ding, L.J. Lee, H. Engelen, Experimental and Theoretical Analysis of Pulling Force in Pultrusion and Resin Injection Pultrusion (RIP) - Part II: Modeling and Simulation, *J. Compos. Mater.* 37 (2003) 195–216. <https://doi.org/10.1177/0021998303037003675>.
- [69] J. Blaurock, Zur Optimierung des Strangziehverfahrens für endlosfaserverstärkte, hochfeste Kunststoffprofile, Mainz, 1999.
- [70] B.T. Åstroöm, R.B. Pipes, A modeling approach to thermoplastic pultrusion. II: Verification of models, *Polym. Compos.* 14 (1993) 184–194. <https://doi.org/10.1002/pc.750140303>.
- [71] A.A. Safonov, P. Carlone, I. Akhatov, Mathematical simulation of pultrusion processes: A review, *Compos. Struct.* 184 (2018) 153–177. <https://doi.org/10.1016/J.COMPSTRUCT.2017.09.093>.
- [72] M.S. Yun, W. Il Lee, Analysis of pulling force during pultrusion process of phenolic foam composites, *Compos. Sci. Technol.* 68 (2008) 140–146. <https://doi.org/10.1016/j.compscitech.2007.05.032>.
- [73] R. Menezes Bezerra, Modelling and Simulation of the Closed Injection Pultrusion Process, Karlsruhe Institute of Technology, 2017. <https://doi.org/10.5445/IR/1000079057>.
- [74] J.E. Sumerak, Understanding pultrusion process variables for the first time, in: *Reinf. Plast. '85*, 40 Th Annu. Conf., 1985: p. 1985.
- [75] J. FANUCCI, S. NOLET, C. Koppernaes, H.-N. CHOU, Thin disposable pressure sensors for composite material process monitoring, in: *Int. SAMPE Symp. Exhib. 35 Th*, Anaheim, CA, 1990: pp. 1205–1219.
- [76] A.L. Kalamkarov, S.B. Fitzgerald, D.O. MacDonald, The use of Fabry Perot fiber optic sensors to monitor residual strains during pultrusion of FRP composites, *Compos. Part B Eng.* 30 (1999) 167–175. [https://doi.org/10.1016/S1359-8368\(98\)00052-3](https://doi.org/10.1016/S1359-8368(98)00052-3).
- [77] H.L.J. Price, Curing and Flow of Thermosetting Resins for Composite Material

- Pultrusion, OLD DOMINION UNIVERSITY, 1979. <https://apps.dtic.mil/docs/citations/ADA303192>.
- [78] J. Krämer, M. Hähnel, F. Wolff Fabris, V. Altstädt, Classification of Internal Release Agents-Evaluation of a Test facility and the Effect on the neat Epoxy Resin properties.pdf, in: 2nd Int. Conf. Thermosets, Fraunhofer Verlag, Berlin, 2011: pp. 79–81.
- [79] T.G. Gutowski, Z. Cai, S. Bauer, D. Boucher, J. Kingery, S. Wineman, Consolidation Experiments for Laminate Composites, *J. Compos. Mater.* 21 (1987) 650–669. <https://doi.org/10.1177/002199838702100705>.
- [80] Y.R. Kim, S.P. McCarthy, J.P. Fanucci, Compressibility and relaxation of fiber reinforcements during composite processing, *Polym. Compos.* 12 (1991) 13–19. <https://doi.org/10.1002/pc.750120104>.
- [81] G.L. Batch, S. Cumiskey, C.W. Macosko, Compaction of fiber reinforcements, *Polym. Compos.* 23 (2002) 307–318. <https://doi.org/10.1002/pc.10433>.
- [82] S. Aranda, F. Klunker, G. Ziegmann, Compaction response of fibre reinforcements depending on processing temperature, in: ICCM Int. Conf. Compos. Mater., 2009.
- [83] N. Shakya, J.A. Roux, A.L. Jeswani, Effect of Resin Viscosity in Fiber Reinforcement Compaction in Resin Injection Pultrusion Process, *Appl. Compos. Mater.* 20 (2013) 1173–1193. <https://doi.org/10.1007/s10443-013-9320-0>.
- [84] N.B. Masuram, J.A. Roux, A.L. Jeswani, Fiber Volume Fraction Influence on Fiber Compaction in Tapered Resin Injection Pultrusion Manufacturing, *Appl. Compos. Mater.* 23 (2016) 421–442. <https://doi.org/10.1007/s10443-015-9466-z>.
- [85] N.B. Masuram, J.A. Roux, A.L. Jeswani, Pull speed influence on fiber compaction and wetout in tapered resin injection pultrusion manufacturing, *Polym. Polym. Compos.* 25 (2017) 419–433. <https://doi.org/10.1177/096739111702500601>.
- [86] S.U.K. Gadam, J.A. Roux, T.A. McCarty, J.G. Vaughan, The impact of pultrusion processing parameters on resin pressure rise inside a tapered cylindrical die for glass-fibre/epoxy composites, *Compos. Sci. Technol.* 60 (2000) 945–958. [https://doi.org/10.1016/S0266-3538\(99\)00181-5](https://doi.org/10.1016/S0266-3538(99)00181-5).
- [87] I. Baran, Pultrusion: state-of-the-art process models, Smithers Rapra Technology Ltd, Shropshire, 2015.
- [88] S. Whitaker, Flow in porous media I: A theoretical derivation of Darcy's law, *Transp. Porous Media.* 1 (1986) 3–25. <https://doi.org/10.1007/BF01036523>.
- [89] C.M. ÓBrádaigh, G.B. McGuinness, R.B. Pipes, Numerical analysis of stresses and deformations in composite materials sheet forming: central indentation of a circular sheet, *Compos. Manuf.* 4 (1993) 67–83. [https://doi.org/10.1016/0956-7143\(93\)90074-l](https://doi.org/10.1016/0956-7143(93)90074-l).
- [90] P. Hubert, A. Poursartip, A review of flow and compaction modelling relevant to thermoset matrix laminate processing, *J. Reinf. Plast. Compos.* 17 (1998) 286–318. <https://doi.org/10.1177/073168449801700402>.
- [91] S. Ranganathan, F.R. Phelan, S.G. Advani, A generalized model for the transverse fluid permeability in unidirectional fibrous media, *Polym. Compos.* 17 (1996) 222–230. <https://doi.org/10.1002/pc.10607>.

- [92] B.R. Gebart, Permeability of Unidirectional Reinforcements for RTM, *J. Compos. Mater.* 26 (1992) 1100–1133. <https://doi.org/10.1177/002199839202600802>.
- [93] H. Faria, H.Q. de Faria, Analytical and numerical modelling of the filament winding process, Universidade do Porto (Portugal), 2013.
- [94] L. Woo II, C.L. Alfred, S.S. George, Heat of Reaction, Degree of Cure, and Viscosity of Hercules 3501-6 Resin, *J. Compos. Mater.* 16 (1982) 510–520.
- [95] M.R. Kamal, S. Sourour, Kinetics and thermal characterization of thermoset cure, *Polym. Eng. Sci.* 13 (1973) 59–64. <https://doi.org/10.1002/pen.760130110>.
- [96] M.R. Kamal, Thermoset characterization for moldability analysis, *Polym. Eng. Sci.* 14 (1974) 231–239. <https://doi.org/10.1002/pen.760140312>.
- [97] D.-H. Kim, P.-G. Han, G.-H. Jin, W.I. Lee, A Model for Thermosetting Composite Pultrusion Process, *J. Compos. Mater.* 31 (1997) 2105–2122. <https://doi.org/10.1177/002199839703102005>.
- [98] C.D. Han, D.S. Lee, H.B. Chin, Development of a mathematical model for the pultrusion process, *Polym. Eng. Sci.* 26 (1986) 393–404. <https://doi.org/10.1002/pen.760260604>.
- [99] P. Akisins, Design of Advanced Pultrusion Processes, RIGA TECHNICAL UNIVERSITY, 2017.
- [100] F.X. Perrin, T.M.H. Nguyen, J.L. Vernet, Kinetic analysis of isothermal and nonisothermal epoxy-amine cures by model-free isoconversional methods, *Macromol. Chem. Phys.* 208 (2007) 718–729. <https://doi.org/10.1002/macp.200600614>.
- [101] S. Vyazovkin, N. Sbirrazzuoli, Kinetic methods to study isothermal and nonisothermal epoxy-anhydride cure, *Macromol. Chem. Phys.* 200 (1999) 2294–2303. [https://doi.org/10.1002/\(SICI\)1521-3935\(19991001\)200:10<2294::AID-MACP2294>3.0.CO;2-V](https://doi.org/10.1002/(SICI)1521-3935(19991001)200:10<2294::AID-MACP2294>3.0.CO;2-V).
- [102] N. Sbirrazzuoli, S. Vyazovkin, Learning about epoxy cure mechanisms from isoconversional analysis of DSC data, *Thermochim. Acta.* 388 (2002) 289–298. [https://doi.org/10.1016/S0040-6031\(02\)00053-9](https://doi.org/10.1016/S0040-6031(02)00053-9).
- [103] S. Vyazovkin, Mechanism and Kinetics of Epoxy - Amine Cure Studied by Differential Scanning Calorimetry, *Macromolecules.* 29 (1996) 1867–1873.
- [104] S.C. Joshi, Y.C. Lam, Integrated approach for modelling cure and crystallization kinetics of different polymers in 3D pultrusion simulation, *J. Mater. Process. Technol.* 174 (2006) 178–182. <https://doi.org/10.1016/j.jmatprotec.2006.01.003>.
- [105] L. Aylward, C. Douglas, D. Roylance, A transient finite element model for pultrusion processing, *Polym. Process Eng.* 3 (1985) 247–261.
- [106] R. Shanku, J.G. Vaughan, J.A. Roux, Rheological characteristics and cure kinetics of EPON 862/W epoxy used in pultrusion, *Adv. Polym. Technol.* 16 (1997) 297–311. [https://doi.org/10.1002/\(SICI\)1098-2329\(199711\)16:4<297::AID-ADV4>3.0.CO;2-Q](https://doi.org/10.1002/(SICI)1098-2329(199711)16:4<297::AID-ADV4>3.0.CO;2-Q).
- [107] Y.R. Chachad, J.A. Roux, J.G. Vaughan, E.S. Arafat, Effects of Pull Speed on Die Wall Temperatures for Flat Composites of Various Sizes, *J. Reinf. Plast. Compos.*

- 15 (1996) 718–739. <https://doi.org/10.1177/073168449601500706>.
- [108] M. Valliappan, J.A. Roux, J.G. Vaughan, E.S. Arafat, Die and post-die temperature and cure in graphite/epoxy composites, *Compos. Part B Eng.* 27 (1996) 1–9. [https://doi.org/10.1016/1359-8368\(95\)00001-1](https://doi.org/10.1016/1359-8368(95)00001-1).
- [109] P. Carlone, G.S. Palazzo, R. Pasquino, Pultrusion manufacturing process development by computational modelling and methods, *Math. Comput. Model.* 44 (2006) 701–709. <https://doi.org/10.1016/j.mcm.2006.02.006>.
- [110] P.J. Halley, M.E. Mackay, Chemorheology of thermosets-An overview, *Polym. Eng. Sci.* 36 (1996) 593–609. <https://doi.org/10.1002/pen.10447>.
- [111] T.G. Mezger, *The rheology handbook: for users of rotational and oscillatory rheometers*, 4th ed., Vincentz Network GmbH & Co KG, Hanover, 2014.
- [112] R.B. PRIME, Thermosets, in: E.A. TURI (Ed.), *Therm. Charact. Polym. Mater.*, Academic Press, Inc., San Jose, 1981: pp. 435–569. <https://doi.org/10.1016/B978-0-12-703780-6.50010-9>.
- [113] H.H. Winter, The Critical Gel, in: R. Borsali, R. Pecora (Eds.), *Struct. Dyn. Polym. Colloid. Syst.*, Springer Netherlands, Dordrecht, 2002: pp. 439–470. https://doi.org/10.1007/978-94-010-0442-8_14.
- [114] D. Doraiswamy, A.N. Mujumdar, I. Tsao, A.N. Beris, S.C. Danforth, A.B. Metzner, The Cox–Merz rule extended: A rheological model for concentrated suspensions and other materials with a yield stress, *J. Rheol. (N. Y. N. Y.)* 35 (1991) 647–685. <https://doi.org/10.1122/1.550184>.
- [115] H.-C. Lee, D.A. Brant, Rheology of concentrated isotropic and anisotropic xanthan solutions. 1. A rodlike low molecular weight sample, *Macromolecules* 35 (2002) 2212–2222.
- [116] S.T. Milner, Relating the shear-thinning curve to the molecular weight distribution in linear polymer melts, *J. Rheol. (N. Y. N. Y.)* 40 (1996) 303–315. <https://doi.org/10.1122/1.550742>.
- [117] C.L. Lee, K.H. Wei, Curing kinetics and viscosity change of a two-part epoxy resin during mold filling in resin-transfer molding process, *J. Appl. Polym. Sci.* 77 (2000) 2139–2148. [https://doi.org/10.1002/1097-4628\(20000906\)77:10<2139::AID-APP6>3.0.CO;2-N](https://doi.org/10.1002/1097-4628(20000906)77:10<2139::AID-APP6>3.0.CO;2-N).
- [118] M.R. Dusi, W.I. Lee, P.R. Ciriscioli, G.S. Springer, Cure Kinetics and Viscosity of Fiberite 976 Resin, *J. Compos. Mater.* 21 (1987) 243–261. <https://doi.org/10.1177/002199838702100304>.
- [119] R.J. Abbott, G.B. Higgins, Surface Tension of a Curing Epoxy, *J. Polym. Sci. Part A Polym. Chem.* 26 (1988) 1985–1988. <https://doi.org/10.1038/043437c0>.
- [120] S. Page, R. Mezzenga, L. Boogh, J. Berg, J. Månson, Surface Energetics Evolution during Processing of Epoxy Resins., *J. Colloid Interface Sci.* 222 (2000) 55–62. <https://doi.org/10.1006/jcis.1999.6613>.
- [121] M. Li, C. Yuan, S.K. Wang, Y.Z. Gu, K. Potter, Z.G. Zhang, Evolution of the wettability between carbon fiber and epoxy as a function of temperature and resin curing, *J. Appl. Polym. Sci.* 128 (2013) 4095–4101. <https://doi.org/10.1002/app.38634>.

- [122] D.N. Staicopolus, The computation of surface tension and of contact angle by the sessile-drop method, *J. Colloid Sci.* 17 (1962) 439–447. [https://doi.org/10.1016/0095-8522\(62\)90055-7](https://doi.org/10.1016/0095-8522(62)90055-7).
- [123] L. Wilhelmy, Ueber die Abhängigkeit der Capillaritäts-Constanten des Alkohols von Substanz und Gestalt des benetzten festen Körpers, *Ann. Phys.* 195 (1863) 177–217. <https://doi.org/10.1002/andp.18631950602>.
- [124] S.-W. Han, N.-S. Choi, M.-S. Lee, Analysis of glass fabric impregnation using a resin drop method, *J. Mech. Sci. Technol.* 26 (2012) 1477–1482. <https://doi.org/10.1007/s12206-012-0341-7>.
- [125] C. Cheng, H. Lin, Measurement of Surface Tension of Epoxy Resins Used in Dispensing Process for Manufacturing Thin Film Transistor-Liquid Crystal Displays, *IEEE Trans. Adv. Packag.* 31 (2008) 100–106. <https://doi.org/10.1109/TADVP.2007.901767>.
- [126] G. Bracco, B. Holst, *Surface Science Techniques*, Springer Berlin Heidelberg, Berlin, Heidelberg, 2013. <https://doi.org/10.1007/978-3-642-34243-1>.
- [127] D.Y. Kwok, T. Gietzelt, K. Grundke, H.-J. Jacobasch, A.W. Neumann, *Contact Angle Measurements and Contact Angle Interpretation. 1. Contact Angle Measurements by Axisymmetric Drop Shape Analysis and a Goniometer Sessile Drop Technique*, 1997. <https://pubs.acs.org/sharingguidelines> (accessed November 6, 2020).
- [128] S.T. Peters, *Composite filament winding*, ASM International, Ohio, 2011.
- [129] H.J. Brauckmann, M. Salewski, B. Eckhardt, Momentum transport in Taylor-Couette flow with vanishing curvature, *J. Fluid Mech.* 790 (2016) 419–452. <https://doi.org/10.1017/jfm.2015.737>.
- [130] H.L. Swinney, Flow regimes in a circular Couette system with independently rotating cylinders, *J. Fluid Mech.* 164 (1986) 155–183. <https://doi.org/10.1017/S0022112086002513>.
- [131] M. Lücke, M. Mihelcic, K. Wingerath, G. Pfister, Flow in a small annulus between concentric cylinders, *J. Fluid Mech.* 140 (1984) 343–353. <https://doi.org/10.1017/S002211208400063X>.
- [132] H.S. Dou, B.C. Khoo, K.S. Yeo, Instability of Taylor-Couette flow between concentric rotating cylinders, *Int. J. Therm. Sci.* 47 (2008) 1422–1435. <https://doi.org/10.1016/j.ijthermalsci.2007.12.012>.
- [133] G.I. Taylor, Stability of a viscous liquid contained between two rotating cylinders, in: *Proc. R. Soc. London. Ser. A, Contain. Pap. a Math. Phys. Character*, The Royal Society, 1923: pp. 541–542. <https://doi.org/10.1098/rspa.1923.0013>.
- [134] D. Sharma, T.A. McCarty, J.A. Roux, J.G. Vaughan, Fluid Mechanics Analysis of a Two-Dimensional Pultrusion Die Inlet, *Polym. Eng. Sci.* 38 (1998) 1611–1622.
- [135] D. Sharma, T.A. McCarty, J.A. Roux, J.G. Vaughan, Investigation of Dynamic Pressure Behavior in a Pultrusion Die, *J. Compos. Mater.* 32 (1998) 929–950. <https://doi.org/10.1177/002199839803201002>.
- [136] C. V Pious, S. Thomas, 2 - Polymeric Materials—Structure, Properties, and Applications, in: *J. Izdebska, S. Thomas (Eds.), Print. Polym., William Andrew*

- Publishing, 2016: pp. 21–39. <https://doi.org/https://doi.org/10.1016/B978-0-323-37468-2.00002-6>.
- [137] DIN EN ISO 286-1:2010, Geometrical product specifications (GPS) — ISO code system for tolerances on linear sizes — Part 1: Basis of tolerances, deviations and fits, 2010.
- [138] R. Thomas, C. Sinturel, S. Thomas, E.M. Sadek El Akiaby, Introduction, in: *Micro- and Nanostructured Epoxy/Rubber Blends*, Wiley-VCH Verlag GmbH & Co. KGaA, Weinheim, Germany, 2014: pp. 1–30. <https://doi.org/10.1002/9783527666874.ch1>.
- [139] EPIKOTE™ Resin MGS® LR285 - Datasheet, (2010).
- [140] Direktroving - Product datasheet, PD Glasseiden GmbH Oschatz, Oschatz, 2012.
- [141] A. Roy, Influence of internal mould release on properties of glass/epoxy composites, Indian Institute of Technology Delhi & University of Stuttgart, 2013.
- [142] PAT® - Release agents - Datasheet, (2012).
- [143] Aqua release 250 - Datasheet, (2015).
- [144] Installation and operation guide: X-Winder 4X-23, (2014).
- [145] D. Ho, Notepad++ v7.8.7 release, (2020). <https://notepad-plus-plus.org/news/v787-released/> (accessed June 8, 2020).
- [146] T. Sofi, S. Neunkirchen, R. Schledjewski, Path calculation, technology and opportunities in dry fiber winding: a review, *Adv. Manuf. Polym. Compos. Sci.* 4 (2018) 57–72. <https://doi.org/10.1080/20550340.2018.1500099>.
- [147] K.K. Kratmann, M.P.F. Sutcliffe, L.T. Lilleheden, R. Pyrz, O.T. Thomsen, A novel image analysis procedure for measuring fibre misalignment in unidirectional fibre composites, *Compos. Sci. Technol.* 69 (2009) 228–238. <https://doi.org/10.1016/J.COMPSCITECH.2008.10.020>.
- [148] I. Baran, I. Straumit, O. Shishkina, S. V. Lomov, X-ray computed tomography characterization of manufacturing induced defects in a glass/polyester pultruded profile, *Compos. Struct.* 195 (2018) 74–82. <https://doi.org/10.1016/j.compstruct.2018.04.030>.
- [149] Unsheathed Fine Gage Thermocouples -Data sheet, (2016). http://www.omega.com/Temperature/pdf/IRCO_CHAL_P13R_P10R.pdf.
- [150] ALMEMO ® Measuring Instruments - Data sheet, (2016). <https://www.ahlborn.com/download/pdfs/kap01/eng/0allge.pdf>.
- [151] D.L. McElroy, F.J. Weaver, C. Bridgman, Thermal expansion of epoxy-fiberglass composite specimens, *Int. J. Thermophys.* 9 (1988) 233–243. <https://doi.org/10.1007/BF00504243>.
- [152] D. Hartman, M.E. Greenwood, D.M. Miller, High strength glass fibers, Aiken, 1996.
- [153] Stainless Steel 316 Datasheet, (2018) 3–5. <https://www.azom.com/article.aspx?ArticleID=863%0A>.
- [154] L. Bjerregaard, K. Geels, B. Ottesen, M. Rückert, Metalog Guide, Struers A/S, Rødovre, Denmark, 2002. <https://www.struers.com/en/Library#brochures>.

- [155] J. Schindelin, I. Arganda-Carreras, E. Frise, V. Kaynig, M. Longair, T. Pietzsch, S. Preibisch, C. Rueden, S. Saalfeld, B. Schmid, J.-Y. Tinevez, D.J. White, V. Hartenstein, K. Eliceiri, P. Tomancak, A. Cardona, Fiji: an open-source platform for biological-image analysis, *Nat. Methods*. 9 (2012) 676–682. <https://doi.org/10.1038/nmeth.2019>.
- [156] The GIMP Development Team, GIMP, (2020). <https://www.gimp.org>.
- [157] G. Höhne, W.F. Hemminger, H.-J. Flammersheim, *Differential scanning calorimetry*, Springer Science & Business Media, 2013.
- [158] A. Cadenato, J.M. Salla, X. Ramis, J.M. Morancho, L.M. Marroyo, J.L. Martin, Determination of gel and vitrification times of thermoset curing process by means of TMA, DMTA and DSC techniques: TTT diagram, *J. Therm. Anal.* 49 (1997) 269–279. <https://doi.org/10.1007/BF01987448>.
- [159] K. Horie, I. Mita, H. Kambe, Calorimetric investigation of polymerization reactions. IV. Curing reaction of polyester fumarate with styrene, *J. Polym. Sci. Part A-1 Polym. Chem.* 8 (1970) 2839–2852. <https://doi.org/10.1002/pol.1970.150081010>.
- [160] Netzsch Kinetics Neo® (Demo Version), (2019).
- [161] DCAT Tensiometer, (2016). DataPhysics Instruments GmbH.
- [162] J. Antony, *Design of Experiments for Engineers and Scientists*, Elsevier, London, 2014. <https://doi.org/10.1016/C2012-0-03558-2>.
- [163] Minitab® 18, (2019). www.minitab.com.
- [164] C.R. Siviour, J.L. Jordan, High Strain Rate Mechanics of Polymers: A Review, *J. Dyn. Behav. Mater.* 2 (2016) 15–32. <https://doi.org/10.1007/s40870-016-0052-8>.
- [165] I. Baran, P. Carlone, J.H. Hattel, G.S. Palazzo, R. Akkerman, The Effect of Product Size on the Pulling Force in Pultrusion, *Key Eng. Mater.* 611–612 (2014) 1763–1770. <https://doi.org/10.4028/www.scientific.net/KEM.611-612.1763>.

Appendix

A. Torque-Time curves of the samples measured on DDS

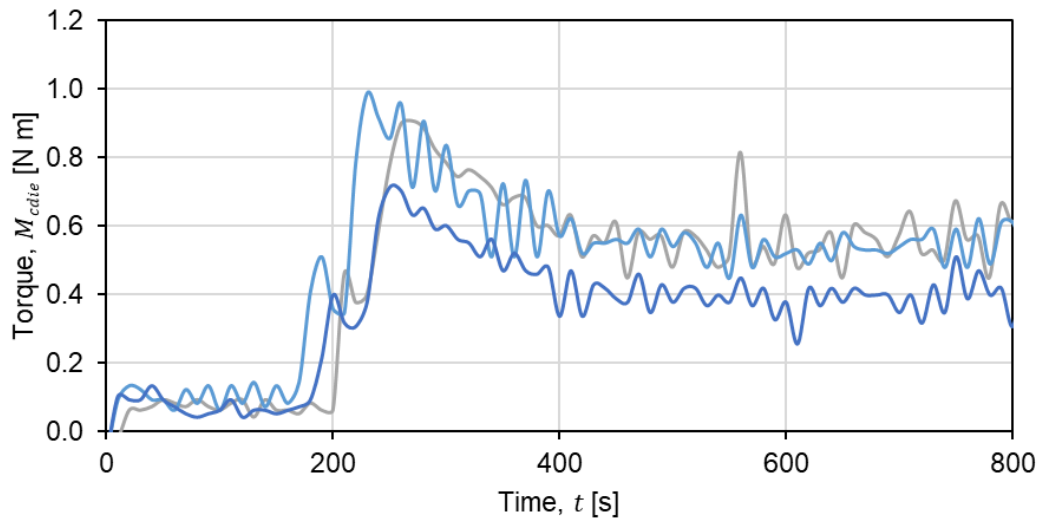


Figure A 1: T120-V100-R5.5-H1-FV0.61-IMR3.0.

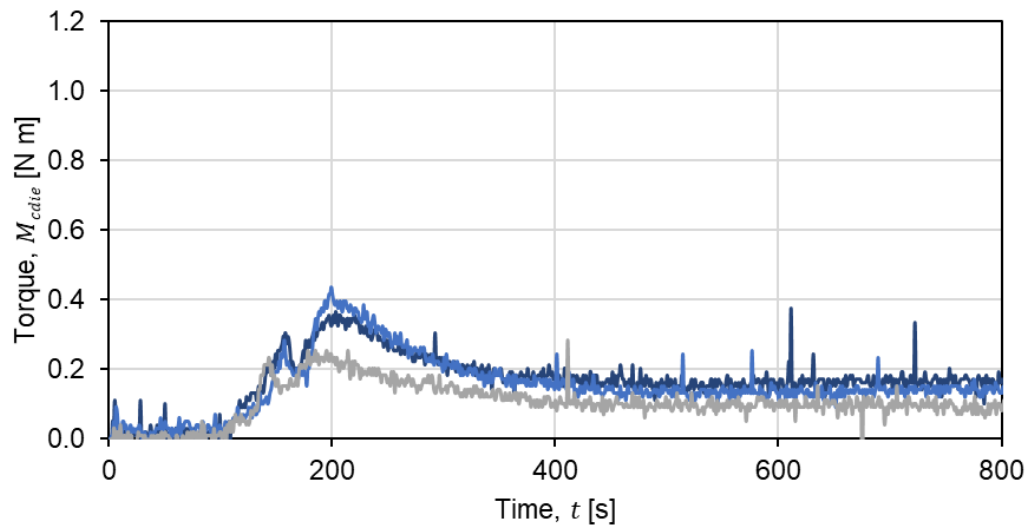


Figure A 2: T140-V100-R5.5-H2-FV0.61-IMR3.0.

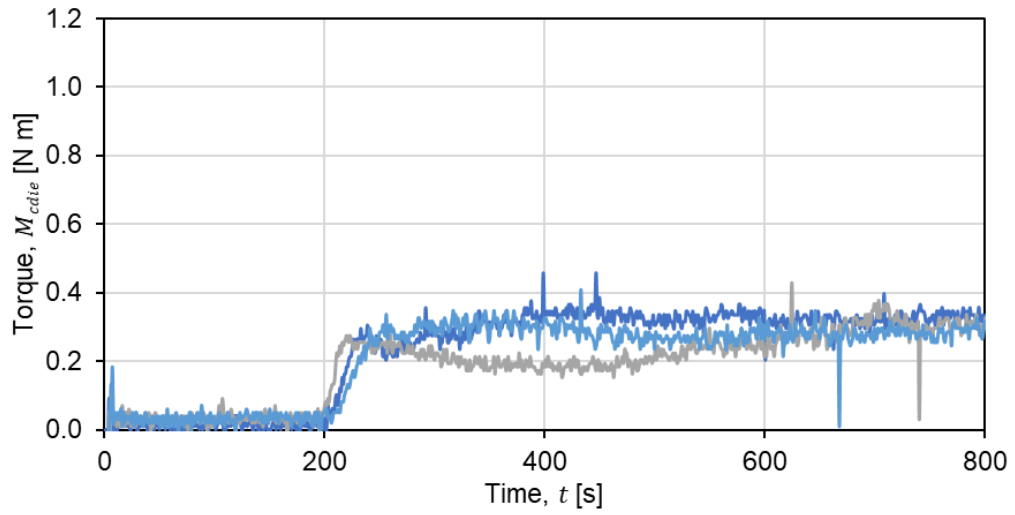


Figure A 3: T120-V300-R5.5-H2-FV0.61-IMR3.0.

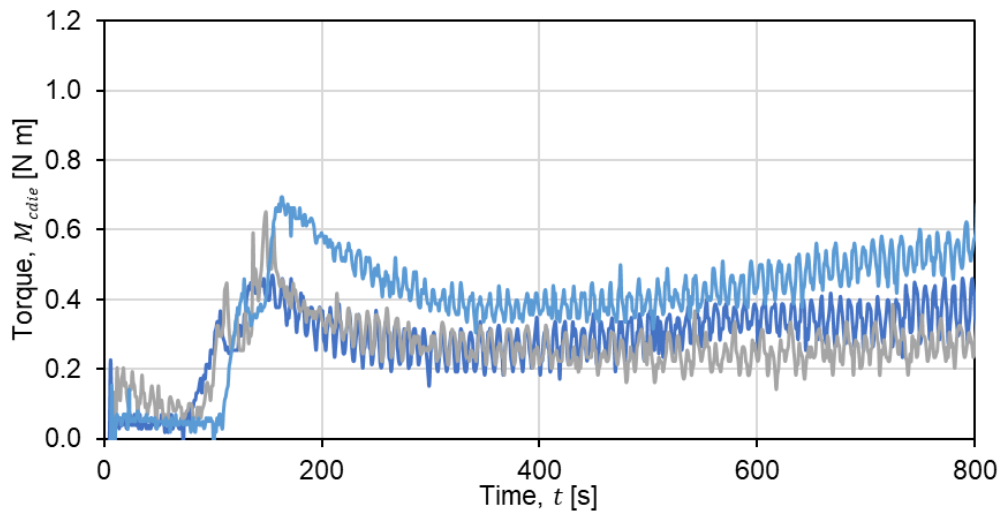


Figure A 4: T140-V300-R5.5-H1-FV0.61-IMR3.0.

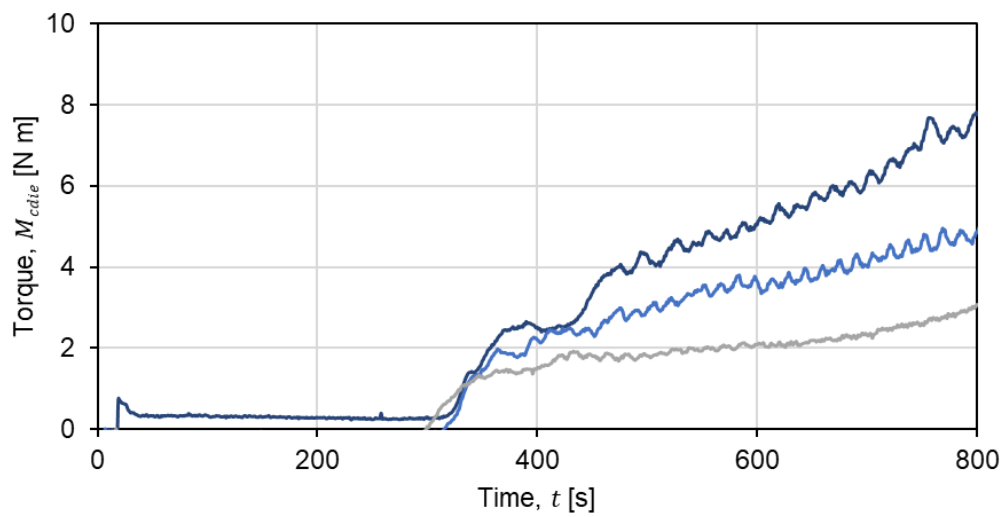


Figure A 5: T120-V300-R11-H1-FV0.56-IMR0.5.

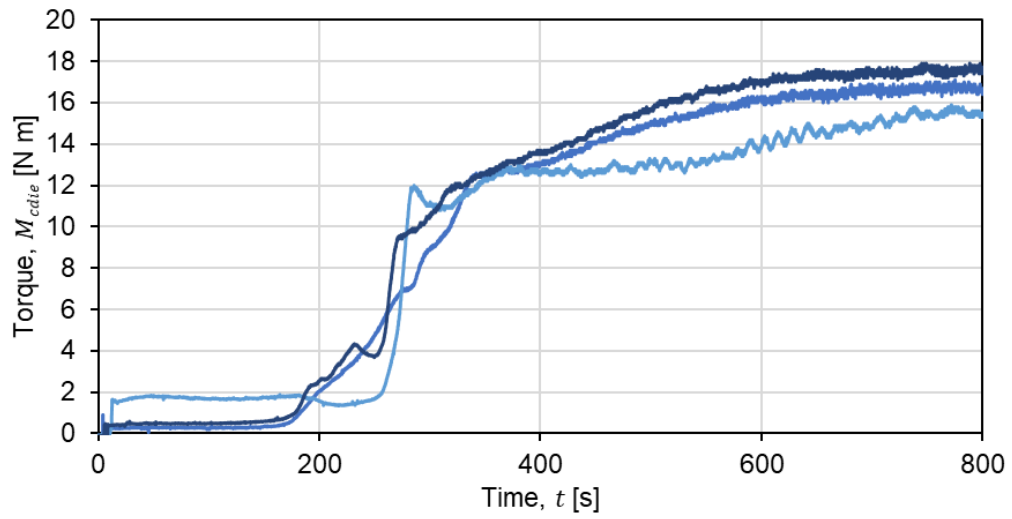


Figure A 6: T140-V300-R11-H1-FV0.61-IMR0.5.

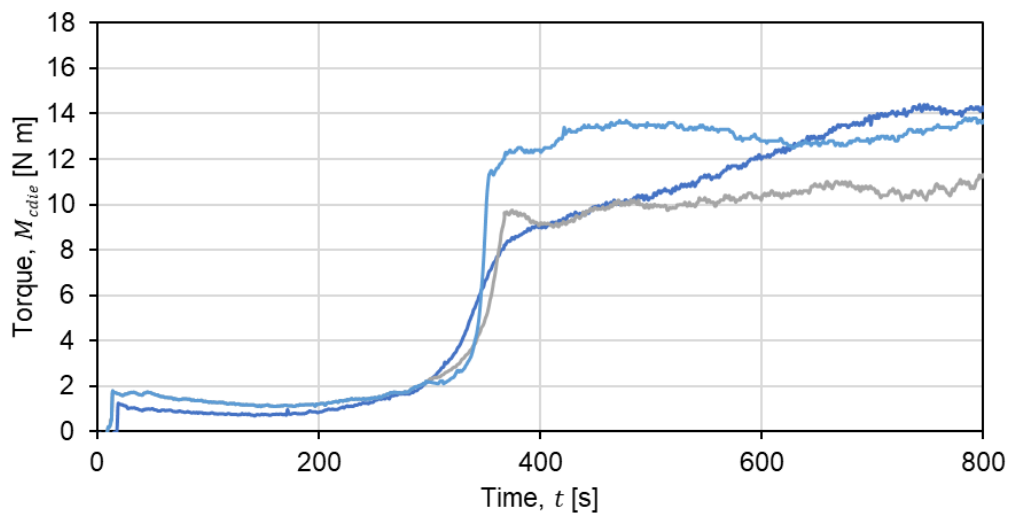


Figure A 7: T120-V300-R11-H1-FV0.61-IMR0.5.

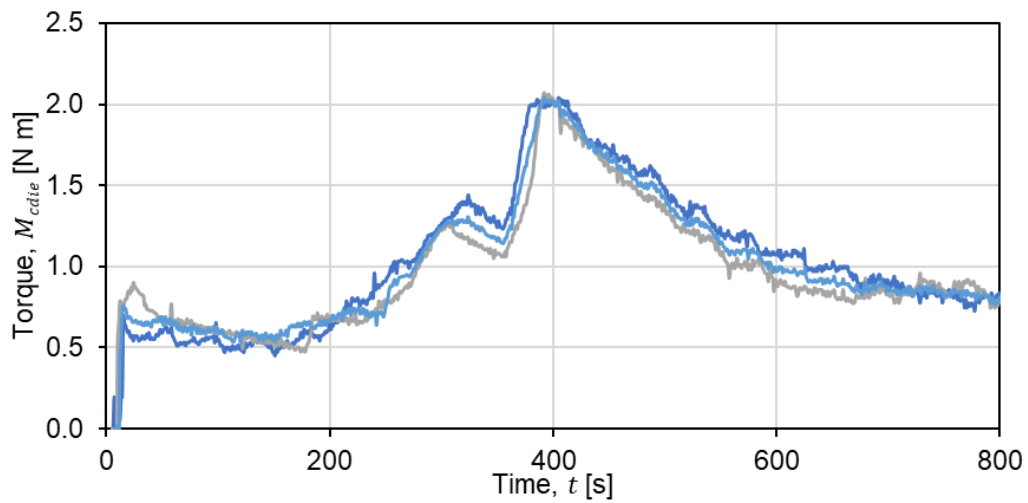


Figure A 8: T120-V100-R11-H2-FV0.61-IMR3.0.

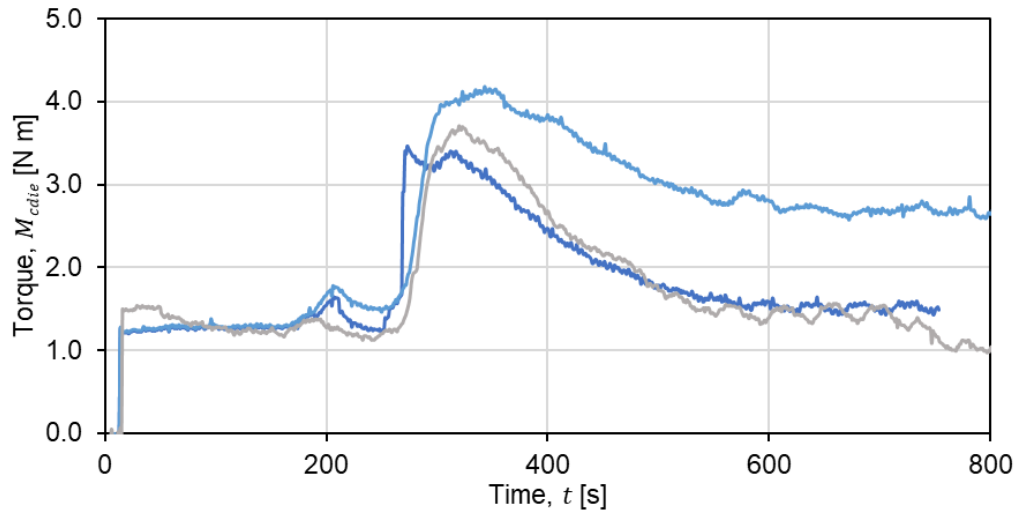


Figure A 9: T140-V100-R11-H1-FV0.61-IMR3.0.

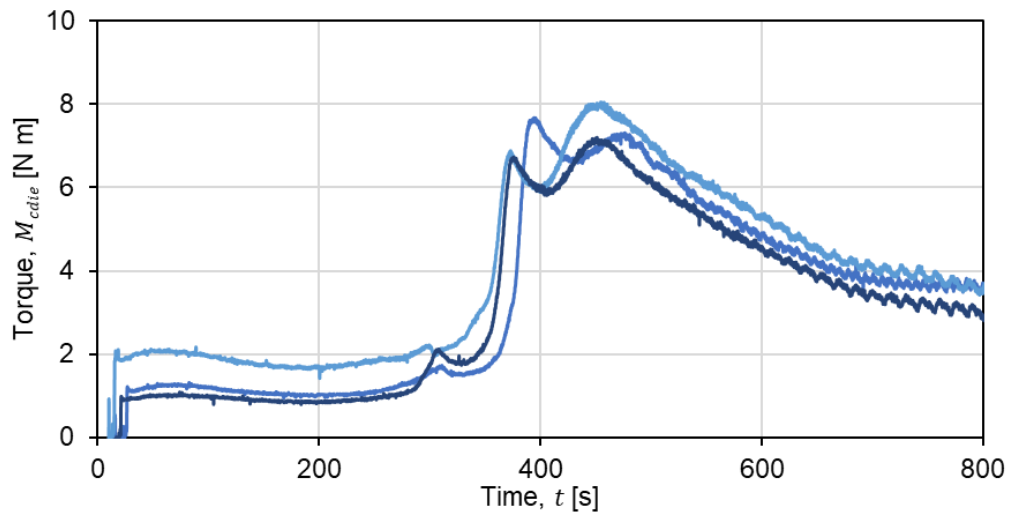


Figure A 10: T120-V300-R11-H1-FV0.61-IMR3.0.

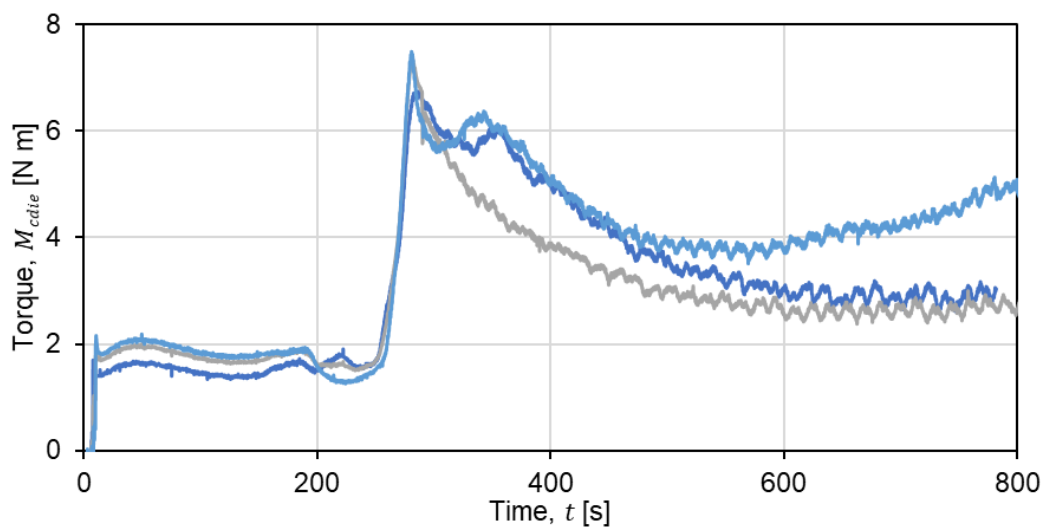


Figure A 11: T140-V300-R11-H1-FV0.61-IMR3.0.

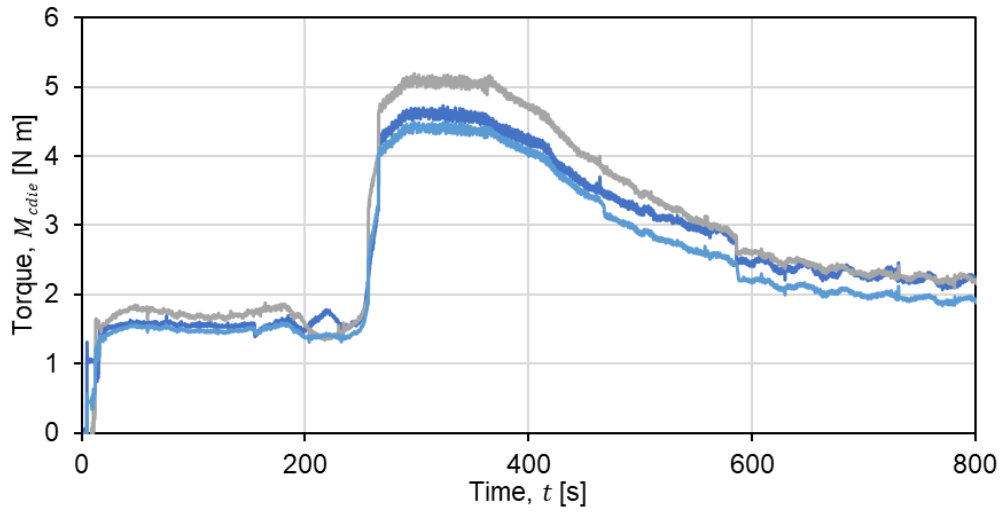


Figure A 12: T140-V200-R11-H1-FV0.61-IMR3.0.

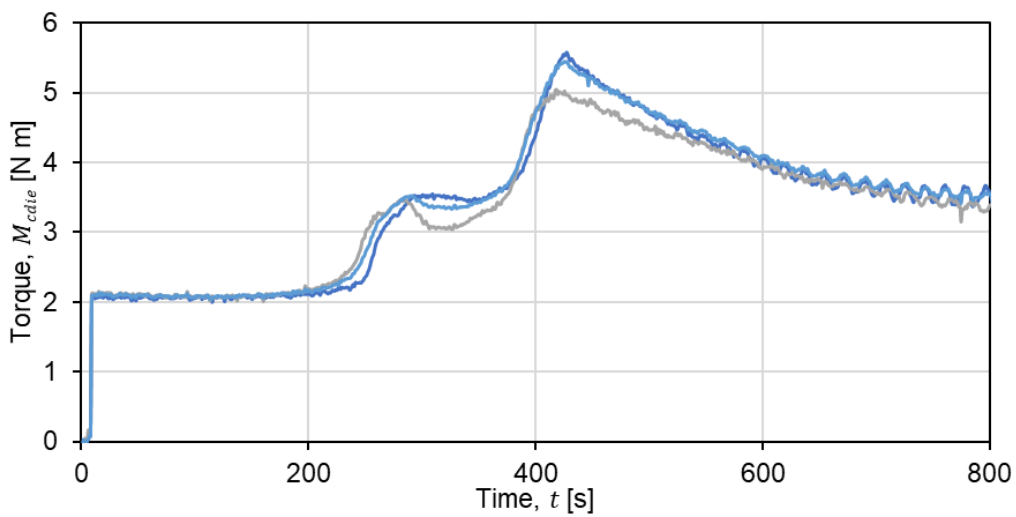


Figure A 13: T120-V300-R11-H2-FV0.61-IMR3.0.

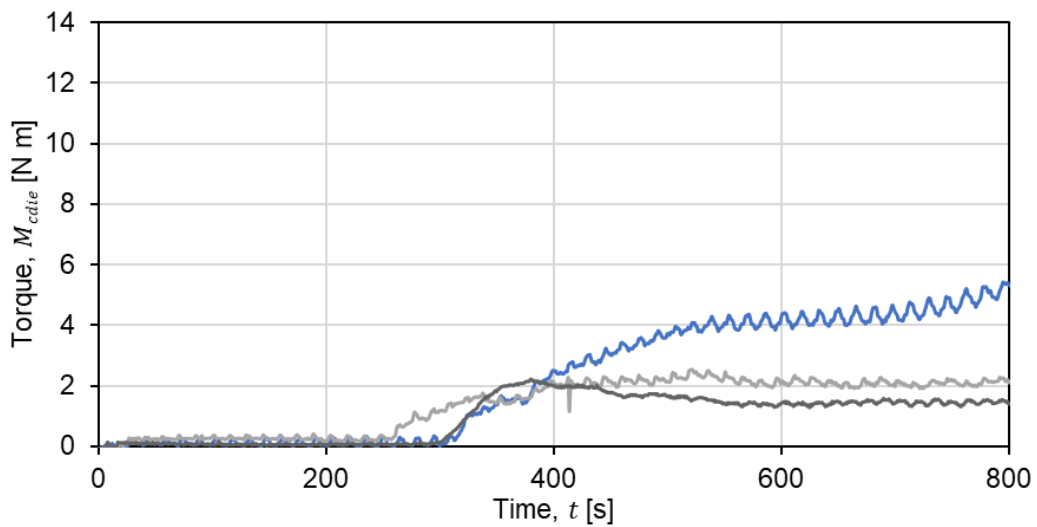


Figure A 14: T120-V300-R11-H1-FV0.56-IMR3.0.

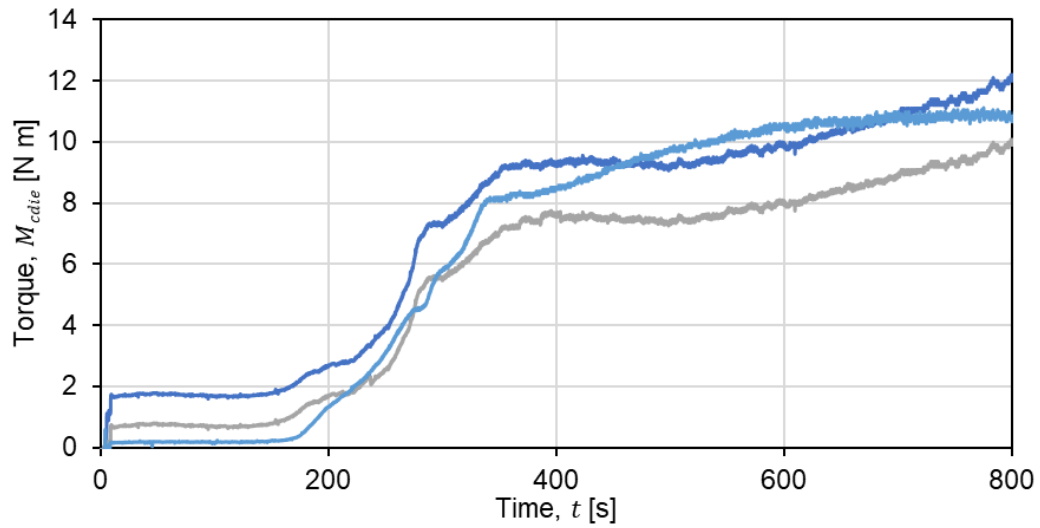


Figure A 15: T140-V300-R11-H1-FV0.61-IMR1.5.

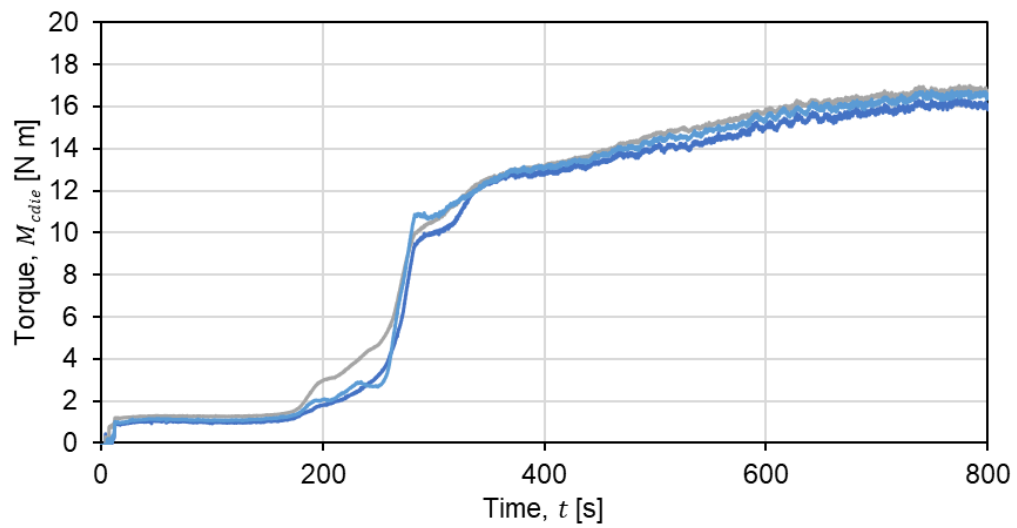


Figure A 16: T140-V100-R11-H1-FV0.61-IMR0.5.

B. Gelation point determination

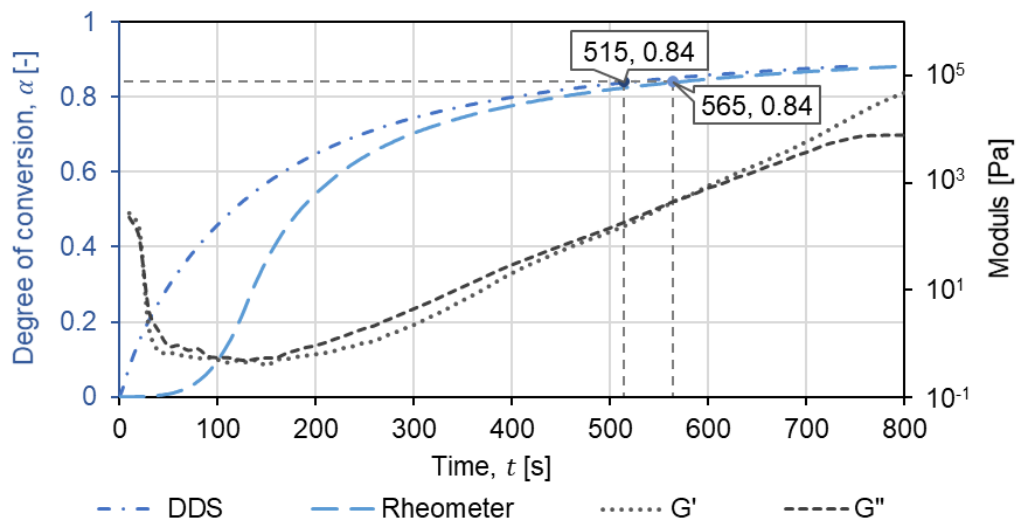


Figure B 1: Gelation point determination for DDS measurements from the degree of conversion determined at the gel point on the rheometer (measurement temperature 120 °C).

C. Pulling force measurement

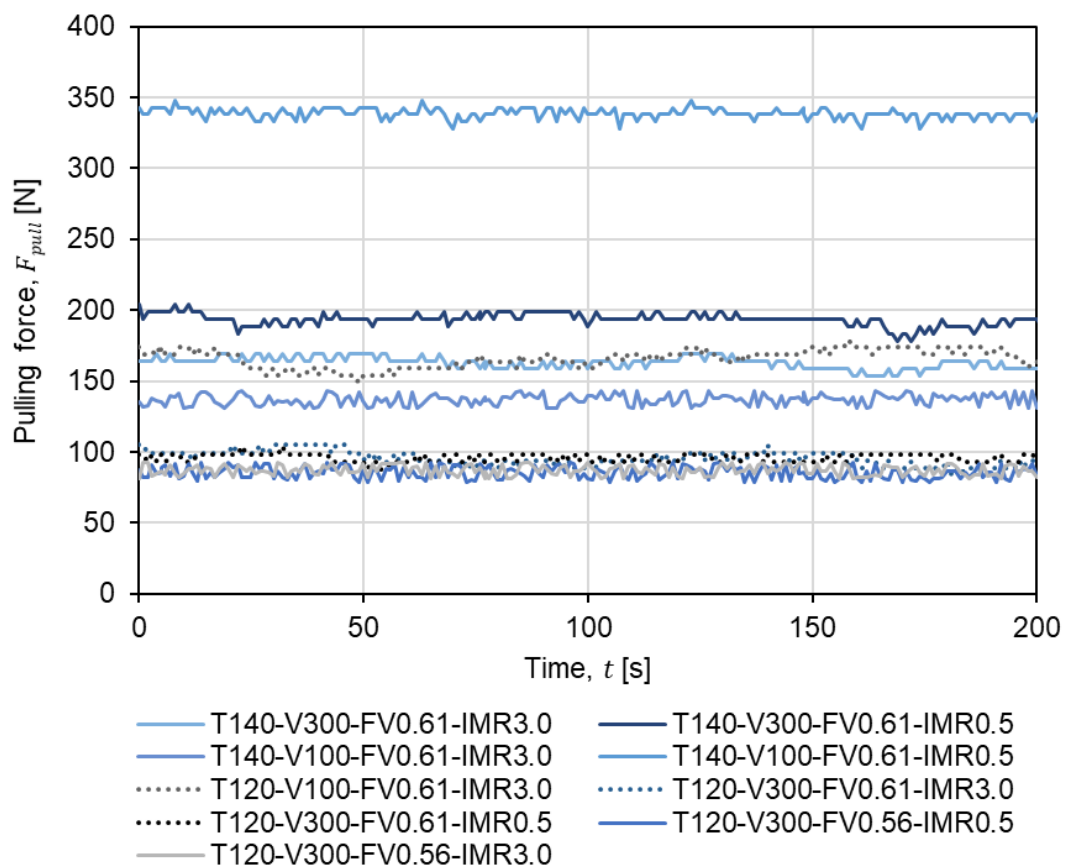


Figure C 1: Characteristic pulling force measured in-line during the pultrusion with the varying process and material parameter

